Universidad de Granada

Dinámica **Ambiental**
UNIVERSIDAD DE GRANADA

Instituto Interuniversitario de Investigación del Sistema Tierra en Andalucía (IISTA)

Programa de Doctorado de Dinámica de Flujos Biogeoquímicos y sus Aplicaciones

Universidad de Granada

Numerical modeling of hydro-morphodynamics in fluvial/tide-dominated coastal environments: from the tidal channel to the inner shelf

Doctoral Thesis

Alfonso M Jiménez Robles
Advisor: Miguel Ortega Sánchez
May 2017

Editor: Universidad de Granada. Tesis Doctorales
Autor: Alfonso M. Jiménez Robles
ISBN: 978-84-9163-296-2
URI: http://hdl.handle.net/10481/47996

El doctorando **Alfonso M Jiménez Robles** y el director de la tesis **Miguel Ortega Sánchez**, garantizamos, al firmar esta tesis doctoral, que el trabajo ha sido realizado por el doctorando bajo la dirección del director de la tesis y hasta donde nuestro conocimiento alcanza, en la realización del trabajo, se han respetado los derechos de otros autores a ser citados, cuando se han utilizado sus resultados o publicaciones.

Granada, a 25 de mayo de 2017.

Director de la tesis:

Fdo.: Miguel Ortega Sánchez

Doctorando:

Alfonso

Fdo.: Alfonso M Jiménez Robles

Acknowledgments

The author wish to express his sincere gratitude to the Environmental Fluid Dynamics Group of the University of Granada for the support and friendship received during these years. Special thanks to my advisor, Miguel Ortega Sánchez, who gave me this opportunity.

The author is also thankful to Stefano Lanzoni and Sergio Fagherazzi for their hospitality and generous collaboration in the development of this Thesis during the stays carried out at Padova University and Boston University respectively. Two real life experiences.

Finally, this work has been financially supported by the *Ministerio de Educación, Cultura y Deporte* of the Spanish Government through a FPU (*Formación de Profesorado Universitario*) grant AP2012-5431.

Introducción, objetivos y conclusiones de la Tesis

Los entornos costeros son complejos enclaves de transición entre la tierra y el mar desde un punto de vista social y medioambiental. Estas regiones albergan importantes núcleos de población, constituyen la base donde se asientan relevantes actividades socio-económicas y han atraído a multitud de formas de vida, tanto animal como vegetal, favoreciendo la biodiversidad. Su continua exposición a contingencias climáticas, al calentamiento global, y a las acciones antropogénicas hacen de ellos unos ecosistemas altamente vulnerables. Nuevos esfuerzos desde la comunidad científica se hacen necesarios con el objetivo de desarrollar y establecer nuevas estrategias que permitan la comprensión de los fenómenos que gobiernan su dinámica y a su vez su adecuada gestión medioambiental. Sin embargo, y pese a la creciente presión social, económica y ambiental existente sobre estos entornos, el conocimiento que sobre numerosos procesos ecológicos que dictan el destino de los mismo es aún limitado.

La morfología de los entornos costeros viene dictada fundamentalmente por la entrada de sedimentos procedentes del aporte fluvial y la posterior redistribución de los mismos por parte de las propias corrientes fluviales, el oleaje, y corrientes mareales. A día de hoy existe una gran cantidad de literatura acerca de los procesos físicos involucrados en la muta interrelación entre estos procesos hidrodinámicos y el correspondiente transporte de sedimentos, esto es, acerca de los procesos hidro-morfodinámicos capaces de modelar estos ecosistemas. Sin embargo, las cuestiones relativas a la dinámica hidro-morfodinámica de entornos costeros abarca un amplio espectro de unidades morfológicas y en condiciones ambientales. En este sentido, estas unidades morfológicas menores de las que se componen los entornos costeros pueden dividirse de acuerdo a los límites espaciales alcanzados por los distintos procesos costeros que tuvieron lugar durante el Cuaternario, dando lugar a una subdivisión en tres zonas: llanura litoral, franja costera y plataforma continental. Estas tres unidades constituyen el escenario sobre el que las descargas fluviales, el oleaje generado por el viento en contacto con las masas de agua oceánicas y las corrientes asociadas a la acción mareal actúan, aportando la energía necesaria para el modelado de las mismas. Es por tanto que el grado de importancia relativa entre la energía aportada por estas fuentes externas (aporte fluvial, oleaje, marea), junto con la inherente variedad geológica y sedimentaria de las distintas unidades costeras (llanura costera, franja costera, plataforma continental), da lugar a una rica variedad de escenarios costeros marcados por unos escalas de variación espacio-temporal muy particulares. Esto ha dado lugar una importantísima riqueza medioambiental que, a su vez, viene acompañada de una gran cantidad de interrogantes que dificultan una racional comprensión de la fenomenología hidro-morfodinámica que en ellos tiene lugar.

El objetivo fundamental de esta Tesis es la exploración y comprensión mediante modelos numéricos de procesos hidro-morfodinámicos cuyo conocimiento a día de hoy es limitado y que tienen lugar a diferentes escalas espaciales y temporales en entornos costeros fundamentalmente dominados por el aporte energético fluvial y mareal, abarcando diferentes unidades costeras: (i) llanura costera (canales mareales que diseccionan llanos mareales; y un sistema de lagunas costeras semicerrado separado del mar por una barrera sedimentaria cuyas aperturas permiten el intercambio con el oceáno), (ii) la franja costera en la que desembocan agentes fluviales, y (iii) la plataforma continental más interior. La división de esta Tesis en diferentes unidades morfológicas y el esfuerzo llevado a cabo para la modelización de los procesos hidro-morfodinámicos que en ellas tienen lugar ejemplifica el modo en el que la comunidad científica aborda e integra las complejidades espacio-temporales de los mismos.

Para la consecución de este objetivo principal, se establecieron una serie de cuestiones relativas a los procesos evolutivos que marcan la dinámica de ciertas unidades costeras y cuya respuesta a día de hoy, no ha sido clarificada de un modo riguroso: (i) ¿Puede la pluma de descarga asociada a un canal mareal afectar su equilibrio desde un punto de vista morfodinámico? (ii) ¿Cómo afectan los eventos de tormenta a la estabilidad y resiliencia de un sistema de lagunas costeras? (iii) ¿Cuáles son las implicaciones que las características geométricas de una desembocadura fluvial pueden tener sobre la dinámica de la propia descarga y sobre los patrones sedimentarios asociados? (iv) ¿Cómo determina la pendiente y fricción de la plataforma continental los depósitos sedimentarios resultantes de una corriente de turbidez?.

La necesidad de dar respuesta a las preguntas formuladas anteriormente constituye los objetivos específicos de esta Tesis, cuya consecución constituye el cuerpo central de esta Tesis. Su planteamiento, junto con un breve resumen de los resultados obtenidos y de las conclusiones derivadas de su abordaje, se presentan a continuación:

- *Desarrollar un modelo que acople de manera dinámica los procesos de un canal mareal y su pluma de descarga con objeto de evaluar la interrelación hidrodinámica y morfodinámica existente entre ambos.*

  Se desarrolló un modelo numérico que acoplaba la hidro-morfodinámica del canal mareal (region *onshore*, modelo 1d) con la hidrodinámica en la región oceánica próxima a la entrada al canal (region *offshore*, modelo 2d). En la región *offshore* el flujo se modela de manera diferente en función de la fase mareal. Durante la fase de vaciante la pluma queda definida por la *jet theory*, mientras que durante la fase de llenante el flujo irrotacional,plano y no viscoso es modelado mediante la teoría potencial una transformación tipo *Schwarz-Christoffel.* La transferencia entre ambas regiones de la masa de sedimento transportado en suspensión se lleva a cabo mediante una ecuación de advección-difusión con la que los fenómenos de desfase entre procesos erosivos y de deposición, fundamentales en este tipo de entornos mareales, son tenidos en cuenta. Los resultados muestran que la pluma juega un papel crucial en el modelado morfodinámico del canal. A consecuencia de la misma, la concavidad del canal en la parte próxima a la desembocadura se reduce y por tanto menores profundidades surgen en estas secciones. Por su parte, la propia evolución del canal afecta a la pluma de descarga, reduciendo su ancho, velocidad y sedimento en suspensión transportado. Además, diferentes simulaciones fueron llevadas a cabo para determinar las consecuencias que diferentes configuraciones tanto del canal como de la plataforma continental tienen sobre la evolución global del sistema. Finalmente, resultados del modelo fueron comparados con datos batimétricos de una canal mareal localizado en el suroeste de España, la ría de Punta Umbría, encontrando que los resultados modelados reproducen de manera satisfactoria las condiciones de este entorno natural.

- *Evaluar la respuesta (resiliencia) de un sistema de lagunas costeras ante la acción de evento de tormenta.*

  Se determinó el balance del flujo sedimentario existente entre un sistema de lagunas costeras localizado en el *Virginia Coast Reserve (VCR)* de la Peninsula de Delmarva, Virgina (USA) y el océano colindante. Mediante una detallada base de datos batimétricos, climáticos, de composición sedimentaria del sistema, se llevó a cabo un proceso previo de calibración y validación del modelo hidro-morfodinámico de alta resolución con el que evaluar la respuesta del sistema a 52 tormentas encontradas entre los años 2009 y 2015. Los resultados mostraron que los eventos de tormenta tienden a incorporar sedimento al sistema y, por tanto, aumenta la resiliencia del mismo ante la amenaza que la continua crecida del nivel del mar supone para estos entornos. De hecho, la acumulación media de sedimento en el sistema generaba una elevación del mismo de entre 2.01 y 5.30 mm al año. De entre los diferentes agente climáticos analizados (intensidad del oleaje, velocidad y dirección del viento, marea meteorológica), la duración y la intensidad de la sobreelevación del nivel del mar a consecuencia de la marea meteorológica durante un evento de tormenta fue el factor más importante que determinaba la tasa de incorporación de sedimento al sistema.

- *Analizar los efectos de la pendiente de la plataforma receptora de una descarga fluvial sobre la dinámica de la descarga y sobre los procesos sedimentarios asociados.*

  Un modelo analítico de *jet theory* junto a un modelo hidro-morfodinámico de alta resolución se emplearon en este caso. El empleo conjunto de ambos permitió extender el primero mediante un coeficiente de *entrainment* variable con la pendiente de la cuenca receptora, por medio del cual, mayores pendientes daban lugar a una mayor capacidad de la pluma de descarga de incorporar agua ambiente. Además, la pendiente de la cuenca determina de manera directa la estabilidad de la descarga. Grandes pendientes tienden a desestabilizar la descarga, dando lugar a las típica estructuras vorticales que le infieren a la descarga un aspecto meandriforme. Estas implicaciones hidrodinámicas tendrán una influencia directa sobre los procesos y patrones de deposición sedimentaria de la descarga tales como la forma en planta de la barra de depósito, la importancia relativa de los procesos de agradación y progradación de la barra, los requerimientos hidrodinámicos para la bifurcación de la descarga en torno a la barra y el tiempo de formación de la misma.

- *Establecer un marco teórico que permita identificar la distintas morfologías sedimentarias que se generarán en una desembocadura fluvial en función de la geometría de la misma.*

  En este caso se busca establecer un diagrama que permita determinar, en función del ángulo que forman la descarga fluvial con la línea de costa y en función de la pendiente de la zona de desembocadura, la tipología de barra sedimentaria que tenderá a generarse. Para ello, un modelo numérico hidro-morfodinámico de alta resolución fue empleado para, en primer lugar, analizar cómo la disposición geométrica de la desembocadura afecta a la propia descarga. Los resultados de las simulaciones mostraron que la descarga se ve alterada en dos sentidos: (i) ve alterada su trayectoria y (ii) ve modificada su forma en planta. Estas implicaciones hidrodinamicas tendrán su respuesta morfodinámica a través de la formación de cinco tipos de barras diferentes: barra central con o sin formaciones sedimentarias laterales o *levees*, barra desviada con o sin formaciones sedimentarias laterales o *levees*, y flecha de arena conectada a la propia línea de costa. Mientras que las cuatro primeras producen la bifurcación del flujo de descarga, la última provoca un giro brusco del mismo. Finalmente, la definición del diagrama de barras sedimentarias se corroboró mediante fotografías satélite de depósitos sedimentarios encontrados en desembocaduras cuyas características geométricas reproducían las simuladas.

- *Determinar la influencia de las características de la plataforma continental (pendiente y fricción) sobre los procesos sedimentarios asociados a una corriente de turbidez.*

  El papel de la pendiente y de la fricción de la plataforma continental sobre los depósitos sedimentarios asociados a un evento de corriente de turbidez es evaluado. Estos eventos suelen estar ligados a cursos fluviales montañosos de carácter estacional de escasa longitud. Los resultados mostraron que si bien la pendiente del fondo ejerce su influencia sobre la cuña sedimentaria (unidad morfológica de gran escala), la fricción de fondo lo hace sobre las ondulaciones sedimentarias formadas sobre la primera (unidades morfológicas de pequeña escala). Mayores pendientes dan lugar a cuñas sedimentarias de mayor longitud, con *topsets* de menor longitud y *foresets* de mayor pendiente. Por su parte, fondos con un coeficiente de fricción mayor generan un mayor número de ondulaciones, reduciendo estas su longitud y altura.

Abstract

The title of this PhD Thesis, "*Numerical modeling of hydro-morphodynamics in fluvial/tide-dominated coastal environments: from the tidal channel to the inner shelf*", may look like somehow multifaceted and ambiguous. It is therefore relevant to state in this preface what we intend to address throughout the present document.

This Thesis is about coastal environments processes linked to a set of factors that drive and control the dynamic of two main basis elements that co-evolve in time and space: water and sediment. The interplay between these two elements introduces the term hydro-morphodynamics as the mutual coupling and bidirectional readjustment of the fluxes of water and sediments and the surface morphology of subaqueous landscapes. The methodology followed to address this feedback interaction is based on the employment of high-resolution, physically-based numerical models and on the self-development of simplified long-term hydro-morphodynamic models. These numerical models provide virtual laboratories that allow to quantitatively investigate the physical processes that produce the rich diversity of coastal landforms. We apply these numerical methods to several morphological units of the coastal environment, encompassing the different regions of coastal environments, from the coastal plain to the continental shelf, and including the intermediate shoreface. These morphological units are controlled by a set of environmental conditions that provide the energy responsible for their evolution. Among these environmental conditions, this work focuses on morphological units dominated by terrestrial (river-dominated) or by marine (tide-dominated) sources of coastal energy.

The structure of this Thesis is then based on a sequential methodology organized around the spatial zonation of different coastal units subjected to fluvial or tidal sources of energy responsible for their evolution:

I. First, we discuss the existence of a long-term equilibrium configuration of **tidal channel** systems dynamically coupled to their offshore plumes. This is accomplished adopting a quasi two-dimensional numerical model that resolves the fully nonlinear unsteady shallow water, sediment bed load transport and suspended sediment advection-diffusion equations along with the Exner equation for the bathymetric changes in the tidal channel. These equation are dynamically coupled to a simple model of the plume hydrodynamics to estimate the net exchange of sediment associated with the two-phase sequence of tidal events. Whereas the ebb-flow is modeled as a bounded plane turbulent jet, a Scharwz-Christoffel conformal transformation is implemented to map a plane, irrotational, sink flood-flood in the physical plane. Results reveals that the offshore plume plays a crucial role on shaping the tidal channel. As a consequence of the offshore plume, the seaward concavity of the profile reduces and smaller inlet depths arise. The model results are also in good agreement with nature in terms of bathymetric profile for the Punta Umbría ría (Southwestern Spain). Numerical experiments with different channel, oceanic and tidal

characteristics are performed, and the hydro-morphodynamic consequences are also examined. Finally, the feedback between channel and plume also alters the plume dynamics and progressively reduces the ability for tidal channel to generate mouth bar deposits.

II. Secondly, the stability of a shallow **coastal bays** system in the face of tropical cyclones and other storms is evaluated and quantified. Under normal conditions, tidal currents is the main mechanism responsible for their sediment dynamics. However, it is still unclear how coastal bays respond to storm events. Developing a sediment budget for these coastal bays is imperative to understanding how storm events affect the resilience of the system. Sediment budgets can be used to gain an understanding of the different sediment inputs (sources) and outputs (sinks) involved. Using high resolution numerical simulations, we show that intense storms import sediment into a system of coastal bays within the Virginia Coast Reserve (VCR), located on the Atlantic side of the Delmarva Peninsula, USA. Duration and magnitude of storm surge are among the most important factors in sediment import, suggesting that intense storms increase the stability of coastal bays by providing the sediment necessary to counteract sea level rise. It must be emphasized that we are using a hard dataset of climate conditions, water levels, bathymetric data and sediment size distributions both inside the VCR bays and for the adjacent coastal ocean. Only with this kind of data it is possible to understand where the sediment is resuspended during a storm and where it goes. We do not provide only model results, we provide hard data.

III. Then, we move forward toward the shoreface (**river mouth**) to analyze the mutual dependence between an exiting sediment-laden turbulent jet and resulting river mouth bar morphology in a fluvial-dominated scenario. This scenario was conceived and dealt with a double focal point:

III.a. We use a high resolution numerical model along with a formulation of jet theory to reproduce the physics of the problem under different receiving basin slopes. An updated turbulent jet theory is proposed with a slope-dependent entrainment coefficient, showing that the rate at which ambient fluid is incorporated into a jet increases with higher basin slopes. This analysis also shows that the basin slope alters jet dynamics, favors the formation of an unstable meandering jet, and consequently determines sedimentary processes responsible for bar formation such as river mouth bar geometry, relative importance of bar aggradation and progradation, hydrodynamic requirements for flow bifurcation, and river mouth bar time formation.

III.b. In a second turbulent jet-river mouth bar formation scenario we address the implications of the river mouth geometry on the discharge dynamics. We study the role of the receiving basin slope and the river discharge angle using a high resolution coupled hydrodynamic- sediment transport model. This analysis shows that the river mouth geometry can deflect jet direction and alter the jet spreading rate. As a consequence of these hydrodynamic alterations, the conditions encountered by the sedimentary processes are modified, resulting in five different river mouth morphologies. We also establish a theoretical framework for the specific morphology of the mouth bar as a function of the river mouth geometry. Finally, predicted mouth bar morphologies display similarities to natural systems.

IV. Finally, this Thesis concludes with the application of a numerical model of turbidity current events in order to understand their interaction with the **inner shelf** in a fluvial-dominated scenario. We focus this study on the influence of the slope of the receiving basin and of the Manning friction coefficient of the seabed on the formation of a deltaic wedge and seafloor undulations developed over the latter. As a general rule, we conclude that the receiving basin slope highly dominates the formation and subsequent development of deltaic wedges, whereas the bottom friction dictates the evolution of their wavy structure. Moreover, preliminary results indicate an agreement with published field observations in some river deltas of the Alboran Sea of the undulations length and height, which encourages us in the task of extending and validating the present model with the aim of reproducing these undulate structures in real situations.

Contents

Contents **xiii**

List of Figures **xvii**

List of Tables **xxix**

1 Introduction **1**
1.1 Motivation and justification of the unity and coherence of the Thesis 1
1.2 Objectives 2
1.3 Outline of the Thesis 3
1.4 Publications derived from this Thesis 3

2 Implications of plume discharge on tidal channel morphodynamics **5**
2.1 Introduction 5
2.2 Mathematical description of the model 7
2.2.1 Model geometry 8
2.2.2 Hydrodynamic model 9
2.2.3 Morphodynamic model 24
2.2.4 Numerical Scheme 32
2.3 Results 34
2.3.1 Influence of offshore plume on the tidal channel evolution 34
2.3.2 Towards an equilibrium configuration of the tidal channel: hydrodynamics and morphodynamics implications 38
2.3.3 Role of external factors on tidal channel-offshore plume dynamics 63
2.4 Discussion 74
2.4.1 Main novelties of the model 74
2.4.2 Temporal scales considerations 77
2.4.3 Comparison with field data: application to Punta Umbria ría 79
2.4.4 Model limitations 81
2.5 Concluding Remarks 82

3 How do intense storms affect the resilience of coastal bays? **85**
3.1 Introduction 85
3.2 Methodology 86
3.2.1 Numerical model 86
3.2.2 Model setup 87
3.2.3 Model calibration 89
3.2.4 Storms definition 91
3.3 Results 92

3.3.1 Cumulative sediment flux in a storm event 93
3.3.2 Sediment dynamics 94
3.3.3 Analysis of a specific storm event 97
3.4 Discussion and conclusion 98

4 Effects of basin bottom slope on jet hydrodynamics and river mouth sedimentary patterns 103
4.1 Introduction 103
4.2 Theoretical framework 105
4.3 Numerical model 108
4.3.1 Hydrodynamic model 108
4.3.2 Sediment transport 109
4.3.3 Model setup 110
4.4 Influence of bottom slope on jet hydrodynamics 112
4.4.1 Time-mean hydrodynamics properties 112
4.4.2 Effects of bottom slope on jet stability 115
4.5 Morphological results: river mouth bar 118
4.5.1 River mouth bar formation 118
4.5.2 River mouth bar geometry 119
4.5.3 Theoretical model for bar formation 122
4.6 Discussion 124
4.6.1 Application to natural river mouths and deltas 124
4.6.2 Comparison with previous works on bar formation 126
4.7 Conclusions 128

5 Influence of river mouth geometry on mouth bar morphology and discharge hydrodynamics 131
5.1 Introduction 131
5.2 Methods 132
5.2.1 Hydrodynamic model 133
5.2.2 Morphological model 133
5.2.3 Experimental setup 134
5.3 Jet hydrodynamic 134
5.4 River mouth bar morphology 136
5.5 Discussion and concluding remarks 137

6 Influence of the inner shelf characteristics on turbidity current deposits 141
6.1 Introduction 141
6.2 Numerical model description 144
6.3 Numerical experiments 149
6.4 Results 150
6.4.1 Characterization of large scale morphological units: deltaic wedges 151
6.4.2 Characterization of small scale morphological units: seafloor undulations . 155
6.5 Discussion and concluding remarks 160

7 Conclusions and future research 161
7.1 Main conclusions 161
7.2 Future research 164

A Sensitive analysis **165**

Bibliography **167**

List of Figures

2.1 Sketch of a tidal channel-offshore plume system and basic notation. 8

2.2 Analytical solutions for the offshore ebb flow close to the tidal inlet. Sketch of a turbulent jet exiting a tidal channel during the ebb-phase. The velocity field magnitude is indicated through the colorbars. 13

2.3 Analytical solutions for the offshore flood flow close to the tidal inlet. Conformal mapping of a flow entering a channel based on Schwarz-Christoffel transformation ($z = f(w)$) and sketch of the flood flow in the (b) transformed (τ-plane) and (c) physical (z-plane) domains. In (a) and (b) the grid of the spacial transformation is preserved (white lines) for clarity. The velocity peaks at the edges of the inlet are due to flow separation where geometrical discontinuities are present. Vectors only indicate flow direction. The velocity field magnitude is indicated through the colorbars. 18

2.4 Analytic solutions of a flat bottom streamlines (a) and from a linearly sloping bottom (b) under the influence of a half-sink. 23

2.5 Definition sketch for the offshore plume sediment concentration in a jet exiting a tidal channel during the ebb phase. 28

2.6 Temporal evolution of the bottom profile from an initially horizontal configuration for a convergent tidal channel (a) with and (b) without the influence of the offshore plume. The bottom elevation at each cross section has been scaled with the initially uniform depth of the channel ($\eta^*/d(t=0)$), while the longitudinal coordinate of the tidal channel has been scaled with the channel length ($\xi = x/L_e$). The values of the relevant parameters imposed in the calculation are $L_e = 30$ km, $L_b = 25$ km, $b_0 = 160$ m, initial bottom depth $d(t=0) = 5$ m, semidiurnal tide with amplitude $a_0 = 2.2$ m, mean sediment diameter of $d_s = 100$ μm. The continental shelf is supposed to be horizontal with a mean Chezy coefficient $C_z = 55$ m$^{1/2}$/s. A comparison between the cases (a) and (b) is depicted in the panel (c) for the sake of clarity. Horizontal dashed lines represent the high tide (H.T.), mean sea level (M.S.L.) and low tide (L.T.) elevations at the channel mouth. 35

2.7 Root-mean-square of the bed level changes between successive tidal cycles computed over all grid cells in the tidal channel as a function of tidal cycles throughout tidal channel evolution. Two cases are depicted: RMS of bed level changes evolution in convergent tidal channel with (red lines) and without (green lines) the influence of the offshore plume. Two inset-zoom are included for a clear display of evolutionary changes between cases at different stages of the simulations. Dashed lines are the median filtered signal of the original RMS series using local window-size of 301 elements. Initial conditions: $L_e = 30$ km, $L_b = 25$ km, $b_0 = 160$ m, $d(t=0) = 5$ m, $a_0 = 2.2$ m, $d_s = 100$ μm, and horizontal continental shelf with $C_z = 55$ m$^{1/2}$/s 37

2.8 Values along the tidal channel of (a) maximum, minimum, difference between maximum and minimum and residual velocity, (b) degree of asymmetry of flood and ebb velocity peaks, (c) degree of asymmetry of the flood and ebb phases duration, (d) extreme values of the dimensionless free surface elevation, (e) dimensionless tidal range, and (e) phase lag between the maximum water surface elevation and the maximum flood speed. Red lines refer to the beginning of the simulation while blue lines refer to the equilibrium configuration. In panel (d) the horizontal dashed line marks mean sea level (M.S.L.) elevations at the channel mouth, while the semitransparent lines depict the normalized bed profiles η^*. Vertical dashed lines indicate the position of the inner shoreline once the equilibrium is reached. Initial conditions: $L_e = 30$ km, $L_b = 25$ km, $b_0 = 160$ m, $d(t=0) = 5$ m, $a_0 = 2.2$ m, $d_s = 100\ \mu$m, and horizontal continental shelf with $C_z = 55$ m$^{1/2}$/s 40

2.9 Velocity (u) and dimensionless free surface elevation (h^*) during three tidal cycles at different locations along the tidal channel: (a) $\xi = 0$, (b) $\xi = 0.2$, (c) $\xi = 0.4$, (d) $\xi = 0.5$, (e) $\xi = 0.6$, and (f) $\xi = 0.8$, at the beginning of the simulation (red lines) and at equilibrium (blue lines). The intermediate tidal cycle is highlighted for clarity. Due to drying process at $\xi = 0.8$, variables at equilibrium are not plotted in this location. Initial conditions: $L_e = 30$ km, $L_b = 25$ km, $b_0 = 160$ m, $d(t=0) = 5$ m, $a_0 = 2.2$ m, $d_s = 100\ \mu$m, and horizontal continental shelf with $C_z = 55$ m$^{1/2}$/s . . . 42

2.10 (a) Residual difference between deposition and erosive sediment fluxes, (b) residual bed load sediment flux, (c) residual contribution of the deposition and erosive sediment fluxes to the bathymetric changes of the tidal channel, and (d) residual contribution of the bed load sediment flux to the bathymetric changes of the tidal channel. Red lines refer to the beginning of the simulation while blue lines refer to the equilibrium configuration. Vertical dashed lines indicate the position of the inner shoreline once the equilibrium is reached. Initial conditions: $L_e = 30$ km, $L_b = 25$ km, $b_0 = 160$ m, $d(t=0) = 5$ m, $a_0 = 2.2$ m, $d_s = 100\ \mu$m, and horizontal continental shelf with $C_z = 55$ m$^{1/2}$/s 44

2.11 Velocity, u, and depositional, D_e, and erosive, E_r, fluxes of suspended sediment during three tidal cycles at different locations along the tidal channel: (a) $\xi = 0$, (b) $\xi = 0.2$, (c) $\xi = 0.4$, (d) $\xi = 0.5$, (e) $\xi = 0.6$, and (f) $\xi = 0.8$, at the beginning of the simulation (red lines) and at equilibrium (blue lines). The intermediate tidal cycle is highlighted for clarity. Due to drying process at $\xi = 0.8$, variables at equilibrium are not plotted in this location. Initial conditions: $L_e = 30$ km, $L_b = 25$ km, $b_0 = 160$ m, $d(t=0) = 5$ m, $a_0 = 2.2$ m, $d_s = 100\ \mu$m, and horizontal continental shelf with $C_z = 55$ m$^{1/2}$/s. 46

2.12 Velocity, u, and depositional, D_e, and erosive, E_r, fluxes of suspended sediment during three tidal cycles at $\xi = 0.2$, at the beginning of the simulation (red lines) and at equilibrium (blue lines). The intermediate tidal cycle is highlighted for clarity. The inset window shows a detailed zoom of the deposition and erosive fluxes and settling lag effects close to slack tide. Dashed regions represents the period of time during which settling lag occurs. An Initial conditions: $L_e = 30$ km, $L_b = 25$ km, $b_0 = 160$ m, $d(t=0) = 5$ m, $a_0 = 2.2$ m, $d_s = 100\ \mu$m, and horizontal continental shelf with $C_z = 55$ m$^{1/2}$/s. 47

2.13 Velocity, u, and difference between depositional and erosive fluxes of suspended sediment, $D_e - E_r$, during three tidal cycles at different locations along the tidal channel: (a) $\xi = 0$, (b) $\xi = 0.2$, (c) $\xi = 0.4$, (d) $\xi = 0.5$, (e) $\xi = 0.6$, and (f) $\xi = 0.8$, at the beginning of the simulation (red lines) and at equilibrium (blue lines). The intermediate tidal cycle is highlighted for clarity. Due to drying process at $\xi = 0.8$, variables at equilibrium are not plotted in this location. Initial conditions: $L_e =$ 30 km, $L_b = 25$ km, $b_0 = 160$ m, $d(t = 0) = 5$ m, $a_0 = 2.2$ m, $d_s = 100$ μm, and horizontal continental shelf with $C_z = 55$ m$^{1/2}$/s. 48

2.14 Temporal evolution of the residual (a) depositional, $\langle D_e \rangle$, and (b) erosive, $\langle E_r \rangle$, fluxes of suspended sediment integrated all along the tidal channel (black line) and integrated along different tidal channel stretches (dashed lines) [first or seaward quarter (blue line), second quarter (green line), third quarter (orange line), and fourth or landward quarter (red line)]. Initial conditions: $L_e = 30$ km, $L_b = 25$ km, $b_0 = 160$ m, $d(t = 0) = 5$ m, $a_0 = 2.2$ m, $d_s = 100$ μm, and horizontal continental shelf with $C_z = 55$ m$^{1/2}$/s. 49

2.15 Temporal evolution of the difference between depositional and erosive fluxes of suspended sediment, $\langle D_e - E_r \rangle$, integrated all along the tidal channel (black line) and integrated along different tidal channel stretches (dashed lines) [first or seaward quarter (blue line), second quarter (green line), third quarter (orange line), and fourth or landward quarter (red line)]. The inset-zoom depicts the asymptotic trend reached by the different curves. Initial conditions: $L_e = 30$ km, $L_b = 25$ km, $b_0 = 160$ m, $d(t = 0) = 5$ m, $a_0 = 2.2$ m, $d_s = 100$ μm, and horizontal continental shelf with $C_z = 55$ m$^{1/2}$/s. 50

2.16 Velocity, u, and dimensionless bed load sediment flux, $q_b/q_{b,0}$, during three tidal cycles at different locations along the tidal channel: (a) $\xi = 0$, (b) $\xi = 0.2$, (c) $\xi =$ 0.4, (d) $\xi = 0.5$, (e) $\xi = 0.6$, and (f) $\xi = 0.8$, at the beginning of the simulation (red lines) and at equilibrium (blue lines). The intermediate tidal cycle is highlighted for clarity. Due to drying process at $\xi = 0.8$, variables at equilibrium are not plotted in this location. Initial conditions: $L_e = 30$ km, $L_b = 25$ km, $b_0 = 160$ m, $d(t = 0) =$ 5 m, $a_0 = 2.2$ m, $d_s = 100$ μm, and horizontal continental shelf with $C_z = 55$ m$^{1/2}$/s. 52

2.17 Temporal evolution of the dimensionless residual bed load sediment flux , $\langle q_b/q_{b,0} \rangle$, integrated all along the tidal channel (black line) and integrated along different tidal channel stretches (dashed lines) [first or seaward quarter (blue line), second quarter (green line), third quarter (orange line), and fourth or landward quarter (red line)]. Initial conditions: $L_e = 30$ km, $L_b = 25$ km, $b_0 = 160$ m, $d(t = 0)$ $= 5$ m, $a_0 = 2.2$ m, $d_s = 100$ μm, and horizontal continental shelf with $C_z = 55$ m$^{1/2}$/s. 53

2.18 Variation of the net suspended sediment concentration field in space and time. The concentration have been normalized with its maximum value. The inset window is a zoom of the main plot. Initial conditions: $L_e = 30$ km, $L_b = 25$ km, $b_0 =$ 160 m, $d(t = 0) = 5$ m, $a_0 = 2.2$ m, $d_s = 100$ μm, and horizontal continental shelf with $C_z = 55$ m$^{1/2}$/s. 53

2.19 Relative influence both in space and time of the different mechanisms that affect the temporal evolution of the net suspended sediment concentration field: (a) erosion-deposition contribution, (b) diffusive contribution, and (c) advective contribution. Initial conditions: $L_e = 30$ km, $L_b = 25$ km, $b_0 = 160$ m, $d(t = 0) = 5$ m, $a_0 = 2.2$ m, $d_s = 100$ μm, and horizontal continental shelf with $C_z = 55$ m$^{1/2}$/s. . 55

2.20 Tidal prism (P) and minimum cross-sectional channel area (A_{min}) at different tidal cycles and at different locations along the tidal channel: (a) $\xi = 0$, (b) $\xi = 0.2$, (c) $\xi = 0.4$, (d) $\xi = 0.5$, (e) $\xi = 0.6$, and (f) $\xi = 0.8$. Due to drying process at $\xi = 0.8$, values of minimum channel area vanish. Initial conditions: $L_e = 30$ km, $L_b = 25$ km, $b_0 = 160$ m, $d(t = 0) = 5$ m, $a_0 = 2.2$ m, $d_s = 100$ μm, and horizontal continental shelf with $C_z = 55$ m$^{1/2}$/s. Notice the different y-scales of the different panels. 56

2.21 Tidal prism, P, versus (a) minimum cross-sectional flow area, A_{min}, and (b) maximum cross-sectional flow area, A_{max}, for various sections along the tidal channel at the beginning of the simulation (red circles) and at equilibrium (blue circles). The black dashed line represents the O'Brien-Jarrett-Marchi relationship of D'Alpaos et al. (2010) for a channel mean value of $k_{ap} = 2 \times 10^{-3}$, and $\alpha_{ap} = 1$. Initial conditions: $L_e = 30$ km, $L_b = 25$ km, $b_0 = 160$ m, $d(t = 0) = 5$ m, $a_0 = 2.2$ m, d_s = 100 μm, and horizontal continental shelf with $C_z = 55$ m$^{1/2}$/s. 57

2.22 Temporal evolution of (a) the dimensionless bottom profile of the tidal channel, (b) plume centerline velocity, (c) plume half-width, and (d) plume centerline sediment concentration. Initial conditions: $L_e = 30$ km, $L_b = 25$ km, $b_0 = 160$ m, $d(t = 0) = 5$ m, $a_0 = 2.2$ m, $d_s = 100$ μm, and horizontal continental shelf with C_z = 55 m$^{1/2}$/s. 59

2.23 Rate contours of bottom erosion and deposition in the continental shelf, K_{jet}, at different stages of tidal channel evolution: (a) beginning of the simulation, (b) 100 tidal cycles, (c) 500 tidal cycles, (d) 2000 tidal cycles, (e) 5000 tidal cycles, and (f) 20000 tidal cycles (equilibrium). Black dashed lines delimits the region in which erosion/deposition processes take place. The continental shelf coordinates have been scaled with the tidal channel mouth half-width ($b_0/2$). Each panel includes an inset with the corresponding state of the tidal channel profile. Initial conditions: $L_e = 30$ km, $L_b = 25$ km, $b_0 = 160$ m, $d(t = 0) = 5$ m, $a_0 = 2.2$ m, $d_s = 100$ μm, and horizontal continental shelf with $C_z = 55$ m$^{1/2}$/s. Erosion in the continental shelf has been neglected in this simulation. 61

2.24 Velocity at the tidal channel mouth (u at $\xi = 0$) and sediment concentration entering the tidal channel from the offshore plume (c) during a tidal cycle, at different stages of tidal channel evolution: (a) beginning of the simulation, (b) 100 tidal cycles, (c) 500 tidal cycles, (d) 2000 tidal cycles, (e) 5000 tidal cycles, and (f) 20000 tidal cycles (equilibrium). Each panel includes an inset with the corresponding state of the tidal channel profile. Initial conditions: $L_e = 30$ km, $L_b = 25$ km, $b_0 = 160$ m, $d(t = 0) = 5$ m, $a_0 = 2.2$ m, $d_s = 100$ μm, and horizontal continental shelf with $C_z = 55$ m$^{1/2}$/s. 62

2.25 (a) Normalized tidal channel planform width investigated in the present numerical tests. The length and width of the tidal channel mouth are kept fixed ($L_e = 30$ km and $b_0 = 160$ m) while the convergence length L_b is varied ($L_b = 10$ km, $L_b = 25$ km, and $L_b \to +\infty$ km). (b) Initial and equilibrium configurations of the bottom profile for the three planform shapes depicted in panel (a). Horizontal dashed lines represent the high tide (H.T.), mean sea level (M.S.L.) and low tide (L.T.) elevations at the channel mouth. Initial conditions: $d(t = 0) = 5$ m, $a_0 = 2.2$ m, $d_s = 100$ μm, and horizontal continental shelf with $C_z = 55$ m$^{1/2}$/s. 64

2.26 Values along the tidal channel of maximum, minimum, and residual velocity at the beginning of the simulation (a) and at equilibrium (b), and dimensionless tidal range at the beginning of the simulation (c) and at equilibrium (d) for different values of the convergence length ($L_b = 10$ km, $L_b = 25$ km, and $L_b \rightarrow +\infty$ km). Vertical dashed lines indicate the position of the inner shoreline once the equilibrium is reached for each convergence length. Initial conditions: $L_e = 30$ km, $b_0 =$ 160 m, $d(t=0) = 5$ m, $a_0 = 2.2$ m, $d_s = 100\ \mu$m, and horizontal continental shelf with $C_z = 55$ m$^{1/2}$/s. 65

2.27 Variation of the net suspended sediment concentration field in space and time for different values of the convergence length: (a) $L_b = 10$ km, (b) $L_b = 25$ km, and (c) $L_b \rightarrow +\infty$ km. The concentration have been normalized with the maximum value of the three cases simulated. Initial conditions: $L_e = 30$ km, $b_0 = 160$ m, $d(t=0) =$ 5 m, $a_0 = 2.2$ m, $d_s = 100\ \mu$m, and horizontal continental shelf with $C_z = 55$ m$^{1/2}$/s. 65

2.28 Tidal prism, P, versus (a) minimum cross-sectional flow area, A_{min}, and (b) maximum cross-sectional flow area, A_{max}, for various sections along the tidal channel at the beginning of the simulation (red markers) and at equilibrium (blue markers) for different values of the convergence length ($L_b = 10$ km, $L_b = 25$ km, and $L_b \rightarrow +\infty$ km). The black dashed line represents the O'Brien-Jarrett-Marchi relationship of D'Alpaos et al. (2010) for a channel mean value of $k_{ap} = 2 \times 10^{-3}$, and $\alpha_{ap} = 1$. Initial conditions: $L_e = 30$ km, $b_0 = 160$ m, $d(t=0) = 5$ m, $a_0 = 2.2$ m, d_s = 100 μm, and horizontal continental shelf with $C_z = 55$ m$^{1/2}$/s. 66

2.29 (a) Plume centerline velocity, (b) plume half-width, and (c) plume centerline sediment concentration both at the beginning of the simulation and at equilibrium for different values of the convergence length ($L_b = 10$ km, $L_b = 25$ km, and $L_b \rightarrow +\infty$ km). Initial conditions: $L_e = 30$ km, $b_0 = 160$ m, $d(t=0) = 5$ m, $a_0 = 2.2$ m, $d_s =$ 100 μm, and horizontal continental shelf with $C_z = 55$ m$^{1/2}$/s. 67

2.30 (a) Plume centerline velocity, (b) plume half-width, and (c) plume centerline sediment concentration both at the beginning of the simulation and at equilibrium for different values of the continental shelf bottom slope ($m_b = 0\%$ and $m_b = 5\%$). Initial conditions: $L_e = 30$ km, $b_0 = 160$ m, $d(t=0) = 5$ m, $a_0 = 2.2$ m, $d_s = 100\ \mu$m, and continental shelf with $C_z = 55$ m$^{1/2}$/s. 69

2.31 Difference along the tidal channel of the normalized bottom profile level at equilibrium for different continental shelf bottom slopes ($m_b = 0\%$, $m_b = 0,1\%$, $m_b = 0,5\%$, $m_b = 1\%$, $m_b = 2\%$, and $m_b = 5\%$) with respect to the reference case in which the continental shelf is assumed to be horizontal ($m_b = 0\%$). The blue line depicts the equilibrium configurations of the bottom profile for the reference case. Initial conditions: $L_e = 30$ km, $L_b = 25$ km, $b_0 = 160$ m, $d(t=0) = 5$ m, $a_0 =$ 2.2 m, $d_s = 100\ \mu$m, and continental shelf with $C_z = 55$ m$^{1/2}$/s. 70

2.32 (a) Plume centerline velocity, (b) plume half-width, and (c) plume centerline sediment concentration both at the beginning of the simulation and at equilibrium for different values of the Chezy friction coefficient of the continental shelf ($C_z = 30$ m$^{1/2}$/s, $C_z = 55$ m$^{1/2}$/s, and $C_z = 80$ m$^{1/2}$/s). Initial conditions: $L_e = 30$ km, $b_0 =$ 160 m, $d(t=0) = 5$ m, $a_0 = 2.2$ m, $d_s = 100\ \mu$m, and an horizontal continental shelf. 71

2.33 Difference along the tidal channel of the normalized bottom profile level at equilibrium for different Chezy friction coefficient of the continental shelf (C_z = 30 m$^{1/2}$/s, C_z = 45 m$^{1/2}$/s, C_z = 55 m$^{1/2}$/s, C_z = 65 m$^{1/2}$/s, C_z = 80 m$^{1/2}$/s) with respect to the reference case in which this Chezy coefficient is assumed to be C_z = 55 m$^{1/2}$/s. The blue line depicts the equilibrium configurations of the bottom profile for the reference case. Initial conditions: L_e = 30 km, L_b = 25 km, b_0 = 160 m, $d(t=0)$ = 5 m, a_0 = 2.2 m, d_s = 100 μm, and an horizontal continental shelf. 72

2.34 Bottom equilibrium profiles for different values of the initial depth of the channel ($d(t0=0)$ = 5 m, $d(t0=0)$ = 6 m, and d(t0=0)= 7 m,). The red line depicts the initial channel profile. Horizontal black dashed lines represent the mean sea level (M.S.L.) at the channel mouth for each case. Initial conditions: L_e = 30 km, L_b = 25 km, b_0 = 160 m, a_0 = 2.2 m, d_s = 100 μm, and horizontal continental shelf with C_z = 55 m$^{1/2}$/s. 72

2.35 Bottom equilibrium profiles scaled with the initially uniform depth of the channel for different values of the tidal amplitude (a_0 = 1.2 m, a_0 = 1.7 m, and a_0 = 2.2 m). The red line depicts the initial channel profile. Horizontal black dashed lines represent the high tide (H.T.), mean sea level (M.S.L.) and low tide (L.T.) elevations at the channel mouth for each tidal amplitude. Initial conditions: L_e = 30 km, L_b = 25 km, b_0 = 160 m, $d(t=0)$ = 5 m, d_s = 100 μm, and horizontal continental shelf with C_z = 55 m$^{1/2}$/s. 73

2.36 Rate contours of bottom erosion and deposition in the continental shelf, K_{jet}, at different stages of tidal channel evolution (a) at the beginning of the simulation, and (b) at equilibrium. Black dashed lines delimits the region in which erosion/deposition processes take place. The continental shelf coordinates have been scaled with the tidal channel mouth half-width ($b_0/2$). Initial conditions: L_e = 30 km, L_b = 25 km, b_0 = 160 m, $d(t=0)$ = 5 m, a_0 = 2.2 m, d_s = 100 μm, and horizontal continental shelf with C_z = 55 m$^{1/2}$/s. 73

2.37 Plume centerline sediment concentration both at the beginning of the simulation and at equilibrium neglecting and considering erosive processes in the continental shelf. Initial conditions: L_e = 30 km, L_b = 25 km, b_0 = 160 m, $d(t=0)$ = 5 m, a_0 = 2.2 m, d_s = 100 μm, and horizontal continental shelf with C_z = 55 m$^{1/2}$/s. 74

2.38 Velocity at the tidal channel mouth (u at $\xi=0$) and sediment concentration entering the tidal channel both from the offshore plume and the eroded material in the continental shelf (c) during a tidal cycle, at different stages of tidal channel evolution: (a) beginning of the simulation, (b) 500 tidal cycles, (c) 5000 tidal cycles, and (e) 20000 tidal cycles (equilibrium). Initial conditions: L_e = 30 km, L_b = 25 km, b_0 = 160 m, $d(t=0)$ = 5 m, a_0 = 2.2 m, d_s = 100 μm, and horizontal continental shelf with C_z = 55 m$^{1/2}$/s. 75

2.39 Temporal evolution of the bottom profile from an initially horizontal configuration for a convergent tidal channel (a) with and (b) without the influence of the eroded material in the continental shelf. The bottom elevation at each cross section has been scaled with the initially uniform depth of the channel ($\eta^*/d(t=0)$), while the longitudinal coordinate of the tidal channel has been scaled with the channel length ($\xi = x/L_e$). The values of the relevant parameters imposed in the calculation are $L_e = 30$ km, $L_b = 25$ km, $b_0 = 160$ m, initial bottom depth $d(t=0) = 5$ m, semidiurnal tide with amplitude $a_0 = 2.2$ m, mean sediment diameter of $d_s = 100$ μm. The continental shelf is supposed to be horizontal with a mean Chezy coefficient $C_z = 55$ m$^{1/2}$/s. Differences between the cases (a) and (b) at each tidal cycle are depicted in panel (c). Horizontal dashed lines represent the high tide (H.T.), mean sea level (M.S.L.) and low tide (L.T.) elevations at the channel mouth. 76

2.40 Plot of different sediment entrainment into suspension pickup functions (E_{ent}) as a function of dimensionless shear velocity (u_*/w_s). The thick black line of van Rijn (1984c) was the function used here. 78

2.41 Satellite image of the ría of Punta Umbría (Spain) planform, including a longitudinal transect along its main tidal channel [cuortesy of Google Earth]. 79

2.42 Model results of temporal evolution of the bottom profile up to reach an equilibrium configuration (continuos colored lines) and measured bottom elevation along the main tidal channel of the Punta Umbría ría (Huelva, Spain) (thick black line). The dashed red line depicts the equilibrium profile for the case in which the offshore plume influence was neglected. The longitudinal coordinate ξ has been scaled with the channel length. The horizontal dashed lines represents mean sea level (M.S.L.). The values of the relevant parameters imposed to the model are L_e = 15 km, $L_b = 10$ km, $b_0 = 200$ m, initial bottom depth $d(t=0) = 6$ m, semidiurnal tide with amplitude $a_0 = 1.6$ m, mean sediment diameter of $d_s = 80$ μm. The continental shelf is supposed to have a slope $m_b = 1\%$ and a mean Chezy coefficient $C_z = 55$ m$^{1/2}$/s. 81

3.1 Location map for the southern Delmarva Peninsula, bounded by Chesapeake Bay to the west and the Atlantic Ocean to the east (USA). The Virginia Coast Reserve (VCR) comprises the barrier islands, bays and marshes on the eastern side of the southern (Virginia portion) of the Delmarva Peninsula. Also shown are the locations of the different stations used in this worl. 86

3.2 Shaded-relief bathymetry of the study area, comprising the VCR coastal bays system, indicating the location of the grids used in the numerical model and the location of the different stations. The bathymetric contours are given in meters below the present sea level. The red dashed line delimits the control volume for the computation of the sediment budget of the VCR lagoons. 88

3.3 Sediment bottom composition in the VCR coastal bays system. Spatial distribution of (a) very fine mud 20μm, (b) mud 63μm, and (c) sand 125μm. Scale is the proportion of the type of sediment, derived from Wiberg et al. (2015) and Fenster et al. (2016). Black lines represent the water-land boundary. 89

3.4 Comparison of the computed (grey) and measured (black) (a) wave height and (b) wave direction at the location of the station 44096 - Cape Charles NOAA during the storm number 40. Blue lines indicate the wave conditions imposed at the boundary of the WAVE domain and collected by the station 44014 - Virginia Beach NOAA. 91

3.5 Comparison of the simulated with Delft3D (grey circles) and measured (black line) water levels at Wachapreague station (ID: 8631044), Virginia. 92

3.6 (a) Peaks Over Threshold (POT) analysis for wind speed. Only events with a wind speed above 11 m/s and a minimum distance between events of 5 days were considered as storms. (b) Example of identification of the storm number 1 period. The storm begins (ends) before (after) four full tides with a storm surge below 0.2 m with respect to the wind peak time. 93

3.7 Total cumulative flux as a function of wind direction. Wind speed was 11 m/s and the simulation time was 15 days. Negative values of the total cumulative flux (sediment budget) indicated sediments entering the VCR. 94

3.8 Relationship between total cumulative flux and the amount of of hours that wind directions is between 60° to 240° during a storm event. There is a negative total cumulative flux (net accumulation of sediment into the system) as total hours during which wind blows from 60° to 240° increase. 94

3.9 Relationship between total cumulative flux and A) maximum wave height, B) maximum wind speed and C) maximum storm surge. There is a negative total cumulative flux (net accumulation of sediment into the system) as all study parameters increase in intensity. 95

3.10 Relationship between total cumulative flux and the product between magnitude and duration of A) wave height above 2m B) wind speed above 10 m/s and C) storm surge above 0.5m. There is a negative total cumulative flux (net accumulation of sediment into the system) as all study parameters increase in magnitude and duration. 96

3.11 Mean cumulative elevation differences in the system for all 52 study storms. Red areas indicate accumulation. Blue areas indicate erosion. Black lines represent the water-land boundary. 97

3.12 Relationship between maximum storm surge and total cumulative flux of A) 20μm very fine mud, B) 63μm mud, and C) 125μm sand. There is a significant negative relationship between total cumulative flux and intensity of storm surge for very fine mud (20μm) and mud (63μm), indicating net accumulation. 98

3.13 Initial spatial distribution of (A) very fine mud 20μm, (B) mud 63μm, and (C) sand 125μm, derived from Wiberg et al. (2015) and Fenster et al. (2016). Average final spatial distribution of (D) very fine mud 20μm, (E) mud 63μm, and (F) sand 125μm, for all 52 study storms. Scale is the proportion of the type of sediment. (G), (H), and (I) depict average change in bottom sediment composition for all 52 study storms, averaged for each kind of sediment, very fine mud 20μm, mud 63μm, and sand 125μm, respectively. Scale is percent change from initial to final bottom composition. 99

3.14 Storm number 38 (from 26-jan-2014 19:00 to 21-jan-2014 20:00) (A) wave height, (B) wind speed, (C) wind direction, (D) storm surge, (E) ratio of deposition area to erosion area within the VCR system, (F) percent change in bottom composition of each sediment specie within the VCR system, and (G) cumulative flux of each specie and total cumulative flux between the VCR system and the ocean (negative fluxes indicate sediment import). 100

4.1 Computational domain and boundary conditions. 110

4.2 (a) Delft3D normalized distribution of the mean longitudinal velocity u and (b) Delft3D normalized distribution of transverse velocity v, both along a cross section located at $\xi = 10$ from the river outlet for different basin slopes, ranging from 0% to 10%. Blue colors represent a near horizontal bottom, whereas the red colors represent higher bottom slopes. Vertical dashed lines mark the width of the jet. The thick black line in (a) represents the slope-mean profile from the Delft3D data, and the dashed curves represent the similarity profiles proposed by several authors (SP-1 : Özsoy and Ünlüata (1982), SP-2: Wang (1984), SP-3: Joshi (1982), SP-4: Giger et al. (1991), and SP-5: Paillat and Kaminski (2014)). 113

4.3 Values of the entrainment coefficient against the receiving basin bottom slope for three different bottom friction values ($C_z = 40$ m$^{1/2}$/s, $C_z = 55$ m$^{1/2}$/s and $C_z = 70$ m$^{1/2}$/s) in planar turbulent jets calculated from both numerical simulations in Delft3D (red elements) and by adjusting analytical solutions to the numerical simulations (blue elements). Dots represent the computed values, and lines show a power law fit of the dots. For α_{JT} adjustments $a_1 = [0.024, 0.022, 0.019]$, $a_2 = [0.504, 0.583, 0.637]$ and $a_2 = [0.002, 0.002, 0.002]$, respectively for $C_z = [40, 55, 70]$ m$^{1/2}$/s. Fittings are significant with 95 % confidence. 114

4.4 Normalized centerline velocity computed with (a) turbulent jet theory and (b) Delft3D, and normalized velocity half-width computed with (c) turbulent jet theory and (d) Delft3D, for different basin slopes ranging from 0% to 10%. 115

4.5 Effects of bottom slope on jet stability. Given river discharge conditions ($u_0 = 1.5$ m/s, $b_0 = 50$ m, $h_0 = 3$ m, and $C_z = 55$ m$^{1/2}$s^{-1}), a sufficient bed slope makes flow unstable. (a) and (c) are snapshots of depth-averaged velocity fields for a horizontal bottom (m = 0%) and a sloping bottom (m = 4%), respectively. (b) and (d) are the vorticity fields corresponding to the velocity fields in (a) and (c), respectively. In (d) the presence of two asymmetric rows of aligned vortices with opposite directions of rotation can be observed. 116

4.6 Jet stability diagram from Canestrelli et al. (2014b). The continuous red line (Eq. (10) from Canestrelli et al. (2014b)) divides the plot space into a stable and unstable jet region. The dotted grey lines delimit a transition zone where both stable and unstable jets can be present. Different sections ($\xi = 0$ (river mouth), 5, 10, 15 and 20) along the jet axis for different bottom slopes (m = 0%, 0.5%, 1%, 2%, 4%, 6%, 8%, and 10%) were characterized. The increase in bottom slope tends to diminish the stability of the flow downstream. The black star depicts the river mouth bar conditions in the different cases. Inset: Corresponding one-dimensional energy spectra of turbulent fluctuations of the cross-stream velocity v' at a point on the x-axis. The data were collected at $\xi = 10$. The black and grey dotted lines follow −3 and −5/3 power laws respectively, and are depicted to highlight changes in spectral decay from the peak for unstable cases. 117

4.7 Centerline relative velocity over the crest of the river mouth bar as a function of the relative depth over the crest of the bar for different basin slopes, ranging from 0% to 10%. The black line shows the decreasing relative water depth necessary to cause bar stagnation with higher slopes. 118

4.8 (a) Stratigraphic record of the cohesive to non-cohesive sediment ratio in the topmost 20 cm of the bottom over the time of bar formation (shown by the colorbar) along the jet axis for a case with an initial bottom slope of $m = 1\%$. Temporal evolution of a river mouth bar for a bottom slope of (b) $m = 1\%$ and (c) $m = 8\%$. Colored dots depict the location of the centroid of every bar profile at every temporal stage (shown by the colorbar). Black dashed lines define the final bar configuration. (d) Temporal evolution of the centroid location of the river mouth bar for different initial bottom slopes. (e) Temporal evolution of the relative aggradation to progradation rate of the river mouth bar for different initial bottom slopes. 120

4.9 (a) Relative time of river mouth bar formation (T_{rmbf}) as a function of basin bottom slope for different suspended load values for non-cohesive sediment. Solid lines represent the best linear regression fit. (b) Relative distance of river mouth bar formation (L_{rmbf}) as a function of the basin bottom slope for different suspended load values for non-cohesive sediment. Solid lines represent the best negative exponential regression fit. All values were normalized using the value of the horizontal bottom and equilibrium non-cohesive suspended discharge case. 121

4.10 Longitudinal (a, b, c, d) and transversal (e, f, g, h) bathymetric profiles of the absolute bar height variation over time (indicated with the color evolution) for different bottom slopes. The transversal section is located 400 m from the river mouth. Black lines indicate the final bar configuration. 122

4.11 (a) Spreading bar factor normalized with respect to the spreading bar factor for the horizontal case as a function of initial bottom slope. Dimensionless water depth map of a river mouth bar forcing the flow to bifurcate around it for cases with initial bottom slope of (b) 0% (stable jet) and (c) 10% (unstable jet). The depth-averaged velocity vectors are superimposed. 123

4.12 Theoretical solutions for normalized fields of bottom deposition and erosion thickness rates (K) for different basin bottom slopes: (a) $m = 0\%$, (b) $m = 1\%$, (c) $m = 5\%$, and (d) $m = 10\%$. The river discharge properties are $c_0 = 0.5$ kg/m^3, $b_0 = 50$ m, $h_0 = 3$ m and $u_0 = 1.5$ m/s. The black dots depict the location of the maximum deposition rate along the centerline. 124

5.1 Sketch of the computational domain and boundary conditions. 132

5.2 Depth-averaged velocity contours lines for different discharge angles ((a) $\alpha = 0^{\circ}$, (b) $\alpha = 30^{\circ}$ and (c) $\alpha = 60^{\circ}$) and basin slopes (m =0, 1 and 3%). In every jet, the velocity contours refer to 1, 0.8, 0.6, 0.4 and 0.2 m/s, being the $0.2 m/s$ contour the external one. 135

5.3 (a) Jet axis path in the receiving basin with respect to the fixed reference system (x-y) for different discharge angles and basin bottom slopes. (b) Deflection Rate for different discharge angles and basin bottom slopes. (c) Spreading Rate for different discharge angles and basin bottom slopes. 136

5.4 Phase space plot of river mouth bar morphology as a function of discharge angle (α) and basin slope (m). Each area identifies a specific morphology of deposited sediments with an example snapshot depicting the bottom depth contour map with superimposed velocity vectors: (a) CRMB: central river mouth bar, (b) SRMB: sided river mouth bar, (c) SS: sand-spit, (d) SRMB+L: sided river mouth bar with lateral levees, and (e) CRMB+L: central river mouth bar with lateral levees. Stars represent the river mouth bar geometry of different natural systems reported in Section 5.5. 137

5.5 Satellite images of (a) Apalachicola river mouth deposits (CRMB) [Apalachicola Bay, USA, 29°44'N, 84°56'W, Image Landsat/Copernicus], (b) Ochlockonee river mouth deposits (SRMB) [Ochlockonee Bay, USA, 29°58'N, 84°26'W, Imagel'2016 DigitalGloble], (c) Batchawana river mouth deposits (SS) [Batchawana Bay, Lake Superior, Canada, 46°55'N, 84°31'W, l'2016 Cnes/Spot Image], (d) Goulais river mouth deposits (SRMB+L) [Goulais Bay, Lake Superior, Canada, 46°43'N, 84°27'W, Imagel'2016 DigitalGloble], and (e) Ramis river mouth deposits (CRMB+L) [Lake Titicaca, Peru, 15°19'S, 69°45'W, Imagel'2016 CNES/Astrium]. Red arrows indicate discharge directions, red lines indicate shoreline alignment, red dashed lines indicate bar deposits and green dashed lines indicate lateral levees. [Images courtesy of Google Earth]. 139

6.1 Triangular classification of deltaic depositional systems of Galloway (1975). [From Masselink et al. (2003)]. 142

6.2 The three generic morpho-stratigraphic units found in a typical deltaic system: delta plain or *topset*, delta front or *foreset*, and prodelta or *bottomset*. [From Masselink et al. (2003)]. 143

6.3 Sketch of a turbidity current and basic notation. 146

6.4 Piecewise linear bathymetric profiles used for the numerical simulations. 150

6.5 Deltaic wedge and seafloor undulations formation and evolution at different stages (every 12 hours) of the numerical simulations during a total period of 5 days. All simulations are carried out over a fixed initial piecewise linear bathymetric profile (initial slope = 1.25°, offshore slope = 0.3°) and different Manning coefficients between simulations: 0.0075 (A), 0.01 (B), 0.0225 (C), and 0.03 (D). Flow inputs, sediment properties and the remaining numerical parameters are given in Section 6.3. 152

6.6 Deltaic wedge and seafloor undulations formation and evolution at different stages (every 12 hours) of the numerical simulations during a total period of 5 days. All simulations are carried out with a fixed Manning coefficient of 0.0225 and over a different initial piecewise linear bathymetric profile with initial slope: 0.3°(A), 1°(B), 1.5°(C), and 2°(d), and offshore slope = 0.3°). Flow inputs, sediment properties and the remaining numerical parameters are given in Section 6.3. 153

6.7 Contour plots of the main morphological parameters that characterize the deltaic wedges as a function of the slope of the receiving basin and the Manning friction coefficient of the seafloor: Deltaic wedge length (A), topset length (B), foreset slope (C), distal limit depth (D), offlap-break elevation (E), and formation of a distal deposit (F). Black markers represents the simulated values of each morphological parameters obtained with our numerical simulations. Flow inputs, sediment properties and the remaining numerical parameters are given in Section 6.3. 155

6.8 Seafloor undulations over the foreset of the deltaic wedge and filtered foreset at the end of the simulation (5 days). This simulation corresponds to the numerical experiments with an initial piecewise linear bathymetric profile with initial slope of 1 and a Manning coefficient of 0.0225. Flow inputs, sediment properties and the remaining numerical parameters are given in Section 6.3. 156

6.9 Seafloor undulations elevations over the foreset of the deltaic wedge at the end of the simulation (5 days). Red stars and blue circles depict the undulation crests and the basis of the undulation respectively. This simulation corresponds to the numerical experiments with an initial piecewise linear bathymetric profile with initial slope of 1 and a Manning coefficient of 0.0225. Flow inputs, sediment properties and the remaining numerical parameters are given in Section 6.3. 157
6.10 Contour plots of the main morphological parameters that characterize the seafloor undulations over a deltaic wedge as a function of the slope of the receiving basin and the Manning friction coefficient of the seafloor: number of seafloor undulations (A), mean seafloor undulations length (B), mean seafloor undulations height (C), mean seafloor undulation form index (D), and mean seafloor undulation asymmetry index (E). Black markers represents the simulated values of each morphological parameters obtained with our numerical simulations. Flow inputs, sediment properties and the remaining numerical parameters are given in Section 6.3. 158

List of Tables

3.1 Starting, ending and wind speed peak dates for the 52 storms simulated in this study. The stations in which wind, WL (water level) and wave data were acquired are also gathered (**WACH**: Wachapreague, VA-Station (ID: 8631044), **CBBT**: Chesapeake Bay Bridge Tunnel, VA - Station (ID: 8638863), **44099**: NOAA 44099 wave station, Cape Henry, VA, **44014**: NOAA 44014 wave buoy, 64 NM East of Virginia Beach, VA). The superscript ^{1} indicates that water level signal at Wachapreague Station was delayed and dampened as indicated in Section 3.2.3. In storms number 1,2 and 3 WACH^1 (CBBT) means that, due to gaps in water level records at Wachapreague, an analog downscaling technique trained with data from the close Chesapeake Bay Bridge Tunnel, VA - Station (ID: 8638863) was applied to derive water levels at Wachapreague Station 102

4.1 User-defined model parameters in Delft3D for numerical experiments in this work. The superscript ^{a} indicates that Chezy values equal to 40 and 70 $\mathrm{m}^{1/2}\mathrm{s}^{-1}$ were used in additional simulations. The superscript ^{b} indicates that incoming suspended sediment discharge for non-cohesive sediment equal to 0.2, 0.5, 0.8 and 1.1 kg/m^3 were used in additional simulations. The superscript ^{c} refers to an equilibrium sand concentration profile adapted to the local inflow conditions at the river mouth boundary. In our simulations, it corresponds to 0.56 kg/m^3. 111

6.1 Sediments properties of the three species composing the granular material of the simulations. 150
6.2 Parameters used in the numerical experiments. 151
6.3 Main geomorphic characteristics of both the deltaic wedge and seafloor undulations obtained as a function of the receiving basin slope and Manning friction coefficient. Flow inputs, sediment properties and the remaining numerical parameters are given in Section 6.3. 159

A.1 Parameters sensitivity analysis. 166

Chapter 1

Introduction

1.1 Motivation and justification of the unity and coherence of the Thesis

It is well known that coastal environments are of enormous relevance from a social and environmental perspective (Small and Nicholls, 2003; Syvitski et al., 2009). These are complex transitional environments that have attracted large settlements of human population and their valuable natural resources have allowed the development of considerable socioeconomic activities. Indeed, in spite of these bordering zones constitute only a 5 percent of the surface of the Earth, they host close to two-thirds of the world's population (Inman and Brush, 1973). At the same time, coastal systems provide unique ecosystems for a wide range of animal and vegetal species, favoring biodiversity. Their exposure to climate hazards and global warming and the continuos threat of human-induced activities makes them highly vulnerable and new efforts to develop efficient strategies are required to their proper management. This vulnerability combined with the socio-economical pressure has led to a significant increase of the scientific interest in the behaviour of these ecosystems. However, despite their critical role for society and biodiversity, numerous processes at the heart of coastal environments are still poorly understood.

Sediment transport and hydrodynamic processes are the major mechanisms responsible for the variety of morphologies observed in these coastal systems. There exists a vast literature concerning the physical processes involved in their mutual interaction, which ultimately dictates coastal environments dynamics. However, questions regarding coastal processes encompass such a large variety of coastal units and environmental conditions (geology, sediment properties, external forcing). Such coastal units of our costal environment can be defined conform the convention presented in Masselink et al. (2003), according to which the spatial boundaries that limit the different units match the limits to which coastal processes during the Quaternary period extended. These boundaries organize the coastal zone in three morphological units that comprise the coastal plain, the shoreface and the continental shelf.

These units constitute the spatial erodible scenario over which the outflow of the rivers, waves generated by wind and tidal currents interact and shape the landscape, being ultimately responsible for the evolution of coastal environments. Therefore, the relative degree of dominance of the three main hydrodynamic processes (waves, tides and river outflow) alongside the variety of inherent geological and sedimentary features that characterize the different morphological units generate a wide range of coastal scenarios that evolve at different spatial and temporal scales, producing a richness of landforms and a number of complexities that hinder the knowledge of their phenomenology. Thus, there are some specific questions that remain unclear related to the effect that hydrodynamic variables have on coastal environments processes.

There is a real need to use and combine different methods and tools when addressing the the morphological evolutionary tendency of the coastal environment. Because field observations or laboratory experimentation to investigate the mutual adjustment of topography and fluid dynamics is hardly possible, in this Thesis we tackle this issue by means of different numerical methods based on theoretical principles of hydrodynamic and sediment transport phenomena. Numerical models have been revealed as a suited tool to unraveled the large-scale structure of the coastal environments, and allow a better understanding and characterization of the main processes and forcing interaction (Fagherazzi and Overeem, 2007).

This dissertation tries to shed light on some specific questions that remain unanswered on coastal environments: Could the offshore plume appreciably affect the morphodynamic equilibrium of a tidal channel? How do storm events affect the resilience and stability of a coastal bays system? What are the effects of the river mouth geometry on the river outflow hydrodynamics and related river mouth bar formation, a key geomorphological process on delta evolution? How do the ocean basin characteristics determine the formation of sedimentary wedges and seafloor undulated structures associated to a turbidity current event? Clarifying these issues may thus help in making correct interpretations of hydro-morphodynamic processes in coastal environments which knowledge is still limited.

The goal of this Thesis is then addressed following a sequential presentation of the numerical modeling of the hydro-morphodynamic evolution of fluvial/tide-dominated coastal environments based on a zoning criterion: (i) coastal plain (the inner tidal channels dissecting the shelf surface and a shallow coastal bays system), (ii) shoreface (the area in front of the mouth of rivers) and (iii) continental shelf (sedimentary morphologies in the relatively shallow waters of the inner shelf). The original research chapters that constitute the main body of this Thesis form an integrated dissertation and constitute an important step in the attainment of a response for the previously outlined questions, ensuring the coherence of the Thesis as a whole.

In conclusion, the subdivision of this Thesis in different morphological units and related efforts to model their dynamics provides an insight into the way in which modelers deal with the complexities of spatial- and temporal-scale and process integration (Fagherazzi and Overeem, 2007).

1.2 Objectives

The main objective of this Thesis is to numerically explore and understand the quantitative testing of specific and unclear hydro-morphodynamic processes that take place at different spatial- and temporal-scales on fluvial/tide-dominated coastal environments, encompassing different coastal units: tidal channel, a shallow coastal bays, river mouth, and inner shelf. Accordingly, the following specific objectives are defined to accomplish the main objective:

- To develop a coupled onshore and offshore numerical model in order to analyze the hydro-morphodynamics feedbacks between tidal channels and related discharge plumes in semienclosed tidal embayments.
- To evaluate how intense storm events affect the resilience of a coastal bays system.
- To analyze the effects of basin bottom slope at the river mouth on the discharge dynamics and on the related sedimentary processes.

- To establish a framework of mouth bar morphologies as a function of the basin slope and the river discharge angle.
- To determine the role of the inner shelf characteristics on the sedimentary processes of turbidity currents.

1.3 Outline of the Thesis

Apart from the introduction (**Chapter 1**) and the final chapter (**Chapter 7**), which summarizes the main conclusions of this Thesis and the future research lines, this document is divided into five main chapters. Each of them responds to one of the objectives outlined above.

Chapter 2 investigates the morphodynamic equilibrium of tidal channels dynamically coupled to their offshore discharge plumes through a self-developed numerical model. After describing the theoretical physics modeled in the numerical scheme, a detailed insight into the transient evolution of the main hydrodynamic and morphodynamic aspects of the system towards equilibrium is provided. Results reveals that the offshore plume plays a crucial role on shaping the tidal channel and that the tidal channel evolution also modifies the offshore plume characteristics over time. Finally, simulated tidal channel morphology is compared to a real tidal channel in the Southwestern Spain. Overall comparison seems to be fairly satisfactory.

Chapter 3 evaluates the resilience of a shallow coastal bays system in Virginia (USA) in the face of intense storm events. A sediment budget is developed to understanding how storm events affect the net import of sediment. A hard database of climate conditions, water levels, bathymetric data and sediment size distributions is imperative and therefore used to calibrate the high-resolution numerical model and to understand where the sediment is resuspended during a storm and where it goes.

The next two chapters concern the role of the river mouth geometry on modifying discharge dynamics and on shaping river mouth bars. **Chapter 4** addresses the role of receiving basin slope in the hydrodynamics of an exiting sediment-laden turbulent jet. We use a high-resolution numerical model along with a theoretical formulation to reproduce the physics of the problem and propose an updated theoretical model with a slope-dependent entrainment coefficient. Numerical simulations suggest that the basin slope alters jet dynamics and favors the formation of an unstable meandering jet. As a consequence of the hydrodynamic implications, receiving basin slope also governs the sedimentary processes at the river mouth. **Chapter 5** expands the previous one and emphasizes from a more practical perspective at providing a framework of river mouth deposits as a function of the receiving basin slope and the river discharge angle. Using a high resolution coupled hydrodynamic-sediment transport model, this analysis shows that the river mouth geometry can deflect jet direction and alter the jet spreading rate. As a consequence of these flow changes, the sedimentary processes are modified, resulting in five different river mouth morphologies. Predicted mouth bar morphologies display similarities to natural systems.

Chapter 6 is dedicated to the application of a numerical model of turbidity currents to analyze the influence of the slope of the inner shelf and of the friction of its seabed on the formation of sedimentary wedges and seafloor undulated structures over the latter.

1.4 Publications derived from this Thesis

Refereed Journal Papers

- **Jiménez-Robles AM**, Castagno KA, Donnelly JP, Wiberg PL, Fenster MS and Fagherazzi S (2017). Intense storms increase the stability of coastal bays. *Nature Geoscience (Under review).*

- **Jiménez-Robles AM** and Ortega-Sánchez M (2017). Implications of the river mouth geometry on the discharge dynamics. *Journal of Hydraulic Engineering (Submitted).*

- Palazzoli I, Leonardi N, **Jiménez-Robles AM** and Fagherazzi S (2017). Identification of the most effective factors responsible for the flushing of a tracer in a system of shallow bays. *Journal of Geophysical Research: Oceans (Under review).*

- **Jiménez-Robles AM**, Ortega-Sánchez M and Losada MÁ (2016). Effects of basin bottom slope on jet hydrodynamics and river mouth bar formation. *Journal of Geophysical Research: Earth Surface*, 121, 11001133. doi:10.1002/2016JF003871.

International Peer-Reviewed Conferences

- Castagno KA, **Jiménez-Robles AM**, Fagherazzi S and Donnelly JP (2016). Impacts of storm events on salt marsh sediment dynamics. *2016 Fall Meeting, AGU.* San Francisco (United States).

- **Jiménez-Robles AM**, Lanzoni S and Ortega-Sánchez M (2016). Implications of plume discharge for tidal channels morphodynamics: a coupled onshore and offshore system. *35th International Conference on Coastal Engineering (ICCE).* Antalya (Turkey).

- **Jiménez-Robles AM**, Ortega-Sánchez M and Losada MÁ (2015). Influence of the river mouth geometry on the morphological evolution of river mouth bars: Importance of water intake angle and basin bottom slope. *36th IAHR World Congress.* The Hague (the Netherlands).

- Tintoré-Parra Á, Reyes-Merlo MÁ, **Jiménez-Robles AM**, Ortega-Sánchez M, Losada MÁ (2015). Management strategies for highly altered estuaries: the case of Punta Umbría (Huelva, Spain). *ASLO, Aquatic Science Meeting.* Granada (Spain).

Spanish Peer-Reviewed Conferences

- **Jiménez-Robles AM**, Lira-Loarca A, Zarzuelo C and Ortega-Sánchez M (2016). Modelado numérico en desembocaduras fluviales. *I Jornadas de Investigadores en Formación. Fomentando la interdisciplinariedad.* Granada (Spain) (*in spanish*).

- **Jiménez-Robles AM**, Ortega-Sánchez M and Losada MÁ (2015). Implicaciones de la geometría de la desembocadura en la hidrodinámica y en los patrones de deposición sedimentaria de una descarga fluvial. *XIII Jornadas Españolas de Ingeniería de Costas y Puertos.* Avilés (Spain) (*in spanish*).

Chapter 2

Implications of plume discharge on tidal channel morphodynamics

In this Chapter the influence of the offshore plume on the long-term equilibrium configuration of a tidal channel is addressed. The equations that dictate the hydro-morphodynamic processes at the tidal channel are dynamically coupled to a simple model of the plume hydrodynamics to estimate the net exchange of sediment through the tidal channel mouth. Whereas the ebb-flow is modeled as a bounded plane turbulent jet, a Scharwz-Christoffel conformal transformation is implemented to map a plane, irrotational, sink flood-flood in the physical plane. Results reveal that the offshore plume plays a crucial role on shaping the tidal channel. As a consequence of the offshore plume, the seaward concavity of the profile reduces and smaller inlet depths arise. Finally, the feedback between channel and plume also alters the plume dynamics and progressively reduces the ability for tidal channel to generate mouth bar deposits. Numerical experiments with different channel, oceanic and tidal characteristics are performed, and the hydro-morphodynamic consequences are also examined. The model results are also in good agreement with nature in terms of bathymetric profile for the Punta Umbría ría (Southwestern Spain).

2.1 Introduction

Recalling the definition of Dalrymple et al. (1992), an estuary is the seaward portion of a drowned valley system which receives sediment from both fluvial and marine sources and which contains facies influenced by tide, wave and fluvial processes. We focus this work on the case of a well-mixed, tide-dominated estuary connected to its offshore plume in which river and waves processes are merely subordinates or neglected. There has been a tendency in the literature to associate tide dominance with mesotidal (tidal range 24 m) or macrotidal (tidal range > 4 m) regimes, but tidal dominance can also occur in microtidal areas provided wave energy is low enough or the tidal prism is large (e.g., Cheasapeake Bay and St. Lawrence Estuary) (Lanzoni and Seminara, 2002; Dalrymple et al., 2012). Well-studied examples of tide-dominated estuaries include Cobequid Bay-Salmon River, Bay of Fundy, the Severn River, Mont-Saint-Michel Bay, Thames, Gironde, Ord, South Alligator, and the Fitzroy River estuaries. These tidal estuaries are valuable transitional environments between ocean and the hinterland that host highly diverse biological and economical activities and, therefore, represent some of the most important ecosystems on Earth. From a management perspective, they are densely populated, constitute strategic navigation channels, comprise extensive industrial areas and agricultural lands due to the fertile soil of the adjacent floodplains, and shelter important fishing grounds (Pont et al., 2002; Ericson et al., 2006; Syvitski and Saito, 2007; Syvitski et al., 2009; Winterwerp et al., 2013). Furthermore, tidal networks exert a fundamental control on hydrodynamic, sediment and nutrient exchanges within tidal environments, which are characterized by highly heterogeneous landscapes and physical and biological properties (D'Alpaos et al., 2007; Kirwan and Murray, 2007; Marani et al., 2007). Thus, understanding the basic mechanisms responsible for their morphological evolution results of obvious practical relevance for the management of these ecosystems highly vulnerable to sea level rise, tectonic uplift, subsidence and anthropogenic interventions.

In recent years, different works have been developed to tackle the issue of the the possible existence of a long-term longitudinal equilibrium of tidal channels. For a detailed discussion of the concept of morphodynamic equilibrium in estuarine ambients the reader is referred to Zhou et al. (2017). Tidal channel morphodynamics is dictated by asymmetries in surface elevations and tidal currents that lead to a net sediment flux directed landward within a tidal cycle (De Swart and Zimmerman, 2009). Laboratory experiments (Tambroni et al., 2005), analytical methods (Schuttelaars and Swart, 1996, 2000; Prandle, 2003; Seminara et al., 2010; Toffolon and Lanzoni, 2010) and numerical techniques (Lanzoni and Seminara, 2002; Hibma et al., 2003; Todeschini et al., 2008; Van der Wegen and Roelvink, 2008; Yu et al., 2012; Bolla Pittaluga et al., 2015) found that, starting from an arbitrary initial bottom profile, the system asymptotically tends to a long-term morphodynamics equilibrium state with a nearly constant value of the maximum flood/ebb speed. In the absence of an upstream input of sediment, this dynamic equilibrium state is characterized by a vanishing net (tidally-averaged) transport in the entire embayment that results in a shoaling bed with water depths decreasing from the inlet to an emerging shore landward. On the other hand, when a given sediment discharge is supplied from upstream, morphodynamic equilibrium requires that the net sediment flux keeps constant along the channel and equal to the sediment flux delivered by the river.

In the above-mentioned numerical works, onshore tidal estuaries and offshore discharge plumes are not treated as a whole. A fixed boundary condition is prescribed at the estuary mouth by which during the ebb phase the sediment load at the inlet simply exits the estuary whereas during the flood phase an entering sediment load in equilibrium with the local instantaneous hydrodynamics is prescribed. On the other hand, works focused on offshore plume processes are carried out in a framework of no connectivity with the issuing channel. Related fluid dynamics and sediment patterns on the oceanic region are based on a boundary condition at the channel mouth (Wright, 1977; Özsoy, 1986; Wang, 1984; Leonardi et al., 2013, 2014; Fagherazzi et al., 2015; Jiménez-Robles et al., 2016; Yao et al., 2016).

However, tidal embayments are dynamically coupled to their offshore plumes, creating an oceanic pattern of sediment fluxes that can dictate the morphological evolution of the tidal channel. Stommel and Former (1952) first suggested the importance of the exchange at the seaward boundary of the tidal channel between the tidal channel itself and the adjacent ocean to regulate the flushing of sediment and in controlling hydro-morphodynamic conditions within a tidal embayment as a whole. Tidal exchange with the adjacent ocean can be characterized by an ebb-flood asymmetry in which the ebb flow exits the tidal channel as a spreading jet, whereas the flood flow enters the tidal channel as a radial sink flow (Chadwick and Largier, 1999; Chen et al., 2012). Recent numerical efforts on the topographic evolution of coastal rivers concerns the dynamically coupling between fluvial and marine processes (Chatanantavet et al., 2012; Lamb et al., 2012; Chatanantavet and Lamb, 2014). They demonstrated, by comparison with field and experimental results, the need of considering a coupled offshore spreading plume for predicting backwater and drawdown regions with implications on scour/aggradation processes and delta avulsion. Hence, the connectivity between the onshore and offshore systems must be a task to be addressed when analyzing tidal channels morphodynamics.

The issue that we address in this contribution concerns the possible existence of a long-term longitudinal equilibrium profile in tide-dominated, well-mixed estuaries linked to their offshore discharge plume. The problem is tackled by adopting a quasi 2-D model of a coupled tidal channel and offshore plume system. We use the one-dimensional shallow water continuity and momentum equations linked to the Exner equation for the bottom evolution in the tidal channel. These equations are dynamically coupled to the flow and sediment patterns in the offshore region by means of a sufficiently simple analytical model of plume hydrodynamics that reduces drastically the computational effort that a 2-D process-based model would demand for a long-term predictive simulation. In the near field, during the ebb-phase tidal plumes behave as a bounded, sediment-laden, turbulent jet: the unconfined flow spreads laterally and decelerates seaward due to bottom friction and lateral diffusion in the ambient fluid (Abramovich, 1963; Rajaratnam, 1976; Özsoy and Ünlüata, 1982; Joshi, 1982; Ortega-Sánchez et al., 2003; Jiménez-Robles et al., 2016). The approximate equations for the jet flow and sediment patterns were derived by Özsoy and Ünlüata (1982) and Özsoy (1986) respectively. On the other hand, the flood flow in the near inlet region is modelled as a two-dimensional, plane, irrotational plane sink flow (Blondeaux et al., 1982). This formulation has been supported from previous laboratory (Wolanski and Imberger, 1987; Tambroni et al., 2005; Tambroni and Seminara, 2006) and field (DelCharco, 1992) works of tidal inlets . The resulting system is closed by the sediment flux transported as a bed and suspended load through an empirical transport capacity formulation and the advection-diffusion equation respectively. Thus, in the present contribution the sediment flux analysis is not restricted to classical algebraic sediment transport equations. Now, we are taking into account the phase lag between local hydrodynamic conditions and sediment fluxes and consider the finite time needed for sediment particles being suspended in the water to settle at slack water. Finally, like in previous works, we assume a funnel shaped estuary of fixed width small enough as compared to the Rossby radius of deformation to ensure that Coriolis forces are dynamically insignificant. We also neglect gravitational circulations due to density stratification and the presence of tidal flats flanking the main channel.

Despite important advances in previous works, with this model we wish to answer some questions about the morphodynamics of ‘short’ tidal channels typically observed in coastal lagoons and wetlands, and related river plumes: Could the offshore plume appreciably affect morphodynamic equilibrium? If so, how does offshore dynamics influence the sediment supply of a tidal channel and the consequent equilibrium configuration? And viceversa, how does the tidal channel evolution modifies the plume dynamics? What are the possible signatures of the oceanic basin configuration (i.e., bottom slope, bottom friction) on the bed profile in the tidal channels? We will then explore the role played by the main agents characterizing the problem (channel convergence, tidal amplitude, initial depth of the channel, eroded material in the continental shelf) with the aim of unravelling the large-scale structure of the entire tidal systems.

2.2 Mathematical description of the model

The present study is referred to an investigation of the hydrodynamic and morphodynamic evolution of a coupled system offshore plume-tidal estuary through a quasi 2-D formulation for conservation of fluid mass and momentum, and conservation of sediment mass. In this section we present the geometry, the mathematical model and the numerical scheme used to tackle this goal.

2.2.1 Model geometry

It has been frequently observed that self-formed tidal channels are generally “funnel” or “trumpet” shaped, with a width that tapers upstream in an apporximately exponential fashion (Davies and Woodroffe, 2010). This exponential decrease in width in the landward direction is the result of the landward decrease in the tidal flux, which reaches zero at the tidal limit (Dalrymple et al., 2012). Thus, a simplified geometry is used to define the characteristic funnel-shaped planimetric configuration of a tide-dominated estuary (Wells, 1995; Lanzoni and Seminara, 1998). Let us considerer a tidal channel of length L_e whose width b decreases exponentially with distance inland:

$$b = b_0 \exp\left(-\frac{x}{L_b}\right), \tag{2.1}$$

where b_0 is the width of the channel mouth, x is the longitudinal coordinate with origin at the channel mouth and pointing landward, and L_b denotes the convergence length. The larger the convergence length is, the smaller the convergence rate of the channel becomes. The channel cross-section is approximated with a rectangular equivalent section with a local depth $d = h - \eta$, where h is the water surface elevation and η is the laterally averaged elevation of the channel bottom, both relative to a horizontal reference level (see Figure 2.1). As a first approximation, the channel width is assumed to be flanked by nonerodible banks and we ignore the possible presence of adjacent tidal flats. These approximations, based on the observation that variations of bed elevations occur at faster temporal scale with respect to the time scale of width variations (Bolla Pittaluga et al., 2015), are widely used when modeling the evolution of tidal channels (Schuttelaars and Swart, 2000; Lanzoni and Seminara, 1998, 2002; Todeschini et al., 2008; Bolla Pittaluga et al., 2015). The oceanic receiving basin will be characterized by a flat sloping bottom with bathymetric lines parallel to the coast.

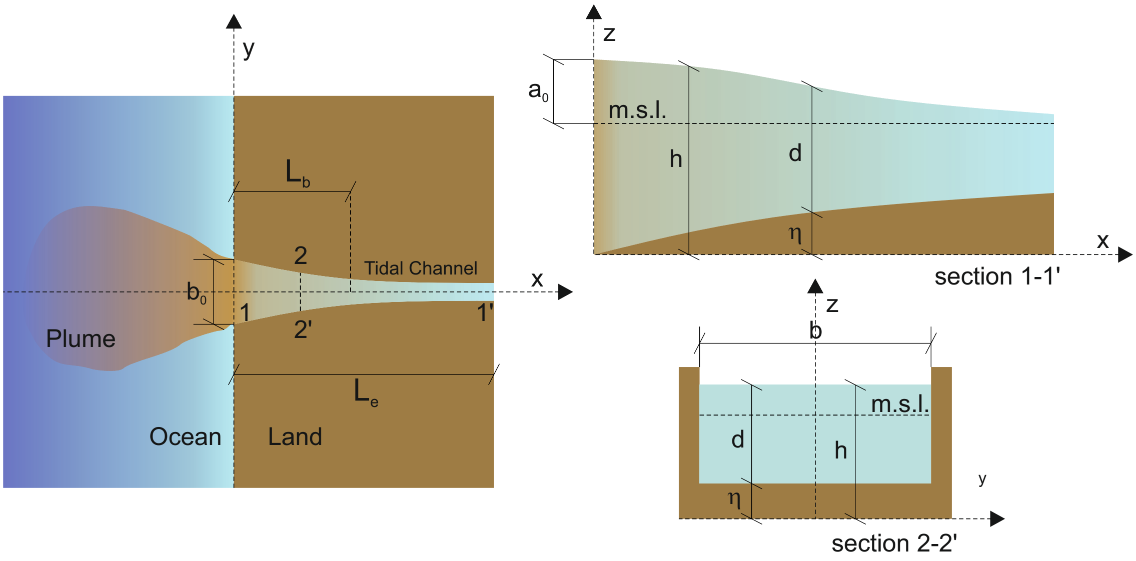

Figure 2.1: Sketch of a tidal channel-offshore plume system and basic notation.

2.2.2 Hydrodynamic model

The hydrodynamic problem considered herein is addressed through different techniques depending on the model region. The flow field inside the tidal channel is solved through a one dimensional numerical scheme that resolve the classical flow movement into an open channel. To complete the hydrodynamics problem in the offshore region and in order to estimate to what extent the availability of sediment in this region may modify the tidal channel evolution, a model for the hydrodynamics of the sea region close to the channel mouth is needed. Employing a two-dimensional model based on the numerical solution of the shallow water equations appears to be prohibitive for our goal of a long term simulation of exchange of sand between the sea and the tidal channel. In fact, the latter models, though accurate, are computationally highly demanding when attempting to reproduce processes occurring from years to decades.

Two well-differentiated phases with a particular flow treatment are considered in the present framework: the ebb and flood offshore flow field (Figure 2.2 and Figure 2.3). We use two distinct analytical models of continental shelf hydrodynamics during these phases of the tide. Whereas during ebb the flow issues from the inlet in the form of a turbulent het, during a flood the inlet functions as a potential sink. These analytical models allow a computational effort away from the prohibitive one that a 2-D numerical model would require for a long-term predictive simulation. A detailed description of the different resolution techniques is present in the next three sections.

2.2.2.1 Tidal channel hydrodynamics

The one-dimensional partial differential equations governing the unsteady water flow in the tidal channel over partially dry areas are the classical shallow water equations of mass and momentum conservation :

$$\Psi_H b \frac{\partial d}{\partial t} + \frac{b u d}{\partial x} = 0 \tag{2.2}$$

$$\frac{\partial u}{\partial t} + u \frac{\partial u}{\partial x} + g \frac{\partial h}{\partial x} + \frac{u|u|}{C^2} \left(\frac{d}{\Phi_H} \right)^2 = 0, \tag{2.3}$$

where t denotes time, u is the local depth-averaged velocity, g is gravity, C is the flow conductance. As stated by van Rijn (1984d), even in uniform flow conditions the morphological behavior of an alluvial channel is rather complicated. The fundamental difficulty is that the channel bed characteristics (bed forms), and thus, hydraulic roughness, depend on flow conditions (flow velocity and depth) and sediment transport rate. These flow conditions are, in turn, strongly dependent on the channel bed configuration and its hydraulic roughness. Thus, the relationship between hydraulic roughness and the flow conditions must be defined. In this sense, for a detailed description of the flow conductance estimation on the basis of bed material and bed form characteristics, the reader is referred to Section 2.2.3.

Besides, as a consequence of the morphological evolution of the tidal channel, a very shallow region tends to form at the landward end of the tidal estuary. In this way, some cells within the tidal channel may undergo a drainage process during the ebb phase while the can be submerged again during the flood phase. This portion is often characterized by sharp changes of water depths due these repetitive flooding and drying stages which, because of the nonlinearity of the flow equations, strongly affect the dynamics of the system. This problem involving partially wet domains is handled by the procedure proposed by Defina (2000), who included the functions Ψ_H and Φ_H in the shallow water equations to overcome these difficulties. The former is the local fraction of wetted domain accounting for the actual area that is wetted or dried during the tidal cycle, and strictly depends on the statistical distribution of bottom elevation within each representative elementary area used to discretize the flow domain. The latter is the value of the effective flow depth, defined as the volume of water per unit area actually ponding the bottom. A brief description of the procedure to obtain this set of shallow water equations for partially wet domains is reported bellow.

2.2.2.1.1 Boundary Conditions. Two boundary conditions are required by the previous system of equations (2.2) and (2.3). At the tidal channel mouth the water motion is forced by a sea level oscillation characterized by a purely semi-diurnal M2 tide:

$$h(t)|_{x=0} = a_0 \sin\left(\frac{2\pi t}{T}\right), \tag{2.4}$$

with a_0 the tidal amplitude and T the tidal period. This coastal tide is clearly the driver of water levels and currents inside the tidal channel. At the landward boundary the river discharge is supposed to be negligible, which corresponds to a reflecting barrier condition. We thus assume a vanishing flow discharge at this section:

$$u(t)|_{x=L_e} = 0. \tag{2.5}$$

2.2.2.1.2 Wetting-drying routine. Let L^* be the characteristic horizontal length scale of the computational elements used to discretize the integration domain Ω. Considerer a small representative elementary area $A^*(x.y)$ within Ω^* and centered on the point (x, y), such that $A^* = O(L^{*2})$, where O stands for “order of magnitude”. Let D_0^* denote the flow depth scale and a_r denote the vertical scale of the topographic pattern that characterizes the irregular bottom profile inside A^*. Although this procedure is focused on the case when a_r is comparable with the flow depth (i.e., $a_r = O(D_0^*)$), it should be take into account that in many cases a_r can be much smaller or much larger that D_0^*.

For the case in which D_0^* and a_r are of the same order of magnitude, we are interested in deriving a set of depth-averaged, shallow water equations valid on the macroscopic scale L^* and suitable to treat partially dry areas. To this end the following phase function is introduced:

$$\psi_H(x, y, z) = \begin{cases} 0 & \text{if } z > \eta \\ 1 & \text{if } z \leq \eta, \end{cases} \tag{2.6}$$

where η is the local bottom elevation and (x, y, z) denotes the vector of spatial coordinates, in which z is the vertical coordinate with the z-axis pointing upward. We deal with ψ_H as a generalized function that depends only on the geometric configuration of the bottom. In particular, $\nabla\psi_H$ behaves as a delta function detecting the bottom surface and has the direction of the normal to the bottom (Drew, 1983). Let denote the phase averaging process of a generic variable of the flow field $f(x, y, z, t)$ as:

$$F(x, y, x, t) = \langle\psi_H(x, y, z) f(x, y, z, t)\rangle = \frac{1}{A^*}\int_{A^*} \psi_H(x, y, z) f(x, y, z, t)\, dA^*, \tag{2.7}$$

where the uppercase is here used to denote the phase-averaged variables representing the macroscopic properties of the representative elementary area A^*. Defina (2000) set $f = 1$, yielding:

$$\Psi_H(x,y,z) = \langle \psi_H(x,y,z) \rangle = \frac{1}{A^*} \int_{A^*} \psi_H(x,y,z) dA^*. \tag{2.8}$$

where the function Ψ_H represents the fraction of area $A^*(x,y)$ lying above the bottom surface and, therefore, becomes wetted. Moreover, it was assumed that the free surface elevation h smoothly changes throughout Ω^*, so that it can be assumed nearly constant over each representative elementary area, and the quantity

$$D = \int_{-\infty}^{h} \Psi_H dz \tag{2.9}$$

represents the water volume per unit area or the effective water depth over A^*.

Recalling that for shallow water flows the vertical momentum equation is usually simplified by neglecting acceleration and stresses such that the hydrostatic pressure distribution is recovered along the vertical and the Boussinesq closure model is considered, the classical Reynolds equations read as follow:

$$b\frac{\partial d}{\partial t} + \frac{bud}{\partial x} = 0 \tag{2.10}$$

$$\frac{\partial u}{\partial t} + u\frac{\partial u}{\partial x} + g\frac{\partial h}{\partial x} + \frac{u|u|}{C^2 d} = 0. \tag{2.11}$$

In order to derive the shallow water equations that allow the treatment of the water flow over a partially dry domain, Defina (2000) applied the previous averaging procedure, by multiplying by ψ_H and averaging over the elementary representative area A^*, to equations (2.10) and (2.11) and then integrated the resulting equations over the depth. The resulting system of equations was the previously presented (equations (2.2) and (2.3)). It is then worthwhile to describe the form of the functions Ψ_H and Φ_H.

The function Ψ_H represents the fraction of $A*$ lying above the bottom. In order to derive an analytical expression for it, it is convenient to regard it from a statistical point of view. Hence, it can be considered as the probability that the local bottom elevation η inside A^* does not exceed the generic elevation z:

$$\Psi_H(x,y,z) = p(\eta \leq z). \tag{2.12}$$

Therefore, $\partial \Psi_H(x,y,z)/\partial z$ is the probability density function of bottom elevation inside A^*, and a proper measure of ground irregularities is then given by the standard deviation σ_b of bottom elevation inside A^*. Hence, a_r can be specify by assuming $a_r = 2\sigma_b$. Besides, as a first approximation, the probability density function is assumed to be Gaussian:

$$\frac{\partial \Psi_H(x,y,z)}{\partial z} = \frac{2}{a_r\sqrt{\pi}} e^{-\xi'^2}, \tag{2.13}$$

where:

$$\xi' = -2\frac{z-\eta}{a_r} \text{ and } \xi'_H = -2\frac{h-\eta}{a_r}. \tag{2.14}$$

Defina (2000) emphasized that this choice of the probability density function is mainly illustrative as, in practice, different distributions might be found to hold and that a Gaussian distribution does not affect the bases of the present reasoning.

Integration of equation (2.13) yields:

$$\Psi_H(x,y,z) = \frac{1}{2}erfc(\xi'_H) = \frac{1}{2}\left[1+erf(-\xi'_H)\right], \tag{2.15}$$

where $erfc(\xi')) = 1 - erf(\xi')$, having denoted by $erf()$ the error function and by $erfc()$ the complementary error function. Recalling equations (2.8) and (2.9), it can be written that:

$$\Psi_H(x,y,z) = \frac{1}{2}erfc(\xi'_H) = \frac{1}{2}\left[1+erf(-\xi'_H)\right], \tag{2.16}$$

$$D = \frac{a_r}{4}\int_{\xi'_H}^{\infty} erfc(\xi')d\xi' = \frac{a_r}{4}\left[\frac{e^{-\xi'^2_H}}{\sqrt{\pi}} - \xi'_H erfc(\xi'_H)\right]. \tag{2.17}$$

Finally, Φ_H can be expressed analytically through the following relationship (Lanzoni and Seminara, 2002):

$$\Phi_H = \left[D + 0.27\sqrt{a_r D}\, e^{-\frac{2D}{a_r}}\right]^{3/2}. \tag{2.18}$$

Although this procedure is of interest in the case when a_r is comparable with the flow depth ($D_0^* \approx a_r$), it should be emphasized that in many cases a_r can be either much smaller or much larger than the flow depth. When a_r is much smaller than the flow depth the dependence of the mean flow on ground irregularities is expected to be negligibly small and a linear approximation of the bottom can be considered sufficiently accurate. Note that in this case, when $D_0^* \gg a_r$, the classical Saint Venant equations are recovered (equations (2.10) and (2.11)) since $\Psi_H \to 1$, $D \to d$ and $\Phi_H \to D^{3/2}$.

On the other hand, when $a_r \gg D_0^*$ the overall picture of the flow is flow field is considerably altered and the subgrid modeling approach proposed by Defina (2000) is likely to fail and negative depths may occur during the calculation. In this case, a simple procedure similar to the one employed by Todeschini et al. (2008) is adopted. This method is based on the exclusion from computational domain of the cells affected by the drying processes in which the flow depth is smaller than a given small value. On the contrary, these cells are reintroduced again in the computational domain when the rise of free surface occurring in the flood phase leads to new submerged areas. The dry cell nearest to the mouth becomes the last active cell at a certain time step and all the succeeding cells in the landward direction are excluded from the computation. At subsequent time steps these cells can be flooded again, since the free surface is subjected to periodic oscillation. In this case, these cells with a water depth larger that the threshold value will be reintroduced into the computational domain again.

2.2.2.2 Continental shelf hydrodynamics during the ebb phase

During the ebb-phase, water exiting a tidal inlet into a semi-infinite ocean behaves like a plane turbulent jet (Wright et al., 1974; Rowland et al., 2009) (Figure 2.2). Jet theory has been extensively used to describe processes experienced by water discharges into resting reservoirs during the ebb-phase (Özsoy, 1977; Ortega-Sánchez et al., 2008; Falcini and Jerolmack, 2010). In coastal areas, vertical motions are negligible with respect to horizontal currents and the exiting flow behaves like a plane turbulent jet, experiencing mixing and diffusion (Bates, 1953; Wright, 1977; Rowland et al., 2009; Falcini and Jerolmack, 2010; Leonardi et al., 2013). Their flow field can be divided into two different zones (Rajaratnam, 1976): (1) a zone of flow establishment (ZOFE), located in the vicinity of the outlet and governed by a triangular inviscid core where centerline velocity can be assumed constant; and (2) a zone of established flow (ZOEF), where lateral shear turbulence reaches the jet axis and centerline velocity starts to decrease, leading to self-similarity conditions.

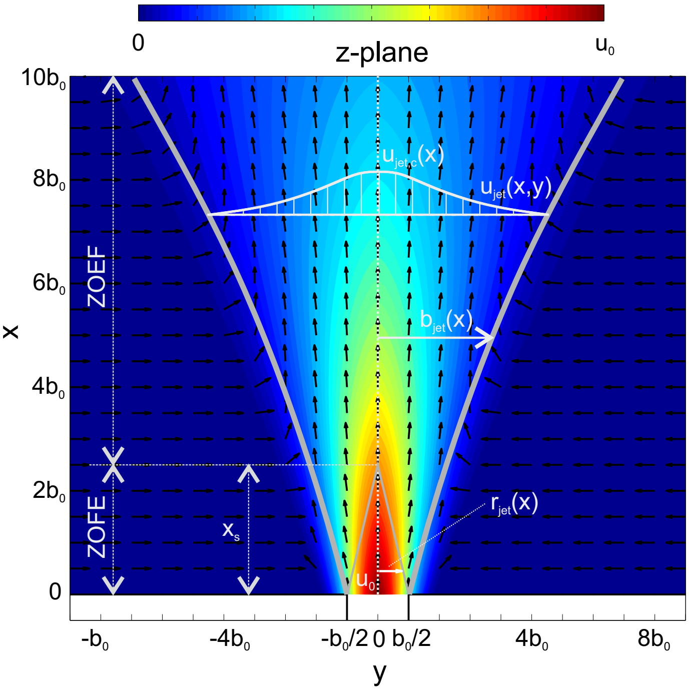

Figure 2.2: Analytical solutions for the offshore ebb flow close to the tidal inlet. Sketch of a turbulent jet exiting a tidal channel during the ebb-phase. The velocity field magnitude is indicated through the colorbars.

The water issuing from the inlet entrains and mixes with the surrounding ambient water as it proceeds offshore, before gradually dissipating its momentum by the frictional resistance of the bottom. Besides, the depth variations of the continental shelf also affect the expansion of the jet. Özsoy and Ünlüata (1982) derived an analytical solution for the stationary turbulent jet hydrodynamics after performing a rigorous order of magnitude analysis, showing that the motion of a tidal jet is described by depth and time averaged Navier-Stokes equations:

$$\frac{\partial}{\partial x}\left(d_{jet}u_{jet}^2\right)+\frac{\partial}{\partial y}\left(d_{jet}u_{jet}v_{jet}\right)=-\frac{g}{C_z^2}u_{jet}^2+\frac{1}{\rho}\frac{\partial}{\partial y}\mathscr{T}_{xy} \tag{2.19}$$

$$\frac{\partial}{\partial x}\left(d_{jet}u_{jet}\right)+\frac{\partial}{\partial y}\left(d_{jet}v_{jet}\right)=0 \tag{2.20}$$

in which the coordinate system of Figure 2.2 is used, d_{jet} is the ebb-phase averaged water depth along the x-axis, u_{jet} and v_{jet} are the velocity components in the offshore and alongshore directions respectively, C_z is the Chezy friction coefficient of the continental shelf bottom, ρ is water density, and $\mathscr{T}_{xy}$ is the depth integrated turbulent shear stress acting laterally on the flow. The solutions of this system of equations are given by the velocity field $u_{jet}(x, y)$, by the characteristic width $b_{jet}(x)$ in which the jet motion is confined and by the core region width, r_{jet}. Experimental observations showed that planar jets have a certain symmetry and can thus be considered self-similar (Abramovich, 1963). Indeed, solutions of jet theory operate on the assumption that the velocity profiles are self-similar with respect to the normalized coordinate $\zeta = y/b_{jet}(x)$, where y is the transversal coordinate. This assumption allows a simple parameterization of the dynamical variables in terms of scaling factors. For planar jets, the centerline velocity is generally used as the local velocity scale, being the velocity field parameterized as follows:

$$F(\zeta)=\frac{u_{jet}(x,y)}{u_{jet,c}(x)} \tag{2.21}$$

where the subscript c refers to values attained by the variables along the jet centerline and $F(\zeta)$ is a similarity functions for velocity profiles (Abramovich, 1963; Stolzenbach and Harleman, 1971). Different analytical closed-forms for the similarity profile have been proposed in different experimental studies of free-shear flows (Joshi, 1982; Stolzenbach and Harleman, 1971; Wang, 1984; Giger et al., 1991; Paillat and Kaminski, 2014). In this work we use the one proposed by (Stolzenbach and Harleman, 1971):

$$F(y)=\begin{cases} 0 & \text{if } |y|>b_{jet} \\ \left(1-\varrho^{1.5}\right)^2 & \text{if } r_{jet}\leq|y|\leq b_{jet} \\ 1 & \text{if } 0<|y|<b_{jet} \end{cases} \tag{2.22}$$

where

$$\varrho=\frac{|y|-r_{jet}}{b_{jet}-r_{jet}}. \tag{2.23}$$

The velocity u_{jet} and the shear force $\mathscr{T}_{xy}$ vanish at $y \to b_{jet}$, but there is a lateral velocity (v_e) due to the entrainment of the surrounding fluid into the jet. This entrainment velocity can be related to the centerline velocity of the jet by:

$$v_e = v_{jet}(x,y)|_{y\to b_{jet}(x)} = \alpha u_{jet,c} \tag{2.24}$$

where α is the entrainment coefficient (Morton et al., 1956), which was found to exhibit a basin slope and basin bed friction dependence by (Jiménez-Robles et al., 2016). Therefore, assuming that bathymetric variations are present in the x-direction only and integrating equations (2.19) and (2.20) across the jet yields:

$$\frac{\partial}{\partial x}\left(d_{jet}\int_{-b_{jet}}^{b_{jet}} u_{jet}^2 dy\right)=-\frac{g}{C_z^2}\int_{-b_{jet}}^{b_{jet}} u_{jet}^2 dy \tag{2.25}$$

$$\frac{\partial}{\partial x}\left(d_{jet}\int_{-b_{jet}}^{b_{jet}} u_{jet} dy\right)=-2hv_e \tag{2.26}$$

Now, using the self-similar velocity profiles and the entrainment assumption in the previous equations, the two ordinary differential equations arise:

$$\frac{\partial}{\partial x}\left(d_{jet}\, b_{jet}\, u_{jet,c}^2\, \bar{I}_2\right)=-\frac{g}{C_z^2}\, b_{jet}\, u_{jet,c}^2\, \bar{I}_2 \tag{2.27}$$

$$\frac{\partial}{\partial x}\left(d_{jet}\, b_{jet}\, u_{jet,c}\, \bar{I}_1\right)=-\alpha\, d_{jet}\, u_{jet,c} \tag{2.28}$$

where

$$\bar{I}_1=\int_0^1 F(\zeta)d\zeta \tag{2.29}$$

$$\bar{I}_2=\int_0^1 F(\zeta)^2 d\zeta. \tag{2.30}$$

Assuming that the inlet is rectangular of width b_0, that d_0 is the ebb-phase averaged inlet depth, and that u_0 is the averaged ebb-phase jet velocity at the channel mouth, equations (2.27) and (2.28) can be written in the normalized form:

$$\frac{\partial}{\partial \xi_b}\left(D_{jet}\, B_{jet}\, U^2\, \bar{I}_2\right)=-\mu\, B_{jet}\, U_{jet,c}^2\, \bar{I}_2 \tag{2.31}$$

$$\frac{\partial}{\partial \xi_b}\left(D_{jet}\, B_{jet}\, U_{jet,c}\, \bar{I}_1\right)=\alpha\, D_{jet}\, U_{jet,c}, \tag{2.32}$$

The following dimensionless variables have been used in the previous equations: $\xi_b=2x/b_0$, $U_{jet,c}(\xi_b)=u_{jet,c}/u_0$, $B_{jet}(\xi_b)=2b_{jet}/b_0$, $D_{jet}(\xi_b)=d_{jet}/d_0$ and the friction parameter $\mu=gb_0/(2d_0C_z^2)$. The core width $r_{jet}(x)$ will also be normalized as $R_{jet}(\xi_b)=2r_{jet}/b_0$.

By virtue of equation (2.22), $\bar{I}_n$, with $n=1,2$, is defined as:

$$\bar{I}_n=\frac{R_{jet}}{B_{jet}}+I_n\left(1-\frac{R_{jet}}{B_{jer}}\right), \tag{2.33}$$

where I_1 and I_2 are numerical constant equal to 0.450 and 0.316 respectively, i.e., the values of $\bar{I}_1$ and $\bar{I}_2$ in the ZOEF since $R_{jet}=0$ as $\xi_b \to \xi_{b,s}=2x_s/b_0$ is this region. $\xi_{b,s}$ and x_s are the dimensionless and dimensional forms of the end coordinate for the core region and marks the passage between ZOFE and ZOEF respectively. Thus, x_s is found imposing the normalized jet core half-width R_{jet} equal to zero in the ZOFE equations. Equations (2.31) and (2.32) are uniformly valid for all ξ_b, and their integration is direct using the initial conditions $D_{jet}(0)=1$, $R_{jet}(0)=1$, $B_{jet}(0)=1$, and $U_{jet}(0)=1$. Equation (2.31) yields:

$$\bar{I}_2 D_{jet} B_{jet} U^2_{jet,c} = \exp\left(-\mu \int_0^{\xi_b} \frac{1}{D_{jet}(\xi_b)} d\xi_b\right) = J_{jet}(\xi_b) \tag{2.34}$$

where it has been noted that $\bar{I}_2 B_{jet} \to 1$ when $\xi_b \to 0$.

Equation (2.32) must be integrated separately in the two zones of the jet. In the ZOFE we set $U_{jet}=1$ to obtain:

$$\bar{I}_1 D_{jet} B_{jet} = 1 + \alpha \int_0^{\xi_b} D_{jet}(\xi_b) d\xi_b = G_{jet}(\xi_b) \tag{2.35}$$

where it has been noted that $\bar{I}_1 B_{jet} \to 1$ as $\xi_b \to 0$. Thus, the solutions for the two unknowns R_{jet} and B_{jet} in the ZOFE is direct by imposing that $U_{jet}=1$ and using equation (2.33):

$$U_{jet,c}(\xi_b) = 1 \tag{2.36}$$

$$R_{jet}(\xi_b) = \frac{I_1 J_{jet}(\xi_b) - I_2 G_{jet}(\xi_b)}{(I_1 - I_2) D_{jet}(\xi_b)} \tag{2.37}$$

$$B_{jet}(\xi_b) = \frac{(1-I_2) G_{jet}(\xi_b) - (1-I_1) J_{jet}(\xi_b)}{(I_1 - I_2) D_{jet}(\xi_b)} \tag{2.38}$$

To obtain solution for the unknowns $U_{jet,c}$ and B_{jet} in the ZOEF, equation (2.34) is utilized to put equation (2.32) into the form:

$$\frac{\partial}{\partial \xi_b}\Psi = \frac{\alpha I_2 D_{jet} J_{jet}}{I_1 \Psi}; \ \Psi = \frac{J_{jet}}{U_{jet,c}}, \tag{2.39}$$

where it has been noted that $\bar{I}_1 = I_1$ and $\bar{I}_2 = I_2$, since $R_{jet}(\xi_b)=0$ for $\xi_b \geq \xi_{b,s}$. Then, equation (2.39) can readily integrated from $\xi_{b,s}=2x_s/b_0$ (given by the roots of $R_{jet}(\xi_{b,s})=0$) to $\xi > \xi_{b,s}$, yielding:

$$\frac{1}{2}\Psi^2(\xi_b) = \frac{1}{2}\frac{J^2_{jet}}{U^2_{jet,c}} = \frac{\alpha I_2}{I_1}\int_{\xi_{b,s}}^{\xi_b} D_{jet}(\xi_b) J_{jet}(\xi_b) d\xi_b + \frac{1}{2}\Psi^2(\xi_{b,s}). \tag{2.40}$$

The constant of integration $\frac{1}{2}\Psi^2(\xi_{b,s})$ is determined by requiring continuity of the centerline velocity $U_{jet,c}$ at $\xi_b = \xi_{b,s}$. Thus, evaluating equation (2.40) at $\xi_b = \xi_{b,s}$:

$$\frac{1}{2}\Psi^2(\xi_{b,s}) = \frac{1}{2}\frac{J^2_{jet}(\xi_{b,s})}{U^2_{jet,c}(\xi_{b,s})} = \frac{1}{2}J^2_{jet}(\xi_{b,s}), \tag{2.41}$$

since $U_{jet,c}(\xi_{b,s}) = U_{jet,c}(\xi_b < \xi_{b,s}) = 1$. Substituting equation (2.41) into equation (2.40) it follows that:

$$U_{jet,c}(\xi_b) = \frac{J_{jet}(\xi_b)}{\left[J^2_{jet}(\xi_{b,s}) + S_{jet}(\xi_b)\right]^{1/2}}, \tag{2.42}$$

and substituting this result into equation (2.34), and taking $\bar{I}_2 = I_2$ we obtain:

$$B_{jet}(\xi_b) = \frac{\left[J^2_{jet}(\xi_{b,s}) + S_{jet}(\xi_b)\right]}{I_2 D_{jet}(\xi_b) J_{jet}(\xi_b)}, \tag{2.43}$$

where

$$S_{jet}(\xi_b) = \frac{2\alpha I_2}{I_1}\int_{\xi_{b,s}}^{\xi} D_{jet}(\xi_b) J_{jet}(\xi_b) d\xi_b. \tag{2.44}$$

These equations complete the general similarity solutions to equation (2.19) and (2.20) in the ZOEF alongside

$$R_{jet}(\xi_b) = 0. \tag{2.45}$$

2.2.2.3 Continental shelf hydrodynamics during the flood-phase

Regarding the flood-phase, during which the inflow draws water from a selective quasi-circular withdrawal region (Figure 2.3), no detailed theoretical analysis of the hydrodynamics of tidal inlets are known to the present authors except for the work of Blondeaux et al. (1982), Wolanski and Imberger (1987), DelCharco (1992), Tambroni et al. (2005) and Tambroni and Seminara (2006). They employed a much simpler analytical model of tidal flow in a neighbourhood of tidal inlets. They modeled this complex flow field as 2-D inviscid, plane and irrotational in the flood phase by assuming the bed to be fixed in time using the potential flow theory, which allows for an analytical treatment of the velocity field.

Potential flow theory leads to the analytic determination of flow characteristics based on a transformation between the physical plane z-plane($= y + ix$) and the transformed plane τ-plane($= \xi_\tau + i\eta_\tau$) using conformal mapping technique (Dias et al., 1987; Kabiri-Samani et al., 2012) (Figure 2.3). Conformal mapping is a mathematical technique in which complicated geometries can be transformed by a mapping function into simpler geometries which still preserves both the angles and orientation of the original geometry. It provides a single expression embodying both the stream function and the potential function for each pattern of flow. In flow situations involving straight boundaries, the application of the Schwarz-Christoffel transformation (Vallentine, 2013; Chanson, 2009), a specific application of conformal mapping, provides a technique to solve analytically this flow field.

A detailed description of the mathematical procedure followed to determined the flow field during the flood phase is presented below.

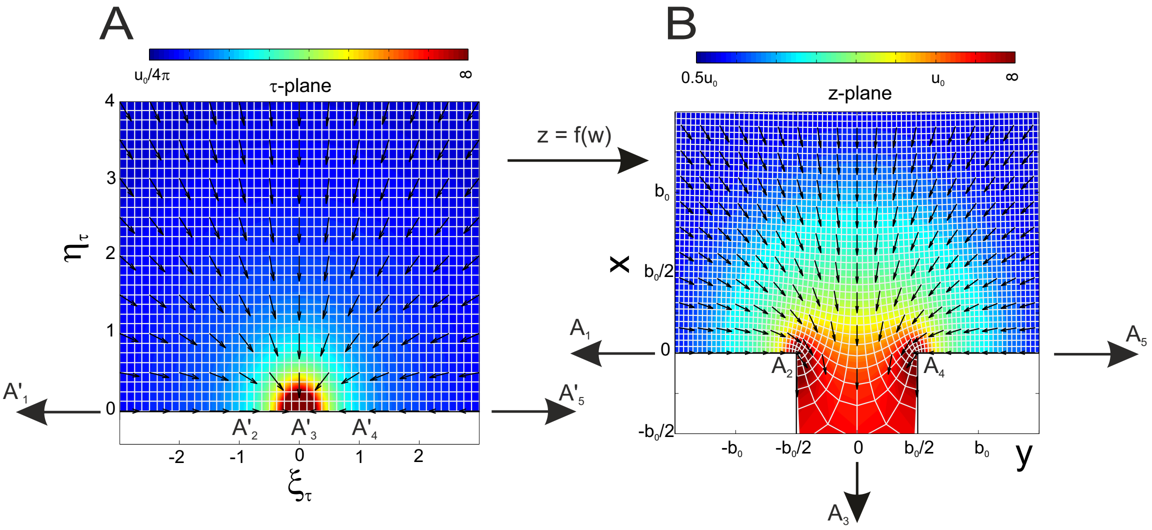

Figure 2.3: Analytical solutions for the offshore flood flow close to the tidal inlet. Conformal mapping of a flow entering a channel based on Schwarz-Christoffel transformation ($z = f(w)$) and sketch of the flood flow in the (b) transformed (τ-plane) and (c) physical (z-plane) domains. In (a) and (b) the grid of the spacial transformation is preserved (white lines) for clarity. The velocity peaks at the edges of the inlet are due to flow separation where geometrical discontinuities are present. Vectors only indicate flow direction. The velocity field magnitude is indicated through the colorbars.

2.2.2.3.1 Analytic functions. The assumption of a plane and irrotational flow lets us to describe the velocity field by means of the complex potential W_p^*, defined as:

$$W_p^* = \phi^* + i\psi^*, \tag{2.46}$$

with ϕ^* velocity potential and ψ^* stream function. The condition that the transformed patterns of ϕ^* and ψ^* lines in a generic z-plane($= x + iy$) does in fact represent a possible pattern of irrotational flow is that the functions ϕ^* and ψ^* satisfy the conditions of continuity and irrotationality. These limitations on ϕ^* and ψ^* restrict W_p^* to a class of function known in the theory of the complex variable as analytic (Vallentine, 2013). A function $W_p^* = f(z)$ is said to be analytic within a region of the z-plane on if, for each point in that region:

a) there is one and only one corresponding value of W_p^* and that value is finite, and

b) $\frac{dW_p^*}{dz}$ is single-valued and neither zero nor infinite.

At singular points, where these conditions are not satisfied, the transformation process is not applicable, although at very small distance from them it may be. From a practical viewpoint, singular points are generally points of theoretically infinite or zero velocity on the physical plane. To the case in study, the points of infinite velocity include the centres of sinks and sharp corners where boundaries are deflected away from the flow.

Condition b) requires that, at any point, $\frac{dW_p^*}{dz}$ must have only one value, whatever the direction of ∂z. It can be shown that it will have only one value for all directions, provided that it has the one value for any pair of directions at right angles to one another, for example the x- and y-directions, at any point. Hence, this condition will be satisfied if

$$\frac{\partial \phi^*}{\partial x} = \frac{\partial \psi^*}{\partial y}, \tag{2.47}$$

and

$$\frac{\partial \phi^*}{\partial y} = -\frac{\partial \psi^*}{\partial x}. \tag{2.48}$$

These equation, the consequence of the condition of one-valued derivatives, are called the Cauchy-Riemann equations. On the condition that the partial derivatives $\frac{\partial \phi^*}{\partial x}$, $\frac{\partial \phi^*}{\partial y}$, $\frac{\partial \psi^*}{\partial x}$ and $\frac{\partial \psi^*}{\partial y}$ exist, and are continuous, the Cauchy-Riemann equations are the sufficient conditions that a continuous one-valued function $W_p^* = f(z)$ is analytic and called complex potential. Differentiating equations (2.47) and (2.48) with respect to x and y respectively, and adding them, results in

$$\frac{\partial^2 \phi^*}{\partial x^2} + \frac{\partial^2 \phi^*}{\partial y^2} = 0. \tag{2.49}$$

Similarly, differentiating equations (2.47) and (2.48) with respect to y and x respectively, and subtracting them, yields:

$$\frac{\partial^2 \psi^*}{\partial x^2} + \frac{\partial^2 \psi^*}{\partial y^2} = 0. \tag{2.50}$$

Hence, the real and the imaginary parts of any function of a complex potential satisfy the Laplace equation and are therefore possible velocity potential functions or stream functions for two-dimensional irrotational flows. This is directly evident from the Cauchy-Riemann equations:

$$\frac{\partial \phi^*}{\partial x} = \frac{\partial \psi^*}{\partial y} = u_{flood} \text{ and } \frac{\partial \phi^*}{\partial y} = -\frac{\partial \psi^*}{\partial x} = v_{flood}. \tag{2.51}$$

Since, from condition b) we have that:

$$\frac{dW_p^*}{dz} = \frac{\partial W_p^*}{\partial x} = \frac{\partial}{\partial x}(\phi^* + i\psi^*) = \frac{\partial \phi^*}{\partial x} + i\frac{\partial \psi^*}{\partial x} = u_{flood} - i \cdot v_{flood} \rightarrow \frac{dW_p^*}{dz} = u_{flood} - i \cdot v_{flood},$$

(2.52)

the derivative $\frac{dW_p^*}{dz}$ can be regarded as a complex velocity in which the real part equals the x-component and the imaginary part the negative of the y-component of the velocity at any point.

2.2.2.3.2 Sink flow pattern. The next simple transformations is a useful analytic function which will be used later in the treatment of the flood flow. A source point in a z-plane at $z = a$ can be treated through the following transformation:

$$W_p^* = -m \ln(z-a). \tag{2.53}$$

In this function, $m = \dfrac{Q'}{2\pi}$, being Q' the strength of the sink and a is a complex constant that indicates the location of the sink. Hence, $z-a$ is simply a radius vector with origin at $z = a$ on the z-plane, i.e.:

$$z-a = r'e^{i\theta'} \text{ and } \ln(z-a) = \ln\left(r'e^{i\theta'}\right)$$

.

Thus, substituting in equation (2.53):

$$\phi^* + i\psi^* = -m\ln(z-a) = -m\ln(r') - im\theta' \rightarrow \phi^* = -m\ln(r') \text{ and } \psi^* = -m\theta'. \tag{2.54}$$

The streamlines ara radial from the point $z = a$ and the equipotential lines are concentric circles with centres at $z = a$. The point $z = a$ is a singular point, and is excluded from the map, since $\dfrac{dW_p^*}{dz}$ is infinite and the function is therefore not analytic at this point.

The velocity at any point is radial towards the sink, with magnitude equal to:

$$|V| = \left|\frac{dW_p^*}{dz}\right| = \frac{m}{r'} = \frac{Q'}{2\pi r'}, \tag{2.55}$$

which is the velocity at a radius r' from the sink point.

2.2.2.3.3 Schwarz-Christoffel transformation. If a z-plane pattern is, or can be transformed into, a pattern of flow within straight-wall boundaries, that is, within a simple polygon, a theorem due to Schwarz and Christoffel provides a standard method for transforming the pattern within this polygon in the z-plane to that of flow occupying the whole of the upper half of a transformed plane (τ-plane). It is then possible to transform the half-plane pattern to that of uniform flow in the W_p^*-plane and, being the relationship between W_p^* and z well established, the flow pattern in the z-plane is mathematically determined (Vallentine, 2013).

If the polygon is in the z-plane and the transformed plane is the τ-plane, the Schwarz-Christoffel theorem states that the interior of this polygon may be mapped into the upper half of a plane and the boundaries of the polygon into the real axis. The transformation is given by:

$$\frac{dz}{d\tau} = \vec{A}\prod_{i=1}^{n}(a_i - \tau)^{-\alpha_i/\pi}, \tag{2.56}$$

where $\vec{A}$ is a complex constant, a_i are the image points on the x_t axis of the τ-plane of the n vertices of the polygon located in the z-plane, and α_i represents the external deflection angle of the polygon at the i vertex. These deflection angles may be positive (anticlockwise) or negative (clockwise) for a traverse in the anticlockwise direction. They may take any value between $-\pi$ and $+\pi$, being these limits corresponding to a boundary folding back along itself. The exterior of the polygon becomes the lower half of the t-plane, the values of a_i are the values of τ along the real axis of the τ-plane to which the vertices of the polygon are transformed, and the sum of α_i obviously equals 2π. Whatever the pattern of flow in the polygon may be, the velocities at the vertices will be either zero (for positive deflection angles) or infinite (for negative deflection angles). These points are singularities and must be excluded from the z-pattern.

The integration of equation (2.56) allows the mapping of the half τ-plane ($Im(\tau) > 0$) into the interior domain of a polygon in the z-plane:

$$z = f(\tau) = \vec{A} \int \prod_{i=1}^{n} (a_i - \tau)^{-\alpha_i/\pi} \, d\tau + \vec{B} \tag{2.57}$$

where $\vec{A}$ and $\vec{B}$ are constant which may be complex that affect the scale and orientation of the z-plane polygon and its position with respect to the origin respectively. Both constant are determined, following integration, by imposing a correspondence between the coordinates of the vertices in the two planes. Usually one or two of the points are at infinity on the real axis of the τ-plane, and the need not be considered in equation (2.57).

In our case, we considered the geometry of the inlet as the one delimited by the vertices A_1, A_2, A_3, A_4 and A_5 in figure 2.3. Thus, the flow region consists of the upper half plane ($x > 0, -\infty < y < \infty$) and the strip ($x < 0, -b_0/2 < y < b_0/2$). This flow region can be seen as a degenerate polygon with three vertices (A_1, A_3 and A_5) at infinity.

The external deflection angle of our polygon at the vertices A_i read respectively:

$$\alpha_2 = -\frac{\pi}{2}, \ \alpha_3 = \pi, \ \alpha_4 = -\frac{\pi}{2}.$$

As far as the values of the coordinates ξ_t are concerned, we set:

$$\xi_{t,1} = -\infty, \ \xi_{\tau,2} = -1, \ \xi_{\tau,3} = 0, \ \xi_{\tau,4} = 1, \ \xi_{\tau,5} = +\infty.$$

The required transformation has then the form:

$$\frac{dz}{d\tau} = \vec{A}(\tau+1)^{\frac{\pi}{2}\frac{1}{\pi}} (\tau-0)^{-\pi\frac{1}{\pi}} (\tau-1)^{\frac{\pi}{2}\frac{1}{\pi}} = \vec{A}\frac{\tau^2-1}{t\sqrt{\tau^2-1}}. \tag{2.58}$$

By integrating the previous equation, it yields:

$$z = f(\tau) = \vec{A}\left[\sqrt{\tau^2-1} + \arcsin\left(\frac{1}{\tau}\right)\right] + \vec{B}, \tag{2.59}$$

where the complex constants $\vec{A}$ and $\vec{B}$ are yet to be determined by imposing that A'_2 and A'_4 in the transformed plane correspond to A_2 and A_4 in the physical plane:

$$f(-1) = -\frac{b_0}{2} + i \cdot 0, \ f(1) = \frac{b_0}{2} + i \cdot 0. \tag{2.60}$$

Whit this conditions we obtain the final form of the transformation (Mathews and Howell, 2012):

$$z = f(\tau) = \frac{b_0}{\pi}\left[\sqrt{\tau^2 - 1} + \arcsin\left(\frac{1}{\tau}\right)\right], \tag{2.61}$$

with b_0 being the tidal channel mouth width. This transformation maps the upper half plane $Im(\tau) > 0$ onto the domain consisting of the upper half plane $Im(z) > 0$ joined to the channel $-b_0/2 < y < b_0/2$, $x < 0$. The point $\tau = 0$ is mapped onto the point $z = -i \cdot \infty$ along the channel. Finally, the τ-plane pattern is evidently that of flow into a half-sink. See figure 2.3 for a visual inspection of this transformation.

2.2.2.3.4 Flow into a rectangular channel flanked by the coastline. The flood flow in the near tidal channel mouth region in the physical plane is driven by a given temporally dependent half-sink flow which, at the scale of the inlet, will be located at $x \to \infty$. The strength of this water discharge will be related to the time-varying values of flow velocity, water depth and channel mouth width computed at the tidal channel through the system of equations (2.2) and (2.3).

In the transformed plane (τ-plane), and assuming an horizontal bottom which depth will vary with the tidal channel mouth depth, this flow corresponds to a half-sink of intensity $2Q(t)$ (with $Q(t) < 0$) at $\tau = 0$, whose complex potential W_p^*, from equation (2.53), is readily written as:

$$W_p^* = \frac{Q}{\pi}\ln(\tau). \tag{2.62}$$

In the physical plane (z-plane), the complex flood velocity $\vec{V}_{flood}$ associated with the latter form of the complex potential is obtained as follows:

$$\vec{V}_{flood} = u_{flood} - i \cdot v_{flood} = \frac{dW_p^*}{dz} = \frac{dW_p^*}{d\tau}\frac{d\tau}{dz}, \tag{2.63}$$

in which the derivative $\frac{dW_p^*}{d\tau}$ represents the velocity field on the transformed plane:

$$\frac{dW_p^*}{d\tau} = \frac{Q}{\pi\tau} = \frac{Q}{\pi}\frac{1}{\xi_\tau + i\eta_\tau} = \frac{Q}{\pi}\left[\frac{\xi_\tau}{\xi_\tau^2 + \eta_\tau^2} - i\frac{\eta_\tau}{\xi_\tau^2 + \eta_\tau^2}\right]. \tag{2.64}$$

Giving that the quantity $\frac{dz}{d\tau}$ is readily calculated by differentiating the transformation given by equation (2.61), the flow field at any point in the continental shelf during the flood phase for the case of an horizontal bottom is given by:

$$\vec{V}_{flood}(z) = u_{flood}(z) - i \cdot v_{flood}(z) = \frac{\frac{dW_p^*}{d\tau}}{\frac{dz}{d\tau}} = \frac{\frac{Q}{\pi\tau}}{\frac{dz}{d\tau}}. \tag{2.65}$$

Figure 2.3 (b) depicts the spatial distribution of the flood flow field. As previously mentioned, it is not surprising that, within the framework of the present irrotational scheme, the velocity peaks at the edges of the inlet edges where geometrical discontinuities are present: the scheme obviously fails in an immediate neighborhood of the edges where flow separation occurs. At these points in a real fluid, not only are infinite velocities impossible but, with the necessarily high velocity gradient involved, viscous effects become appreciable and significant departures from the irrotational flow pattern, such as rotational vortex flow or separation from boundaries, results.

2.2.2.3.5 The sloping bottom case: modified streamlines lines. Wolanski and Imberger (1987) examined patterns of flood flow at tidal inlets, with particular reference to non-uniform or selective water withdrawal influenced by bottom topography. For the case of a oceanic basin with a linearly varying flat bathymetry, they derived a streamline analytical model in a transformed plane for the case of a half-sink flow:

$$\psi^*_{slope} = \frac{Q}{D\pi}\left[\frac{\xi_\tau \eta_\tau}{\left(\xi_\tau^2 \eta_\tau^2\right)^2} + \arctan\left(\frac{\xi_\tau}{\eta_\tau}\right)\right], \tag{2.66}$$

where D reflects the dimensionless bathymetric changes along the η_τ axis. Using the above streamline function, the velocity field (u_τ, v_τ) in the transformed plane can be computed from:

$$u_\tau = -\frac{\partial \psi^*_{slope}}{\partial \xi_\tau} \quad \text{and} \quad v_\tau = \frac{\partial \psi^*_{slope}}{\partial \eta_\tau} \tag{2.67}$$

Finally, the velocity field in the physical plane ($\vec{V}_{flood}(z)$) can be directly derived from equation (2.65).

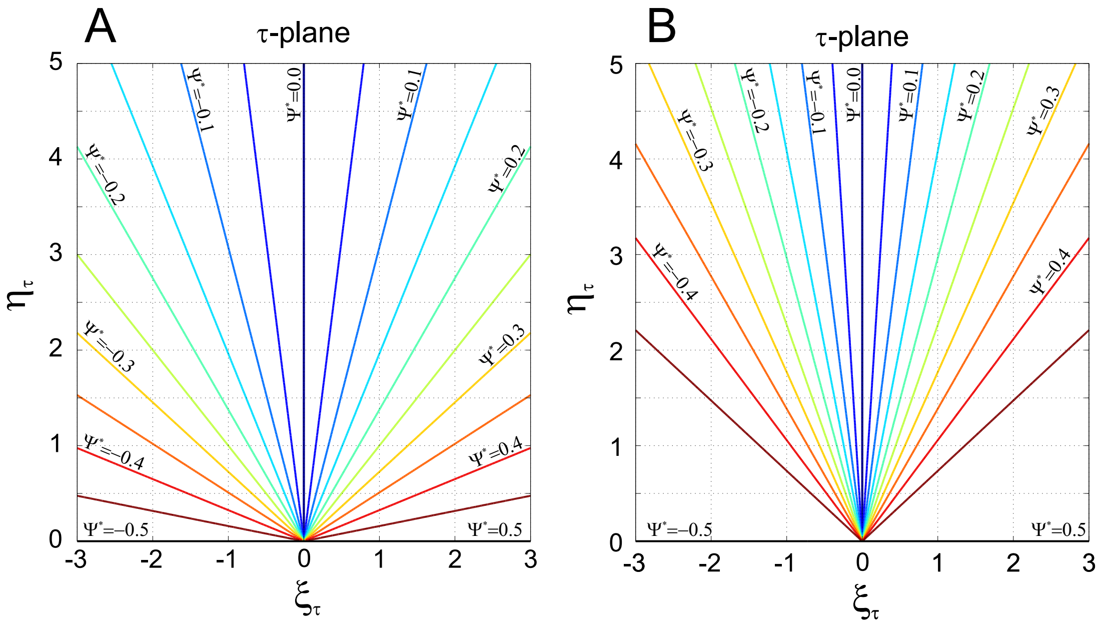

Figure 2.4: Analytic solutions of a flat bottom streamlines (a) and from a linearly sloping bottom (b) under the influence of a half-sink.

They noticed that, on the contrary to the horizontal case, where the streamlines were equally distributed, a concentration of streamlines around the axis pointing orthogonally with respect to the coast arises, showing that a selective withdrawal takes place offshore (see Figure 2.4). The flat bottom streamlines, with sink only (Figure 2.4 (a)), show that the sink draws water evenly from the whole water body. The withdrawal in this case is spread evenly across the entire domain. The streamlines that result from the linearly sloping bottom show a withdrawal that concentrates around the η_τ axis (Figure 2.4 (b)). Because the difference in adjacent streamlines defines a volumetric flux, it is apparent that a greater volume of water is being drawn from offshore than from the near shore region.

The applicability of these conceptually simple analytic solutions were tested and verified by a field study carried out with drogues in a realistic sandy inlet in Koombana Bay (Australia) and by a Hele-Shaw cell experiment. Thus, they showed that simple analytical solutions that include the effects of sloping bottom can be used to show the selective withdrawal patterns of flood flow.

2.2.3 Morphodynamic model

2.2.3.1 Bathymetric changes formulation

Having determined the structure of the tidally driven flow field both in the tidal channel and in the offshore region, we can proceed to determine the sediment balance in the tidal channel. In this work we consider an uniform bottom composed by noncohesive sediment. The source of this material is double: it may derive both from the tidal channel bottom and from the erosion of the continental shelf. However, despite erosive and deposition processes will be accounted for in the continental shelf to compute sediment transport, hydrodynamics computations in this region will be carried out assuming a fixed flat continental shelf of constant slope, thus neglecting bathymetric changes for the sake of simplicity. Thus, only bathymetric changes on the tidal channels will attract the attention of the present work.

In the tidal channel region ($x > 0$), the width of the erosional/depositional zone is equivalent to the channel width (b). On the contrary, the offshore depositional zone ($x < 0$) spans a much higher area limited by the spreading width of the offshore plume ($2b_{jet}$).

Sediment load in this work refers to the sediment that is in motion in the tidal channel and in the offshore region. Depending on the mechanism for transport there are two common ways of classifying the sediment load: (a) bed load transport, defined as that in which the successive contacts of the particles with the bed are strictly limited by the effect of gravity and that will be computed only in the tidal channel, and (2) suspended load transport, defined as that in which the excess weight of the particles is supported by random successions of upward impulses imported by turbulent eddies that diffuse suspended sediment throughout the vertical column, and that will be computed both in the tidal channel and in the offshore region.

The morphodynamic evolution of the tidal channel bottom is governed by the Exner equation for sediment continuity (Paola and Voller, 2005):

$$(1-p)b\frac{\partial \eta}{\partial t}+\frac{\partial (bq_b)}{\partial x}=D_e-E_r, \tag{2.68}$$

where b is the channel width, p is bottom porosity, q_b is the bed load transport rate per unit width, and D_e and E_r are the deposition and erosion rates of suspended sediment per unit channel length. Thus, bed level changes with time t due to bed load transport, sediment entrainment into suspension, and sediment deposition onto the bed can be predicted with this partial differential equation. This equation can be solved along with the shallow water equations (equations (2.2) and (2.3)) to predict aggradation or degradation of tidal channel bed.

To solve this equation, it is necessary to have relations to compute bed load transport (i.e., q_b) and erosive and depositional fluxes of suspended sediment (i.e., D_e an E_r).

2.2.3.2 Bed load transport formulation

A large number of bed load relations can be expressed in the following general form (Garcia, 2008):

$$q_b = q_{b,0} f(\theta) \tag{2.69}$$

Here q_b is the volumetric bed load sediment transport rate and $q_{b,0}$ is a dimensionless bed load transport rate known as the Einstein bed load number given by:

$$q_{b,0} = \sqrt{\Delta g d_s^3}, \tag{2.70}$$

where g is the acceleration of gravity, Δ is the submerged specific gravity of the sediment ($\Delta = \rho_s/\rho - 1$, where ρ denotes the density of water and ρ_s denotes the density of sediment), and d_s represents the characteristic particle diameter. Estuarine sediments are derived both from fluvial and marine sources, with grain sizes ranging from sands to mud. In tide-dominated estuaries a dominance of sand is typically found in channels, whereas a dominance of silt and clay characterizes the adjacent tidal flats and/or salt marsh deposits (Wells, 1995). In the above equation (2.69) θ is a dimensionless measure of boundary shear stress known as the Shields parameter. It is given by the definition:

$$\theta = \frac{u_*^2}{\Delta g d_s} \tag{2.71}$$

with u_* the bed-shear velocity.

The bed load sediment transport in the tidal channel is here computed employing the Meyer-Peter and Müller (1948) equilibrium formula. This expression, empirical in nature, is widely used in nearshore sediment applications (Soulsby, 1997). It reads:

$$q_b = q_{b,0} f(\theta) \text{ with } f(\theta) = 8(\theta - \theta_{cr})^{\frac{3}{2}}. \tag{2.72}$$

In this formulation, θ_{cr} is the threshold value of the Shield stress for beginning of bed load transport. Whereas Soulsby (1997) assumed a value of $\theta_{cr} = 0.047$, we use the value given by the Shields curve for initiation of motion of van Rijn (1984b), in which θ_{cr} depends on the sand particle properties through the parameter D_* as follows:

$$\theta_{cr} = \begin{cases} 0.240 D_*^{-1} & \text{if } D_* \leq 4 \\ 0.140 D_*^{-0.64} & \text{if } 4 < D_* \leq 10 \\ 0.040 D_*^{-0.10} & \text{if } 10 < D_* \leq 20 \\ 0.013 D_*^{0.29} & \text{if } 20 < D_* \leq 150 \\ 0.055 & \text{if } D_* > 150, \end{cases} \tag{2.73}$$

where $D_* = R_{ep}^{2/3}$, being R_{ep} the particle Reynolds number:

$$R_{ep} = \frac{\sqrt{\Delta g d_s^3}}{\nu}, \tag{2.74}$$

with ν being the kinematic viscosity of water.

2.2.3.3 Suspended load transport in the tidal channel and in the offshore region during the flood phase

We compute the suspended sediment concentration inside the tidal channel and during the flood-phase in the offshore region with the one dimensional advection-diffusion equation:

$$\frac{\partial c}{\partial t} + \frac{\partial uc}{\partial x} = \frac{E_r - D_e}{A} + \frac{1}{A}\frac{\partial}{\partial x}\left(k_x A \frac{\partial c}{\partial x}\right), \tag{2.75}$$

where c is the cross-sectionally averaged concentration, $A = b \cdot d$ is the cross-sectional area, and k_x is a longitudinal diffusivity coefficient. As suggested by field observations in estuaries (Sanford and Halka, 1993), the above formulation allows simultaneous erosion and deposition.

The instantaneous rate at which sand is picked up is given in terms of a pickup function E_{ent} such that:

$$E_r = E_{ent} w_s b, \tag{2.76}$$

where w_s is the fall velocity of non-spherical sediment particles and b_{ent} is a parameter accounting for the presence of bedforms. Falling under the action of gravity, a particle will reach a constant, terminal velocity once the drag equals the submerged weight of the particle. The relation for terminal fall velocity for a spherical particle in quiescent fluid can be presented as (van Rijn, 1984c):

$$w_s = \begin{cases} \dfrac{\Delta g d_s^2}{18\nu} & \text{if } d_s < 100\mu\text{m} \\ 10\dfrac{\nu}{d_s}\left[\sqrt{1 + \dfrac{0.01\Delta g d_s^3}{\nu^2}} - 1\right] & \text{if } 100\mu\text{m} \le d_s \le 1000\mu\text{m} \\ 1.1\sqrt{\Delta g d_s} & \text{if } d_s > 1000\mu\text{m}. \end{cases} \tag{2.77}$$

Several different relationships for estimating the pick-up rate of sediments into suspension are available in the literature (Chaudhry, 2007; Garcia and Parker, 1991; van Rijn, 1984a; Nielsen, 1992). According to Nielsen (1992) we can infer the pick-up function from near-bed sediment concentration. In this sense we use the the relationship of van Rijn (1984c) for uniform sediment bottom, that according to Chaudhry (2007), may be written as:

$$E_{ent} = 0.015 \frac{d_s}{b_{ent}} \left(\frac{\theta}{\theta_{cr,s}} - 1\right)^{1.5} R_{ep}^{-0.2}, \tag{2.78}$$

in which $\theta_{cr,s}$ is the critical Shields parameter for beginning of suspension evaluated on the basis of the criterion proposed by van Rijn (1984c). On the basis of some results of experimental research at the Delft Hydraulics Laboratory, van Rijn determined the critical flow conditions at which instantaneous upward turbulent motions of the sediment particles (bursts) with jump lengths of the order of 100 particle diameters were observed. Under these observation, van Rijn defined a criterion at which locally turbulent bursts of sediment particles are lifted from the bed into suspension:

$$\theta_{cr,s} = \begin{cases} \dfrac{16 w_s^2}{D_*^2 \Delta g d_s} & \text{if } 1 < D_* \leq 10 \\ \dfrac{0.16 w_s^2}{\Delta g d_s} & \text{if } D_* > 10. \end{cases} \tag{2.79}$$

According to van Rijn (1984d) b_{ent} can be taken as (i) 0.5 times the average bedform amplitude if bedforms are present and larger than the Nikuradse roughness height ($k_s = 3d_{90}$, with d_{90} being the grain size such that 90% of the sediment is finer) or (ii) equal to $0.01d$ if bedforms are not present, where d is water dept. The existence or not of bed forms depends on a transport stage parameter controlled mainly by the bed-load transport that reads:

$$T_s = \frac{\theta - \theta_{cr}}{\theta_{cr}}, \tag{2.80}$$

and influences also the flow conductance. For $T \leq 0$ and $T \geq 25$ the bed surface is almost flat. In these cases, van Rijn (1984d) showed that and the overall bed roughness height e_r will only depend on the Nikuradse or effective grain rough:

$$e_r = k_s. \tag{2.81}$$

On the contrary, for $0 < T < 25$, dune-type bed forms are present and their contribution is added to the Nikuradse roughness as:

$$e_r = k_s + 1.1 A_d (1 - \exp(-25\Psi_d)), \tag{2.82}$$

in which $\Psi_d = A_d / L_d$ is the bed form steepness, with A_d and L_d amplitude and wavelength of the bedforms respectively (van Rijn, 1984d):

$$L_d = 7.3d \tag{2.83}$$

$$A_d = 0.11d \left(1 - \exp\left(-\frac{T}{2}\right)\right)(25 - T)\left(\frac{d_s}{d}.\right)^{0.3} \tag{2.84}$$

With the above expressions, the Chezy flow conductance C is computed as:

$$C = 2.5 \ln\left(12 \frac{e_r + d}{e_r}\right). \tag{2.85}$$

In regard to the deposition fluxes, Winterwerp (2007) suggested that the deposition rate can be represented by the settling flux:

$$D_e = c_b\, w_s\, b, \tag{2.86}$$

where c_b is the sediment concentration close to the bed and is supposed to be twice the depth-averaged concentration c (García, 1993; Altinaker et al., 1996).

2.2.3.4 Averaged mass transport in the offshore region during the ebb phase

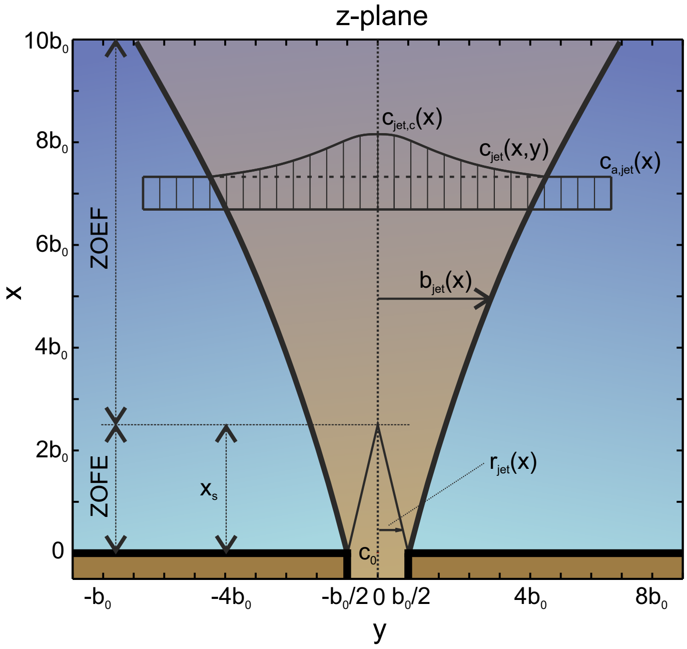

Figure 2.5: Definition sketch for the offshore plume sediment concentration in a jet exiting a tidal channel during the ebb phase.

As in the hydrodynamic problem presented in Section 2.2.2.2, the sediment concentration in the plume exiting the tidal channel is determined on the basis of the turbulent jet theory. We employ the quasi-stationary model of suspended sediment and mass transport in the vicinity of tidal inlets presented by Özsoy (1986):

$$\frac{\partial}{\partial x}(d_{jet}\, u_{jet}\, c_{jet}) + \frac{\partial}{\partial y}(d_{jet}\, v_{jet}\, c_{jet}) = -S_{jet} + \frac{\partial}{\partial y}\mathscr{F}_y, \tag{2.87}$$

where the coordinate system of Figure 2.5 is used, d_{jet} is the ebb-phase averaged water depth along the x-axis, u_{jet} and v_{jet} are the velocity components described in Section 2.2.2.2, c_{jet} is the depth-averaged sediment concentration, $S_{jet} = w_s\, c_{jet}\left(1 - \frac{\theta}{\theta_{cr,s}}\right)$ is a sediment source/sink term, and $\mathscr{F}_y$ is the turbulent flux of concentration perpendicular to the jet axis. Note that the jet is assumed to be in a steady state. The presence of an ambient concentration distribution variable along the jet axis $c_{a,jet} = c_{a,jet}(x)$ is taken into account. The basic variable to be calculated here is the concentration distribution $c_{jet}(x, y)$, which is assumed to be self-similar with respect to the normalized coordinate $\zeta = y/b_{jet}(x)$.

$$\frac{c_{jet}(x,y)-c_{a,jet}(x)}{c_{jet,c}(x)-c_{a,jet}(x)}=G(\zeta). \tag{2.88}$$

The sediment concentration fields is parameterized using a similarity function related to the velocity profile $G(\zeta)=F(\zeta)^{1/2}$, since the eddy diffusivity of the scalar concentration doubles that of the momentum in turbulent jets (Abramovich, 1963; Stolzenbach and Harleman, 1971; Özsoy, 1986):

$$G(\zeta)=F^{1/2}(\zeta)=\begin{cases}0 & \text{if } |y|>b_{jet}\\ 1-\varrho^{1.5} & \text{if } r_{jet}\le|y|\le b_{jet}\\ 1 & \text{if } 0<|y|<b_{jet}\end{cases} \tag{2.89}$$

where:

$$\varrho=\frac{|y|-r_{jet}}{b_{jet}-r_{jet}}. \tag{2.90}$$

The self-similar structure of concentration and velocity profiles in classical two-dimensional turbulent jets allows for an integration of equation (2.87) across the jet cross-section, yielding:

$$\frac{\partial}{\partial x}\left(d_{jet}\int_{-b_{jet}}^{b_{jet}}u_{jet}c_{jet}dy\right)-2d_{jet}v_e c_{a,jet}=-w_s\int_{-b_{jet}}^{b_{jet}}c_{jet}\left(1-\frac{\theta^2}{\theta^2_{cr,s}}\right)dy. \tag{2.91}$$

With the similarity hypothesis (equation (2.89)), the entrainment relationship (equation (2.24)) and assuming that when $y \rightarrow b_{jet}$ the velocity u_jet and the lateral diffusive flux $\mathscr{F}_y$ vanish, equation (2.91) becomes:

$$\frac{\partial}{\partial \xi_b}(\bar{I}_4 D_{jet}B_{jet}U_{jet,c}C_{jet,c})-\alpha C_{a,jet}D_{jet}B_{jet}U_{jet,c}=-\gamma B_{jet}C_{jet,c}(\bar{I}_3-\phi^2\bar{I}_5U^2_{jet,c}), \tag{2.92}$$

where following dimensionless variables have been used in the previous equation: $C_{jet,c} = c_{jet,c}/c_0$, $C_{a,jet} = c_{a,jet}/c_0$, $\gamma = b_0w_s/(2d_0u_0)$ is a sediment settling velocity parameter, and $\phi = u_0/u_{s,cr}$ is an erosion parameter. Besides, c_0 is the ebb-phase averaged concentration at the inlet, $c_{a_{jet,c}}$ is the plume axis ambient concentration in the receiving basin, i.e., the exiting concentration before the ebb-phase beginning, $c_{jet,c}$ is the plume centerline concentration, and $u_{cr,s}$ is the critical shear velocity por sediment erosion in the receiving basin computed according to equation (2.79). The expression of $\bar{I}_3$, $\bar{I}_4$ and $\bar{I}_5$ are:

$$\bar{I}_n=\int_0^1\left(\frac{c_{jet}}{c_{jet,c}}\right)\left(\frac{u_{jet}}{u_{jet,c}}\right)^{n-3}d\zeta,\ \text{ for } n=3,4,5, \tag{2.93}$$

which are evaluated making use of equation (2.89):

$$\bar{I_n} = \frac{R_{jet}}{B_{jet}} + \left[I_n + (I_{n-3} - I_n)\frac{C_a, jet}{C_{jet,c}} \right]\left(1 - \frac{R_{jet}}{B_{jet}}\right), \text{ for } n = 3,4,5, \tag{2.94}$$

where I_3, I_4, and I_5 are numerical constant equal to 0.600, 0.368 and 0.278 respectively, with:

$$I_n = \int_0^1 (1 - \zeta^{1.5})^{2n-5} d\zeta, \text{ for } n = 3,4,5. \tag{2.95}$$

Making use of equation (2.95), equation (2.92) takes the form:

$$\frac{\partial X_{jet}}{\partial \xi_b} + Q_{jet} X_{jet} = M_{jet}, \tag{2.96}$$

where:

$$X_{jet}(\xi_b) = (I_1 - I_4)(B_{jet} - R_{jet}) D_{jet} U_{jet,c} C_{a,jet} + [R_{jet} + I_4(B_{jet} - R_{jet})] D_{jet} U_{jet,c} C_{jet,c}, \tag{2.97}$$

$$Q_{jet}(\xi_b) = \frac{\gamma[R_{jet} + I_3(B_{jet} - R_{jet})] - \gamma\phi^2 U_{jet,c}^2 [R_{jet} + I_5(B_{jet} - R_{jet})]}{D_{jet} U_{jet,c}[R_{jet} + I_4(B_{jet} - R_{jet})]}, \tag{2.98}$$

and

$$\begin{aligned} M_{jet}(\xi_b) = {} & \alpha D_{jet} U_{jet,c} C_{a,jet} + \gamma\left[\phi^2 U_{jet,c}^2 (I_2 - I_5) - (1 - I_3)\right](B_{jet} - R_{jet}) C_{a,jet} + \\ & (I_1 - I_4) D_{jet} U_{jet,c} (B_{jet} - R_{jet}) Q_{jet} C_{a,jet}, \end{aligned} \tag{2.99}$$

where it must be considered that $U_{jet,c} = 1$ in the ZOFE and $R_{jet} = 0$ in the ZOEF, and solutions for $U_{jet,c}$, B_{jet} and R_{jet} where obtained in Section 2.2.2.2. Applying the initial conditions at the tidal inlet mouth ($D_{jet} = R_{jet} = B_{jet} = C_{jet,c} = 1$), equation (2.96) can be integrated, yielding:

$$X_{jet}(\xi_b) = \frac{1}{P_{jet}(\xi_b)}\left(\int_0^{\xi_b} P_{jet}(\xi_b) M_{jet}(\xi_b) d\xi_b + 1\right), \tag{2.100}$$

where $P_{jet}(\xi_b)$ is an integration factor:

$$P_{jet}(\xi_b) = \exp\left(\int_0^{\xi_b} Q_{jet}(\xi_b) d\xi_b\right). \tag{2.101}$$

Hence, the centerline concentration is obtained from equation (2.97) as:

$$C_{jet,c}(\xi_b) = \frac{X_{jet} - (I_1 - I_4) D_{jet} U_{jet,c} (B_{jet} - R_{jet}) C_{a,jet}}{[R_{jet} + I_4(B_{jet} - R_{jet})] D_{jet} U_{jet,c}}, \tag{2.102}$$

Note that for obtaining solutions for $C_{jet,c}$, $U_{jet,c} = 1$ in the ZOFE ($\xi_b < \xi_{b,s}$), while for the ZOEF ($\xi_b \geq \xi_{b,s}$) $R_{jet} = 0$.

2.2.3.5 Shield parameter for partially dry areas

To evaluate the bottom shear stresses θ associate to a generic representative elementary area A^* we apply the averaging procedure presented in Section 2.2.2.1 (Defina, 2000; Lanzoni and Seminara, 2002) again. The local value of the Shields parameters read:

$$\theta(x,y,t)=\frac{|\tau_b|/\rho}{\Delta g d_s}, \tag{2.103}$$

where τ_b is the local shear stress acting at the bottom. If it is assumed that the spatial variations of η are small enough, τ_b can be approximate with the longitudinal component of the stress acting at the bed. Recalling that $\nabla\psi_H$ behaves as a delta function picking out the bottom surface and that $\partial\psi_H/\partial z$ is a delta distribution centered at $z=\eta$, and assuming that in a gradually varying flow gravity is mainly balanced by friction , τ_b can be appropriately approximated as follows:

$$\tau=\rho g\frac{\partial h}{\partial x}\int_{-\infty}^{h}(h-z)\frac{\psi_H}{\partial z}dz=\rho g\frac{u^2}{C^2}\left(\frac{d}{\Phi_H}\right)^2\int_{-\infty}^{h}(h-z)\frac{\psi_H}{\partial z}dz. \tag{2.104}$$

Hence, the averaged value of the Shields parameter over the representative elementary area A^* is found to be:

$$\theta=\frac{1}{A^*}\int_{A^*}\frac{|\tau_b|/\rho}{\Delta g d_s}dA^*=\frac{1}{\Delta g d_s}\frac{du^2}{C^2}\left(\frac{d}{\phi_H}\right)^2. \tag{2.105}$$

This value of θ will be used to evaluate the bed load (equation (2.72)) and the sediment entrained into suspension (equation (2.78)) associated with each representative elementary area A^*.

2.2.3.6 Boundary conditions for sediment transport formulation

The morphodynamic problem is completed by imposing several conditions to the sediment fluxes. Regarding the instantaneous bed load transport, it must vanish at the inner end of the channel. This condition is automatically satisfied having imposed that the instantaneous cross-sectionally averaged velocity must also vanish at this locations. As previously stated, bed load transport is only computed in the tidal channel.

Regarding the advection-diffusion equation of sediment concentration in the channel, a suitable coupling offshore-tidal channel boundary condition is employed during the flood phase, since it is at this stage when the sediment that comes from the offshore region is entering into the channel. This boundary is applied at the tidal channel mouth ($x=0$) and allows for the transference of the sediment concentration existing in the basin due to the sediment-laden plume an that is entering into the channel during the flood phase. To this end, at the channel mouth ($x=0$), we add a sediment source to the existing sediment concentration.

Finally, in the offshore region two distinct procedures have been employed to determine de sediment transport and different conditions are imposed:

- During the ebb phase the sediment concentration distribution is simply averaged through a model of mass transport by turbulent jets in the vicinity of tidal inlets (Özsoy, 1986). In this case, the model is fed by the velocity, jet width and core width of the outflow presented in Section 2.2.2.2. The morphological variables required to determine the sediment concentration field will be (i) the averaged sediment concentration exiting the tidal channel (at $x = 0$) during the ebb-phase (c_0) and (ii) the ambient concentration field remaining in the continental shelf after the flood-phase.
- During the flood phase, the advection-diffusion equation of sediment concentration in the channel is computed assuming a vanishing sediment concentration at the seaward end of the receiving basin ($x \to -\infty$). The exiting sediment concentration at the tidal channel mouth ($x = 0$) will be transferred to the tidal channel, as previously mentioned. Obviously, at the beginning of the flood phase, the initial sediment concentration will be that resulting of the ebb phase.

2.2.4 Numerical Scheme

2.2.4.1 Computational procedure

The differential system governing the dynamics of the liquid phase (equations (2.2) and (2.3)) and the solid phase (equations (2.68) and (2.75) is a set of nonlinear hyperbolic equations that must be solved by numerical schemes. We use the two-step predictor-corrector finite difference scheme of MacCormack (Bhallamudi and Chaudhry, 1991; MacCormack, 2003).

The MacCormack scheme is an explicit scheme (the solution at time $k+1$ depends only on the solution at time k and on the boundary conditions), is simple to implement, and does not require inversion of large matrices. Since the differential equations are written in conservative form and are solved simultaneously, this scheme can capture shocks and discontinuities without any special treatment. It is also easy to incorporate general empirical equations for bottom roughness or vertical sediment fluxes due to erosive processes. The time step employed in the numerical simulations was determined through the Courant-Friedrichs-Lewy (CFL) condition in order to fulfill a stability criterium. Furthermore, unavoidable numerical oscillations near the steep wave front that arise during its propagation, typical of higher-order schemes like the MacCormack scheme, are dampened by introducing an artificial viscosity technique. The stability criterion and the artificial viscosity technique are described below.

The scheme is a fractional-step predictor-corrector method that achieves second order accuracy in space and time. In the predictor part, forward finite differences are used for approximating the spatial partial differential terms. In the corrector step, they are approximated by backward finite differences, but using the predicted variables.

The predictor step is given by:

$$\frac{\partial f}{\partial t} = \frac{f_j^p - f_j^k}{\Delta t} \ , \ \frac{\partial f}{\partial x} = \frac{f_{j+1}^k - f_j^k}{\Delta x}, \tag{2.106}$$

whereas the corrector step is:

$$\frac{\partial f}{\partial t} = \frac{f_j^c - f_j^p}{\Delta t} \ , \ \frac{\partial f}{\partial x} = \frac{f_j^k - f_{j-1}^k}{\Delta x}, \tag{2.107}$$

where j is the spatial index of the computational grid, k is the temporal index, the superscripts p an c indicate the predictor and corrector value of the variable respectively, and dx and dt represents the distance and time steps, respectively. The values of the unknown at the next time step, i.e., at time $k+1$, is evaluated as the average value between the value at the previous time step and the corrector one as:

$$f_j^{k+1} = \frac{1}{2}(f_j^k + f_j^c). \tag{2.108}$$

2.2.4.2 Global boundary conditions

As far as the value of the variables at the boundaries is concerned, the MacCormack method requires a numerical implementation of the these values (Hirsch, 2007). Note that the advection-diffusion equations for resolving the sediment concentration field has second order spatial derivatives which forces to determine global boundary values the most extreme points of the numerical scheme by interpolation. The procedure followed in the present work for obtaining global boundary values was:

- The predictor values of water and bottom elevations at the landward boundary were specified by a zero-order time extrapolation.(Lanzoni and Seminara, 2002).
- The corrector values of water speed and bed elevation at the tidal channel mouth, on the other hand, were calculated using a first-order space extrapolation (Lanzoni and Seminara, 2002).
- The predictor values of sediment concentration at the two sections of the tidal channel closest to the landward boundary were determined by a first-order space extrapolation. Additionally, the incoming sediment during the flood phase from the offshore plume was added to the predictor value of concentration at the channel mouth.
- The corrector values of sediment concentration at the two sections of the tidal channel closest to the channel mouth were determined by a first-order space extrapolation. Additionally, the incoming sediment during the flood phase from the offshore plume was added to the predictor value of concentration at the channel mouth.
- Regarding the sediment concentration within the offshore plume during the flood phase, the predictor values of the two grid points closest to the tidal channel mouth were determined by a first-order space extrapolation, whereas the corrector values of the two farthest seaward points were specified by a zero-order time extrapolation.

Finally, as stated by Lanzoni and Seminara (2002), the morphological evolution of the estuary is characterized by the formation of a sediment front which migrates landward. As this discontinuous front reaches the inner end of the estuary and until it is completely reflected, the above procedure employed to estimate the predictor and corrector values of bed elevation at the landward boundary must be temporarily modified. The bottom elevation is then estimated on the basis of an integral (i.e., weak) formulation of the sediment balance equation which allows us to write the relationship between bottom elevations and sediment fluxes on both sides of the sediment front.

2.2.4.3 Artificial viscosity technique

Higher-order schemes like the MacCormack scheme usually produce numerical oscillations near the steep wave fronts which may be dampened by introducing artificial viscosity. For this purpose, the procedure presented by Bhallamudi and Chaudhry (1991) is be used. This procedure smoothens the high-frequency oscillations and leaves the smooth areas relatively undisturbed. The following algorithm, applied to each variable (u, h, η, q_b and c) at the end of every time step, reads:

$$\upsilon = \frac{|f_{j+1} + 2f_j + f_{j-1}|}{|f_{j+1}| + |2f_j| + |f_{j-1}|}, \tag{2.109}$$

$$\epsilon_{j-1/2} = k_{av} \max(\upsilon_{j-1}, \upsilon_j) \tag{2.110}$$

where f refers to the value of the variable after applying the MacCormack procedure and k_{av} is a dissipation coefficient which value depends on the smoothed variable f. The final value of f at the new time step is given by:

$$f_j^{k+1} = f_j^{k+1} + \epsilon_{j+1/2}(f_{j+1}^{k+1} - f_j^{k+1}) - \epsilon_{j-1/2}(f_j^{k+1} - f_{j-1}^{k+1}). \tag{2.111}$$

2.2.4.4 Numerical stability

For numerical stability, the MacCormack scheme must satisfy the Courant-Friedrichs-Lewy (CFL) condition at every grid point of the domain given by:

$$CFL = \frac{dt}{dx}\left(u + \sqrt{gd}\right) \leq 1. \tag{2.112}$$

2.3 Results

2.3.1 Influence of offshore plume on the tidal channel evolution

In this Section the long-term hydro-morphodynamic evolution of a tide-dominated estuary coupled to its offshore plume is investigated. In order to introduce the reader to our numerical simulations and the physical processes simulated in this contribution, it is preliminarily convenient to start this section with a reference case in which the influence of the offshore plume on the tidal channel evolution is addressed. Figure 2.6 compares the long-term bottom equilibrium profiles without and with the influence of the plume dynamics. The first case is achieved by assuming that the suspended sediments of the plume settle immediately after the end of the ebb-phase, i.e., no plume sediment enters the tidal channel during the flood phase. This is, for example, the case treated by Lanzoni and Seminara (2002), Hibma et al. (2003), Todeschini et al. (2008), Van der Wegen and Roelvink (2008), Yu et al. (2012) and Bolla Pittaluga et al. (2015), where simply a sediment load in equilibrium with the local hydrodynamics at the channel mouth is prescribed. On the other hand, unless otherwise indicated, the only source of sediment will be the material coming from the tidal channel bottom, i.e., erosion in the offshore region will be ignored.

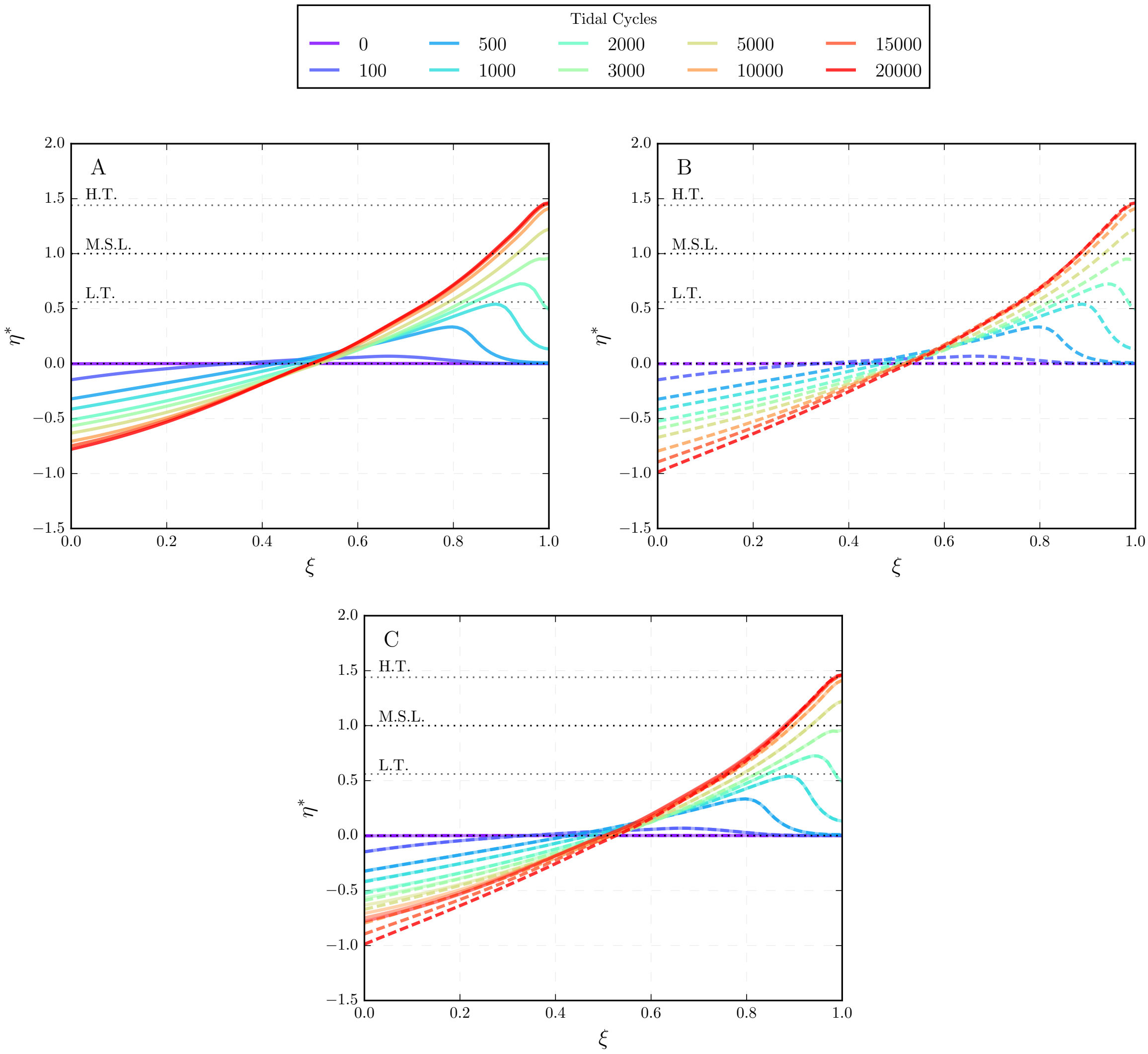

Figure 2.6: Temporal evolution of the bottom profile from an initially horizontal configuration for a convergent tidal channel (a) with and (b) without the influence of the offshore plume. The bottom elevation at each cross section has been scaled with the initially uniform depth of the channel ($\eta^*/d(t=0)$), while the longitudinal coordinate of the tidal channel has been scaled with the channel length ($\xi = x/L_e$). The values of the relevant parameters imposed in the calculation are $L_e = 30$ km, $L_b = 25$ km, $b_0 = 160$ m, initial bottom depth $d(t=0) = 5$ m, semidiurnal tide with amplitude $a_0 = 2.2$ m, mean sediment diameter of $d_s = 100$ μm. The continental shelf is supposed to be horizontal with a mean Chezy coefficient $C_z = 55$ m$^{1/2}$/s. A comparison between the cases (a) and (b) is depicted in the panel (c) for the sake of clarity. Horizontal dashed lines represent the high tide (H.T.), mean sea level (M.S.L.) and low tide (L.T.) elevations at the channel mouth.

In both cases an identical transient process takes place during the first stages of the channel bed evolution. Starting from an initial horizontal bed profile, the material is scoured at the seaward portion of the channel forming a sediment front that aggrades and migrates landward generating a shoaling bed profile. Later, the front tends to be completely reflected, eventually leading to bed emersion and the formation of a shore (Figure 2.6 (a) and (b)). Nevertheless, once the sediment front is reflected, the bed configurations attained in the two cases differ substantially in their seaward portions. Whereas in the absence of any plume influence a quasi-linear profile of constant slope forms (Figure 2.6 (b)), similar to the one reported by Lanzoni and Seminara (2002) and Todeschini et al. (2008), when considering the plume-tidal channel coupling the bed profile tends to increase its concavity, reducing the channel mouth depth (Figure 2.6 (a)). We observe that the plume limits its influence to seaward region of the channel. Besides, changes in bottom elevation as a consequence of the offshore plume tend to decrease in the landward direction, almost vanishing at the position at which the front begins to form (Figure 2.6 (c)). This is related to the reduction of the ability of carrying sediment with distance from the tidal channel mouth of the advective and diffusive processes that control the mass transference from the offshore plume towards the tidal channel. Notice that results presented herein refer to relatively large values of the tidal amplitude a_0 with respect to the initial water depth of the tidal channel $d(t=0)$ and consequent large values of flow velocity, which implies a fast evolution of the system.

The long-term simulations shown in Figure 2.6 eventually reach a stable bathymetric pattern characterized by an upward concavity and by a well-defined depth at the inlet section. In order to evaluate how far is this profile from an equilibrium configuration, we observe that, based on the Exner equation (2.68), a tidal channel is in a strict morphodynamic equilibrium provided the gradient of the bed load sediment transport equals the balance of erosion and sedimentation fluxes of suspended sediment. This is a highly severe requirement, that is unlikely to establish in nature. Considering the complexity on the investigated dynamic system, the uncertainty in boundary conditions, and the effects of possible heterogeneities, a weakly dynamic equilibrium state should rather be used to characterize the system. In order to explore the tendency of the system to approach a quasi-equilibrium configuration, we considered the root-mean-square (RMS) of the bed level changes integrated all along the estuary between successive tidal cycles (Van Maanen et al., 2011). This metric can be used to reveal a reduction in the rate of morphodynamic activity over time as a relatively stable morphologic pattern is attained. The RMS value for the tidal cycle k, with $k > 0$, is given by:

$$RMS(k) = \left[\frac{1}{N} \sum_{i=1}^{N} \left(\eta_i^k - \eta_i^{k-1} \right)^2 \right]^{1/2}, \tag{2.113}$$

where N is the number of points used to discretize the bottom profile. Figure 2.7 reveals a reduction in the rate of morphodynamic activity over time and relatively stable morphologic patterns evolve. It allows us to establish a quasi-equilibrium configuration state based on the requirement that the RMS evolution attains an asymptotic trend over successive tidal cycles.

According to the the results depicted in Figure 2.7, four stages can be distinguished during the morphodynamic evolution of a tidal channel:

1. The initiation of channel evolution causes considerable bathymetric changes, resulting in relatively large RMS-deviation values. Indeed, during the initial tidal cycles it reaches a peak value of about 3 mm independently of the influence of the offshore plume. This high intensity of the morphodynamic activity is mainly related to the severe erosive processes that take place at the seaward portion of the tidal channel and to the formation of the sediment front.

2. From this initial maximum, the RMS follows a negative-exponential trend characterized by a decreasing rate of the morphodynamic activity. During this exponential behaviour two distinct regions are well-defined in the two curves obtained by considering or excluding offshore plume effects. An initial region where the overall morphological evolution

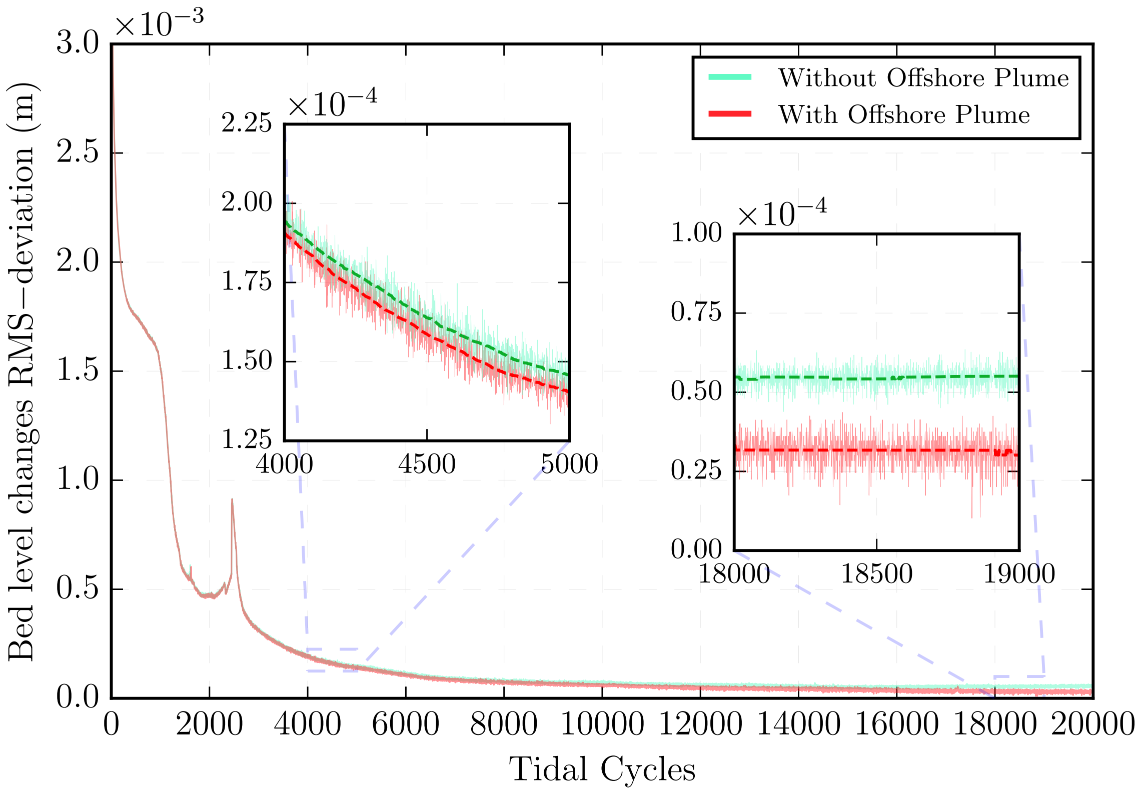

Figure 2.7: Root-mean-square of the bed level changes between successive tidal cycles computed over all grid cells in the tidal channel as a function of tidal cycles throughout tidal channel evolution. Two cases are depicted: RMS of bed level changes evolution in convergent tidal channel with (red lines) and without (green lines) the influence of the offshore plume. Two inset-zoom are included for a clear display of evolutionary changes between cases at different stages of the simulations. Dashed lines are the median filtered signal of the original RMS series using local window-size of 301 elements. Initial conditions: $L_e = 30$ km, $L_b = 25$ km, $b_0 = 160$ m, $d(t=0) = 5$ m, $a_0 = 2.2$ m, $d_s = 100$ μm, and horizontal continental shelf with $C_z = 55$ m$^{1/2}$/s

occurs at a faster pace and the RMS trend decays rapidly. During this period the sediment front migrates landward. This stage of channel evolution eventually finishes approximately in 2500 tidal cycles, just the moment when the sediment front is completely reflected. It produces a "morphological-readjustment" peak that coincides with the time at which a turbidity maximum zone arises close to the landward boundary of the tidal channel and an acceleration of the deposition processes occurs in this region. The formation of this turbidity maximum zone will be studied in Section 2.3.2.2.

3. After this point a second region of morphodynamic activity characterized by following a trend of weak morphodynamic activity in which the RMS decays slowly arises. This phase is extended until 16000 tidal cycles and covers the period in which the more remarkable differences arise between the case in which the offshore is taken into account and the case in which this influence is not considered. In the case without the offshore plume sedimentation processes at the landward portion and erosive processes at the seaward portion occur (Figure 2.6 (c)). There is not a sediment reentry from the offshore region and the bed level close to the channel mouth tends to go down. On the contrary, in the case with the offshore plume only deposition processes close to the landward part of the tidal channel take place (Figure 2.6 (b)). In this case no net bathymetric changes take place at the seaward chan-

nel portion. Thus, as a consequence of the offshore plume influence, the morphodynamic activity of the tidal channel reduces its intensity. It can be observed with a high degree of clarity in the inset-zooms included in Figure 2.7. In these inset-zooms the median filtered signal of the original RMS series is plotted using two dashed lines for clarity.

4. The final stage of the tidal channel evolution starts when the beach emerges above the high water level. It is achieved approximately after 18000-20000 tidal cycles. At this stage, both the case without and the case with the influence of the offshore plume reach an asymptotic state or a dynamic state of equilibrium. Now the bathymetric changes are negligible and constant over time. Besides, the magnitude of these changes is weaker (almost a half) in the presence of the offshore plume. It reveals the net sediment exchange processes between the offshore plume and the tidal channel as a key factor that favors the development of stable channel patterns.

2.3.2 Towards an equilibrium configuration of the tidal channel: hydrodynamics and morphodynamics implications

The feedback-interactions between hydrodynamics, sediment transport and bed level changes play a crucial role during the morphological evolution of a tidal channel towards a quasi-equilibrium state. These interplays are synthesized in this Section.

Notice that hereafter we will refer to simulations in which the plume influence is taken into account. We suggest that considering the plume dynamics is not a modeling choice. Indeed, the action of the offshore plume contributes to the evolution of the entire system and hence, must be included in the computations. Furthermore, it is worth mentioning that at equilibrium the inner part of the channel dries up during the low tide corresponding to the ebb phase. Thus, results beyond this coordinate (called hereafter 'inner shoreline' and indicated in the plots through a semitransparent dashed vertical line), must not be considered as part of the general dynamics of the analyzed system. Analogously to the previous Section, erosion in the offshore region will be ignored as a first approximation.

2.3.2.1 Hydrodynamics implications

The flow field evolves on a faster scale with respect to the sediment bed, thus adapting quite rapidly to the topographic configuration attained by the system. The influence of the morphologic evolution of the tidal channel on the hydrodynamics is depicted in Figure 2.8.

In order for the tidal channel to be morphydanamically stable, it has been postulated that the system must maximize entropy (Masselink et al., 2003). To this aim, the flow velocity field is modified until temporal variations of bottom elevation due to along channel gradients in erosion and deposition fluxes and in the bed load transport rate should tend to vanish. Actually, the importance of tidal distortion in the transport and accumulation and consequent long term erosion/deposition process of sediment in shallow well-mixed estuaries is well established (Friedrichs and Aubrey, 1988). This tidal distortion is usually expressed as an asymmetry of the tidal wave because the tidal wave crest migrates landward faster that the trough (Masselink et al., 2003). The shorter rising tide with respect to the falling tide, i.e., the shorter duration of the flood phase with respect to the ebb phase, causes the flood currents to be faster than the ebb currents, thus inducing a flood dominance and a net landward movement of bed material.

The tidal channels modeled in the present contribution have a strong tendency towards flood dominance and tend to import sediment (Figure 2.6). This occurs because the amount of bed material that can be moved is a power function of the tidal current speed (equations (2.72) and (2.78)), so that the direction of net sediment movement is determined more by an inequality in the peak speeds rather than by differences in the durations of the flood and ebb currents (Dalrymple et al., 2012). As previously mentioned, this net landward sediment transport tends to vanish when the bottom profile reaches its equilibrium configuration. Clearly, the presence of intertidal areas flanking the main channel, as well as the possible presence of overtides in the forcing tide can alter this scenario, favoring the transition to ebb dominance (Friedrichs and Aubrey, 1988; Speer et al., 1991; Lanzoni and Seminara, 1998). In this sense, Figure 2.8 (a) shows the the maximum (flood peak) and minimum (ebb peak) values of the flow velocity, their difference and the residual velocity during the initial cycle of the simulation (red lines) and during a cycle at equilibrium. It is interesting to note that at equilibrium the residual velocity along the tidal channel decreases and becomes negligible at channel portion located between the channel mouth and the inner shoreline limit.

A parameter that allows for a direct measure of such velocity asymmetry during a tidal cycle is given by:

$$\beta_V(\xi) = \log 10\left(\frac{u_{max}(\xi)}{|u_{min}(\xi)|}\right), \tag{2.114}$$

where β_V is the degree of asymmetry of maximum flood/ebb flow velocities, u_{max} is the peak flood velocity, and u_{min} is the peak ebb velocity. As expected, it is shown in Figure 2.8 (b) that the initial asymmetry between velocity peaks reveals the existence of higher flood velocities and a consequent net landward movement of sediment. However, this velocity differences become smaller during the transient process toward a quasi-equilibrium configuration. Eventually, the velocity asymmetry almost disappears at every point along the the estuary up to the inner shoreline location.

In addition to the velocity peaks asymmetry reduction, the long term morphodynamic evolution leads to a decrease of the tidal distortion in terms of flood/ebb phases duration (Dronkers, 1986). Since the volume of water flowing through the channel during the flooding tide matches the corresponding volume during the ebbing tide, the difference between flood and ebb velocity peaks must produces and asymmetry in the duration of flood and ebb phases duration during a tidal cycle. Thus, a second way to measure tidal distortion is through the index:

$$\beta_T(\xi) = \log 10\left(\frac{T_{ebb}(\xi)}{T_{flood}(\xi)}\right), \tag{2.115}$$

where β_T is the degree of asymmetry of ebb and flood phases duration, T_{ebb} is the ebb phase duration, and T_{flood} is the flood phase duration. Figure 2.8 (c) depicts the reduction of the asymmetry between ebb and flood phases duration, showing that the ebb phase reduces its duration whereas the flood phase increases its duration throughout tidal channel evolution. At equilibrium, the duration of the ebb and flood phases tend to be equal in every section of the tidal channel and the asymmetry in ebb/flood duration almost disappears.

Thus, we can state in terms of tidal asymmetry that the initially non-symmetric (flood-dominated) character of the tidal channel evolves toward a much more symmetrical configuration when the bottom profile increases its slope and reaches an quasi-equilibrium configuration.

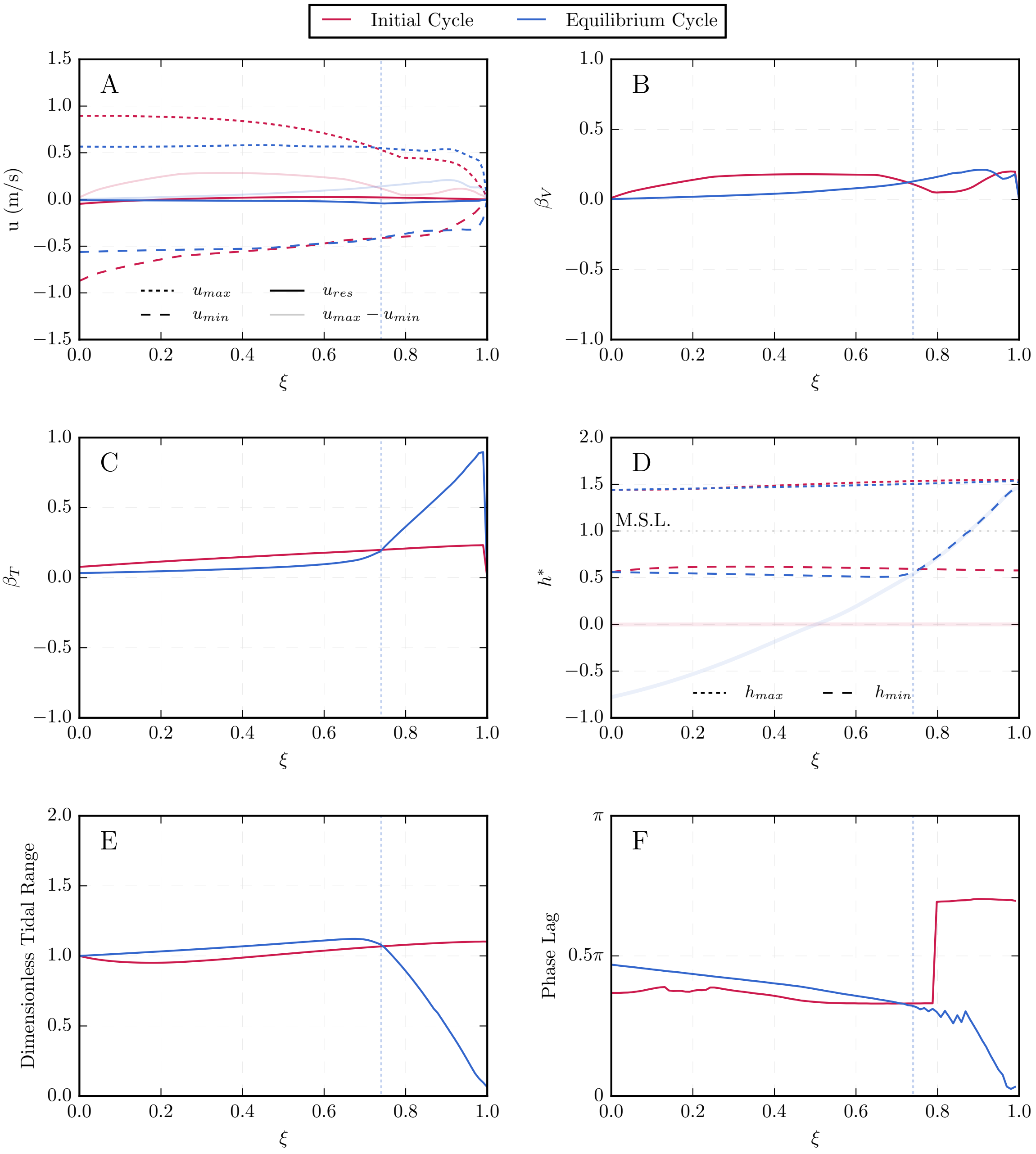

Figure 2.8: Values along the tidal channel of (a) maximum, minimum, difference between maximum and minimum and residual velocity, (b) degree of asymmetry of flood and ebb velocity peaks, (c) degree of asymmetry of the flood and ebb phases duration, (d) extreme values of the dimensionless free surface elevation, (e) dimensionless tidal range, and (e) phase lag between the maximum water surface elevation and the maximum flood speed. Red lines refer to the beginning of the simulation while blue lines refer to the equilibrium configuration. In panel (d) the horizontal dashed line marks mean sea level (M.S.L.) elevations at the channel mouth, while the semitransparent lines depict the normalized bed profiles η^*. Vertical dashed lines indicate the position of the inner shoreline once the equilibrium is reached. Initial conditions: $L_e = 30$ km, $L_b = 25$ km, $b_0 = 160$ m, $d(t = 0) = 5$ m, $a_0 = 2.2$ m, $d_s = 100\,\mu$m, and horizontal continental shelf with $C_z = 55$ m$^{1/2}$/s

In the channel configuration simulated here, both the velocity peaks and the phase duration tend to become equal with time, and hence $\beta_V \simeq 0$ and $\beta_T \simeq 0$ (up to the inner shoreline position). However, notice that a certain degree of flood dominance remains at equilibrium (Figure 2.8 (b) and (c)).

A second aspect related to the tidal wave hydrodynamics to be analyzed is the behaviour of the tidal range during the wave propagation. Figure 2.8 (d) shows the maximum and minimum values of the free surface elevation normalized by the initial depth ($h^* = h/d(t=0)$) along the tidal channel, with the initial and final bottom profiles and the value of the mean sea level (M.S.L.) superimposed for clarity. It appears that that no significant modifications affect the tidal range as the channel bottom evolves, mainly with respect the the high tide levels. However, a decrease in the low tide level is observed at equilibrium.

In Figure 2.8 (e) the normalised tidal range of Figure 2.8 (d) is scaled with the value of the tidal range at the channel mouth. The normalised tidal range is defined as:

$$\text{Dimensionless Tidal Range}(\xi) = \frac{h_{max}(\xi) - h_{min}(\xi)}{2a_0}. \tag{2.116}$$

At equilibrium, it clearly appears that in the portion of the estuary which never dries up, the tidal range tends to slightly increase landward. On the contrary, in the inner reaches of the estuary, where the bottom dries during the low tide at equilibrium, the tidal range tends to decrease appreciably. Because of the channel convergence, the energy of the incoming tidal wave is concentrated into an progressively decreasing cross-sectional area as it propagates up the tidal channel. This tendency is not initially offset fully by friction, so in order to conserve the energy flux, the tidal range tends to slightly increase landward, amplifying the tidal wave. Such a hydrodynamic pattern in which convergence effects exceed frictional effects and the tidal range increases with distance from the channel mouth is termed hypersynchronous (Dyer, 1973). On the contrary, in the inner reaches of the estuary, where the bottom dries during the low tide, the tidal range at equilibrium decrease due to the abrupt reduction in water depth as a consequence of the emerging bottom. However, modifications on the tidal range do not seem to be significant as a consequence of the evolution of the tidal channel towards an equilibrium configuration. It is important to remark that this is not a specific requirement for equilibrium, since the geometric (mainly convergence length) and dynamics conditions (bottom friction and tidal amplitude) imposed to the tidal channel can determine amplification or damping of the tidal wave (Lanzoni and Seminara, 1998; Savenije and Veling, 2005; Toffolon et al., 2006). Thus, it is shown that no clear relation exists between the changes in tidal range and the evolution towards equilibrium.

Figure 2.8 (f) depicts the phase lag between the maximum water surface elevation and the maximum flood speed along the channel. No significant changes are observed for the initial cycle and quasi-equilibrium cycle. In both cases the phase lag is slightly smaller than the value $\pi/2$, typical value of strongly dissipative and strongly convergent estuaries (Lanzoni and Seminara, 1998). For the initial cycle an almost constant value is attained up to the region close to inner end of the channel. In this region the tidal wave propagation and the wave reflection with the inner boundary distorts the sinusoidal behaviour of the the flow velocity and two distinct flood peaks that increase the phase lag between water level and flood peaks arise. On the other hand, for the quasi-equilibrium configuration, the phase lag decreases almost linearly in the portion of the estuary that always remains submerged, whereas it decreases drastically in the region that dries up during the ebb phase.

The tendency towards a quasi-equilibrium configuration whereby a symmetric tidal wave tends to form that reduces the tidal distortion and the related morphodynamics changes in the channel can be clearly observed by plotting the flow velocity and the free surface elevation during one tidal cycle at different locations of the tidal channel ($\xi = 0$, $\xi = 0.2$, $\xi = 0.4$, $\xi = 0.5$, $\xi = 0.6$, and

$\xi = 0.8$) (Figure 2.9). Note that in the locations located beyond the inner shoreline the channel dries up once the system reaches the quasi-equilibrium and, hence, collected measurements of velocity will depict an erratic behaviour.

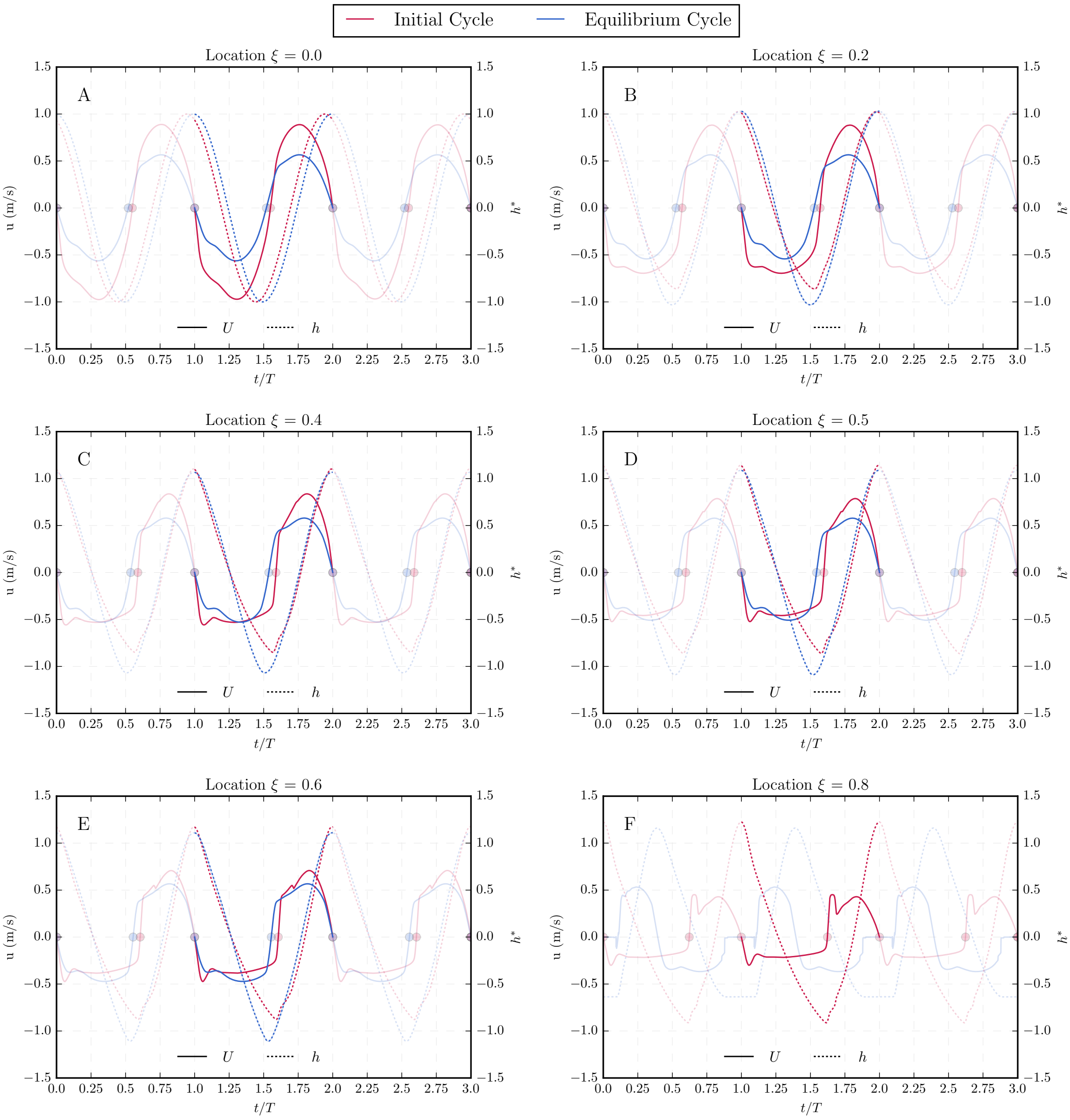

Figure 2.9: Velocity (u) and dimensionless free surface elevation (h^*) during three tidal cycles at different locations along the tidal channel: (a) $\xi = 0$, (b) $\xi = 0.2$, (c) $\xi = 0.4$, (d) $\xi = 0.5$, (e) $\xi = 0.6$, and (f) $\xi = 0.8$, at the beginning of the simulation (red lines) and at equilibrium (blue lines). The intermediate tidal cycle is highlighted for clarity. Due to drying process at $\xi = 0.8$, variables at equilibrium are not plotted in this location. Initial conditions: $L_e = 30$ km, $L_b = 25$ km, $b_0 = 160$ m, $d(t=0) = 5$ m, $a_0 = 2.2$ m, $d_s = 100$ μm, and horizontal continental shelf with $C_z = 55$ m$^{1/2}$/s

At the beginning of the simulation the strong asymmetry between the ebb and flood velocity peaks and between the ebb and flood phases duration is displayed. The differences in velocity peaks and tidal phases duration between the flood and ebb phases increases in the landward direction, being more pronounced when ξ increases. On the other hand, at the channel mouth (Figure 2.9 (a)), no perceptible difference exists in the velocity peaks magnitude since it is the sections at which the boundary condition given by equation (2.4) is imposed. Besides, the sinusoidal behaviour of the tidal wave velocity becomes deformed due to channel convergence, frictional effects and the proximity of the reflecting landward boundary during its propagation through the tidal channel. Besides, the non linear terms in continuity and momentum equations (equations (2.2) and (2.3) respectively) produce the distortion of the tidal wave that can be represented by the growth of higher harmonics (Prandle, 1991). This is observed with the formation of two maximum values both during the ebb and during the flood phases. This distortion is responsible for the sharp phase lag increase observed in Figure 2.8 (f) at the farthest landward sections. On the contrary, at equilibrium, the phases duration and the velocity peaks tend to be symmetrical along the channel and the velocity deformation mitigates considerably if compared with those at the beginning of the simulation. Moreover, the peak values of velocity keep almost constant at the different sections of the tidal channel, as it is observed in many real tidal estuaries (Friedrichs, 1995; Todeschini et al., 2008).

The changes experienced by the free surface elevation are not as significant as the ones in the flow velocity (Figure 2.9). The channel evolution is not able to considerably alter the tidal range along the channel. Tidal range variations are mainly dictated by channel convergence and bottom friction, which are fixed in our simulations (Savenije and Veling, 2005; Toffolon et al., 2006). Nevertheless, three aspects arises from the evolution of the free surface elevation along the tidal channel and along its evolution. The first one is related to the shape of the free surface elevation. It alters its sinusoidal profile of the seaward sections, becoming sharper and reaching a characteristic “sawtooth” profile in the landward direction. The second one is the reduction of the duration asymmetry between the rising and the falling tides. At equilibrium, both the rising and the falling tides tend to match their duration, while at the beginning of the simulation the falling tide (linked to the ebb phase) is longer the the rising tide (linked to the flood phase). Finally, the third aspect that arises from Figure 2.9 is that whereas the high tide level remains almost fixed, the low tide level decreases noticeably at equilibrium. This low tide level fall allows for the increase in the tidal range at equilibrium observed in Figure 2.8 (e). Obviously, at the channel mouth (Figure 2.9 (a)), free surface elevations are identical since it is the sections at which the free surface elevation is imposed (2.4). Beyond the inner shoreline (Figure 2.9 (f)), the drying process makes the low tide level equals the bed elevations.

2.3.2.2 Morphodynamics Implications

Figure 2.10 collects the main morphodynamics implications derived from the evolution of the tidal channel towards an equilibrium configuration. It compares the residual (tidally averaged) values of suspended load and bed load transport and the related bottom changes both at the beginning of the simulations, i.e., when the bottom is still horizontal, and at the moment at which the channel reaches a quasi-the equilibrium configuration, along the tidal channel length.

Specifically, Figure 2.10 (a) depicts the exiting residual difference between the erosion and deposition fluxes of suspended material, $< D_e - E_r >$, where angle brackets indicate average over a tidal cycle. If a net flux of sediment from the bed to the flow occurs, or vice versa, then a resulting change in the bathymetry occurs. At the initial stage of evolution two regions are clearly identified. A first one, close to the channel mouth ($\xi < 0.3$), in which erosive processes prevail, and a second that extends up to the landward end of the channel in which the eroded material of the first region is deposited through the migrating sediment front. At equilibrium, this difference tends to vanish everywhere in the tidal channel. On the other hand, Figure 2.10 (b) shows the residual sediment bed load fluxes existing at every section of the tidal channel

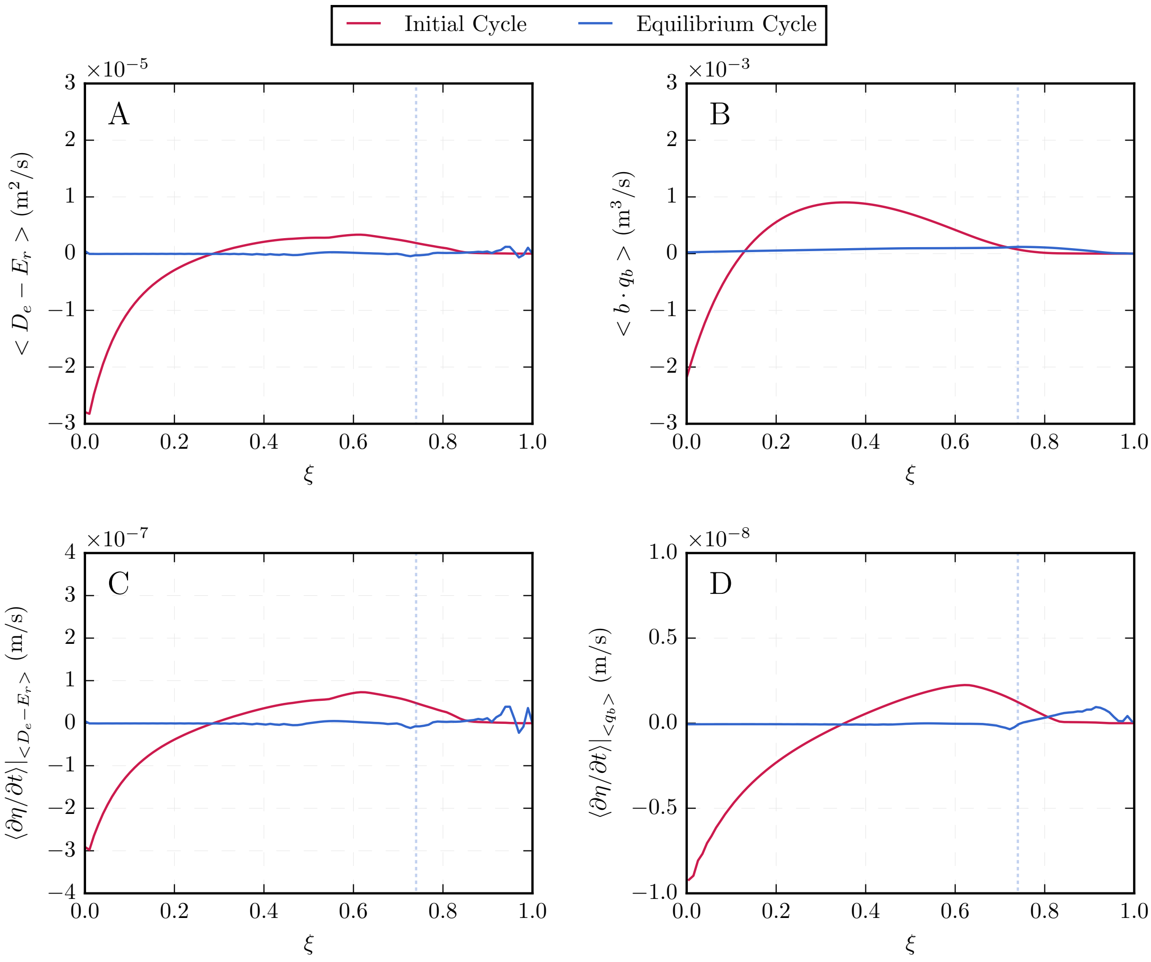

Figure 2.10: (a) Residual difference between deposition and erosive sediment fluxes, (b) residual bed load sediment flux, (c) residual contribution of the deposition and erosive sediment fluxes to the bathymetric changes of the tidal channel, and (d) residual contribution of the bed load sediment flux to the bathymetric changes of the tidal channel. Red lines refer to the beginning of the simulation while blue lines refer to the equilibrium configuration. Vertical dashed lines indicate the position of the inner shoreline once the equilibrium is reached. Initial conditions: $L_e = 30$ km, $L_b = 25$ km, $b_0 = 160$ m, $d(t=0) = 5$ m, $a_0 = 2.2$ m, $d_s = 100$ μm, and horizontal continental shelf with $C_z = 55$ m$^{1/2}$/s

both at the beginning of the simulation and at equilibrium. Positive values indicate that the flux is directed landward, while negative values points seaward transport.

The influence of the channel evolution on the sediment fluxes implies a strong feedback effect on the gradients of bathymetric variations since, according to equation (2.68), the sediment transport determines the evolution of the bottom profile. With respect to the suspended load of sediment, bottom changes are given by:

$$\left\langle\frac{\partial \eta}{\partial t}\right\rangle\bigg|_{\langle D_e - E_r\rangle} = \frac{1}{T}\int_T \frac{1}{1-p}\frac{D_e - E_r}{b}\,dt, \tag{2.117}$$

where T is the tidal cycle period, b is the channel width, and p is bottom porosity. Thus, as a lineal consequence of these vertical fluxes of sediment, bottom evolves with an identical trend than the one followed by the residual gradient between D_e and E_r: at the beginning of the simulation bottom level tends to decrease close to the channel mouth ($\xi < 0.3$), whereas bottom level tends to increase beyond this point (Figure 2.10 (c), red line). At equilibrium, residual bed level changes throughout a tidal cycle due to the suspended load of sediment become negligible (Figure 2.10 (c), blue line). With respect to the bed load flux, its spatial gradient is even more important than the magnitude for determining bottom changes (see equation (2.68)). Bottom changes related to bed load fluxes are then given by:

$$\langle\frac{\partial \eta}{\partial t}\rangle\bigg|_{\langle q_b\rangle} = \frac{1}{T}\int_T \frac{1}{1-p}\frac{1}{b}\frac{\partial}{\partial x}(b\cdot q_b)dt. \qquad (2.118)$$

If the spatial gradient of bed load sediment flux is negative, there must be net sediment deposition on the bed, while if the gradient is positive, erosion takes place. Thus, Figure 2.10 (d) shows an erosive seaward region in which the longitudinal gradient of this flux is positive and extends up to the point where it falls to zero (approximately at $\xi = 0.35$). Beyond this point, this gradient is negative, net sediment deposition on the bed occurs and the bottom tends to rise. At equilibrium, these gradients tend to vanish and no net bottom changes occur.

More importantly, the bottom changes related to suspension transport is one order of magnitude higher than those due to bed load transport. Thus, the evolution of the entire system is mainly dominated by suspended load, and it is therefore important to model the residual fluxes of suspended sediment through the advection-diffusion equation (equation (2.75)) for predicting the channel shaping in this kind of dynamics ambients.

After studying the general aspects of the morphodynamic mechanisms that enable the attainment of a equilibrium profile in the tidal channel, it is of interest to describe in a more detailed way how the sediment load evolves according to the behaviour experienced by the mechanism for transport: bed load and suspended load. This section will end with the analysis of the evolution of sediment concentration within the channel and the assessment of the mechanisms responsible for this evolution.

2.3.2.2.1 Suspended transport. The tendency toward an equilibrium configuration was proved to be mainly dictated by the the vertical exchange of suspended sediment between the bed and the flow (Figure 2.10 (b)). The erosion and deposition fluxes during a tidal cycle at different locations along the tidal channel clearly display significant differences at the beginning of the simulation and at equilibrium (Figure 2.11).

This figure clearly evidences the existing time-lag between erosive and deposition fluxes. It is worthwhile to stress the fact that considering scour and settling lags to compute sediment fluxes is one of the main advantages of the present model. This consideration is particularly significant close to the slack water periods when equilibrium between entrainment into suspension and deposition cannot occur, as sediments simple settle in a quasi-quiescent water body (Lanzoni and Seminara, 2002). This behaviour is clearer displayed in the inset-zoom close to slack tide in a section located at $\xi = 0.2$ of Figure 2.12. It shows that sediment particles can be kept moving at velocities below the threshold of initial motion, and consequent deposition occurs. Dashed regions represents the period of time during which settling lag occurs. Despite this lag period is larger at equilibrium, its influence on the channel evolution is more pronounced at equilibrium of the simulations since deposition rates are higher. As the particles settle they are moving along on the waning current so that they eventually reach the bed some distance from the point at which settling commenced. This effect is the previously termed as settling lag (Dyer, 1995).

Hence, this finite time needed for sediment particles being suspended in the water to settle at slack water is shown to be an important mechanisms that induce net sediment transport.

A second aspect to be underlined from Figure 2.11 is the existing peak of deposition flux at the tidal channel mouth at the beginning of the flood phase. This peak is related to the incoming sediment from the offshore plume. Even though the existence of the plume eventually affects half part of the estuary close to the adjacent sea (Figure 2.6 (c)), this deposition peak is only displayed at the farthest seaward section.

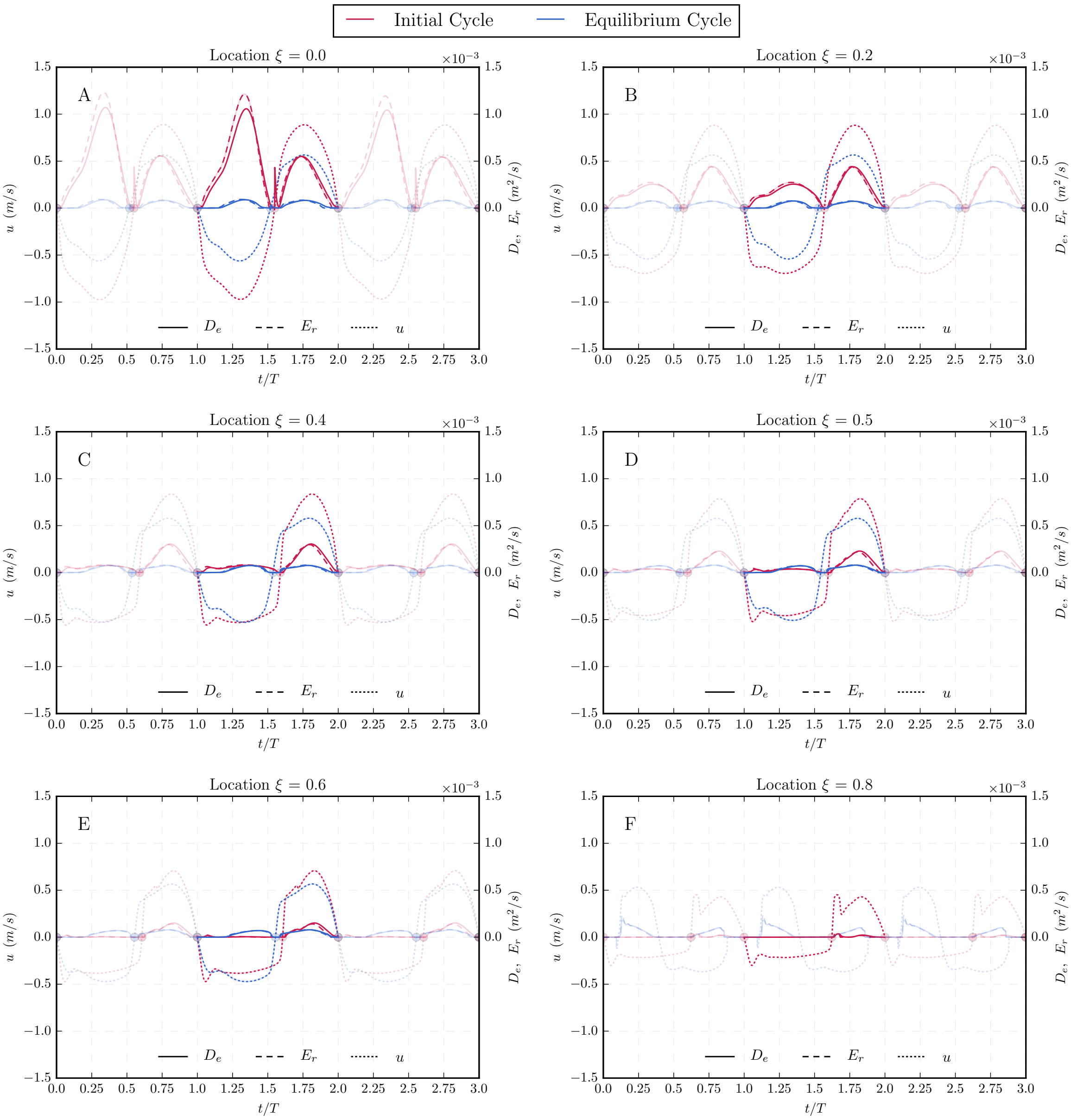

Figure 2.11: Velocity, u, and depositional, D_e, and erosive, E_r, fluxes of suspended sediment during three tidal cycles at different locations along the tidal channel: (a) $\xi = 0$, (b) $\xi = 0.2$, (c) $\xi = 0.4$, (d) $\xi = 0.5$, (e) $\xi = 0.6$, and (f) $\xi = 0.8$, at the beginning of the simulation (red lines) and at equilibrium (blue lines). The intermediate tidal cycle is highlighted for clarity. Due to drying process at $\xi = 0.8$, variables at equilibrium are not plotted in this location. Initial conditions: $L_e = 30$ km, $L_b = 25$ km, $b_0 = 160$ m, $d(t = 0) = 5$ m, $a_0 = 2.2$ m, $d_s = 100$ μm, and horizontal continental shelf with $C_z = 55$ m$^{1/2}$/s.

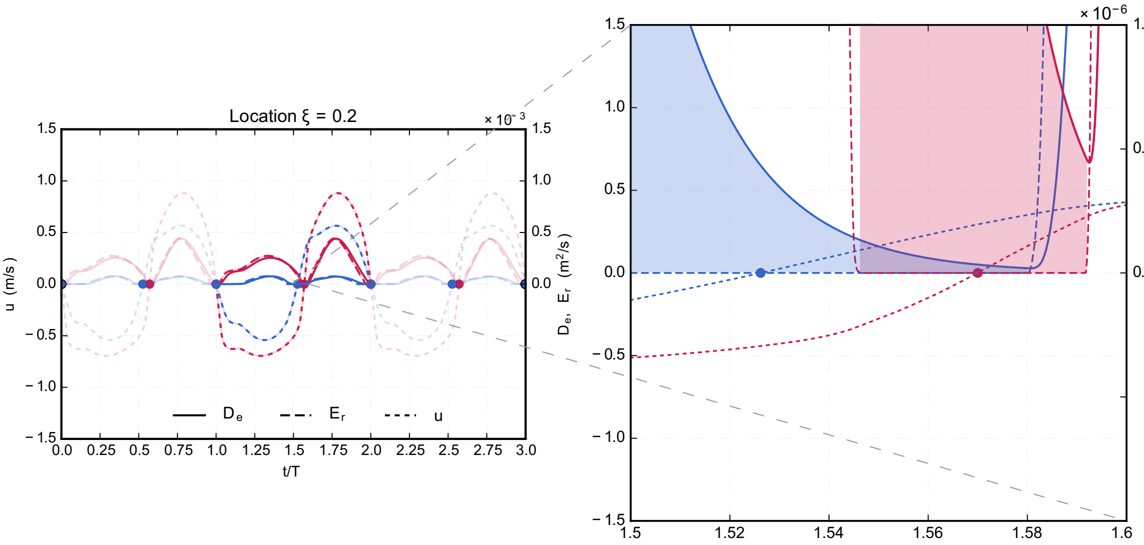

Figure 2.12: Velocity, u, and depositional, D_e, and erosive, E_r, fluxes of suspended sediment during three tidal cycles at $\xi = 0.2$, at the beginning of the simulation (red lines) and at equilibrium (blue lines). The intermediate tidal cycle is highlighted for clarity. The inset window shows a detailed zoom of the deposition and erosive fluxes and settling lag effects close to slack tide. Dashed regions represents the period of time during which settling lag occurs. An Initial conditions: $L_e = 30$ km, $L_b = 25$ km, $b_0 = 160$ m, $d(t=0) = 5$ m, $a_0 = 2.2$ m, $d_s = 100$ μm, and horizontal continental shelf with $C_z = 55$ m$^{1/2}$/s.

Finally, Figure 2.11 depicts strong differences between deposition and erosive fluxes at the beginning of the simulation which dictates instantaneous bathymetric changes within the tidal channel according to:

$$\left.\frac{\partial \eta}{\partial t}\right|_{D_e - E_r} = \frac{1}{1-p}\frac{D_e - E_r}{b}. \tag{2.119}$$

Positive values of equation (2.119) lead to sediment deposition (bed level increases) and negative values lead to erosion (bed level goes down). These differences are collected in Figure (2.13). At the beginning of the simulation the strong differences between deposition and erosive fluxes determines the high rate of bathymetric changes shown in (Figure 2.10 (c)). The sign of this difference varies along the tidal channel length. Although the behaviour of $D_e - E_r$ seems to depicts a high degree of asymmetry between the flood and ebb phases during a tidal cycle, the general trend is that net erosion prevails in the seaward part whereas net deposition prevails in the inner part of the tidal channel. An important feature that arises from Figure (2.13) is the evidence that deposition exists despite the flow is incapable of entrains sediment into suspension. This circumstance, related to the settling lag of the suspended particles, is mainly observed at the final stages of both ebb and flood phases close to slack waters. On the contrary, at equilibrium, differences between deposition and erosion fluxes reduces considerably all along the tidal channel. Besides, the remaining differences tend to be symmetrical during a tidal cycle, which makes the net bottom changes almost disappear.

Finally, a peak in the rate $D_e - E_r$ at the channel mouth is shown in Figure (2.11) (a). This peak is related to the incoming sediment from the offshore plume and is not counterbalanced by erosion due to the low velocities of the flow at the beginning of the flood phase. It causes short and high deposition rates close to the tidal channel mouth.

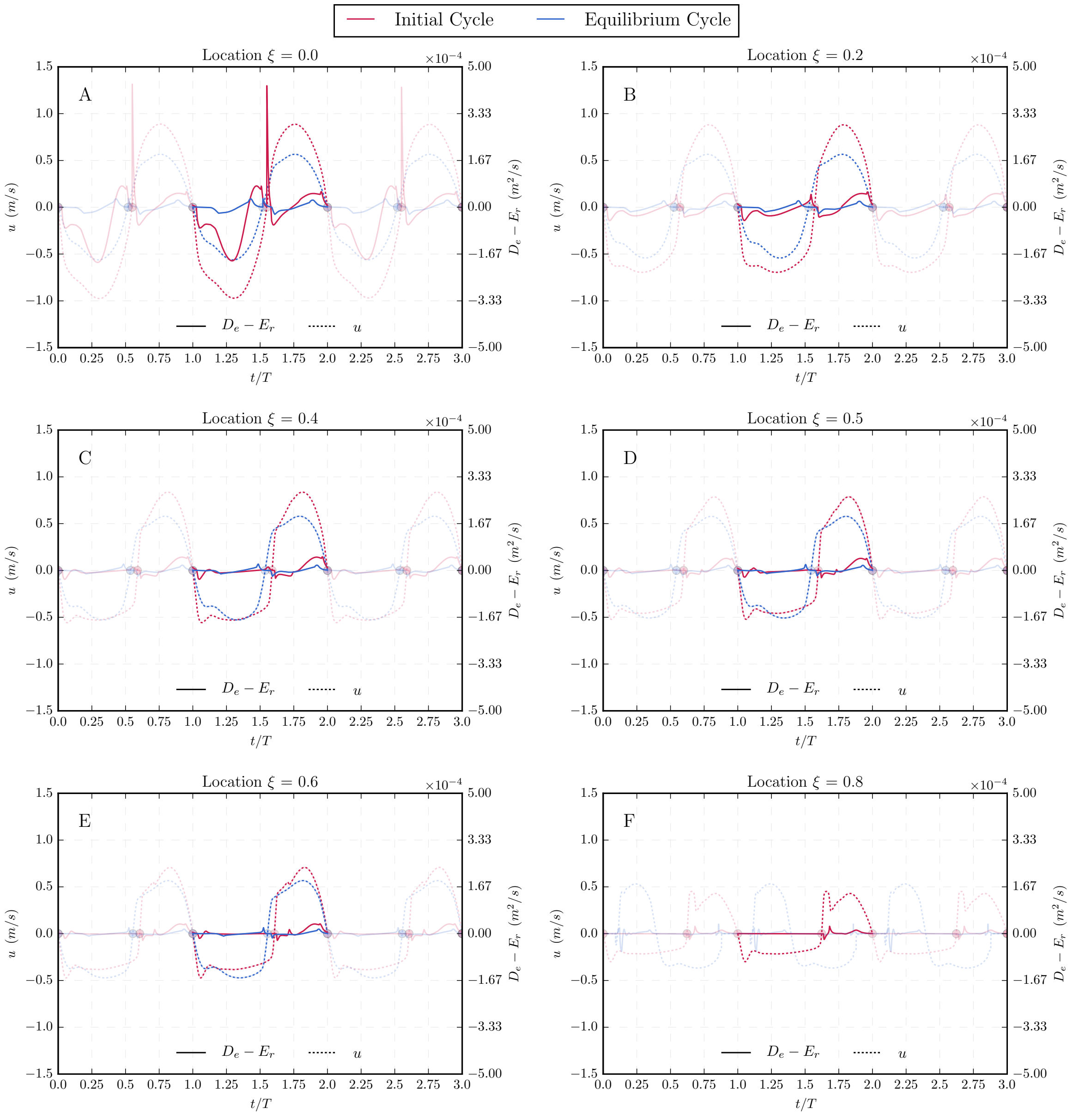

Figure 2.13: Velocity, u, and difference between depositional and erosive fluxes of suspended sediment, $D_e - E_r$, during three tidal cycles at different locations along the tidal channel: (a) $\xi = 0$, (b) $\xi = 0.2$, (c) $\xi = 0.4$, (d) $\xi = 0.5$, (e) $\xi = 0.6$, and (f) $\xi = 0.8$, at the beginning of the simulation (red lines) and at equilibrium (blue lines). The intermediate tidal cycle is highlighted for clarity. Due to drying process at $\xi = 0.8$, variables at equilibrium are not plotted in this location. Initial conditions: L_e = 30 km, L_b = 25 km, b_0 = 160 m, $d(t=0)$ = 5 m, a_0 = 2.2 m, d_s = 100 μm, and horizontal continental shelf with $C_z = 55$ m$^{1/2}$/s.

Tidal channel eventually reaches a state of dynamic equilibrium due to, mainly, an asymptotic trend followed by the deposition and erosion residual fluxes through which they reduce both their intensity and their differences. Figure 2.14 shows the temporal evolution of the residual fluxes of erosion and deposition of suspended material integrated all along the tidal channel and integrated at different stretches of the tidal channel. It allows for a division into zones with the aim of illustrating how the different regions of the tidal channel evolve. No significant differences arise between the trend followed by $\langle D_e \rangle$ (Figure 2.14 (a)) and by $\langle E_r \rangle$ (Figure 2.14 (b)).

The global value along the whole tidal channel depicts a negative exponential curve (black lines). However, vertical fluxes of suspended sediment behaves differently depending on the region of the tidal channel. A similar trend than the global value is found in the first and second quarter of the tidal channel, i.e., those closer to the tidal channel mouth. However, the third and fourth stretches, i.e., those closer to the inner boundary, are characterized by an initial growth followed by an exponential drop. This initial growth is linked to the time that the sediment front takes to reach each stretch. A final conclusion we can extract from Figure 2.14 is that the more intense vertical fluxes of sediment take place at the third quarter of the tidal channel. The lower intensities are found in the landward quarter, likely related to the wetting and drying processes that occur at this stretch and that reduce the period during which these residual sediment fluxes can take place.

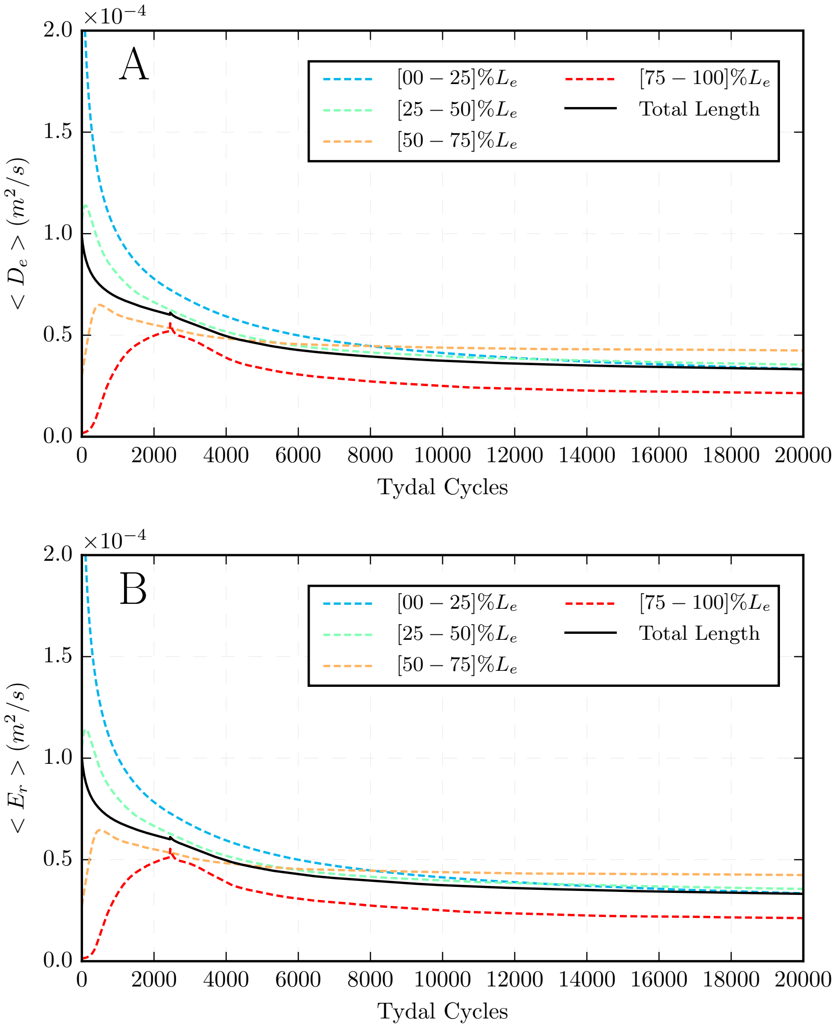

Figure 2.14: Temporal evolution of the residual (a) depositional, $\langle D_e \rangle$, and (b) erosive, $\langle E_r \rangle$, fluxes of suspended sediment integrated all along the tidal channel (black line) and integrated along different tidal channel stretches (dashed lines) [first or seaward quarter (blue line), second quarter (green line), third quarter (orange line), and fourth or landward quarter (red line)]. Initial conditions: $L_e = 30$ km, $L_b = 25$ km, $b_0 = 160$ m, $d(t=0) = 5$ m, $a_0 = 2.2$ m, $d_s = 100$ μm, and horizontal continental shelf with $C_z = 55$ m$^{1/2}$/s.

Nevertheless, more important than the intensity of the residual fluxes $\langle D_e \rangle$ and $\langle E_r \rangle$ is

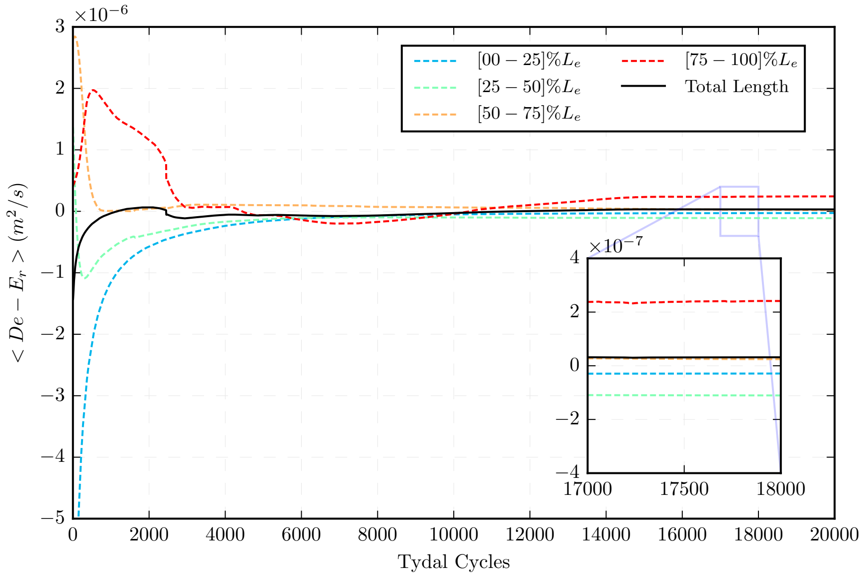

Figure 2.15: Temporal evolution of the difference between depositional and erosive fluxes of suspended sediment, $\langle D_e - E_r\rangle$, integrated all along the tidal channel (black line) and integrated along different tidal channel stretches (dashed lines) [first or seaward quarter (blue line), second quarter (green line), third quarter (orange line), and fourth or landward quarter (red line)]. The inset-zoom depicts the asymptotic trend reached by the different curves. Initial conditions: $L_e = 30$ km, $L_b = 25$ km, $b_0 = 160$ m, $d(t=0) = 5$ m, $a_0 = 2.2$ m, $d_s = 100$ μm, and horizontal continental shelf with $C_z = 55$ m$^{1/2}$/s.

their difference. It ultimately dictates the bathymetric evolution of the tidal channel (equation (2.119)). In this sense, Figure 2.15 shows the temporal evolution of the difference between $\langle D_e\rangle$ and $\langle E_r\rangle$ integrated all along the tidal channel and integrated at different stretches of the tidal channel. It shows an highly dynamic evolution of the tidal channel during the first 6000 tidal cycles. During this period net erosion prevails in the first and second quarter of the tidal channel, whereas at the the third and fourth stretches closer to the inner boundary net deposition predominates. Thus, this lapse in the tidal channel evolution determines the bathymetric profile that the tidal channel will reach at equilibrium.

The residual vertical flux of sediment of the whole system reduces as the bottom evolves (back line in Figure 2.15). Starting from an initial net erosion of the whole system, the rate at which $\langle D_e - E_r\rangle$ decreases is relatively high in the initial stages of the morphological evolution, but it tends to vanish asymptotically as the equilibrium is reached.

Regarding the behaviour of the different regions of the tidal channel, Figure 2.15 reveals net erosion in the stretches located closer to the tidal channel mouth, whereas those placed in the inner reach of the tidal channel experience residual deposition. However, over the tidal channel evolution, all the stretches tend to asymptotically reduce these residual fluxes of vertical sediment up to attain a constant value as the equilibrium is achieved (see inset-zoom in Figure 2.15. It is interesting to note that in the landward quarter this asymptotic value is higher than in the remain parts of the tidal channel. We suggest that, once again, drying and wetting process are the responsible for this behaviour.

2.3.2.2.2 Bed load transport. Although the influence of the bed load flux in shaping the tidal channel bottom profile was found to be one order of magnitude lower than the one of the suspended load, the analysis of its behaviour results interesting from an illustrative point of view.

From equation (2.68), it is readily seen that bottom changes if a spatial gradient in these fluxes exists. The corresponding rate of bathymatric variation is then given by:

$$\left.\frac{\partial \eta}{\partial t}\right|_{q_b} = \frac{1}{1-p}\frac{1}{b}\frac{\partial}{\partial x}(b \cdot q_b). \tag{2.120}$$

Figure 2.16 shows the instantaneous velocity and dimensionaless bed load fluxes during a tidal cycle at different locations along the tidal channel both at the beginning of the simulation and once equilibrium is reached. It is interesting to note that at equilibrium (blue lines) the differences among the various sections of the domain not only in the peak values but also in the shape of velocity and bed load sediment flux are attenuated if compared with those at the beginning of the simulation (red lines). At the beginning of the simulation the strong asymmetry of velocity causes a large difference in the sediment transport during flood and ebb phases, which is more pronounced inside the channel, i.e., for $\xi \geq 0.4$, where a landward directed sediment flux prevails. Regarding the sections located seaward ($\xi \leq 0.2$), this asymmetry is lower but the seaward transport during the ebb phase prevails. On the contrary, at equilibrium, velocity and sediment transport tend to be symmetrical along the entire length of the tidal channel. Figure 2.16 also suggest that the differences among the various sections along the channel are reduced not only in terms of the peak values but also in terms of the time of velocity and sediment flux.

In addition, it should be noted that this bed load flux is assumed to adapt instantaneously to local flow conditions. According to that, no bed load transport occurs as the flow velocity does not exceed the critical velocity for beginning of sediment motion. This is a particularly severe assumption that was overcome in the present work through an advection-diffusion equation that allows for a detailed evaluation of the temporal evolution of the concentration profile close to slack water periods.

To conclude the bed load transport, Figure 2.17 shows the temporal evolution of the residual bed load flux integrated all along the tidal channel and integrated at different stretches of the tidal channel. The global value along the entire tidal channel depicts a negative exponential curve that asymptotically reaches a constant value (black line). However, bed load fluxes behaves differently depending on the region of the tidal channel, although all of them reach an asymptotic behaviour. The first quarter, i.e., the one located closest to the sea, change the direction of the residual bed load flux. At the beginning of the simulation it is directed seaward, but it turns out to be landward directed after 1000 tidal cycles. The second quarter depicts an exponential decrease of the residual bed load from the beginning, being always directed landward. On the contrary, the third and fourth stretches, i.e., those closer to the inner boundary, are characterized by an initial growth followed by an exponential drop, being also always directed landward.

It is interesting to note that the temporal evolution of the residual bed load flux shown in Figure 2.17 decreases but does not disappear. It attains an asymptotic value that along with the asymptotic value reached by the deviation between residual erosion and deposition fluxes (Figure 2.15) make the bathymetric changes vanish everywhere in the tidal channel. Thus, although a residual sediment transport persists, it is so low that leads to a dynamically stable situation.

2.3.2.2.3 Evolution of the sediment concentration within the tidal channel. To conclude with the analysis of the sediment transport mechanisms we tackle the problem of the suspended sediment concentration dynamics over the tidal channel evolution.

Firstly, we try to elucidate how the net concentration field of suspended sediment evolves both in space and time. Figure 2.18 shows a first period that covers the first 5000 tidal cycles

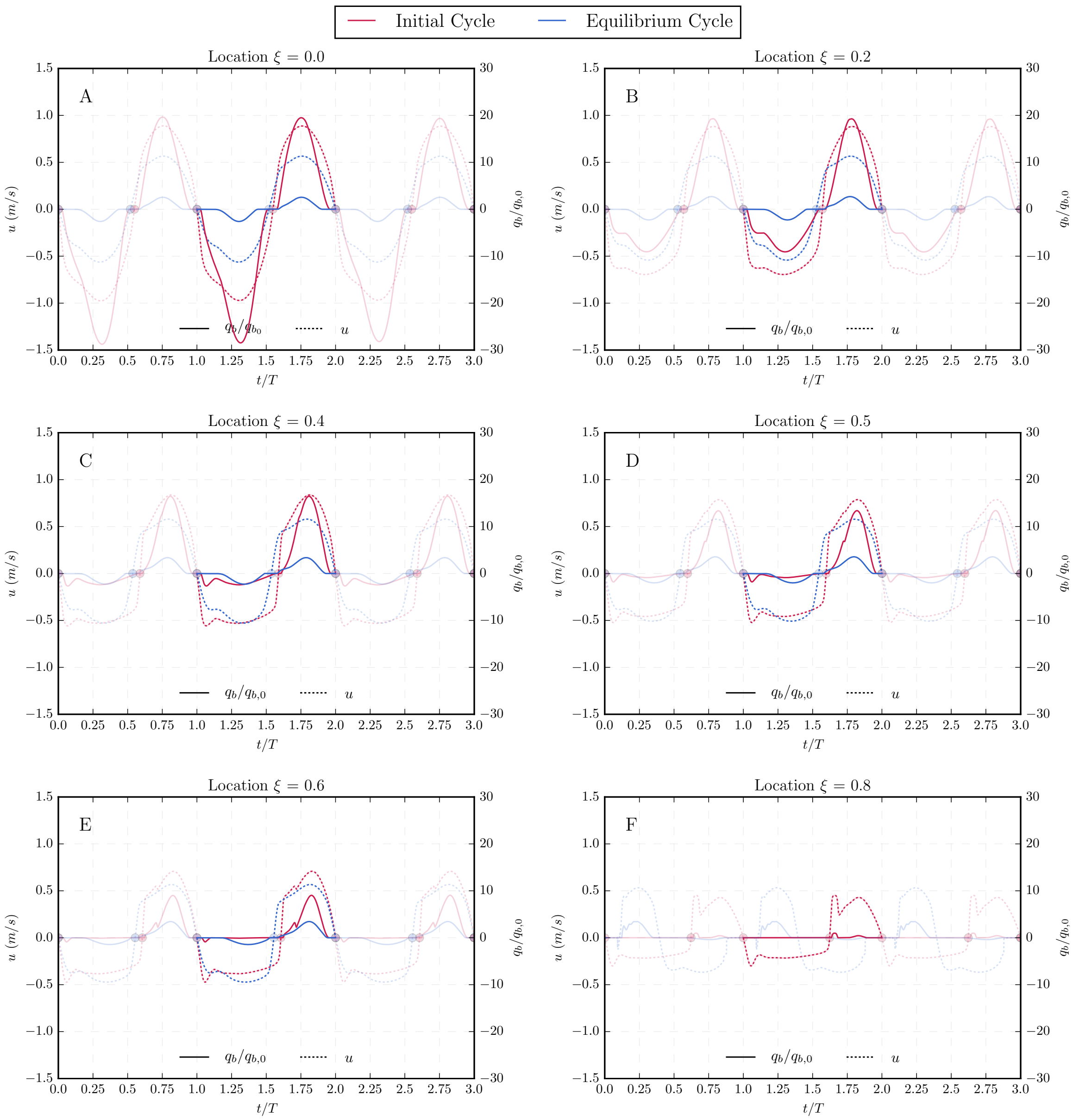

Figure 2.16: Velocity, u, and dimensionless bed load sediment flux, $q_b/q_{b,0}$, during three tidal cycles at different locations along the tidal channel: (a) $\xi = 0$, (b) $\xi = 0.2$, (c) $\xi = 0.4$, (d) $\xi = 0.5$, (e) $\xi = 0.6$, and (f) $\xi = 0.8$, at the beginning of the simulation (red lines) and at equilibrium (blue lines). The intermediate tidal cycle is highlighted for clarity. Due to drying process at $\xi = 0.8$, variables at equilibrium are not plotted in this location. Initial conditions: $L_e = 30$ km, $L_b = 25$ km, $b_0 = 160$ m, $d(t = 0) = 5$ m, $a_0 = 2.2$ m, $d_s = 100\ \mu$m, and horizontal continental shelf with $C_z = 55\ \text{m}^{1/2}$/s.

of the channel evolution in which the sediment concentration field highly varies. The inset-zoom allows for a better inspection of these variations, showing two turbidity maximum zones in which the a suspended sediment concentration (i.e., water turbidity) is on average higher than the waters further seaward of landward. A first turbidity maximum zone appears in the seaward part of the tidal channel just at the beginning of the simulations. It is related to the intense erosive processes that take place in this region. A second turbidity maximum zone arises close to the landward boundary approximately at 2500 tidal cycles, just the moment when the sediment front is being reflected.

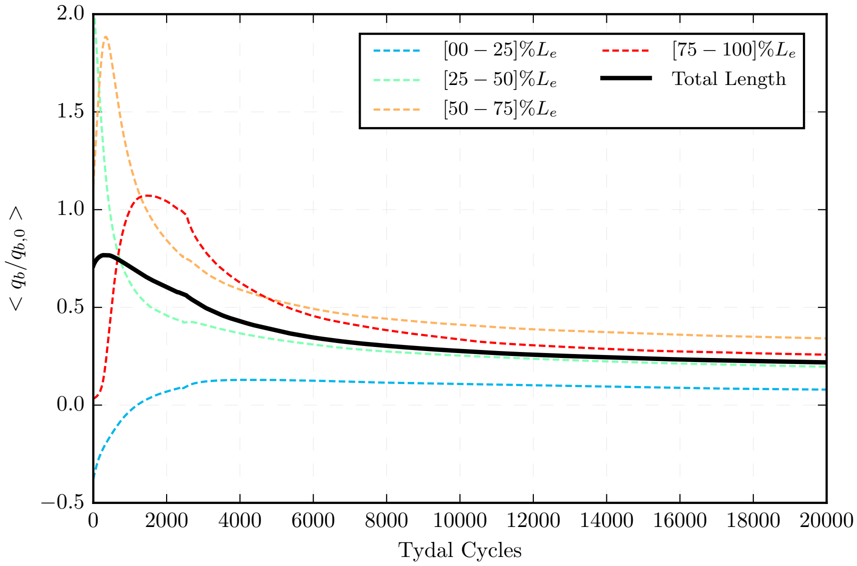

Figure 2.17: Temporal evolution of the dimensionless residual bed load sediment flux , $\langle q_b/q_{b,0}\rangle$, integrated all along the tidal channel (black line) and integrated along different tidal channel stretches (dashed lines) [first or seaward quarter (blue line), second quarter (green line), third quarter (orange line), and fourth or landward quarter (red line)]. Initial conditions: $L_e = 30$ km, $L_b = 25$ km, $b_0 = 160$ m, $d(t=0) = 5$ m, $a_0 = 2.2$ m, $d_s = 100$ μm, and horizontal continental shelf with $C_z = 55$ m$^{1/2}$/s.

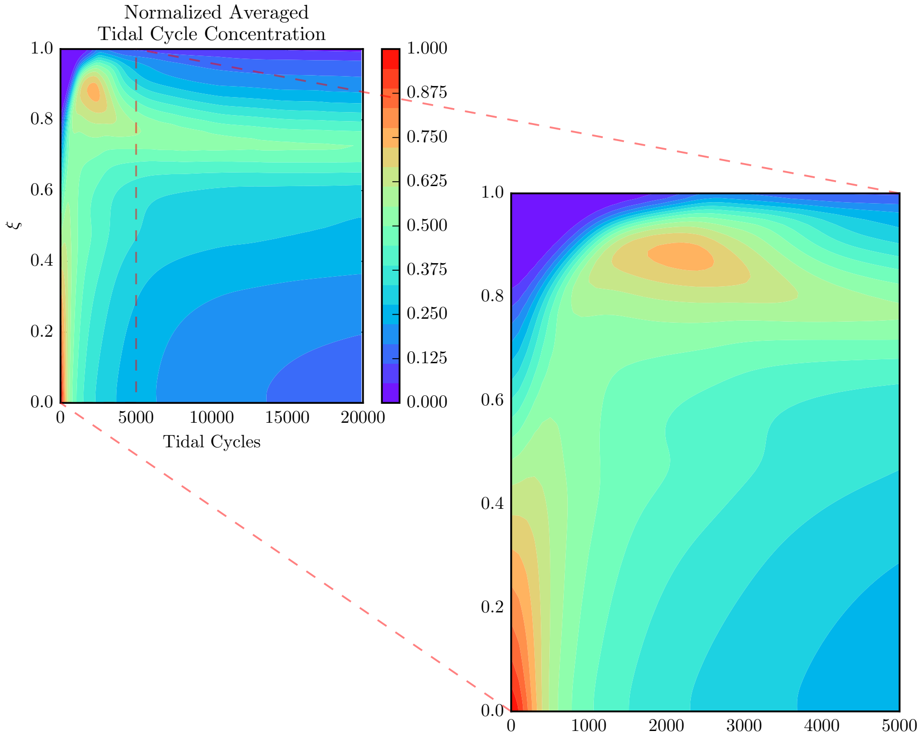

Figure 2.18: Variation of the net suspended sediment concentration field in space and time. The concentration have been normalized with its maximum value. The inset window is a zoom of the main plot. Initial conditions: $L_e = 30$ km, $L_b = 25$ km, $b_0 = 160$ m, $d(t=0) = 5$ m, $a_0 = 2.2$ m, $d_s = 100$ μm, and horizontal continental shelf with $C_z = 55$ m$^{1/2}$/s.

After 2500 tidal cycles the suspended concentration field reaches an asymptotic behaviour with time that reveals that equilibrium is reached. It can be inferred through the horizontal trend that the different contour lines show over time. Besides, this equilibrium configuration displays a concentration field that increases in the landward direction, reaching a maximum around $\xi = 0.8$, beyond which starts to decrease. We suggest that the location of this maximum at equilibrium is placed at this regions due to the influence of the drying and wetting procceses. This is a region in which water depth reduces considerably during the ebb phase, giving rise to sediment concentration peaks.

A second aspect of interest related to the sediment concentration field is the assessment of the relative influence of each of the mechanisms that affect its temporal changes. These mechanisms, collected in equation (2.75), are the advective term, the erosion-deposition, term and the diffusive term. Namely:

$$\underbrace{\frac{\partial c}{\partial t}}_{concentration\,time\,variations} + \overbrace{\frac{\partial uc}{\partial x}}^{advective\,term} = \underbrace{\frac{E_r - D_e}{A}}_{erosion-deposition\,term} + \overbrace{\frac{1}{A}\frac{\partial}{\partial x}\left(k_x A\frac{\partial c}{\partial x}\right)}^{diffusive\,term}. \tag{2.121}$$

As observed in Figure 2.19, the influence of the diffusive mechanism is negligible, having a certain degree of influence close to the landward boundary (Figure 2.19 (b)). Erosion-deposition mechanism (Figure 2.19 (a)) and the advective mechanism (Figure 2.19 (c)) control the sediment concentration field, being the first one, with approximately a 80%, the main factor. As in the sediment concentration field, the horizontal trend that the different contour lines show over time reveals that the relative influence of each mechanism evolves asymptotically toward stable values. As a general rule, the importance of the erosion-deposition mechanism decreases in the landward direction, reaching a maximum around $\xi = 0.8$, beyond which start to increase. An inverse trend is followed by the advective mechanism. Again, the region of the tidal channel under drying and wetting processes determines the change in the trend followed by this mechanisms.

2.3.2.3 Assessment of tidal channel equilibrium: tidal prism-tidal channel area relation evolution

The evolutionary scenario observed in Figure 2.6 is characterized by an adjustment of the tidal channel bed profile until an equilibrium configuration is asymptotically reached. Two tidal channel descriptors of geomorphic relevance, such as, the minimum cross-sectional flow area during the flood phase, A_{min}, and the volume of water flowing through a given cross section during the flood phase (tidal prism, P), defined as:

$$P = \int_{T_{flood}} u d b\, dt, \tag{2.122}$$

where u is the depth-averaged flow velocity, d is the local depth, and b is the local width, also show an asymptotic trend throughout the channel evolution (black circles in Figure 2.20). As a general rule, tidal prism values (P) increase during the first stages of evolution in the outer part of

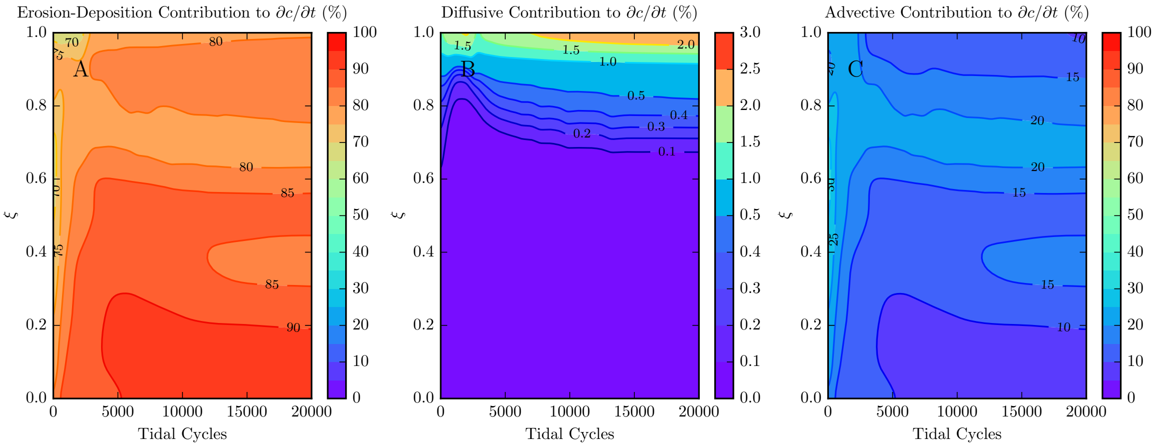

Figure 2.19: Relative influence both in space and time of the different mechanisms that affect the temporal evolution of the net suspended sediment concentration field: (a) erosion-deposition contribution, (b) diffusive contribution, and (c) advective contribution. Initial conditions: $L_e = 30$ km, $L_b = 25$ km, $b_0 = 160$ m, $d(t = 0) = 5$ m, $a_0 = 2.2$ m, d_s = 100 μm, and horizontal continental shelf with $C_z = 55$ m$^{1/2}$/s.

the tidal channel ($\xi < 0.5$), but once they reach a peak value, they decrease asymptotically up to attain a constant value. On the other hand, tidal prism follows an asymptotic decrease from the beginning of the simulation in the sections located in the inner part of the tidal channel ($\xi \geq 0.5$). Also note that the spatial distribution of the asymptotic magnitude attained by the tidal prism decreases in the landward direction.

On the other hand, the minimum cross-sectional flow area (A_{min}) shows a quite different trend depending on its location withing the tidal channel (red diamonds in Figure 2.20). Due to the scour experienced in the outer part of the channel and the deposition in the inner part as a consequence of the sediment front propagation, sections in which $\xi < 0.5$ increase their minimum cross-sectional area asymptotically with time, whereas the minimum cross-sectional area decreases asymptotically in sections located beyond the half channel length. Observe that the sections closest to the landward boundary are subjected to wetting and drying processes and the minimum cross sections tend to vanish (Figure 2.20 (f)).

Furthermore, it has been proved that this final state of asymptotic equilibrium satisfies a power law relationship between the minimum cross-sectional area at a given section within a tidal embayment and its corresponding tidal prism (O'Brien, 1969; Jarrett, 1976). This geomorphic relationship, termed by D'Alpaos et al. (2010) as the O'Brien-Jarret-Marchi law, becomes a valuable tool for studies on long-term tidal geomorphology as the one reported in this work. This relationship reads as:

$$A = k_{ap} P^{\alpha_{ap}}, \tag{2.123}$$

where k_{ap} and α_{ap} are scaling coefficients obtained on the basis of a cross section stability criterium in which the bed shear stress under maximum tidal velocity must be equal to the critical shear stress for incipient sediment motion. According to the formulation for estimating flow conductance C in this work (Keulegan, 1938), the values of k_{ap} and α_{ap} are then given by (D'Alpaos et al., 2010):

$$\alpha_{ap} = 1, \tag{2.124}$$

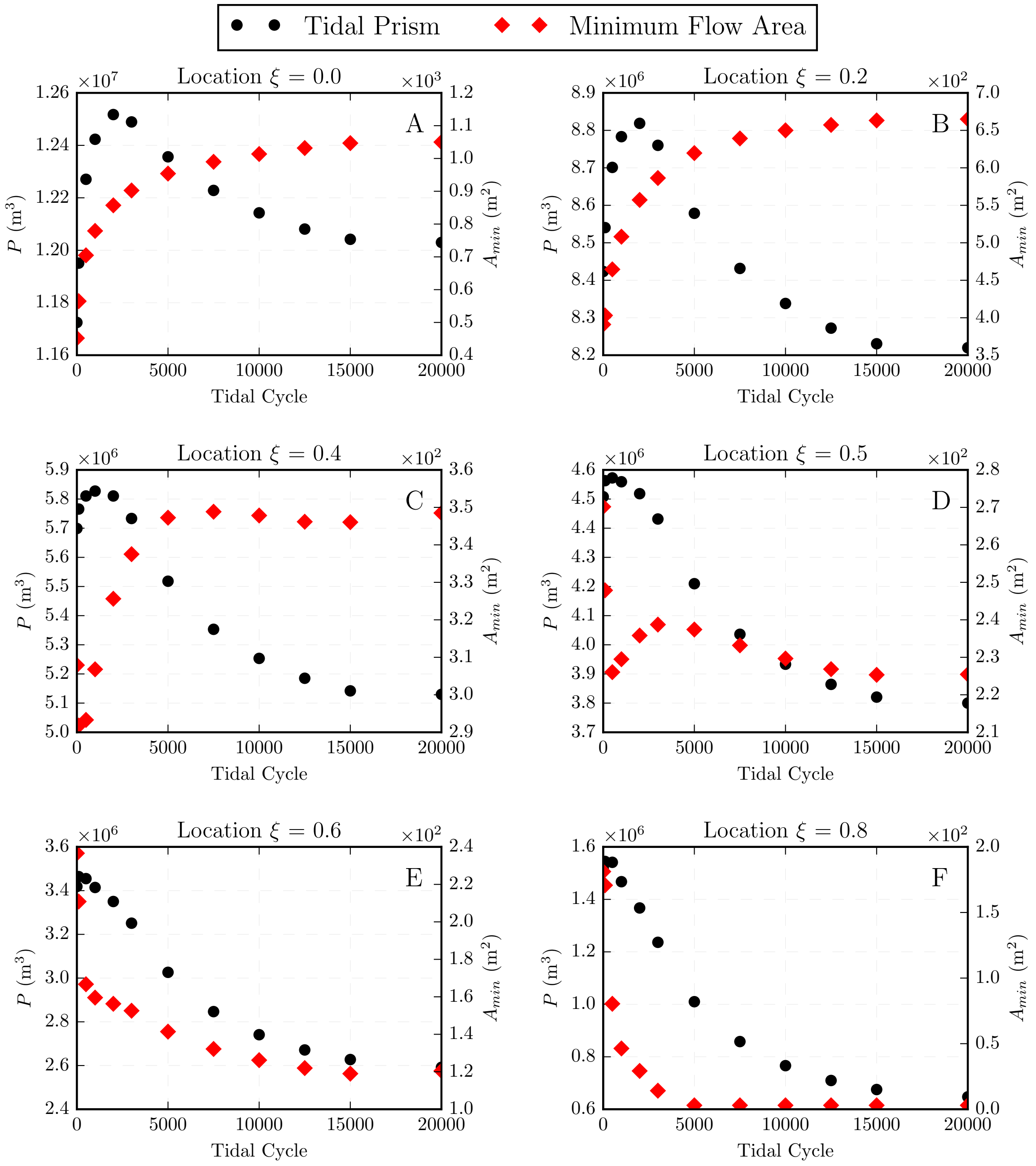

Figure 2.20: Tidal prism (P) and minimum cross-sectional channel area (A_{min}) at different tidal cycles and at different locations along the tidal channel: (a) $\xi = 0$, (b) $\xi = 0.2$, (c) $\xi = 0.4$, (d) $\xi = 0.5$, (e) $\xi = 0.6$, and (f) $\xi = 0.8$. Due to drying process at $\xi = 0.8$, values of minimum channel area vanish. Initial conditions: $L_e = 30$ km, $L_b = 25$ km, $b_0 = 160$ m, $d(t=0) = 5$ m, $a_0 = 2.2$ m, $d_s = 100$ μm, and horizontal continental shelf with $C_z = 55$ m$^{1/2}$/s. Notice the different y-scales of the different panels.

and:

$$k_{ap} = \frac{\omega}{2Cu_{*,cr}}, \tag{2.125}$$

where ω is the frequency of the tidal forcing, and $u_{*,cr}$ is the critical friction velocity for beginning of sediment movement. While the coefficient α_{ap} is fixed, the parameter k_{ap} cannot be universal since it depends on the flow conductance, which may within the tidal channel.

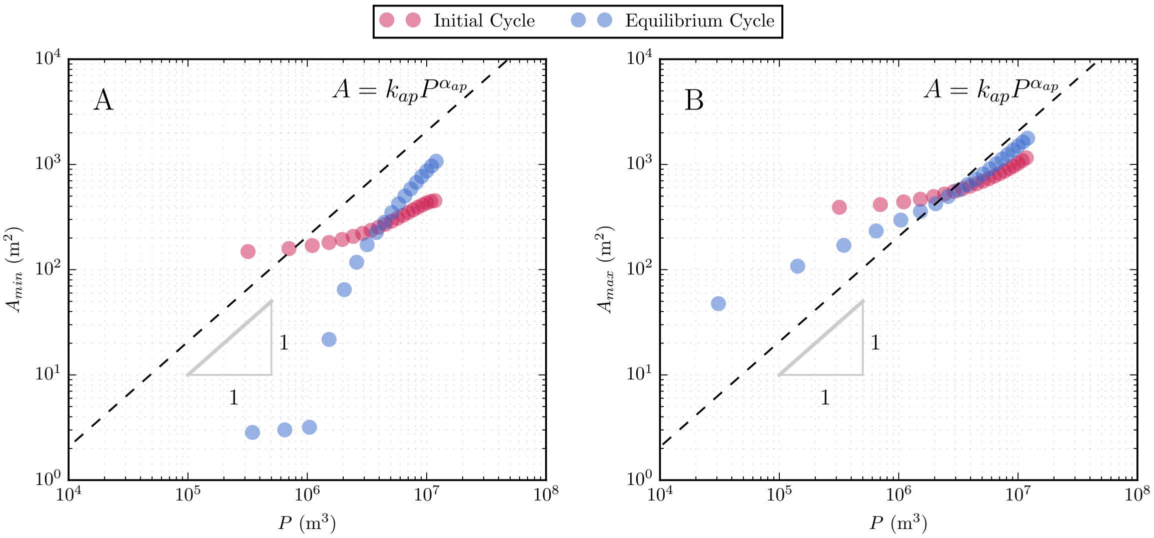

Figure 2.21: Tidal prism, P, versus (a) minimum cross-sectional flow area, A_{min}, and (b) maximum cross-sectional flow area, A_{max}, for various sections along the tidal channel at the beginning of the simulation (red circles) and at equilibrium (blue circles). The black dashed line represents the O'Brien-Jarrett-Marchi relationship of D'Alpaos et al. (2010) for a channel mean value of $k_{ap} = 2 \times 10^{-3}$, and $\alpha_{ap} = 1$. Initial conditions: $L_e = 30$ km, $L_b = 25$ km, $b_0 = 160$ m, $d(t = 0) = 5$ m, $a_0 = 2.2$ m, $d_s = 100$ μm, and horizontal continental shelf with $C_z = 55$ m$^{1/2}$/s.

Figure 2.21 shows the relationship between the minimum and maximum cross-sectional area as a function of the related tidal prism for the various sections along the longitudinal profile of a tidal channel both at the beginning of the simulation, with an horizontal bottom profile, and at equilibrium. We adopt a mean value of C along the entire tidal channel at equilibrium, we obtain that $k_{ap} = 0.0002$. As expected, it clearly emerges that the cross-sectional area-tidal prism relationship attains the O'Brien-Jarrett-Marchi power law along most of the channel as the bottom profile reaches an equilibrium configuration . A relevant feature exhibited by the results is that the values of the tidal prism at equilibrium as a function of the cross-sectional flow area are better fitted by the O'Brien-Jarrett-Marchi power law when we considerer the maximum area (Figure 2.21 (b)), rather than the minimum area (Figure 2.21 (a)). This fact was also shown by Lanzoni and Seminara (2002). Besides, Figure 2.21 (a) shows a break in the power law, i.e., a deviation from the line characterized by a slope equal to 1, at equilibrium in the inner sections of the tidal channels where wetting and drying processes are likely to affect significantly the dynamics conditions of the system.

2.3.2.4 Influence of tidal channel evolution on offshore plume dynamics

The offshore plume resulting from the tidal discharge into the adjacent open sea undergoes a consequent evolution as a result of the tidal channel evolution itself. Therefore, the plume hydrodynamic and morphodynamic properties, obviously, will be also altered during the simulation due to the global evolution of the coupled system towards a state of quasi-equilibrium.

As the tidal channel debouches into a receiving basin, it experiences a decrease in velocity and flow momentum with consequent plume (or jet) expansion, sediment deposition and mouth-bar formation (Wright and Coleman, 1974). The present modeling approach allows us to readily evaluate (at the different stages of the channel evolution (Figure 2.22 (a))) the along-plume normalized centerline velocity (Figure 2.22 (b)), plume half width (Figure 2.22 (c)) and plume centerline sediment concentration (Figure 2.22 (d)). These three variables, that characterize the offshore plume dynamics, are dictated by tidal channel variables at the mouth during the ebb-phase, namely, water depth, velocity, channel width and exiting sediment concentration.

We have already seen that the evolution toward an equilibrium configuration is achieved by progressively reducing the asymmetry between ebb and flood duration and velocities (Lanzoni and Seminara, 2002). This tendency eventually implies a reduction of velocity peaks and a consequent reduction in the gradients of the bed load transport and of erosive and deposition vertical fluxes. These changes are clearly displayed in the behaviour of the velocities and in the sediment fluxes at the channel mouth, which ultimately control the plume dynamics.

At the beginning of the simulation, the strong velocity peaks that occur the ebb-phase give rise to higher velocities on plume. Once a quasi-equilibrium state is attained both the velocity asymmetries and the intensity of the velocities during the tidal cycle decrease considerably. This velocity peaks reduction is reflected in the less energetic velocity field in the offshore plume (Figure 2.22 (b)).

A second consequence of the tidal evolution on the velocity field of the offshore plume is the increase of the zone of flow establishment (plume core or jet core) where centerline velocity can be assumed constant. The length of this zone, located nearby the outlet, depends on the competition between advective and frictional terms of the plume. While smaller advective terms favors the reduction of the plume core length, a smaller influence of the frictional terms increases the length of this core. As observed in Figure 2.22 (b), the zone of flow establishment is enlarged at the end of the simulation. Since the frictional term is inversely proportional to the water depth, as the channel mouth deepens the friction experienced by the plume along its axis reduces. Consequently, the reduction of the friction experienced by the plume once it debouches into the offshore sea basin prevails over the decrease in the channel velocities, thus leading to an increase in the plume core length.

A direct consequence of the vanishing of velocity asymmetries, of the reduction of velocity peaks, and of the increase in channel mouth depth is that the plume narrows during the channel evolution (Figure 2.22 (c)). The cause for this progressive contraction is related to mass conservation and, mainly, to the variation of frictional effects. The frictional parameter μ combines a number of effects (water depth, mouth width and bottom friction), such that when friction is large or the inlet width is large as compared to depth, the jet merely explodes as it faces the bottom resistance and loses its momentum (Özsoy and Ünlüata, 1982). Since both the bottom friction of the offshore basin and the tidal channel planform are kept fixed during our simulations, the only parameter of this relationship that is allowed to vary during the channel evolution is the channel mouth depth. While at the beginning of the simulation these three effects will be acting concurrently to the expansion of the plume, at equilibrium the increase of water depth will prevail, reducing the rate of plume expansion. Thus, as depicted from Figure 2.22 (b) and Figure 2.22 (c), the increase in depth experienced by the tidal channel mouth during its morphodynamic evolution tends to counteract the effects of offshore friction and the lateral entrainment of ambient non-turbulent water into the plume. Consequently, narrower plumes arise during the evolution of the system towards a quasi-equilibrium configuration.

A third direct consequence of the tidal channel evolution is the considerable decrease of the centerline concentration of sediment forming the offshore plume once the tidal channel tends

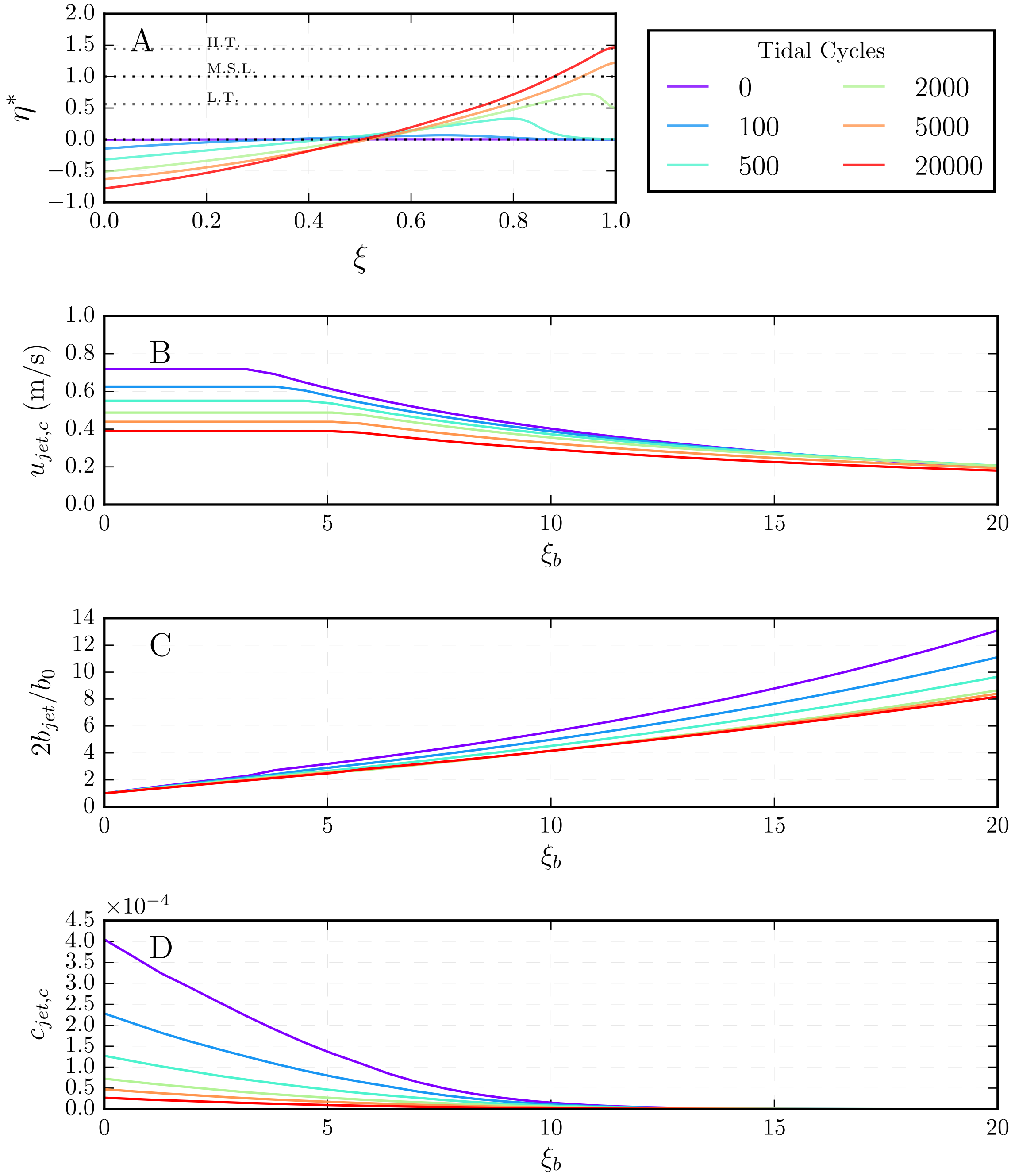

Figure 2.22: Temporal evolution of (a) the dimensionless bottom profile of the tidal channel, (b) plume centerline velocity, (c) plume half-width, and (d) plume centerline sediment concentration. Initial conditions: L_e = 30 km, L_b = 25 km, b_0 = 160 m, $d(t=0)$ = 5 m, a_0 = 2.2 m, d_s = 100 μm, and horizontal continental shelf with C_z = 55 m$^{1/2}$/s.

towards equilibirum (Figure 2.22 (d)). Since erosive processes in the sea shelf have been ignored in this simulation, the only sediment that can be carried by the plume is the material scoured in the channel. A comparison between the exiting sediment concentration (values of $c_{jet,c}$ at ξ_b = 0) both at the beginning of the simulation and at the quasi-equilibrium state reveals that the gradient between erosion (E_r) and deposition (D_e) reduces considerably inside the tidal channel. Hence, the reduction in exported sediment, the less energetic velocity field that favors the speed up of the material deposition, and the reduced ability of the flow to carry sediments further caused by a less energetic velocity field gives rise to a drastic fall of the concentration within the offshore region encompassed by the plume.

Given the solutions for velocity and concentration along the plume centerline, the amount of material deposited or eroded per unit time and unit area of the offshore sea bottom can be obtained by considering source and sink sources (Özsoy, 1986). In dimensionless form, the rate of change in bottom elevation reads:

$$K_{jet}(x,y)=\frac{\partial \sigma_{jet}}{\partial t}=\frac{2c_0 d_0 u_0}{b_0}\frac{\gamma}{p}\left[C_{a,jet}(x)+\left(C_{jet,c}(x)-C_{a,jet}(x)\right)G(\zeta)\right]\left[1-\phi^2 F^2(\zeta)U^2_{jet,c}(\zeta)\right], \tag{2.126}$$

where σ_{jet} is the amount of material per unit area of the bottom (in units of concentration × length), p is the porosity of the sea bed, and K_{jet} is a dimensionless deposition and erosion rate.

Figure 2.23 shows that the trend in erosion/deposition patterns in the continental shelf strongly depends on the evolution of the tidal channel. Note that the distribution of K_{jet} is only a measure of possible bottom erosion/deposition occurring on the continental shelf that have not been considered in the present contribution. Hence, herein we can only outline some conceptual considerations on the processes allowing the formation of mouth bars (Wright, 1977; Nardin and Fagherazzi, 2012; Leonardi et al., 2013; Canestrelli et al., 2014b; Jiménez-Robles et al., 2016). Bathymetric changes in offshore region may ultimately affect the flow and the diffusion patterns, which remains beyond the scope of this work. Recalling that the material of the continental shelf can not be entrained into suspension, no negative values appear in Figure 2.23. An initial deposition region of high intensity next to the channel mouth and an important lateral diffusion of sediments arises at the beginning of the simulation due to the larger quantity of eroded material close to the channel outlet (Figure 2.23 (a)). This trend of the deposition function indicates the possible formation of a mouth bar with a thickness that decreases seaward and toward the plume margins. A sharp decrease in K_{jet} takes place once the sediment front reaches the inner boundary of the tidal channel and is completely reflected (Figure 2.23 (d) and (e)). Finally, and as a consequence of the jet narrowing and the reduction of both flow velocities and sediment fluxes exiting the tidal channel during its evolution, the deposition rates on the offshore sea basin reduce sharply. This reduction is both in extension and, mainly, in intensity, since it is reduced by an order of magnitude once the tidal channel reaches a state of dynamic equilibrium (Figure 2.23 (f)).

On the contrary, the offshore plume also exerts a feedback influence on the tidal channel through sediment transference. The sediment concentration field existing in the plume after the ebb-phase starts to enter the tidal channel once the flood phase starts and the velocity field reverses. This sediment concentration behaves as an extra sediment concentration source at the tidal channel mouth. Hence, this source of sediment concentration is advected-diffused through the tidal channel. As shown in Figure 2.6 (c), the bottom aggradation as a consequence of the deposition of this source of sediment is limited to the outer part of the tidal channel.

How the offshore plume impacts the channel evolution over time is shown in Figure 2.24. This figure shows both the velocity magnitude at the tidal channel mouth ($\xi_b = \xi = 0$) and the

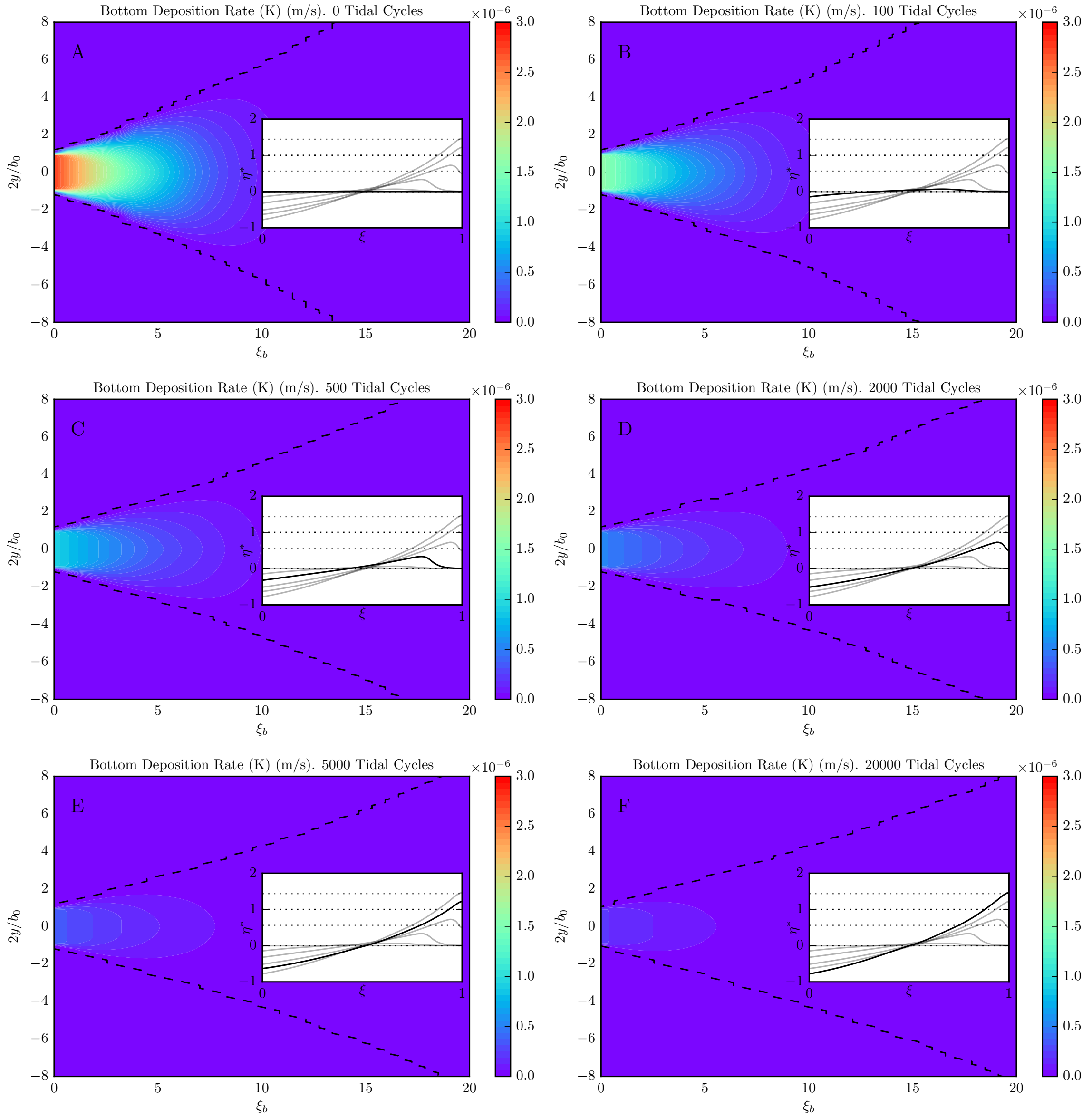

Figure 2.23: Rate contours of bottom erosion and deposition in the continental shelf, K_{jet}, at different stages of tidal channel evolution: (a) beginning of the simulation, (b) 100 tidal cycles, (c) 500 tidal cycles, (d) 2000 tidal cycles, (e) 5000 tidal cycles, and (f) 20000 tidal cycles (equilibrium). Black dashed lines delimits the region in which erosion/deposition processes take place. The continental shelf coordinates have been scaled with the tidal channel mouth half-width ($b_0/2$). Each panel includes an inset with the corresponding state of the tidal channel profile. Initial conditions: $L_e = 30$ km, $L_b = 25$ km, $b_0 = 160$ m, $d(t = 0) = 5$ m, $a_0 = 2.2$ m, $d_s = 100$ μm, and horizontal continental shelf with $C_z = 55$ m$^{1/2}$/s. Erosion in the continental shelf has been neglected in this simulation.

sediment concentration entering the tidal channel from the offshore plume during the flood phase, at different stages of the channel evolution. Two remarks can be outlined:

1. The first one is related to the amount of sediment entering the channel. It decreases with time as a consequence of the reduction of sediment concentration into the offshore plume (Figure 2.22 (d)) up to the sediment front reaches the inner end of the tidal channel and is completely reflected (Figure 2.24 (d) and (e)). After that, and once the tidal channel reaches

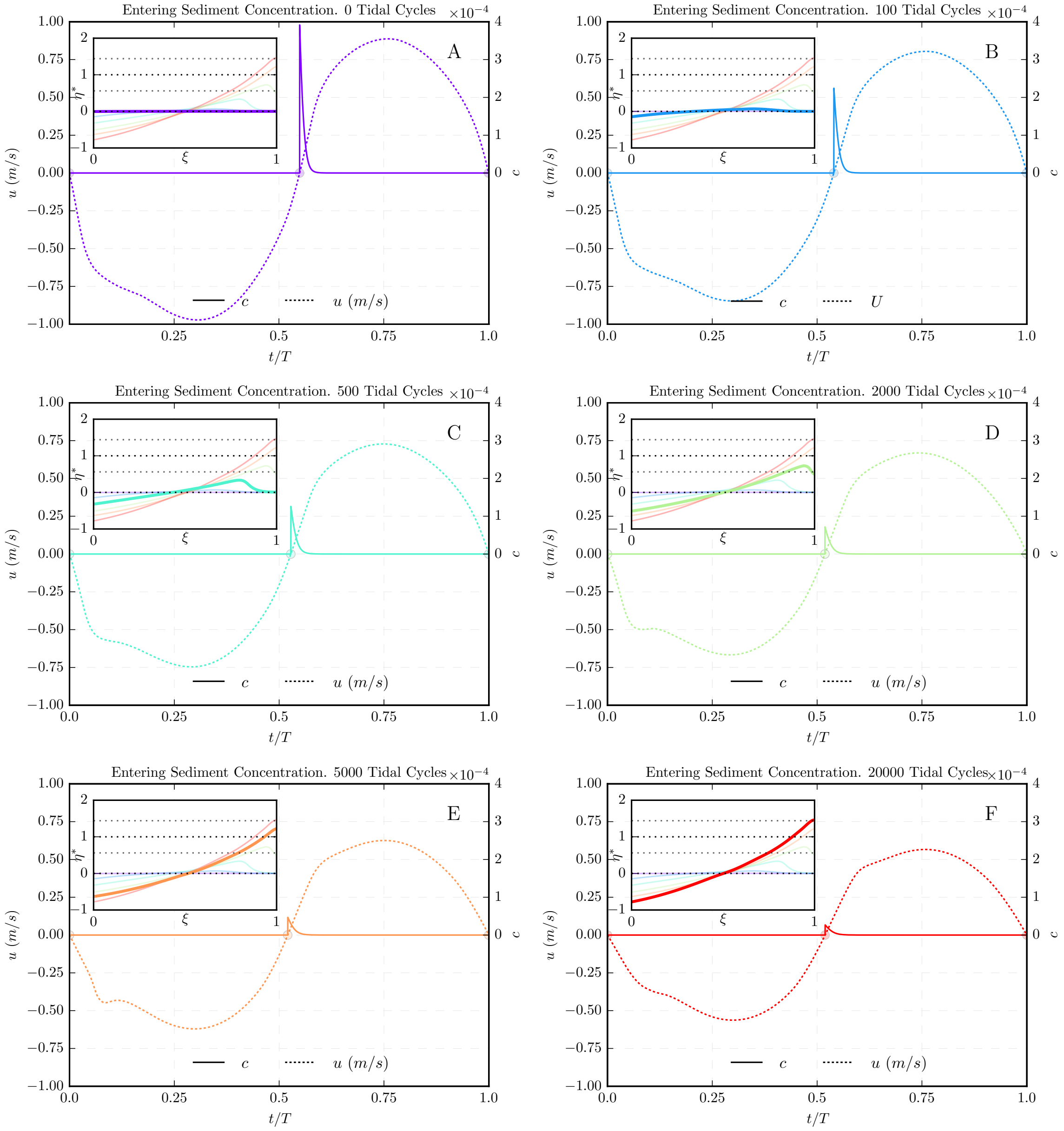

Figure 2.24: Velocity at the tidal channel mouth (u at $\xi = 0$) and sediment concentration entering the tidal channel from the offshore plume (c) during a tidal cycle, at different stages of tidal channel evolution: (a) beginning of the simulation, (b) 100 tidal cycles, (c) 500 tidal cycles, (d) 2000 tidal cycles, (e) 5000 tidal cycles, and (f) 20000 tidal cycles (equilibrium). Each panel includes an inset with the corresponding state of the tidal channel profile. Initial conditions: $L_e = 30$ km, $L_b = 25$ km, $b_0 = 160$ m, $d(t = 0) = 5$ m, $a_0 = 2.2$ m, $d_s = 100$ μm, and horizontal continental shelf with $C_z = 55$ m$^{1/2}$/s.

the equilibrium, a low and asymptotically constant value of the entering sediment concentration maintains over time (Figure 2.24 (f)).

2. The second one is linked to to time during which sediment is entering the channel. It is reduced due to the moment in which this sediment concentration starts entering the channel. The plume limits its influence to about a tenth of the flood phase period as a consequence of the low velocities existing in the tidal channel mouth at the beginning of the

flood phase (Figure 2.24). Thus, settling velocities prevails and the rate at which sediment concentration within the plume decays is faster than the rate at which this sediment concentration enters the tidal channel. Furthermore, the numerical model does not consider hindered settling effects whereby the fall velocity of particles in high concentration mixtures is reduced due to the presence of other particles. Thus, the rate at which the plume diminishes its sediment concentration is the same regardless of the stage of the channel evolution.

2.3.3 Role of external factors on tidal channel-offshore plume dynamics

In the previous sections the attention has been concentrated on the transient process of the intrinsic mechanisms whereby, starting from an initial bed configuration and for given conditions of both the tidal channel and the ocean, the channel evolves toward some equilibrium configuration. Now we focus this section on how external parameters that characterize the system are able to influence the asymptotic equilibrium configuration of the tidal channel and the offshore plume dynamics. The role of (i) channel convergence, (ii) macroscopic characteristics of the continental shelf, i.e., slope and Chezy friction coefficient, (iii) the initial depth of the tidal channel, (iv) the amplitude of the forcing tide, and (v) the eroded sediment from the continental shelf are addressed.

2.3.3.1 The role of tidal channel convergence

It is worth analyzing our results in terms of the variation of the tidal channel planform configuration obtained from equation 2.1. Various degrees of funneling obtained for different values of the convergence length, L_b, with prescribed values of both mouth width, b_0, and channel length, L_e, have been imposed (Figure 2.25 (a)). Although tidal channels of constant width ($L_b \to \infty$) are quite uncommon in natural channels (Savenije, 2006), considering it as allows us to investigate the tidal channel evolution separating the effect of convergence.

Figure 2.25 (b) shows the equilibrium bed profiles calculated for different values of L_b. As it is of interest to consider differences in the shape of the tidal channels independent of their size, a statistic termed the funnel-shape parameter (Davies and Woodroffe, 2010) that reads:

$$S_b = \frac{L_b}{b_0}, \tag{2.127}$$

is used. S_b is identical for exponential width profiles of he same shape but different sizes. Further, lower values of S_b are associated with more strongly funnel-shaped or convergent width profiles. The picture emerging from this figure confirms the findings of Lanzoni and Seminara (2002); Todeschini et al. (2008); Toffolon and Lanzoni (2010) and Bolla Pittaluga et al. (2015). Starting from an identical initial configuration, at equilibrium tidal channels react to funneling of the cross section by modifying the bed profile. In particular, a decrease in the value of S_b leads to a progressive seaward bed aggradation associated with sediment deposition, leading to a reduction of the flow depth. Conversely, prismatic (constant width) tidal channels increase the depth at the mouth and consequently a larger value of bottom slope arises.

The influence of the convergence implies a strongly effect also on the hydrodynamic response of a tidal channel. Different trends in the hydrodynamic aspects to those described in

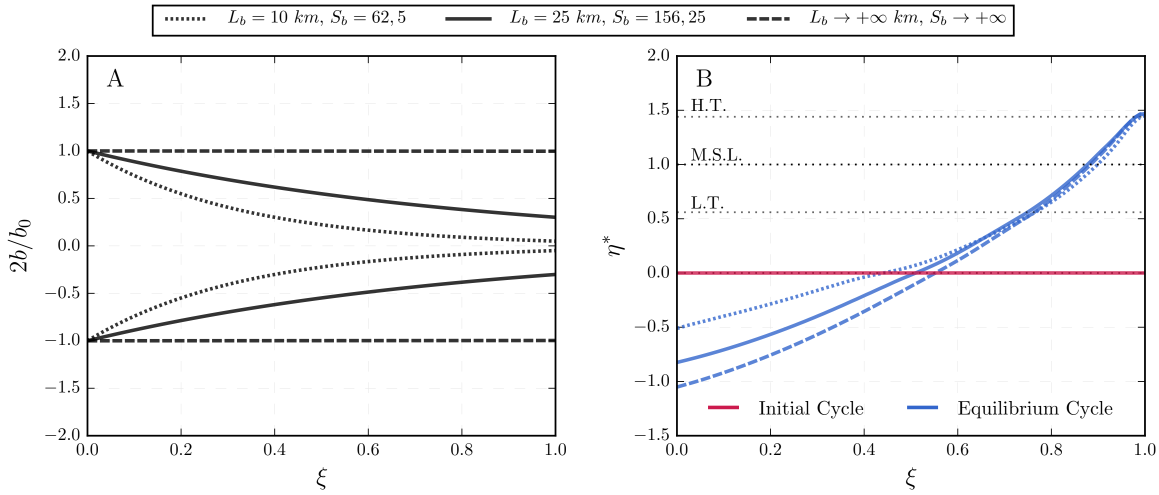

Figure 2.25: (a) Normalized tidal channel planform width investigated in the present numerical tests. The length and width of the tidal channel mouth are kept fixed ($L_e = 30$ km and $b_0 = 160$ m) while the convergence length L_b is varied ($L_b = 10$ km, $L_b = 25$ km, and $L_b \to +\infty$ km). (b) Initial and equilibrium configurations of the bottom profile for the three planform shapes depicted in panel (a). Horizontal dashed lines represent the high tide (H.T.), mean sea level (M.S.L.) and low tide (L.T.) elevations at the channel mouth. Initial conditions: $d(t = 0) = 5$ m, $a_0 = 2.2$ m, $d_s = 100$ μm, and horizontal continental shelf with $C_z = 55$ m$^{1/2}$/s.

Section 2.3.2.1 are obtained if the convergence length is varied with respect to the reference in which $L_b = 25$ km (Figure 2.26).

Figure 2.26 (a) reports that the higher is the convergence length the more the velocity peaks are enhanced (and their asymmetry) and the higher is the residual value of the velocity. At equilibrium (Figure 2.26 (b)), the velocity peaks are almost constant along the tidal channel and residual velocities vanish regardless the convergence length.

Tidal channel convergence can also determine amplification or damping of the tidal wave. The influence of L_b clearly emerges when the dimensionless tidal range (equation (2.116)) is plotted at the initial stage of the simulation, when the bottom is still horizontal (Figure 2.26 (c)). The more convergent is the channel, the more the tidal amplitude grows with the wave propagation and higher is its hypersynchronous character. For the case of constant width, channel bottom friction offsets the influence of convergence and a landward decrease in tidal range is observed, enhancing its hyposynchronous character. Conversely, an interesting feature emerges at equilibrium (Figure 2.26 (d)): all the simulations leads to an invariably landward amplification of the tidal range along the estuary, indicating the hypersynchronous character of the tidal channel. In the inner reaches of the estuary, beyond the inner shoreline, the tidal range at equilibrium decrease due to the abrupt reduction in water depth as a consequence of the emerging bottom.

The sediment concentration field existing in the tidal channel at equilibrium is a direct consequence of its hydrodynamics. In particular, the higher velocity peaks in less convergent tidal channels lead to higher values of the sediment concentration field (Figure 2.27). However, the distribution of the contour lines of the sediment concentration field does not show particular differences for different convergence lenghs. All of them exhibit a turbidity maximum zone close to the landward boundary approximately at the moment in which the sediment front is being reflected. In addition, suspended concentration field reaches an asymptotic behaviour with time characterized by an increase of the concentration in the landward direction that reaches a maximum around $\xi = 0.8$. Beyond this section, the concentration starts to decrease.

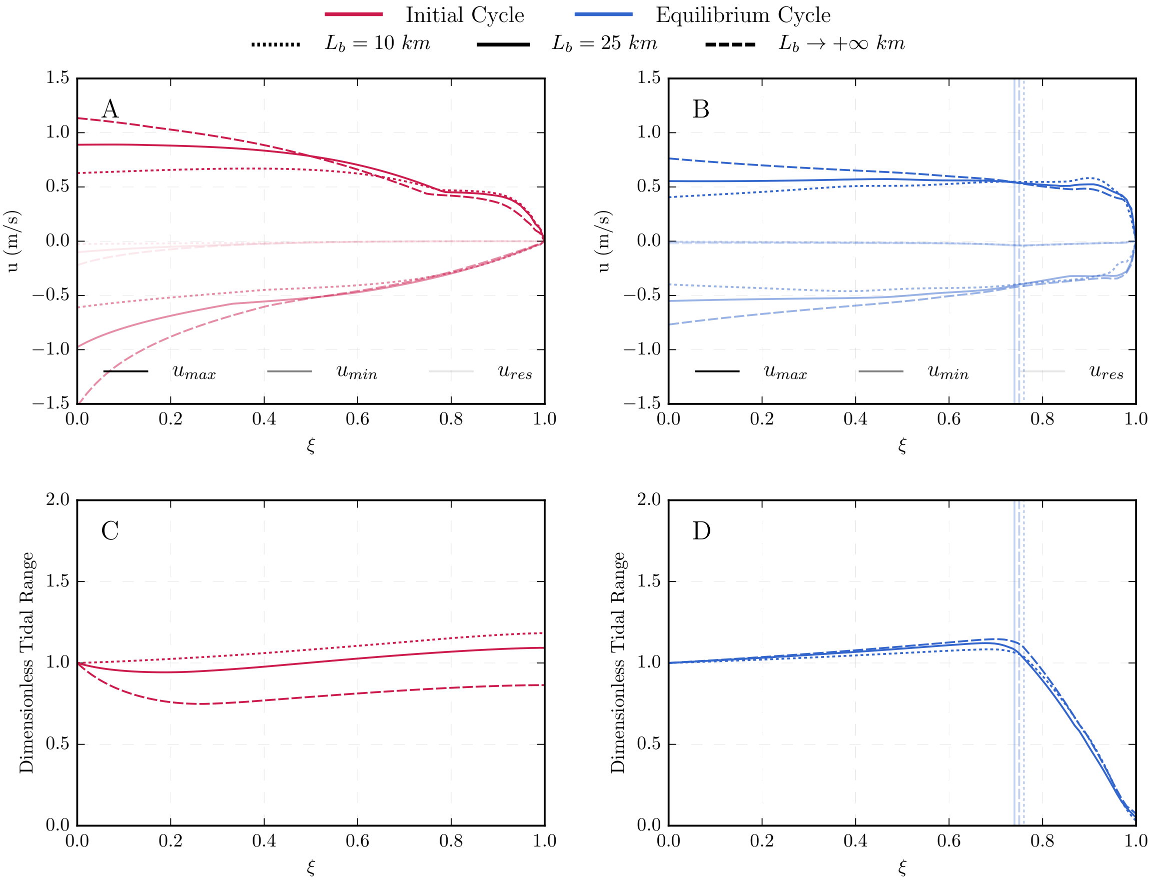

Figure 2.26: Values along the tidal channel of maximum, minimum, and residual velocity at the beginning of the simulation (a) and at equilibrium (b), and dimensionless tidal range at the beginning of the simulation (c) and at equilibrium (d) for different values of the convergence length ($L_b = 10$ km, $L_b = 25$ km, and $L_b \to +\infty$ km). Vertical dashed lines indicate the position of the inner shoreline once the equilibrium is reached for each convergence length. Initial conditions: $L_e = 30$ km, $b_0 = 160$ m, $d(t = 0) = 5$ m, $a_0 = 2.2$ m, $d_s = 100\ \mu$m, and horizontal continental shelf with $C_z = 55$ m$^{1/2}$/s.

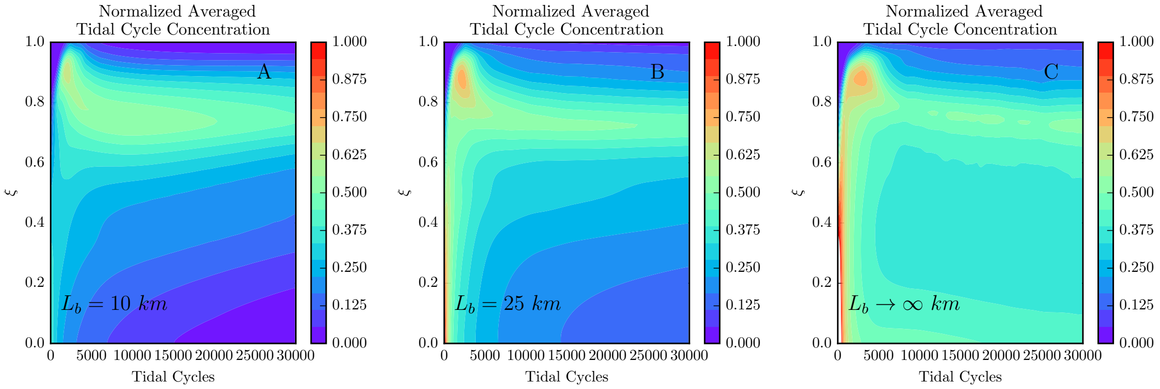

Figure 2.27: Variation of the net suspended sediment concentration field in space and time for different values of the convergence length: (a) $L_b = 10$ km, (b) $L_b = 25$ km, and (c) $L_b \to +\infty$ km. The concentration have been normalized with the maximum value of the three cases simulated. Initial conditions: $L_e = 30$ km, $b_0 = 160$ m, $d(t = 0) = 5$ m, $a_0 = 2.2$ m, $d_s = 100\ \mu$m, and horizontal continental shelf with $C_z = 55$ m$^{1/2}$/s.

The final equilibrium state of a tidal channel verify the power law relationship between the cross-sectional area and the corresponding tidal prism seen in Section 2.3.2.3 regardless its funneling shape. Figure 2.28 reports that, at equlibrium, the more convergent is the planform of the tidal channel, the better is the agreement attained with the O'Brien-Jarrett-Marchi relationship power law of D'Alpaos et al. (2010), both for the case in which the minimum and maximum cross sectional flow areas are considered.

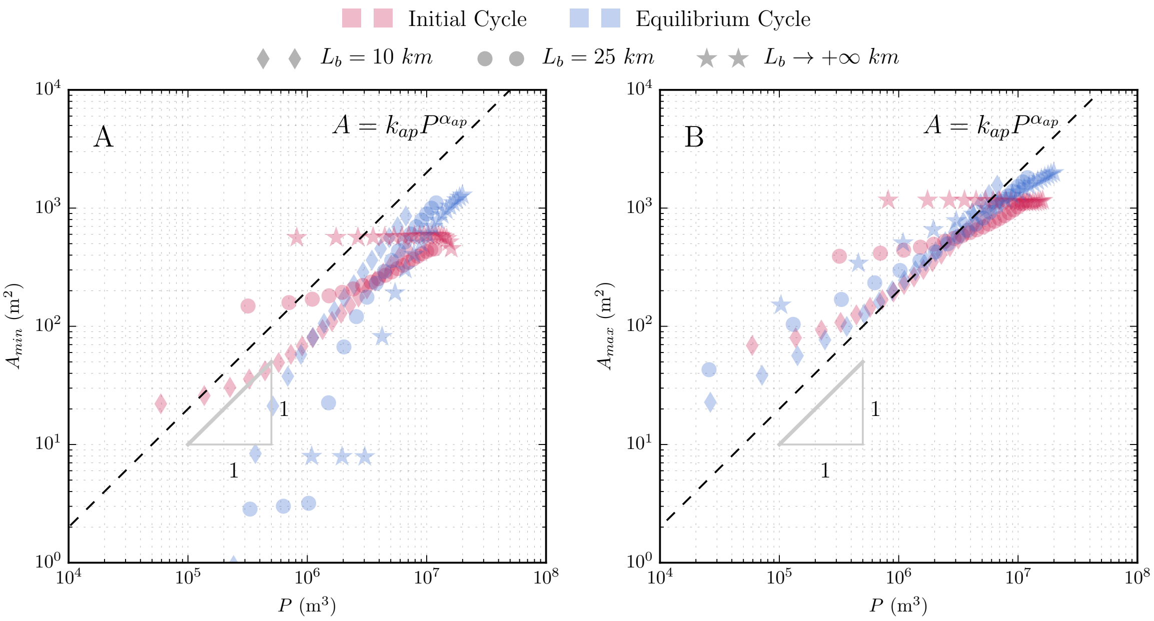

Figure 2.28: Tidal prism, P, versus (a) minimum cross-sectional flow area, A_{min}, and (b) maximum cross-sectional flow area, A_{max}, for various sections along the tidal channel at the beginning of the simulation (red markers) and at equilibrium (blue markers) for different values of the convergence length (L_b = 10 km, L_b = 25 km, and $L_b \to +\infty$ km). The black dashed line represents the O'Brien-Jarrett-Marchi relationship of D'Alpaos et al. (2010) for a channel mean value of $k_{ap} = 2 \times 10^{-3}$, and $\alpha_{ap} = 1$. Initial conditions: $L_e = 30$ km, $b_0 = 160$ m, $d(t = 0) = 5$ m, $a_0 = 2.2$ m, $d_s = 100\ \mu$m, and horizontal continental shelf with $C_z = 55$ m$^{1/2}$/s.

An important feature of the influence of the degree of convergence of the tidal channel is the remarkable influence that exerts on the dynamics of the offshore plume (Figure 2.29). A decrease of the convergence degree (higher L_b) implies a further increase of both the plume axis velocity (Figure 2.28 (a)) and plume axis sediment concentration (Figure 2.28 (c)). It is directly linked to the higher velocities present in less convergent tidal channels and the consequent higher ability to entrain sediment into suspension. This trend followed by velocity and sediment concentration along the plume axis remains both at the beginning of the simulation and at equilibrium.

Conversely, plume half-width exhibits a different behaviour depending on the stage of channel evolution. At the beginning of the simulations, when the tidal channel depth is still the same for all the cases, a decrease of the convergence degree (higher L_b) leads to a wider plume due to mass conservation. Conversely, at equilibrium, an offshore plume with a lower widening rate arises. Thus, the narrowing experienced by a plume as a consequence of the tidal channel evolution is more pronounced in cases with higher values of the channel convergence length. We suggest that this behaviour is dictated by the higher decrease of the bed level at the channel mouth showed in less convergent channels at equilibrium (Figure 2.25 (b)). It leads to an increase of the flow depth and a consequent reduction of the bottom friction experienced by the plume which, in turns, reduces the rate of plume spreading.

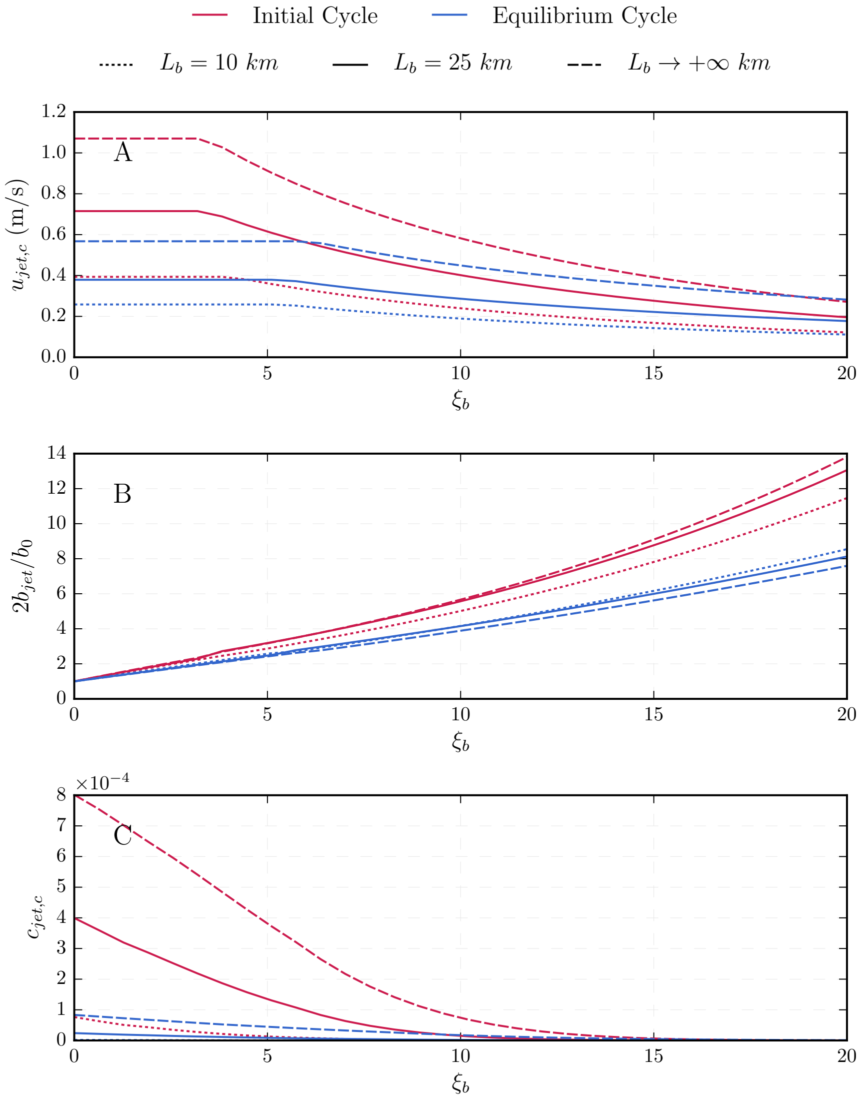

Figure 2.29: (a) Plume centerline velocity, (b) plume half-width, and (c) plume centerline sediment concentration both at the beginning of the simulation and at equilibrium for different values of the convergence length ($L_b = 10$ km, $L_b = 25$ km, and $L_b \to +\infty$ km). Initial conditions: $L_e = 30$ km, $b_0 = 160$ m, $d(t=0) = 5$ m, $a_0 = 2.2$ m, $d_s = 100$ μm, and horizontal continental shelf with $C_z = 55$ m$^{1/2}$/s.

2.3.3.2 The role of macroscopic characteristics of the continental shelf: bottom slope and Chezy friction coefficient

Apart from the tidal channel inherent parameters, those that characterized the adjacent continental shelf also plays a significant role in the offshore plume and tidal channel evolution. We here investigate the influence of two macroscopic parameters that globally characterize the continental shelf: its bottom slope and friction. Their influence over the offshore plume has already been addressed (Özsoy and Ünlüata, 1982; Özsoy, 1986), however how their ability to control the channel evolution is a task that remains unclear.

2.3.3.2.1 Continental shelf bottom slope. We now consider linear variations in depth by taking $d_{jet} = d_0 + m_b x$, with d_{jet} being the water depth at a distance x from the tidal channel mouth, m_b the continental shelf bottom slope and d_0 the tidal channel mouth depth.

Figure 2.30 reports the main sediment laden offshore plume characteristics under two different values of the continental shelf bottom slope. It is seen that the jet width depends critically on the continental shelf slope m_b. That is, with increasing m_b values, the centerline velocity remains approximately unmodified both at the beginning of the simulation and at equilibrium (Figure 2.30 (a)) and the plume contracts significantly due to mass conservation (Figure 2.30 (b)). A remarkable feature of the plume width when $m_b = 5\%$ is that contraction is suppressed despite the increasing depth at the channel mouth related to channel evolution. The changes in bottom slope displayed in Figure 2.30 (c) show that higher values of m_b lead to higher values of sediment concentration and that the material is jetted further offshore. We suggest that it is due to the higher time needed for the sediment to reach the bed and the narrower plume that arise, which reduces the lateral expansion of sediments.

The second question we raised concerns the long term tidal channel response to changes the continental shelf slope. Changes in plume dynamics have direct implications on the asymptotic equilibrium profile of the tidal channel. Figure 2.31 shows the bed level differences of equilibrium tidal channel bathymetric profiles under different values of m_b with respect to the reference case in which the continental shelf was supposed to be horizonta ($m_b = 0\%$). It can be observed that the increase of the continental shelf slope determines a significant progressive increase of the channel bed level in the seaward direction (from $\xi = 1$ to $\xi = 0$). Furthermore, the higher m_b becomes, the higher is the channel bed level, which can reach values of the order of $\mathcal{O}(10^{-1}$ m) for the higher m_b values. This aggradation experienced by the tidal channel is related to (i) the concentration of streamlines around the plume axis during the flood phase in the adjacent sea as a consequence of the sloping bottom that give rise to a selective withdrawal and higher velocities that favors the transfer of sediment from the plume to the tidal channel (Figure 2.4), and (ii) the higher availability of suspended material in sloping continental shelf plumes (Figure 2.31 (c)).

2.3.3.2.2 Continental shelf bottom friction. To investigate the effect of the Chezy coefficient of the continental shelf (C_z) on the evolution of the entire system, the comparison between three simulations corresponding to different values of C_z equal to 30, 55 and 80 $\mathrm{m}^{1/2}/\mathrm{s}$ is made. Recall that C_z is more a flow conductance parameter than a parameter of flow resistance, since higher values implies less bottom friction. The values of these three variables are reduced and follow the same trend both at the beginning of the simulation and once the equilibrium is reached.

Figure 2.32 summarizes the effect of C_z on the offshore plume. When plume resistance is increased, the centerline velocity decays (Figure 2.32 (a)) and the plume width grows (Figure 2.32 (b)) exponentially. On the other hand, the suspended sediment concentration is not significantly affected by these frictional changes, at least within the range of values investigated here (Figure 2.32 (c)).

Conversely to the continental shelf slope case, changes experienced by the offshore plume due to different Chezy friction parameters in the continental shelf do not alter the equilibrium profile of the tidal channel. Figure 2.33 depicts bed level differences of equilibrium tidal channel bathymetric profiles under different values of C_z with respect to the reference case in which C_z =55 $\mathrm{m}^{1/2}/\mathrm{s}$. It is observed that higher bed resistance favors the aggradation of the tidal channel bed level, while a low value leads to bed aggradation, both with increasing intensity in the

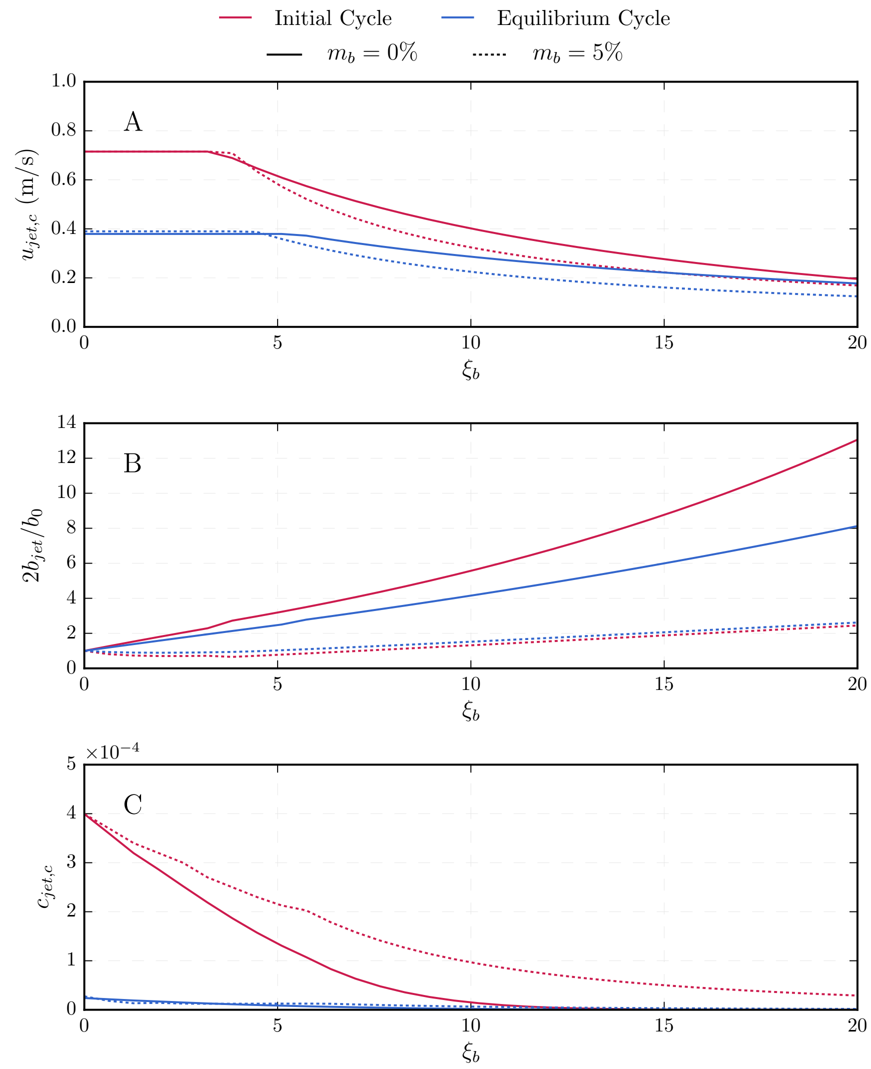

Figure 2.30: (a) Plume centerline velocity, (b) plume half-width, and (c) plume centerline sediment concentration both at the beginning of the simulation and at equilibrium for different values of the continental shelf bottom slope ($m_b = 0\%$ and $m_b = 5\%$). Initial conditions: $L_e = 30$ km, $b_0 = 160$ m, $d(t=0) = 5$ m, $a_0 = 2.2$ m, $d_s = 100$ μm, and continental shelf with $C_z = 55$ $\mathrm{m}^{1/2}/\mathrm{s}$.

seaward direction. However, this bathymetric changes are not significant from a macroscopic perspective, being two orders of magnitude smaller, $\mathcal{O}(10^{-3}$ m), than in the case of continental shelf slope variations. We argue that this insensitivity to C_z values is the result of (i) insignificant differences of the sediment concentration in the plume (Figure 2.32 (c)) and (ii) mainly to the inability of the model to consider friction effects when computing velocity field in the adjacent sea during the flood phase: it was modeled as frictionless, irrotational and inviscid flow.

2.3.3.3 The role of the initial depth

The role of one of the imposed initial conditions for the whole system, the initial depth of the tidal channel, $d(t=0)$, which is assumed horizontal, is now investigated. It is natural to expect the solution to be dependent on this initial condition for a given tidal forcing and channel planform shape. This is confirmed by the results reported in Figure 2.34, where the equilibrium

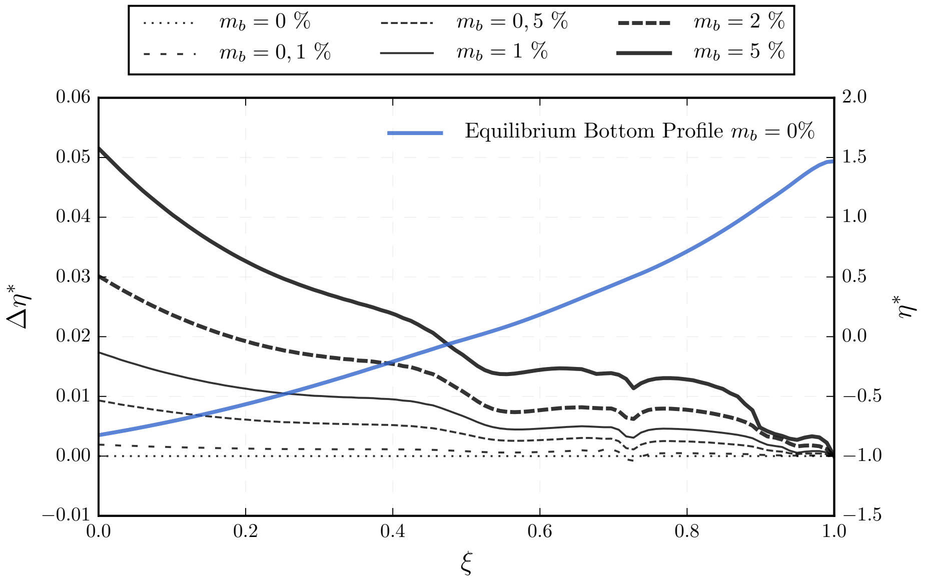

Figure 2.31: Difference along the tidal channel of the normalized bottom profile level at equilibrium for different continental shelf bottom slopes ($m_b = 0\%$, $m_b = 0,1\%$, $m_b = 0,5\%$, $m_b = 1\%$, $m_b = 2\%$, and $m_b = 5\%$) with respect to the reference case in which the continental shelf is assumed to be horizontal ($m_b = 0\%$). The blue line depicts the equilibrium configurations of the bottom profile for the reference case. Initial conditions: $L_e = 30$ km, $L_b = 25$ km, $b_0 = 160$ m, $d(t = 0) = 5$ m, $a_0 = 2.2$ m, $d_s = 100$ μm, and continental shelf with $C_z = 55$ m$^{1/2}$/s.

profiles corresponding to three different values of the initial channel depth and subject to the identical tidal forcing are plotted. The shape pf the resulting channel profiles are quite similar. If we define roughly the average slope of the equilibrium bed profile as the difference between the bed elevation at the inner boundary and the bed elevation at the channel mouth divided by the channel length, it remains more or less constant regardless the initial depth. However, a higher value of the initial depth leads to an equilibrium channel profile which lies above the one corresponding to a shallower initial depth. In addition, our simulations suggest that the morphological evolution of initially deeper channels takes more time than those with smaller values of the initial depth. Thus, the initial depth affects the time required to reach an equilibrium state.

2.3.3.4 The role of the tidal amplitude

Results of simulations performed varying the tidal amplitude at the tidal channel mouth are shown in Figure 2.35. The tidal amplitude, a_0, has a strong influence on the solution, since it controls the scale of velocity in the tidal channel. Given the same geometrical conditions, a larger tidal amplitude leads to a progressively higher bed slope, as well as to an increasing bed degradation in the seaward portion and aggradation in the landward portion of the tidal channel. In addition, simulations reveal that the morphological evolution of a tidal channel forced by a higher tidal amplitude shows a slower pace. Similar results were reported by (Todeschini et al., 2008; Bolla Pittaluga et al., 2015).

2.3.3.5 Continental shelf as a source of sediment. Implications over the tidal channel

Up to now the only source of sediment than can be transported by the flow was the material existing in the active layer of the channel bed. Now we extend this active layer, imposing that

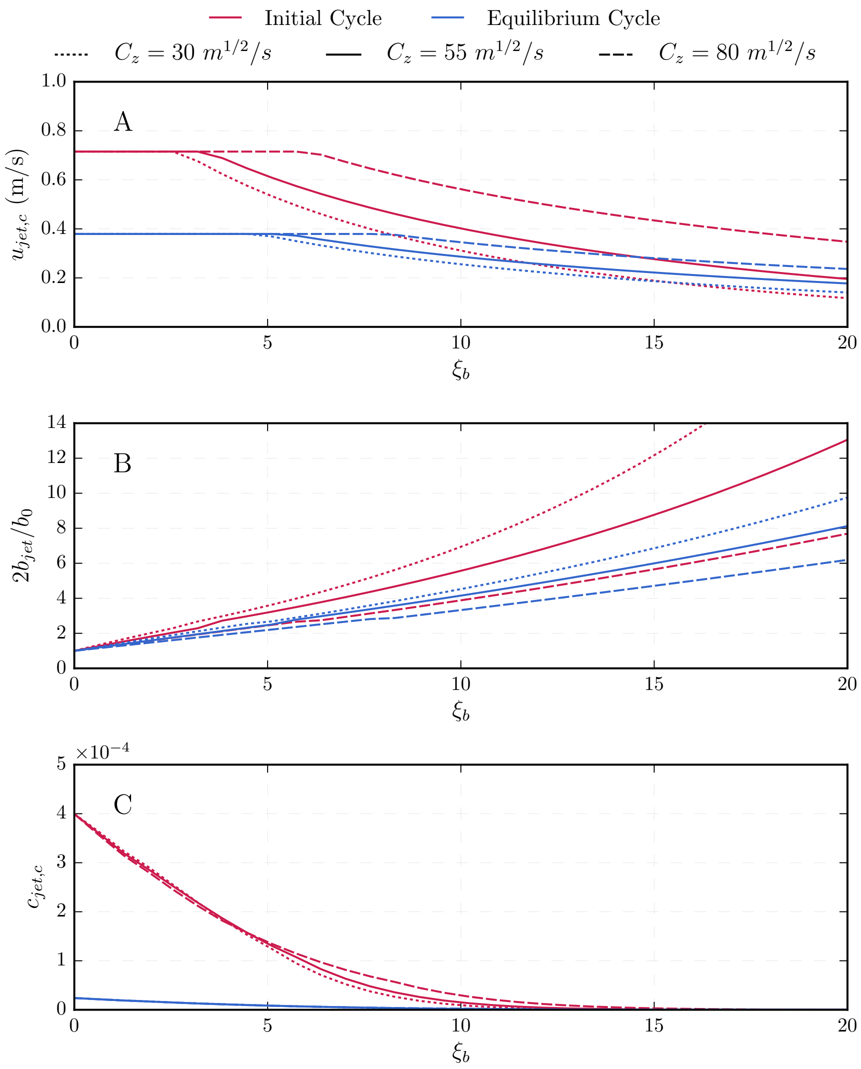

Figure 2.32: (a) Plume centerline velocity, (b) plume half-width, and (c) plume centerline sediment concentration both at the beginning of the simulation and at equilibrium for different values of the Chezy friction coefficient of the continental shelf ($C_z = 30$ m$^{1/2}$/s, $C_z = 55$ m$^{1/2}$/s, and $C_z = 80$ m$^{1/2}$/s). Initial conditions: $L_e = 30$ km, $b_0 = 160$ m, $d(t = 0) = 5$ m, $a_0 = 2.2$ m, $d_s = 100$ μm, and an horizontal continental shelf.

the material of the continental shelf is able to be entrained into suspension and be transported by the flow and, subsequently, may affect the availability of sediment in the tidal channel. In addition, sediment properties in the continental shelf were set to be the same as the material of the tidal channel. However, as stated in Section 2.2.3, despite erosive and deposition processes will be accounted for in the continental shelf, bathymetric changes on region will be neglected and a fixed flat bottom of constant slope will be assumed.

Thus, now we focus our attention on the influence of this source of sediment on the tidal channel evolution. In this sense, Figure 2.36 reports the deposition patterns in the continental shelf related to the ebb flow both at the beginning of the simulation and at equillibrium. During the initial stages the flow velocity is higher than the critical velocity for sediment entrainment into suspension and hence the ebb flow causes very strong erosion in the vicinity of the tidal channel mouth. The loci of maximum deposition border the scoured region giving rise to lateral

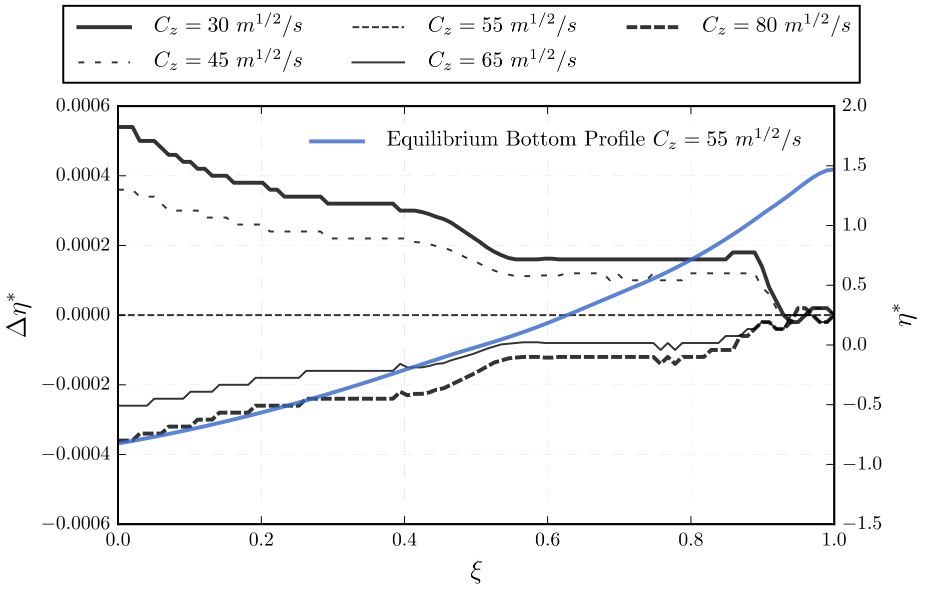

Figure 2.33: Difference along the tidal channel of the normalized bottom profile level at equilibrium for different Chezy friction coefficient of the continental shelf (C_z = 30 m$^{1/2}$/s, C_z = 45 m$^{1/2}$/s, C_z = 55 m$^{1/2}$/s, C_z = 65 m$^{1/2}$/s, C_z = 80 m$^{1/2}$/s) with respect to the reference case in which this Chezy coefficient is assumed to be C_z = 55 m$^{1/2}$/s. The blue line depicts the equilibrium configurations of the bottom profile for the reference case. Initial conditions: L_e = 30 km, L_b = 25 km, b_0 = 160 m, $d(t=0)$ = 5 m, a_0 = 2.2 m, d_s = 100 μm, and an horizontal continental shelf.

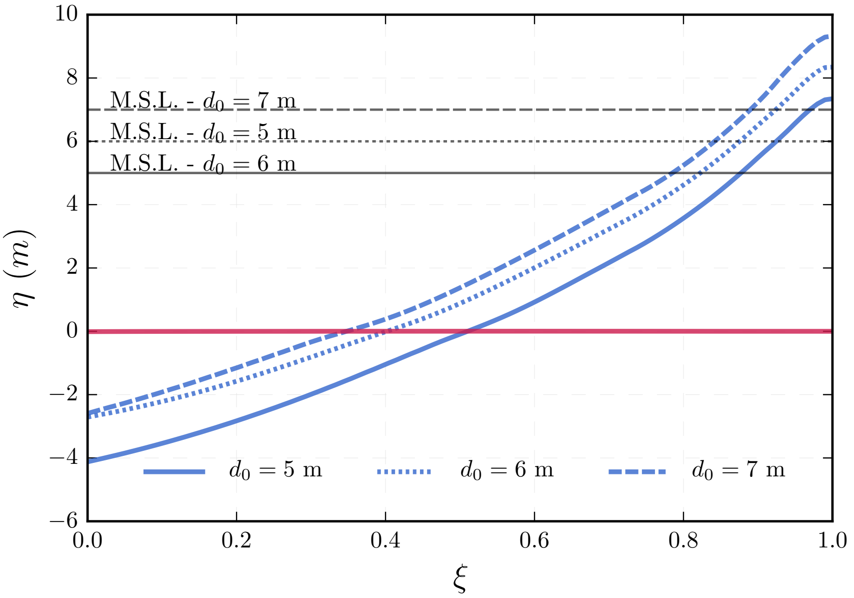

Figure 2.34: Bottom equilibrium profiles for different values of the initial depth of the channel ($d(t0 = 0)$ = 5 m, $d(t0 = 0)$ = 6 m, and d(t0=0)= 7 m,). The red line depicts the initial channel profile. Horizontal black dashed lines represent the mean sea level (M.S.L.) at the channel mouth for each case. Initial conditions: L_e = 30 km, L_b = 25 km, b_0 = 160 m, a_0 = 2.2 m, d_s = 100 μm, and horizontal continental shelf with C_z = 55 m$^{1/2}$/s.

levees that merge into a single maximum at some distance from the inlet (Wright, 1977; Mariotti et al., 2013). Along the center line of the plume, maximum deposition is observed at some distance from the mouth where a mouth bar would be expected to build up (Figure 2.36 (a)). On

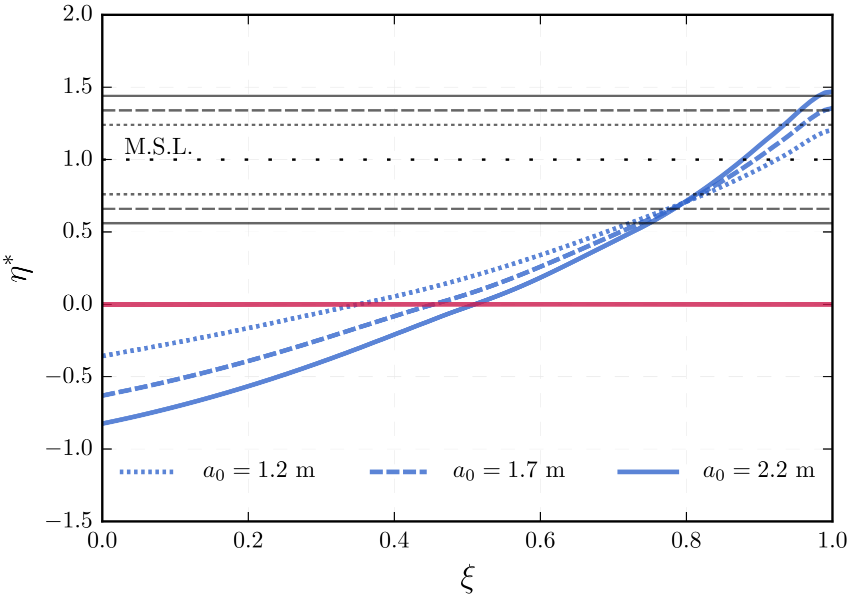

Figure 2.35: Bottom equilibrium profiles scaled with the initially uniform depth of the channel for different values of the tidal amplitude ($a_0 = 1.2$ m, $a_0 = 1.7$ m, and $a_0 = 2.2$ m). The red line depicts the initial channel profile. Horizontal black dashed lines represent the high tide (H.T.), mean sea level (M.S.L.) and low tide (L.T.) elevations at the channel mouth for each tidal amplitude. Initial conditions: $L_e = 30$ km, $L_b = 25$ km, $b_0 = 160$ m, $d(t = 0) = 5$ m, $d_s = 100$ μm, and horizontal continental shelf with $C_z = 55$ m$^{1/2}$/s.

the contrary, once the tidal channel reaches equilibrium, and as a consequence of jet narrowing and the reduction of both flow velocities and sediment fluxes exiting the tidal channel, erosion in the continental shelf vanishes and only weak deposition rates exist (Figure 2.36 (b)).

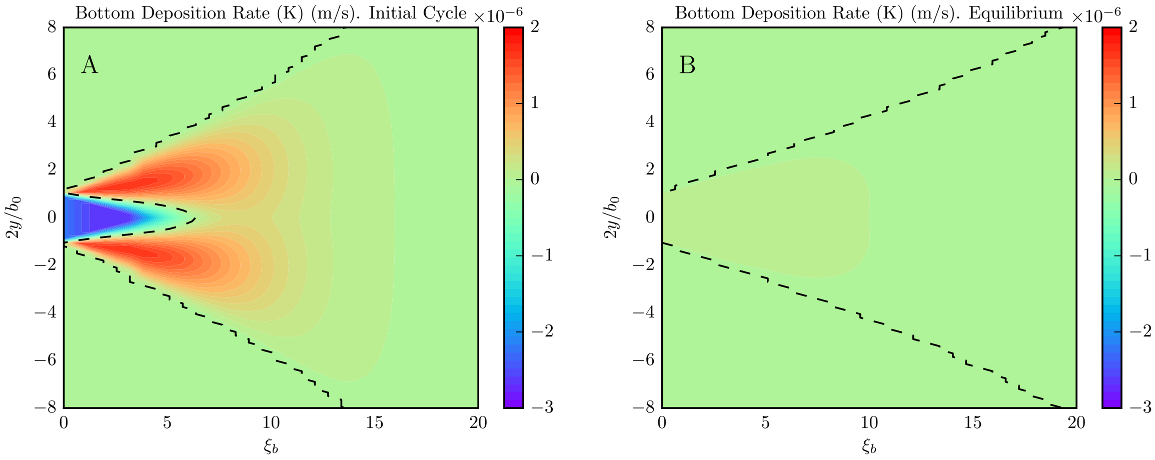

Figure 2.36: Rate contours of bottom erosion and deposition in the continental shelf, K_{jet}, at different stages of tidal channel evolution (a) at the beginning of the simulation, and (b) at equilibrium. Black dashed lines delimits the region in which erosion/deposition processes take place. The continental shelf coordinates have been scaled with the tidal channel mouth half-width ($b_0/2$). Initial conditions: $L_e = 30$ km, $L_b = 25$ km, $b_0 = 160$ m, $d(t = 0) = 5$ m, $a_0 = 2.2$ m, $d_s = 100$ μm, and horizontal continental shelf with $C_z = 55$ m$^{1/2}$/s.

The material eroded in the continental shelf have important consequences on the plume concentration. On the contrary to the case in which erosion in the continental shelf was neglected and the sediment concentration in the plume constantly decreases seawards, when erosion is allowed plume centerline concentration reaches a maximum value at some distance offshore as shown in Figure 2.37. In this case, eroded material in the vicinity of the tidal channel mouth increases the sediment concentration field and is jetted offshore where it eventually settles.

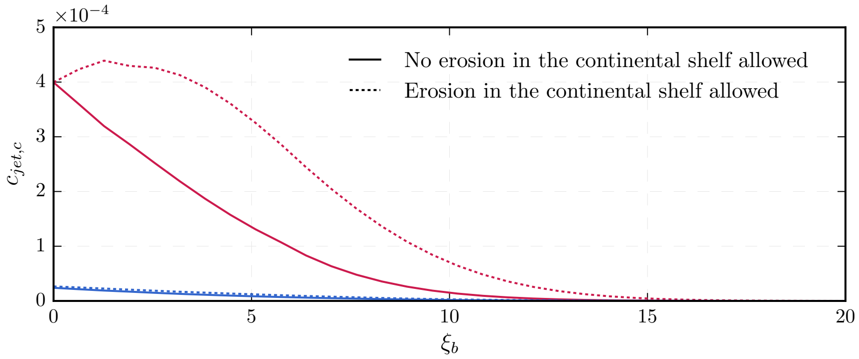

Figure 2.37: Plume centerline sediment concentration both at the beginning of the simulation and at equilibrium neglecting and considering erosive processes in the continental shelf. Initial conditions: $L_e = 30$ km, $L_b = 25$ km, $b_0 = 160$ m, $d(t=0) = 5$ m, $a_0 = 2.2$ m, $d_s = 100\ \mu$m, and horizontal continental shelf with $C_z = 55$ m$^{1/2}$/s.

Apart from the increase in the plume concentration, the availability of continental shelf material to be entrained into suspension will modify the amount of material entering into the tidal channel during the flood phase. Figure 2.38 focuses its attention on the incoming material once the plume totally disappears, i.e., concentration peaks at the beginning of the flood phase. After that, scoured material in the continental shelf tends to enter the tidal channel. The amount of this material reduces with tidal channel evolution due to the less ability of flow in eroding material. Besides, the time during which material from the continental shelf is entering the channel also reduce over channel evolution. Finally, it should be note that the concentration peaks related to the plume are now higher, although it is not displayed in Figure 2.38 for clarity.

Obviously, this eroded material will alter the evolution of the tidal channel bottom profiles. Figure 2.39 reports a comparison between the tidal channel evolution neglecting and considering the influence of the incoming material from the continental shelf bed. It reveals that this amount of eroded material have direct implications on the evolution the tidal channel. The asymptotic equilibrium profile tends to increase the concavity of the bottom profile, reducing the final channel mouth depth. This profile also tends to get flat (i.e., with constant depth) towards the mouth, a condition typical of an "ideal estuary", as defined by (Savenije and Veling, 2005). Differences in bed elevations are plotted in Figure 2.39 (c). It reveals that the influence of this material is higher in the seaward portion of the tidal channel, reaching the peak values in the channel mouth. Finally, differences of the order of $\mathcal{O}(10^{-1}$ m) at equilibrium are obtained.

2.4 Discussion

2.4.1 Main novelties of the model

Two are the main contributions of this work to the study of the morphological evolution of tidal channel an their equilibrium configuration:

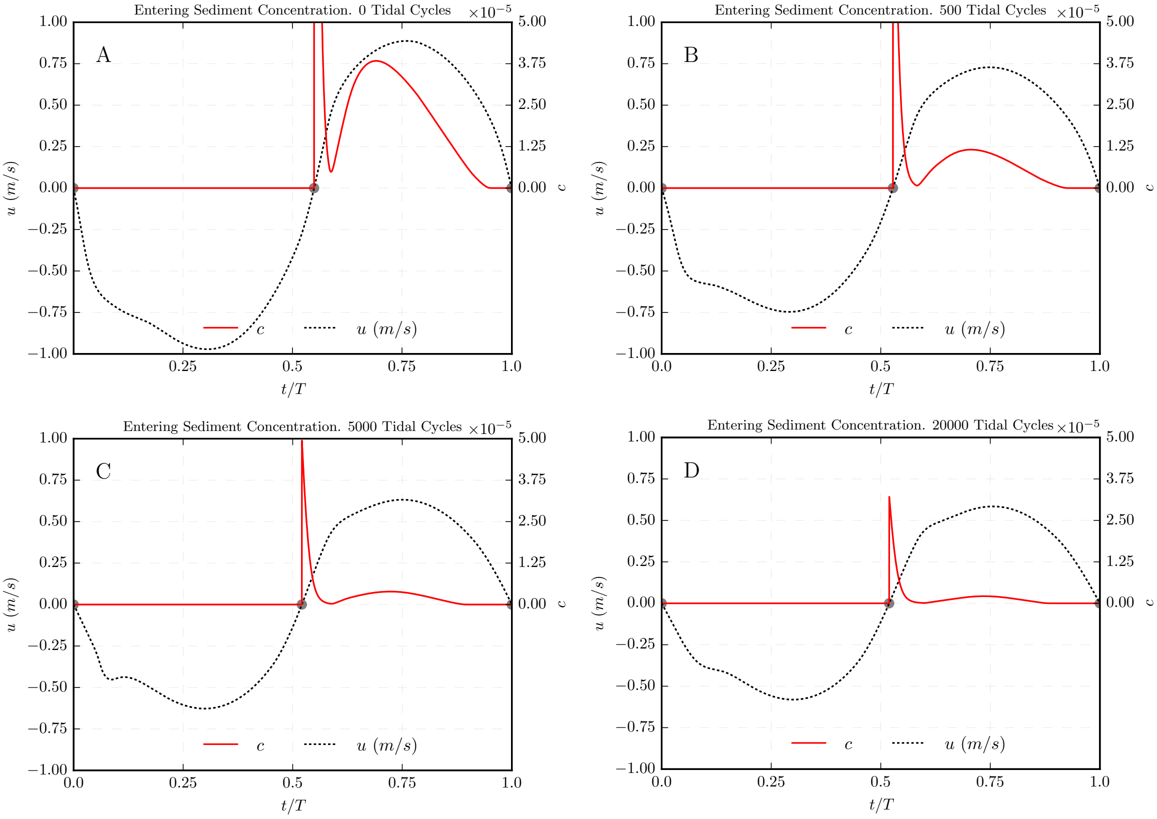

Figure 2.38: Velocity at the tidal channel mouth (u at $\xi = 0$) and sediment concentration entering the tidal channel both from the offshore plume and the eroded material in the continental shelf (c) during a tidal cycle, at different stages of tidal channel evolution: (a) beginning of the simulation, (b) 500 tidal cycles, (c) 5000 tidal cycles, and (e) 20000 tidal cycles (equilibrium). Initial conditions: $L_e = 30$ km, $L_b = 25$ km, $b_0 = 160$ m, $d(t = 0) = 5$ m, $a_0 = 2.2$ m, $d_s = 100\ \mu$m, and horizontal continental shelf with $C_z = 55$ m$^{1/2}$/s.

1. Previous works on the long-term morpholofical evolution of tidal channels already stress the necessity of considering the separate contributions of the bed load and the suspended flux and solving for the latter a suitable transport equation to compute suspended sediment concentration (Lanzoni and Seminara, 2002; Todeschini et al., 2008). In these previous works suspended load are assumed to adapt instantaneously to local flow conditions. They used equilibrium expressions by which the sediment particles respond instantaneously to local flow conditions. It implies that the movement of the sediment would be in the residual flow direction. Suspended load transport, however, does not have such a behaviour because it takes time (time lag effects) to transport the particles upwards and downwards over the depth and therefore it is necessary to model the vertical advection-diffusion process. They also indicated that this was the major assumption employed in their models. This assumption is particularly severe close to the slack water periods when equilibrium between entrainment and deposition cannot occur, as sediments simply settle in a quasi-quiescent water body.

   However, in non-steady flow the actual sediment transport rate may be smaller (underload) or larger (overload) than the transport capacity resulting in net erosion or deposition assuming sufficient availability of bed material. A tidal environment is characterized by flow unsteadiness that may lead to nonequilibrium effects that makes the sediment response lags with respect the flow through scour and settling lags (Postma, 1967). This

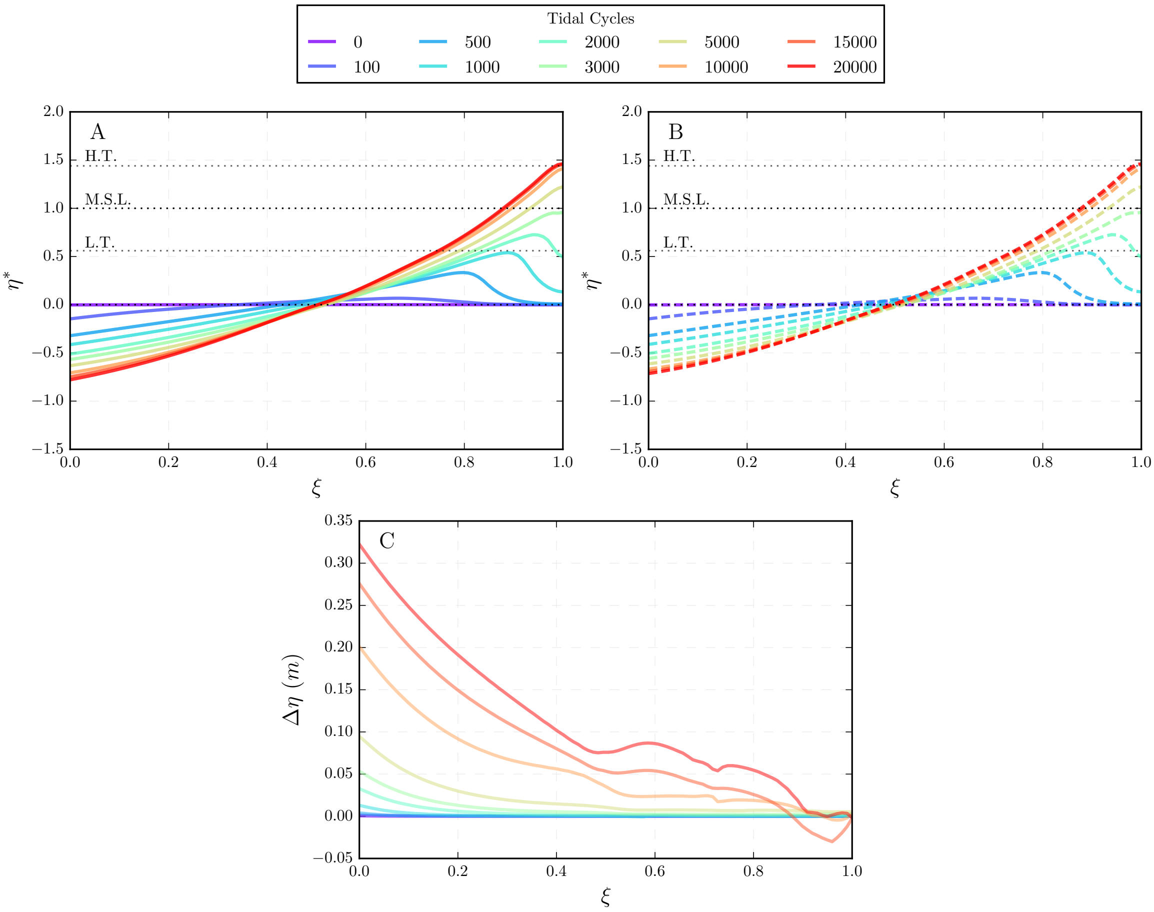

Figure 2.39: Temporal evolution of the bottom profile from an initially horizontal configuration for a convergent tidal channel (a) with and (b) without the influence of the eroded material in the continental shelf. The bottom elevation at each cross section has been scaled with the initially uniform depth of the channel ($\eta^*/d(t=0)$), while the longitudinal coordinate of the tidal channel has been scaled with the channel length ($\xi = x/L_e$). The values of the relevant parameters imposed in the calculation are $L_e = 30$ km, $L_b = 25$ km, $b_0 = 160$ m, initial bottom depth $d(t=0) = 5$ m, semidiurnal tide with amplitude $a_0 = 2.2$ m, mean sediment diameter of $d_s = 100$ μm. The continental shelf is supposed to be horizontal with a mean Chezy coefficient $C_z = 55$ m$^{1/2}$/s. Differences between the cases (a) and (b) at each tidal cycle are depicted in panel (c). Horizontal dashed lines represent the high tide (H.T.), mean sea level (M.S.L.) and low tide (L.T.) elevations at the channel mouth.

phase difference between the suspended sediment concentration and the water velocity can produce a residual flux of sediment even when there is no residual movement of water (Dyer, 1995; Friedrichs et al., 1998). Quantifying these nonequilibrium effects on sediment dynamics is a task which must be addressed in this framework of long-term morphological evolution of tidal channels and that, to the authors' knowledge, has not been explored so far.

An important feature of the present work is that the numerical simulations carried out here considerer a full description of sediment fluxes through equations (2.72) and (2.75). Thus, we reproduce correctly the settling lag associated with suspended load, which may be important in natural estuaries, in particular for short channels (Todeschini et al., 2008). Besides, and according the (van Rijn, 2013), time lag effects cannot be neglected for sediments smaller than about 0.3 mm and hence a quasi-steady approach is not a reliable formulae to be applied.

2. Estuaries and offshore plumes are usually treated separately with a fixed boundary condition at the channel mouth (Lamb et al., 2012; Chatanantavet et al., 2012). However, sediment supply from the open sea is particularly relevant as it has been suggested as one of the key factors in estuarine morphology (Yu et al., 2012). In particular, the presence of a nonnegligible flux of marine sediments at the tidal channel mouth can alter considerably its equilibrium configuration (Lanzoni and Seminara, 2002). However, there are limited experimental and modeling studies on sediment transport and morphodynamics of coupled estuaries and offshore plume systems.

   Thus, the main reason for including a detailed description of the suspended sediment load was a linkage between the channel and offshore plume dynamics, thereby dynamically coupling these regions. It is well known that estuarine discharges produce offshore plumes that expands in the direction of propagation and that may carry sediments and affect coastal circulation and mixing patterns (Bates, 1953; Wright, 1977; Edmonds and Slingerland, 2007; Rowland et al., 2009; Falcini and Jerolmack, 2010). Besides, the main plume properties (spreading rate and velocity and sediment concentration fields) are certainly dictated by the channel evolution.

   However, little work has explored whether tidal channels dynamics and sediment fluxes in turn are a function of plume behaviour. Our modeling results suggest that the offshore plume characteristics, which in turn are modified by the continental shelf bathymetry and friction, can affect the sediment fluxes in the tidal channel and lead to different equilibrium configurations. Tidal channel dynamics must be necessarily linked to the oceanic environment by its offshore plume. Furthermore, despite neglecting bottom changes on the continental shelf, we have seen that the evolution of the tidal channel results in a decrease of net erosion/sediment deposition in the continental shelf, with implications for delta evolution. We suggest that there exists a potential feedback between tidal channel and the offshore plume that must be considerer when estimating estuarine hydrodynamics and sediment transport processes.

2.4.2 Temporal scales considerations

Though the general trend of the evolution process of a tidal channel seems to confirm adequately the findings of previous works that tackled this problem numerically (Lanzoni and Seminara, 2002; Todeschini et al., 2008), our channel profile evolves faster. It is then of interest to address the typical temporal scales that control the evolution of the system. Our characteristic timescale for the channel to evolve up to reach equilibrium, $\mathscr{O}(10^1)$ years, differs differ from those of Lanzoni and Seminara (2002), $\mathscr{O}(10^2)$ years, and Todeschini et al. (2008), $\mathscr{O}(10^2)$ years. These discrepancies are related to the sediment transport formulation employed. To derive a typical morphological scale ($\mathscr{T}_0$) for the time for a tidal channel to come into equilibrium we considerer the mass balance equation (2.68):

$$\mathscr{T}_0 = (1-p)\frac{\mathscr{B}^*\mathscr{D}^*}{(D_e - E_r) + \dfrac{\mathscr{B}^* q_b}{\mathscr{L}^*}} \simeq (1-p)\frac{\mathscr{B}^*\mathscr{D}^*}{(D_e - E_r)}, \tag{2.128}$$

where $\mathscr{B}^*$, $\mathscr{L}^*$ and $\mathscr{D}^*$ are characteristic scales for channel width ($\sim 10^2$ m), length ($\sim 10^4$ m) and depth ($\sim 10^1$ m) respectively. Without any special information on the tidal channel conditions, we can estimate the scales of the terms of sediment fluxes according to Figure 2.10. Hence, we can assume $D_e - E_r \sim 10^{-6}$ m^2/s and $\mathscr{B}^* q_b \sim 10^{-3}$ m^3/s, thus ensuring that the the influence of the bed load can be neglected when estimating the morphological time scale. A key feature of the physics involved in the present problem is then the description of the entrainment of sediment into suspension E_{ent}. Different relationships for estimating the entrainment rate of sediment into suspension were evaluated in Figure 2.40 (Einstein (1950), Engelund and Fredsøe (1976), Smith and McLean (1977), van Rijn (1984c), Akiyama and Fukushima (1985), Garcia and Parker (1991), Nakagawa and Tsujimoto (1980), and Fernandez-Luque and Van Beek (1976)).

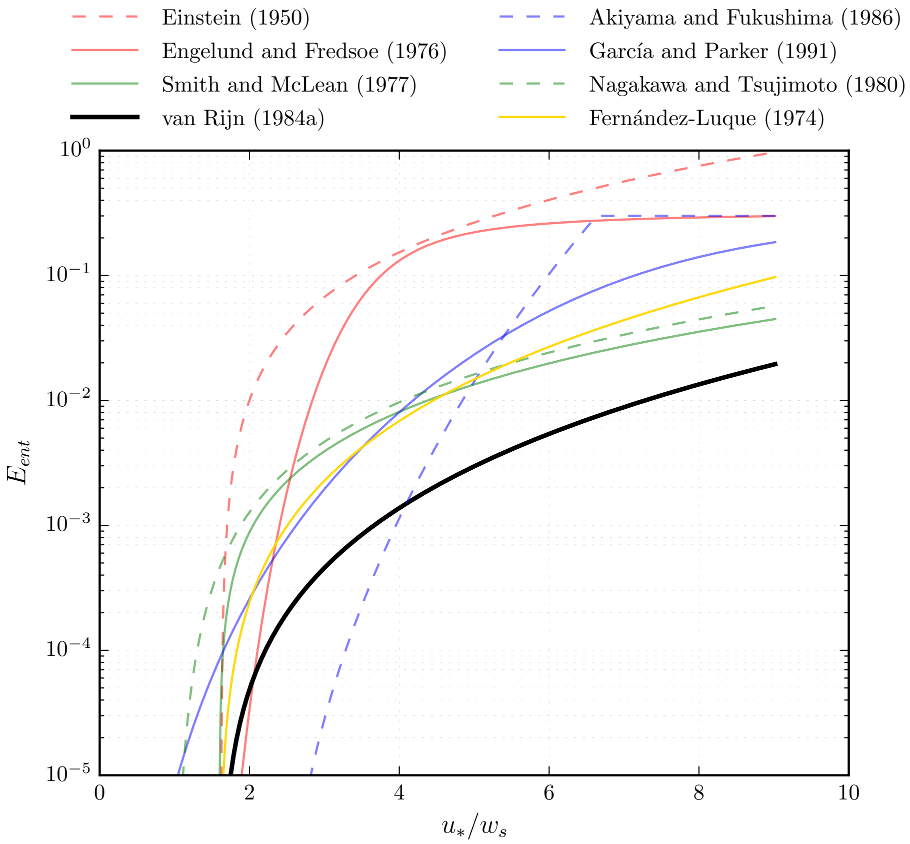

Figure 2.40: Plot of different sediment entrainment into suspension pickup functions (E_{ent}) as a function of dimensionless shear velocity (u_*/w_s). The thick black line of van Rijn (1984c) was the function used here.

It is clear that estimates of sediment entrainment E_{ent} can be quite different depending on which relationship is used. The literature abounds with apparently conflicting relations for predicting the entrainment rate of noncohesive bed sediment into suspension. After a review of various relations we decided to use the formulation of van Rijn (1984c). It was found to perform best against a set of experimental data of direct measurements by Garcia and Parker (1991).

It is worthwhile to note that model results indicated that the adopted formulation was not crucial for the long-term simulation of the channel profiles. A qualitative general tendency was reproduced regardless the employed formulation of E_{ent}. The only differences were related to the simulation time. In this sense, $\mathscr{T}_0$, $\mathscr{O}(10^8)$ seconds, is some orders of magnitude larger than the hydrodynamic time scale:

$$\mathscr{T}_h = \frac{2\pi}{\omega^*}, \tag{2.129}$$

where ω^* is the characteristic angular frequency of the tidal wave, and $\mathscr{T}_h$ is $\mathscr{O}(10^4)$ seconds. The condition $\mathscr{T}_0 \gg \mathscr{T}_h$ reveals that morphological developments take place on a time scale several times longer than typical flow changes, which allows for an instantaneous adjustment of the flow to changes in the bottom configuration. In this regard, the employment of one formulation for E_{ent} or another simply multiplies the sediment fluxes between the bed and the flow and accelerates bed-level changes likewise a "morphological acceleration factor" (Roelvink, 2006).

2.4.3 Comparison with field data: application to Punta Umbria ría

We have seen that the equilibrium bed profile os a short tidal channel is essentially controlled by (i) a nearly symmetrical distribution of the tidal flow during flood and ebb phases that leads to an asymptotic vanishing of both the residual difference between erosive and deposition suspended fluxes and of the spatial gradient of bed load fluxes, and (ii) external parameters, such as the degree of channel funneling, the tidal forcing, the initial depth of the tidal channel, and as confirmed by the present contribution, the offshore system dynamics, i.e., plume and the macroscopic characteristics of the continental shelf.

Although it is hard to find data of the temporal evolution of the bed profile of real tidal channels and it is not obvious to determine if a real system is at equilibrium, it is of interest to explore the model results using parameters that scale roughly a natural systems that are thought to be at equilibrium. Here we choose the Punta Umbría ría located in the Southwestern part of the Iberian Peninsula (Spain), facing to the Gulf of Cádiz (Figure 2.41).

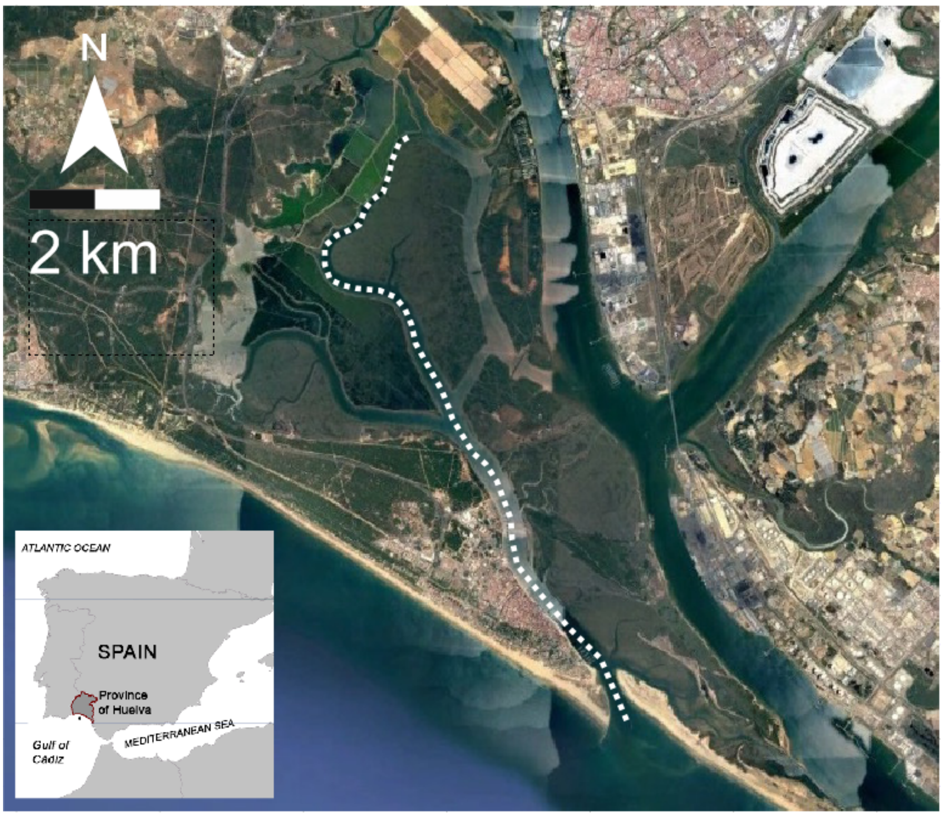

Figure 2.41: Satellite image of the ría of Punta Umbría (Spain) planform, including a longitudinal transect along its main tidal channel [cuortesy of Google Earth].

The digital elevation model of the Spanish Geographic Institution (IGN) along with a detailed multi-beam bathymetry in the Punta Umbría ría supplied by the Regional Government through the Agencia Pública de Puertos de Andalucía (APPA) were used to define the channel profile (Reyes-Merlo, 2016). The nearshore slope in the inlet and surroundings is smooth with values $\leq 1/100$ obtained from the Hydrographic Marine Institute of Spain (IHM). In the inner part of the channel and tidal flats areas the material vary from fine/medium sand, with organic-rich muddy matrix, to medium/very coarse sand (Morales et al., 2014). In the inlet, medium sand ($d_s \sim 250$ μm) dominates. Finer sands are located southwestern to the entrance, changing to coarser material (including gravels) when getting closer to the mouth. The main incoming wave directions are W (43%) and SW (29.2%), while the most common values for the significant wave height are between 0.5 and 1 m, with peak periods from 4 to 6 s. However, the presence of a curved jetty at the entrance of the inlet since mid 80's to ensure safety access to inland ports reduces the impact of waves on the tidal channel dynamics. The estuary is mesotidal and the most energetic tidal constituent is the semidiurnal M_2 (12.42 h). Tidal range varies from 1.1 to 3.2 m during neap and spring tides, respectively. Depth average currents near the mouth vary from 0.9 to 0.6 m/s, depending on ebb/flood phase. The tidal prism in the Punta Umbría ría inlet is $\sim 2 \times 10^7$ m^3 (Reyes-Merlo et al., 2015). The fresh water discharge is not considered in this study, since it represents around 10% of the global estuarine tidal prism in the ría of Huelva (Borrego, 1992).

The main concern is related to the election of the parameters that feed the model. Although the ría planform displays a complex patterns of several tidal channels dissecting the tidal flats, some comparison can be made with the bottom profile of the main tidal channel identified with white transect of Figure 2.41. This tidal channel is 14.2 km long with an approximately mouth width of 200 m, a inner end width of 50 m and a low degree of channel funneling given by a convergence length of 10 km. The tidal range during spring tides of 3.2 m was imposed since it is the most energetic component to shape the channel profile. The bottom is homogeneously composed of fine/medium sand with grain diameter $d_s = 80$ μm that characterizes most of the tidal channel. Regarding the initial depth scale, we use the expression of Toffolon and Lanzoni (2010) that provides a typical morphological scale of the depth at the mouth (d_m) for weak convergent estuaries:

$$d_m \simeq \frac{r_s a_0 \omega}{\sqrt{2} u_{cr,s}} L_e, \tag{2.130}$$

in which r_s accounts for storage effects of tidal flats flanking the channel relating the width of the tidal flat to the width of the tidal channel. In our case, we assume $r_s = 1$. According to this expression, we adopt an initial depth of 6 m.

The model results and its comparison with the measured bottom profile are shown in Figure 2.42. Despite the uncertainties related with the simplifications of the model, the evolution of the bed profile is somewhat similar to that observed in the Punta Umbría ría, even though it displays a more intense erosion in the seaward portion of the channel comprised between $\xi =$ 0.1 and 0.4. We argue that this deviation from the modeled results is related to drainage activities forced to maintain the operability of fisheries and recreational activities distributed along this reach of the channel. In addition, oscillations of the longitudinal bed profile are due to various mesoscale processes, namely, meandering, the presence of junctions, and large-scale bed forms (Lanzoni and Seminara, 2002), which are not accounted for our formulation. The presence of morphological patterns at scales smaller than the estuary length (e.g., bars, dunes, and

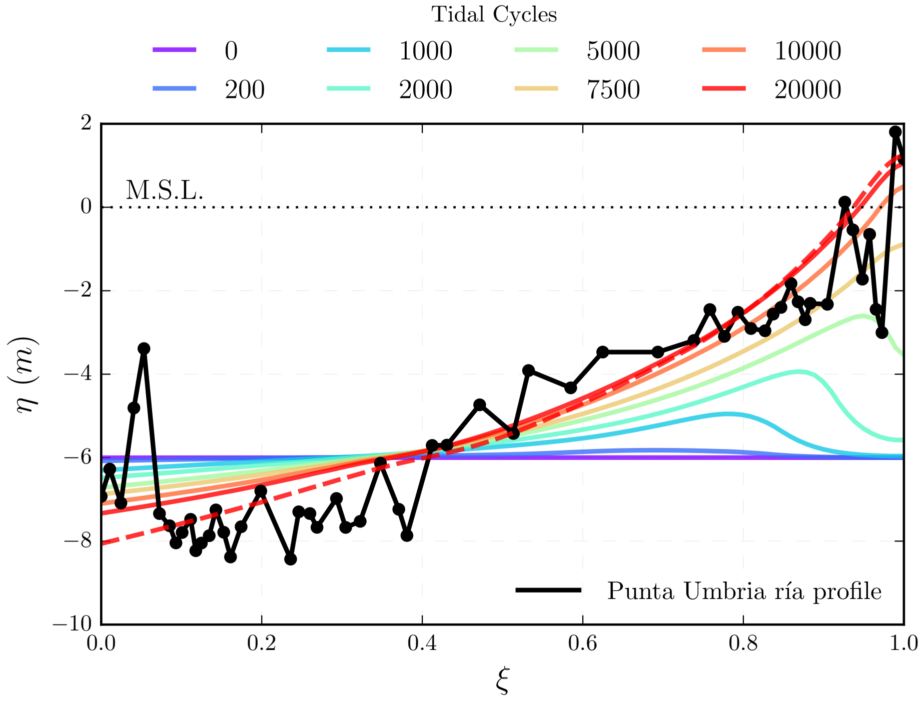

Figure 2.42: Model results of temporal evolution of the bottom profile up to reach an equilibrium configuration (continuos colored lines) and measured bottom elevation along the main tidal channel of the Punta Umbría ría (Huelva, Spain) (thick black line). The dashed red line depicts the equilibrium profile for the case in which the offshore plume influence was neglected. The longitudinal coordinate ξ has been scaled with the channel length. The horizontal dashed lines represents mean sea level (M.S.L.). The values of the relevant parameters imposed to the model are L_e = 15 km, L_b = 10 km, b_0 = 200 m, initial bottom depth $d(t=0) = 6$ m, semidiurnal tide with amplitude a_0 = 1.6 m, mean sediment diameter of $d_s = 80\ \mu$m. The continental shelf is supposed to have a slope m_b = 1% and a mean Chezy coefficient $C_z = 55$ m$^{1/2}$/s.

ripples) on the overall evolution of the tidal channel are considered only through flow conductance formulation. The morphology of the Punta Umbría ría inlet is characterized by a shoaling area resulting from the predominant northwest-to-southeast littoral drift of the zone. This peak in the ría profile is not captured by the model. However, despite these discrepancies, it is worth noting that the final profile seem adequately reproduced in the numerical model. The qualitative agreement between numerical predictions and field data is fairly satisfactory. Finally, the equilibrium profile in the case in which the offshore plume influence was neglected tends to overpredict the scour depth at the inlet, suggesting the importance of considering the exchange of sediments between the tidal channel and the adjacent sea through the offshore plume.

2.4.4 Model limitations

Several approximations are embodied in our numerical model. First of all, a simplified and fixed planform geometry in the absence of significant meanders is employed, an approach widely used in the study of the evolution of tidal channels and estuaries (Lanzoni and Seminara, 2002; Todeschini et al., 2008; Seminara et al., 2010; Toffolon et al., 2006; Bolla Pittaluga et al., 2015; Canestrelli et al., 2014a). Essentially, this approach is based on the observation that variations of bed elevation act at a temporal scale typically much smaller than the time scale of width variations. Besides, storage effects of tidal flats flanking the channel are also neglected. However, their dynamic role is typically small in micro and mesotidal systems simulated here (Savenije and Veling, 2005; Seminara et al., 2010; Toffolon and Lanzoni, 2010).

Moreover, the effects of wave action and fluvial discharge were not accounted for in the present model, whose validity is strictly restricted to estuaries where the tide action is the dominant forcing mechanisms. While the role of riverine discharge can be easily incorporated by feeding the landward boundary with some prescribed freshwater discharge as well as with an empirical equilibrium relations for sediment load as done by Canestrelli et al. (2014a) and Bolla Pittaluga et al. (2015), the waves influence may alter the picture arising from the present work in a more complex way. A first attempt to address this latter effect can be done by modifying plume dynamics in presence of frontal waves taking advantage of previous work on this topic (Ismail and Wiegel, 1983; Nardin et al., 2013). Finally, gravitational circulations driven by salinity and density gradients were not considered in the present framework.

2.5 Concluding Remarks

It is convenient to start this Section answering the first question we raised in the introduction of this chapter: Could the offshore plume appreciably alter the morphodynamic equilibrium of a short tidal channel? The answer is indeed positive. To tackle this question we employed the numerical model of Lanzoni and Seminara (2002) for tidal channels evolution and extended it with the aim of including the influence of their discharge plumes, thereby dynamically coupling the onshore (tidal channel) and offshore (continental shelf) systems. It results in a one-dimensional model in the tidal channel linked to a numerical/analytical 2D model in the oceanic region where the plume is simulated as a jet/sink flow. We observe that sediment and flow exchange between this onshore-offshore systems dictate significant morphologic features both in the tidal channel and in the continental shelf. Our numerical experiments show that the tidal channel bed evolves asymptotically leading to a progressive decrease of the tidal distortion and therefore of the net sediment flux everywhere up to reach an equilibrium state characterized by a concave upwards profile and by a well-defined depth at the inlet section. Such a profile obeys the classical O'Brien-Jarrett-Marchi law. In particular, the cross-sectional area appears to be related to the tidal prism by a power law at different sections along the tidal channels.

As a consequence of the offshore plume the seaward concavity of the profile increases and smaller inlet depths arise. Our results also suggest that this condition can be also attained for tidal channels as the convergence length decreases. Thus, in the presence of a plume, a tidal channel can attain a concave profile with a less stronger degree of convergence (i.e., higher values of the convergence length). Simulations also indicate that larger tidal amplitude implies a larger scour at the tidal channel mouth and a more pronounced bottom channel slope. The feedback between channel and plume also makes the plume reduce its velocity, width and sediment concentration over time, which in turn reduces the net erosion/deposition of material in the continental shelf and the consequent ability for tidal channel to form mouth bars. Other external factors of the continental shelf, mainly the bottom slope and the eroded material, substantially alter equilibrium scenario and the plume structure. The effect of higher slopes of the continental shelf and the material coming from its bottom is to induce bed aggradation in the region of the tidal channel close to the inlet. On the contrary, the bottom friction of the continental shelf has little influence on the tidal channel evolution. We argued that it is due to the inability of the sink model to consider friction effects in the adjacent sea.

A simplified approach of the tide-dominated estuary and plume dynamics allows long-term simulations with an acceptable computational effort thanks to the usage of a reliable and suitably simplified formulation of the most relevant hydrodynamics and morphological processes responsible for describing the offshore plume and shaping the tidal channel. The inclusion of the advection-diffusion equation to calculate the suspended sediment concentration allows the transference of material between the tidal channel and the offshore region. Solutions of this equation indicate that concentration patterns inside the channel tends to equilibrium, being characterized by a increase of the concentration in the landward direction, reaching a maximum around $\xi = 0.8$. The influence of the different mechanism responsible for sediment concentration distribution also attaches an equilibrium distribution along the channel. While the influence of the diffusive mechanism is negligible (only have a certain degree of influence ∼2% close to the landward boundary), the main mechanism in importance is the erosion-deposition (relative influence of ∼80%). Its influence decreases in the landward direction, reaching a maximum around $\xi = 0.8$, beyond which start to increase. An inverse trend is followed by the advective mechanism, with a mean relative influence of ∼20%. Needless to say, as argued in Section 2.4.2, the entrainment of sediment into suspension formulation may alter this latter scenario.

Despite the simplified forcings and idealized geometrical configuration adopted in our model, it is remarkable the qualitative agreement between predicted real tidal channel profiles. This fact suggest that this kind of model can be used to gain some clarification about the general tendency of much more complex natural systems subject to land subsidence, sea level rise, tectonic uplift, and man-made interventions as dredging of tidal channels essential to navigation.

Chapter 3

How do intense storms affect the resilience of coastal bays?

Coastal bays host productive ecosystems, coastal communities and critical infrastructure. As sea level continues to rise and tropical cyclones and other storms increase in intensity, these coastal systems are increasingly at risk for destruction. Developing a sediment budget for coastal bays is imperative to understanding how storm events affect the resilience of the system, where net import of sediment indicates growth and resilience against sea level rise, and net export of sediment indicates deterioration. Using high resolution numerical simulations, here we show that intense storms import sediment into a system of bays in Virginia, USA. Duration and magnitude of storm surge are among the most important factors in sediment import, suggesting that intense storms increase the stability of coastal bays by providing the sediment necessary to counteract sea level rise. Given that climate models project that tropical cyclones will increase in intensity in coming decades, our results have significant implications for the resilience of coastal bays and the future of coastal communities.

3.1 Introduction

Coastal bay systems and barrier island shorelines provide a variety of ecosystem services and play an integral role in protecting coastal communities from flooding and other destruction associated with hurricanes and noreasters (Barbier et al., 2011). Coastal communities are growing increasingly more vulnerable to flooding from tropical cyclones due to increases in sea level rise (Woodruff et al., 2013), and continuing greenhouse gas-forced warming may augment the intensity and frequency of tropical cyclones (Sobel et al., 2016; Walsh et al., 2016). Because of sea level rise, coastal bays must trap sediments so that tidal flats and salt marshes can accrete and maintain the same elevation with respect to mean sea level (Fagherazzi et al., 2013). Developing a sediment budget for these coastal bays is imperative to understanding how storm events affect the resilience of the system, where net import of sediment indicates growth of the system and net export of sediment indicates deterioration (Ganju et al., 2015). In this study, we explore the sediment fluxes into and out of the coastal bays of the Virginia Coast Reserve (VCR) during storms.

The Virginia Coast Reserve consists of a system of barrier islands, salt marshes, and coastal bays along the Atlantic side of the Delmarva Peninsula, USA (Figure 3.1). Previous research on VCR salt marshes has included quantifying the main contributors to salt marsh erosion, a major threat to marsh ecosystem services. Though wave action is the main contributor to erosion (Fagherazzi and Wiberg, 2009; Mariotti et al., 2010; McLoughlin et al., 2015), vegetation changes and invertebrate burrowing also play a large role (Thomas and Blum, 2010). Previous geomor-

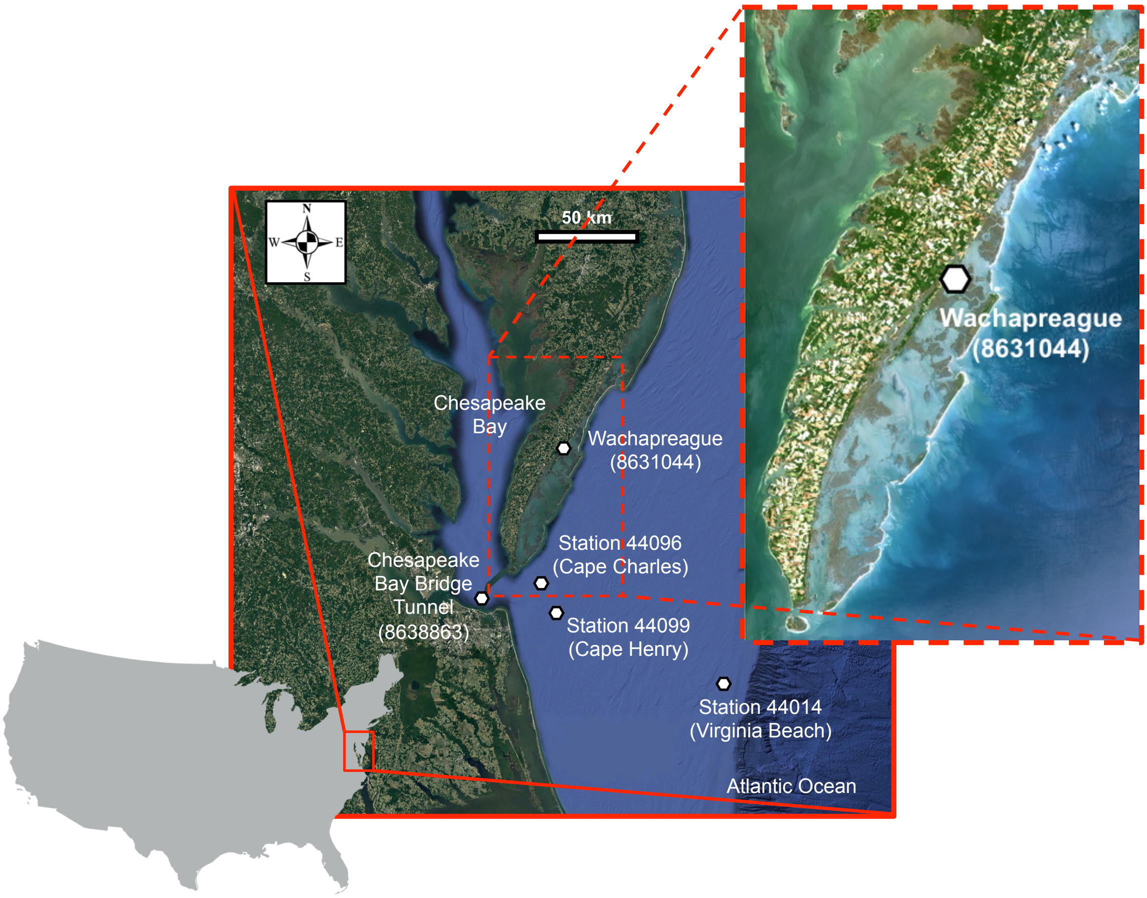
N
W
E
S
50 km
Chesapeake Bay
Wachapreague (8631044)
Station 44096 (Cape Charles)
Chesapeake Bay Bridge Tunnel (8638863)
Station 44099 (Cape Henry)
Station 44014 (Virginia Beach)
Atlantic Ocean
Wachapreague (8631044)

Figure 3.1: Location map for the southern Delmarva Peninsula, bounded by Chesapeake Bay to the west and the Atlantic Ocean to the east (USA). The Virginia Coast Reserve (VCR) comprises the barrier islands, bays and marshes on the eastern side of the southern (Virginia portion) of the Delmarva Peninsula. Also shown are the locations of the different stations used in this worl.

phic modeling in this location has focused on developing numerical models for marsh evolution (Mariotti and Fagherazzi, 2010; Fagherazzi et al., 2012), detailing how waves shape marsh form and function (Leonardi and Fagherazzi, 2014, 2015), and quantifying how barrier islands and marshes interact (Walters et al., 2014; Deaton et al., 2017). Given the robust nature of previous research in the VCR, it is an ideal location to formulate a sediment budget to determine the resilience of coastal bays in the face of sea level rise and increasing storminess.

3.2 Methodology

3.2.1 Numerical model

Hydrodynamic and sediment-transport simulations were conducted using the high-resolution, fluid dynamics model Delft3D-FLOW (Lesser et al., 2004) and the Delft3D-WAVE module, which is based on the SWAN (Simulating WAves Nearshore) wind wave generation and propagation model (Booij et al., 1999). This coupled system is suitable for simulating nonsteady flows, wave generation and propagation, sediment transport phenomena, and related morphological developments in a coupled modality in shallow seas, coastal areas, estuaries, lagoons, rivers and lakes.

In this study, Delft3D-FLOW solves the shallow water equations derived from the three-dimensional Reynolds-averaged NavierStokes equations for continuity and horizontal momentum for unsteady, incompressible, turbulent flows. The vertical momentum equation is reduced to the hydrostatic pressure relation, so vertical accelerations are assumed to be small compared to gravitational acceleration and are neglected. The modification of these equations due to the wave forces for a wave-current interaction is achieved by an online-coupling of FLOW and WAVE modules at a regular interval of 60 minutes. It allows us to account for the effects of waves on the flow and to provide flow boundary conditions for the wave transformation. Delft3D-WAVE is a spectral wave model which solves the wave action balance equation and accounts for refraction, shoaling, blocking and reflections due to opposing currents, wind wave generation, whitecapping, depth-induced wave breaking, bottom friction, and nonlinear wavewave interactions.

For the sediment transport computations, the Van Rijn et al. (2001) approach is followed for the transport of non-cohesive sediment while cohesive transport is calculated through the advectiondiffusion equation with erosion and deposition terms based on the formulation of Partheniades et al. (1965). Spatial gradients in bed load transport and the source and sink terms associated with suspended sediment fluxes ultimately determine changes in bed bathymetry through the Exner equation (Paola and Voller, 2005).

3.2.2 Model setup

The model domain for simulating the storm events that took place in the shallow lagoons system of the Virginia Coast Reserve during the period from 2009 to 2016 consists of two grids for the wave propagation and a third grid for the hydrodynamic and morphodynamic computations (Figure 3.2). The elevations of the grid nodes within the shallow lagoons system were interpolated from existing Digital Elevation Models datasets used in previous modeling studies (Wiberg et al., 2015). This bathymetry was merged with grids and map images from multibeam bathymetry data from the NCEI (National Centers for Environmental Information) in order to extend the offshore area of the computation domain up to the higher WAVE grids limits.

Two different grids configurations were defined depending on wave data availability (see Table 3.1). For the wave modeling, a system of two nested grids was used to simulate the wave generation and propagation (Figure 3.2). The first grid is a curvilinear coarse grid wave domain with cell sizes that decrease with decreasing depth and that covers the lagoons system area and extends up to the location of the NOAA 44014 wave buoy, 64 NM East of Virginia Beach, VA (162×324 computational cells), or up to the location of the NOAA 44099 wave station, Cape Henry, VA (54×324 computational cells) when no data from the Virginia Beach station are available. The second grid is a nested quadrangular grid covering the lagoons area with 105×376 cells with a 250 m constant resolution over the whole domain. For the spectral resolution of the frequency space, 24 wave frequency bins ranging from 0.05 to 1 Hz were used, whereas for the directional space, 36 directions were defined. The offshore wave conditions of the corresponding NOAA wave station for the storm period are imposed using a JONSWAP wave spectrum along the offshore boundary. Finally, to homogenize analysis of the results of different simulations, the maximum wave height during each simulation was determined using simulated data at the offshore NOAA station 44096, Cape Charles, VA.

The numerical grid used for the FLOW module had the same propertied than the nested grid used in WAVE. Two different values of the Chezy roughness coefficient are used: 65 $m^{1/2}s^{-1}$ for

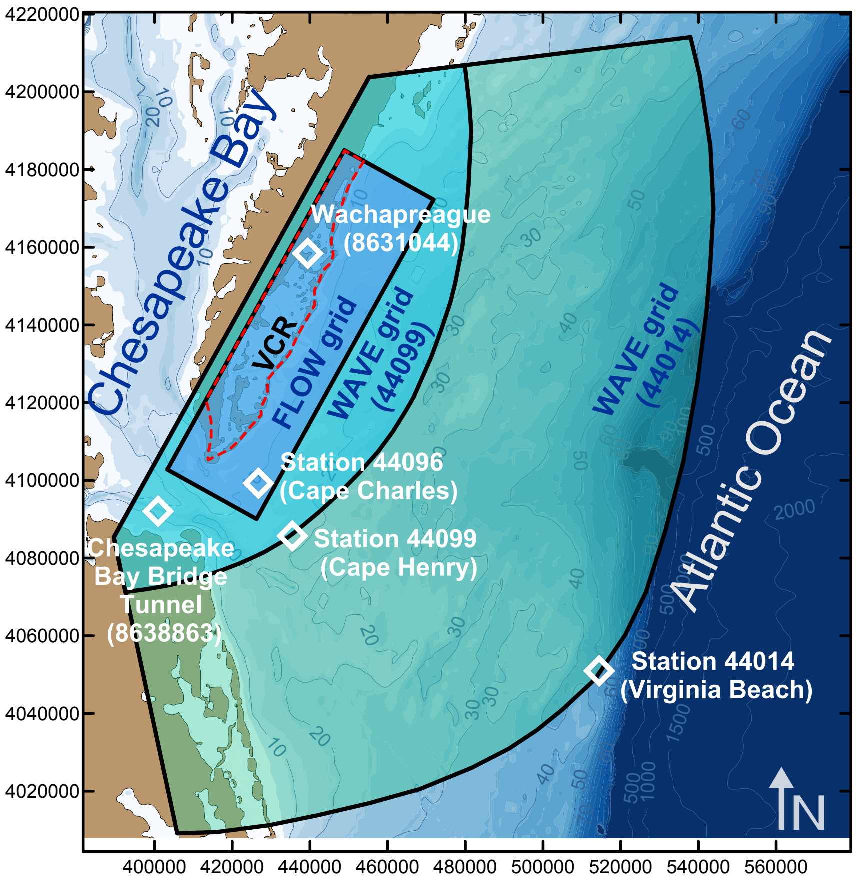
4220000
4200000
4180000
4160000
4140000
4120000
4100000
4080000
4060000
4040000
4020000
400000
420000
440000
460000
480000
500000
520000
540000
560000
Chesapeake Bay
Wachapreague
(8631044)
VCR
FLOW grid
WAVE grid
(44099)
WAVE grid
(44014)
Station 44096
(Cape Charles)
Station 44099
(Cape Henry)
Chesapeake
Bay Bridge
Tunnel
(8638863)
Atlantic Ocean
Station 44014
(Virginia Beach)
N

Figure 3.2: Shaded-relief bathymetry of the study area, comprising the VCR coastal bays system, indicating the location of the grids used in the numerical model and the location of the different stations. The bathymetric contours are given in meters below the present sea level. The red dashed line delimits the control volume for the computation of the sediment budget of the VCR lagoons.

the tidal flats, channels and the seaward of the barrier islands, and 45 $m^{1/2}s^{-1}$ for the barrier island and salt marshes due to the different vegetation cover. The water level is imposed at the southern, northern and seaward open boundaries. It was set equal to the water level measured at Wachapreague, VA-Station (ID: 8631044) (see Figure 3.2) with a phase shift and an amplitude correction to account for tidal propagation and dissipation in the domain. During the first 3 storms water level data were not measured at Wachapreage Station. Thus, an analog downscaling technique trained with data from the close Chesapeake Bay Bridge Tunnel, VA - Station (ID: 8638863) was applied to derive water levels at Wachapreague Station (Vanvyve et al., 2015). The model was forced with a spatially uniform wind data taken from Wachapreague, VA-Station (ID: 8631044) and was extended to the WAVE's grids. According to the work of Mariotti et al. (2010) in this system of shallow lagoons in VCR, assuming a uniform wind field is acceptable, particularly in stormy conditions.

The bottom consists of an initial sediment distribution of three grain sizes constant with depth and 10 m thick and enabling no restrictions on morphological changes. A bed stratigraphy model containing 3 layers of constant porosity equal to 0.7 tracks the sediment distribution during the storm event. The topmost active layer of 5 cm thickness guarantees stability of results by affecting the availability of sediment for erosion during every time step computation. Initial sediment distribution throughout the FLOW domain and sediment properties were taken from Wiberg et al. (2015) and Fenster et al. (2016). While high-resolution maps of bottom sediment size distributions established by Wiberg et al. (2015) where used within the bays of the VCR, nearshore bottom samples of Fenster et al. (2016) were imposed in the offshore region (Figure 3.3). A non-cohesive sand fraction with a median grain diameter of 125 μm (sand) and two cohesive mud fractions of 20 μm (very fine mud) and 63 μm (mud) compose the bottom stratigraphy. While both cohesive species shares the same shear stress for erosion (0.04 Nm^{-2}) and the erosion parameter for the Partheniades-Krone formulation (10^{-5} kg/m^2s), a settling velocity of 3.6 mm/s for the 63 μm and 0.75 mm/s for the 20 μm species was specified. Delft3D internally calculates the settling velocity for sand. Finally, a critical shear stress for deposition equal to 1000 Nm^{-2} was chosen to avoid mutually exclusive erosion and deposition processes (Edmonds and Slingerland, 2010). At the start of each simulation, mud fractions of 20 μm was primarily distributed closer to the mainland. Sand (125 μm) was primarily distributed closer to the inlets and the tidal flats. Mud fraction of 63 μm was relatively evenly distributed throughout the system.

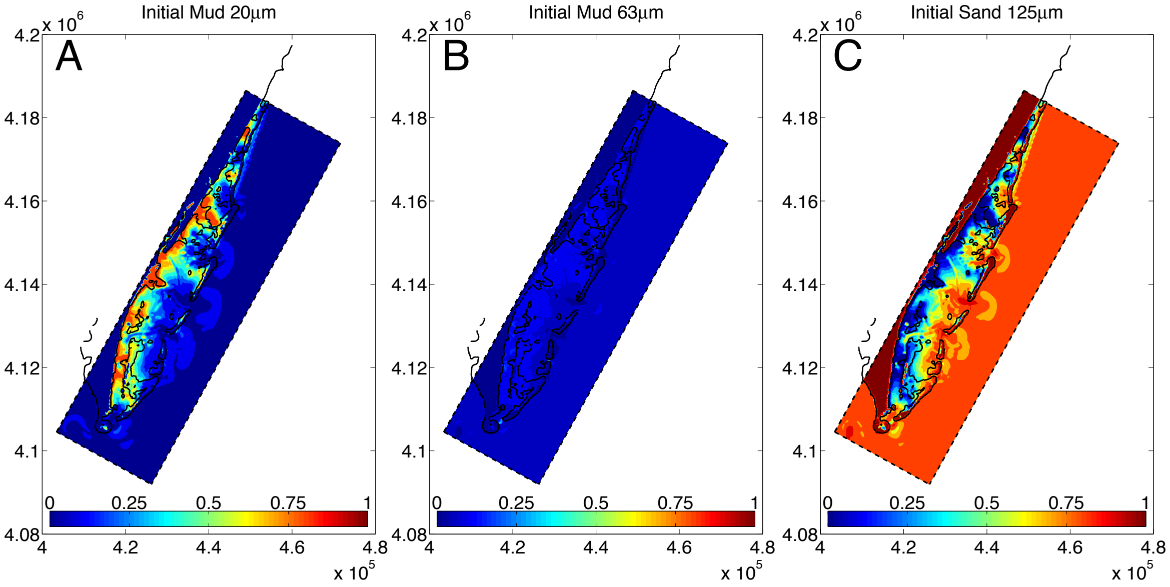

Figure 3.3: Sediment bottom composition in the VCR coastal bays system. Spatial distribution of (a) very fine mud 20μm, (b) mud 63μm, and (c) sand 125μm. Scale is the proportion of the type of sediment, derived from Wiberg et al. (2015) and Fenster et al. (2016). Black lines represent the water-land boundary.

3.2.3 Model calibration

The Delft3D WAVE module was calibrated for storm number 40 by comparing wave height and wave direction results to field data of NOAA station 44096, Cape Charles, VA (see Figure 3.2), the closest wave station to the VCR shallow lagoons. Storm number 40 (from 28-feb-2014 22.00 to 11-mar-2014 07:00) is an event long enough and characterized by an important variability in wave and water level conditions, permitting us to evaluate the efficiency of the model under different conditions.

The coherence between the computed and measured data was analyzed in terms of the Model Efficiency (ME, which measures the ratio of the model error to variability in observational data, equation (3.1)), root-mean square error (RMSE, equation (3.2)), the correlation coefficient (R, which ranges from 0 (bad correlation) to 1 (good correlation), equation (3.3)), and the model performance (skill S, which ranges from 0 (bad skill) to 1 (good skill), equation (3.4)), as in previous calibration tasks (Mariotti et al., 2010; Olabarrieta et al., 2011). Considering that M_n and D_n are the measured data and the simulated data with Delft3D, respectively, at N discrete points, these statistics are given by:

$$ME = 1 - \frac{\sum_{n=1}^{N}(M_n - D_n)^2}{\sum_{n=1}^{N}(M_n - \overline{M_n})^2} \tag{3.1}$$

$$RMSE = \sqrt{\frac{1}{N}\sum_{n=1}^{N}(M_n - D_n)^2} \tag{3.2}$$

$$R = \frac{1}{N\sigma_M\sigma_D}\sum_{n=1}^{N}(M_n - \overline{M_n})(D_n - \overline{D_n}) \tag{3.3}$$

$$S = 1 - \frac{\sum_{n=1}^{N}|D_n - M_n|^2}{\sum_{n=1}^{N}\left(|D_n - \overline{M_n}|^2 + |M_n - \overline{M_n}|^2\right)} \tag{3.4}$$

In these expressions the overbar represents the mean value, and σ_M and σ_D are the standard deviations of the measured and simulated data respectively.

An excellent agreement between simulated and measured wave height (ME = 0.8475, RMSE = 0.3000 m, R = 0.9269, S = 0.9113) was achieved by modifying some of the parameters that define the physical processes simulated (i.e., directional spreading, bottom friction formulation, bottom friction coefficient and non-linear triad interactions parameters) (Figure 3.4 (a)). The agreement between computed and measured wave directions showed a bigger discrepancy (ME = -0.3359, RMSE = 20.7374°, R = 0.5884, S = 0.4224) (Figure 3.4 (b)). We argue that this disagreement can be caused by some simplifications introduced in the input-data, since we are assuming a spatially uniform wind field over the entire domain and the bathymetry outside the lagoons was not as accurate as the one inside them.

Finally, Delft3D-FLOW performing was evaluated by adjusting the water level forcing (both phase and amplitude) at the southern, northern and seaward open boundaries in order to obtain the measured water levels at Wachapreague station. A really good agreement both in tidal amplitude and tidal phase was obtained (ME = 0.9814, RMSE = 0.0624 m, R = 0.9943, S = 0.9898) imposing a water level signal shifted by a lag time of -54 min and dampened by a factor of 88% (Figure 3.5). Thus, the dynamic inside the the shallow water lagoon system can be assumed to be properly simulated since the main agent governing it (tidal forcing) is satisfactory recreated by the numerical model.

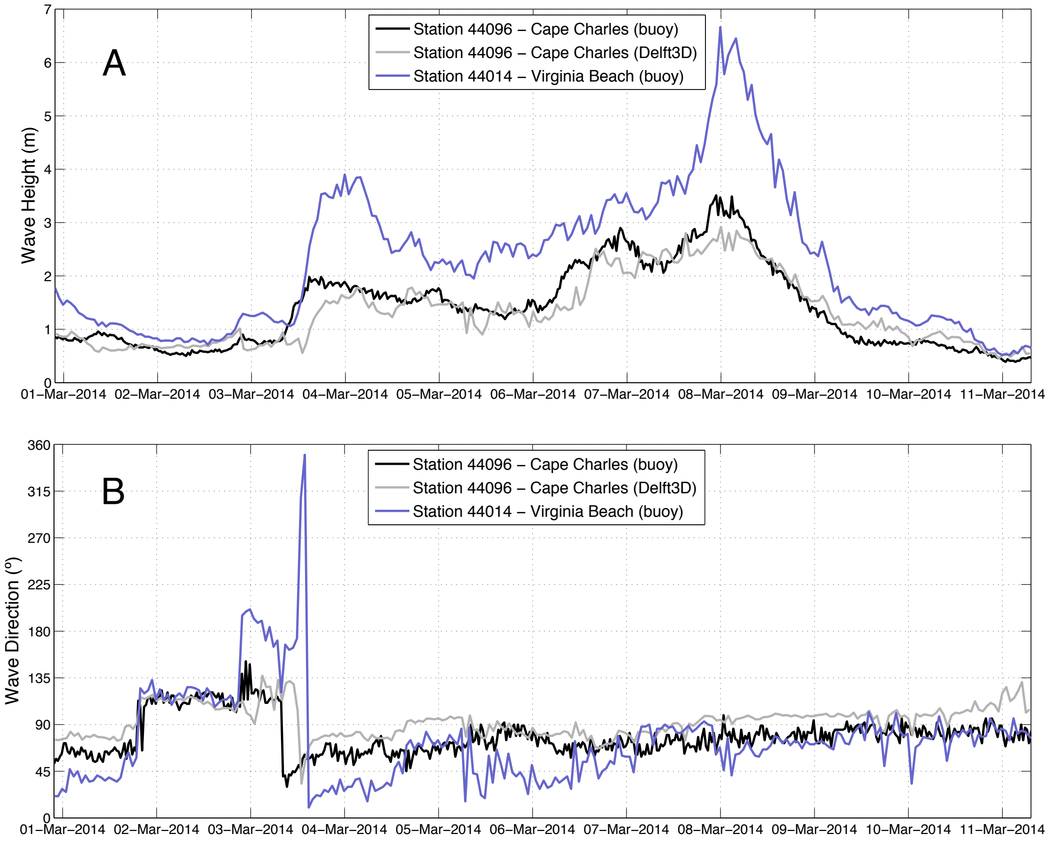

Figure 3.4: Comparison of the computed (grey) and measured (black) (a) wave height and (b) wave direction at the location of the station 44096 - Cape Charles NOAA during the storm number 40. Blue lines indicate the wave conditions imposed at the boundary of the WAVE domain and collected by the station 44014 - Virginia Beach NOAA.

3.2.4 Storms definition

During the period between 1 January 2009 and 31 December 2015 a total of 52 storm events where identified through the Peaks Over Threshold (POT) method using wind data from Wachapreague station (Figure 3.6 (a)). The choice of the wind speed threshold constitutes a critical issue for the extreme value analysis with a threshold-based approach. In this study we use 11 m/s as wind speed threshold and a minimum distance between events of 5 days in order to guarantee independent events. This wind speed threshold value corresponds to the lower limit of a strong breeze according to the Beaufort wind scale. Besides, it is consistent with the selected value based on the use of Anderson-Darling EDF-statistic and goodness of fit test (Solari et al., 2017).

Once the 52 storms were identified, the duration of every storm to be simulated was determined on the basis of the storm surge recorded at Chesapeake Bay Bridge Tunnel, VA Station (ID: 8638863), the closest station located offshore the lagoons to avoid the generation of additional overharmonics. We defined as storm a period with at least one wind measurement above 11m/s confined before and after by four tides with a storm surge value below 0.2 m (Figure 3.6 (b)). Beginning and end dates for every storm are presented in Table 3.1, together with time of wind peak, water level station and buoy for wave data.

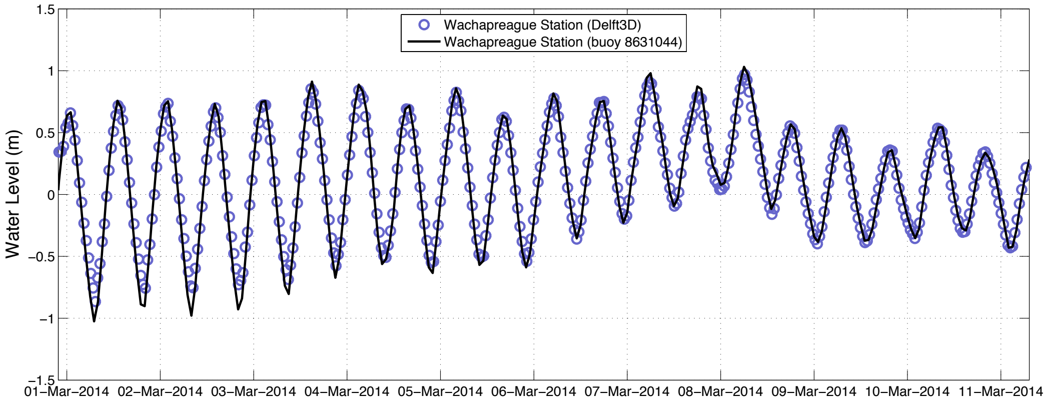

Figure 3.5: Comparison of the simulated with Delft3D (grey circles) and measured (black line) water levels at Wachapreague station (ID: 8631044), Virginia.

3.3 Results

The goal of this study was to determine the sediment budget of the VCR lagoons during large storm events, as well as to determine the storm characteristics that most influence the sediment budget. Per Ganju et al. (2017) a sediment budget was developed for each storm to determine resilience of the system and to determine how this system responds to storm events. Using high-resolution maps of bottom sediment size distributions within and offshore the bays of the VCR established by Wiberg et al. (2015) and Fenster et al. (2016) respectively (Figure 3.3), sediment resuspension and flux were modeled for each storm over a domain that included the full VCR and adjacent coastal ocean.

Trends in cumulative sediment flux were analyzed for relationships with a variety of parameters, including wind speed, wave height, storm surge, and wind direction. Analysis focused primarily on wind direction, wind speed, wave height, and storm surge, as well as the time each storm was above a given threshold of each parameter.

Wind direction was not found to significantly influence sediment flux, likely due to its high variability during each storm. 16 additional simulations were carried out in order to evaluate the influence of the wind direction on the sediment budget. These simulations were forced by the only influence of a wind of constant wind speed (11 m/s) and direction, which value was modified between simulations (0°, 30°, 45°, 60°, 90°, 120°, 135°, 150°, 180°, 210°, 225°, 240°, 270°, 300°, 315°, 330°, and 360°), neglecting the effects of the remaining parameters (waves, tides or wind variability). The wind direction is defined according to the nautical definition, i.e. relative to true North and positive measured clockwise, i.e., a wind direction of +60° is equivalent to an East-North-East wind. Results of the sediment budget after 15 days simulations are reported in Figure 3.7. It is observed that winds between 60° and 240° tend to incorporate sediments into the VCR system. These directions corresponds to winds blowing towards the bays inlets. However, wind direction does not display statistically significant relationship ($R^2 = 0.1030$, $p \nless 0.001$) with cumulative sediment flux during a storm events (Figure 3.8), since the total hours that during a storm event the wind has a direction between 60° and 240° is not revealed as a reliable proof that sediment enters the VCR system.

After discarding wind direction as a key parameter capable of dictating sediment budget behavior, due to its high variability during storm periods, trends in sediment dynamics, including (1) deposition and erosion areas and (2) bottom sediment composition were also analyzed in terms of wind speed, wave height and storm surge.

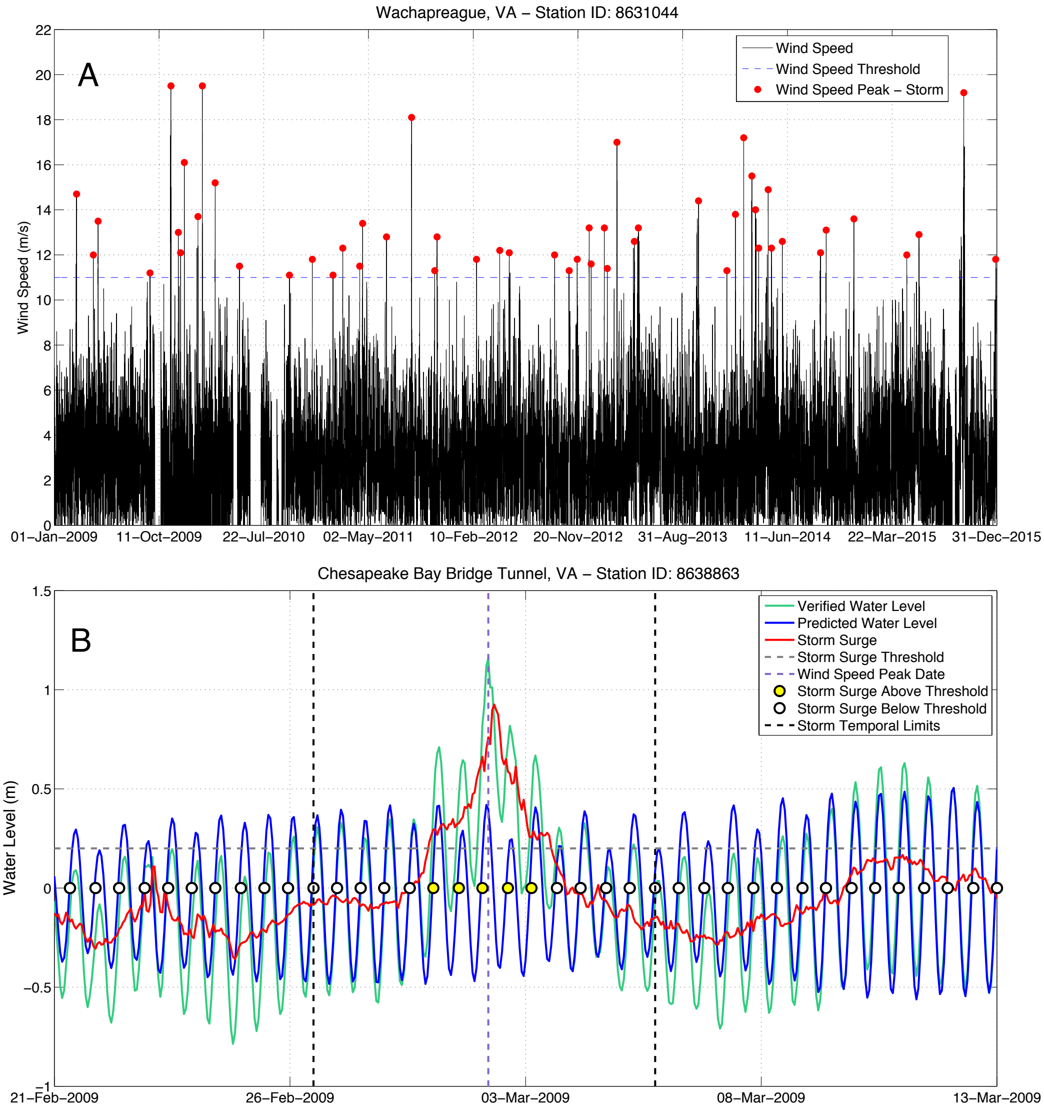

Figure 3.6: (a) Peaks Over Threshold (POT) analysis for wind speed. Only events with a wind speed above 11 m/s and a minimum distance between events of 5 days were considered as storms. (b) Example of identification of the storm number 1 period. The storm begins (ends) before (after) four full tides with a storm surge below 0.2 m with respect to the wind peak time.

3.3.1 Cumulative sediment flux in a storm event

Maximum wind speed, wave height, and storm surge displayed statistically significant negative relationships with cumulative sediment flux (Figure 3.9). This suggests that there is increased sediment accumulation in the study region as each parameter increases in intensity. A multiple regression analysis of the three variables indicates that storm surge is contributing the most to the relationship (p <0.001).

Cumulative sediment flux also displayed statistically significant negative relationships with the amount of time each parameter remained over the following thresholds: wave height > 2 m, wind speed > 10 m/s, and storm surge > 0.5 m (Figure 3.10). Relationships were determined using the product of the total time over the threshold and the magnitude of the corresponding variable for each storm. The product of magnitude and duration of storm surge over 0.5m alone

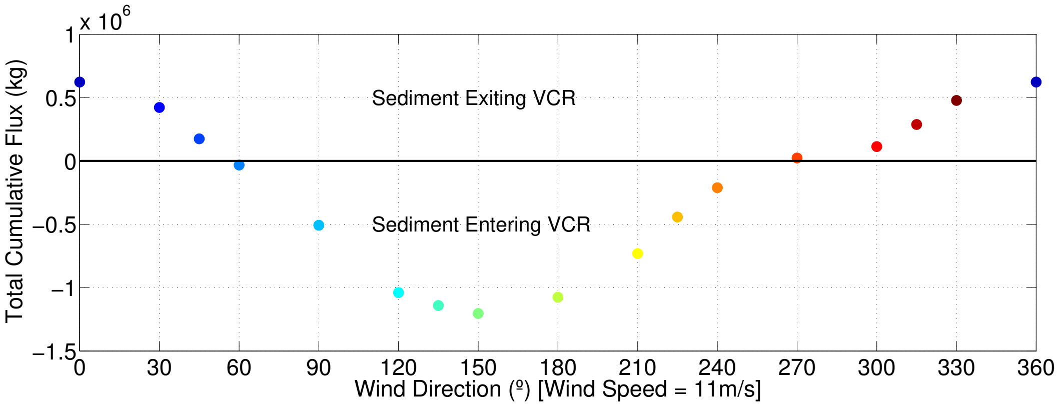

Figure 3.7: Total cumulative flux as a function of wind direction. Wind speed was 11 m/s and the simulation time was 15 days. Negative values of the total cumulative flux (sediment budget) indicated sediments entering the VCR.

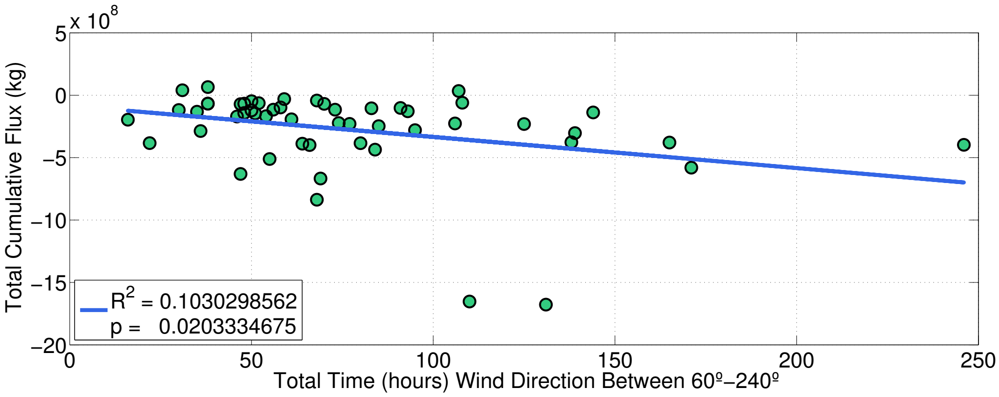

Figure 3.8: Relationship between total cumulative flux and the amount of of hours that wind directions is between 60° to 240° during a storm event. There is a negative total cumulative flux (net accumulation of sediment into the system) as total hours during which wind blows from 60° to 240° increase.

explains the most of the variance in cumulative sediment flux. A multiple regression analysis of the three variables indicates that, similarly, storm surge threshold is contributing the most to the relationship (p <0.001). As a result, the influence of the storm surge, particularly its duration and magnitude, seems to be critical for the sediment budget of the lagoon.

More intense storms, regardless of wind direction, tend to cause more sediment accumulation. Averaging sediment accumulation and erosion spatially over all 52 storms, a relationship of deposition to erosion areas within the VCR system equal to 1.3626 is obtained, which shows that storms favors bottom accretion. Sediment accumulation is concentrated at the mouth of inlets and continues into the bays behind the inlets, further emphasizing the importance of the entire coastal system. Erosion is focused largely along the ocean-side edges of the barrier islands, and sediment is largely accumulated on the tidal flats close to the bay inlets (Figure 3.11). Using values for bed porosity consistent with Wiberg et al. (2015), yearly accumulation of sediment within the domain from the modeled storms ranged from 2.01 mm to 5.30 mm.

3.3.2 Sediment dynamics

The bottom sediment composition both inside and outside of the VCR is of great importance to the sediment dynamics during large storms, since sediment can be suspended during these

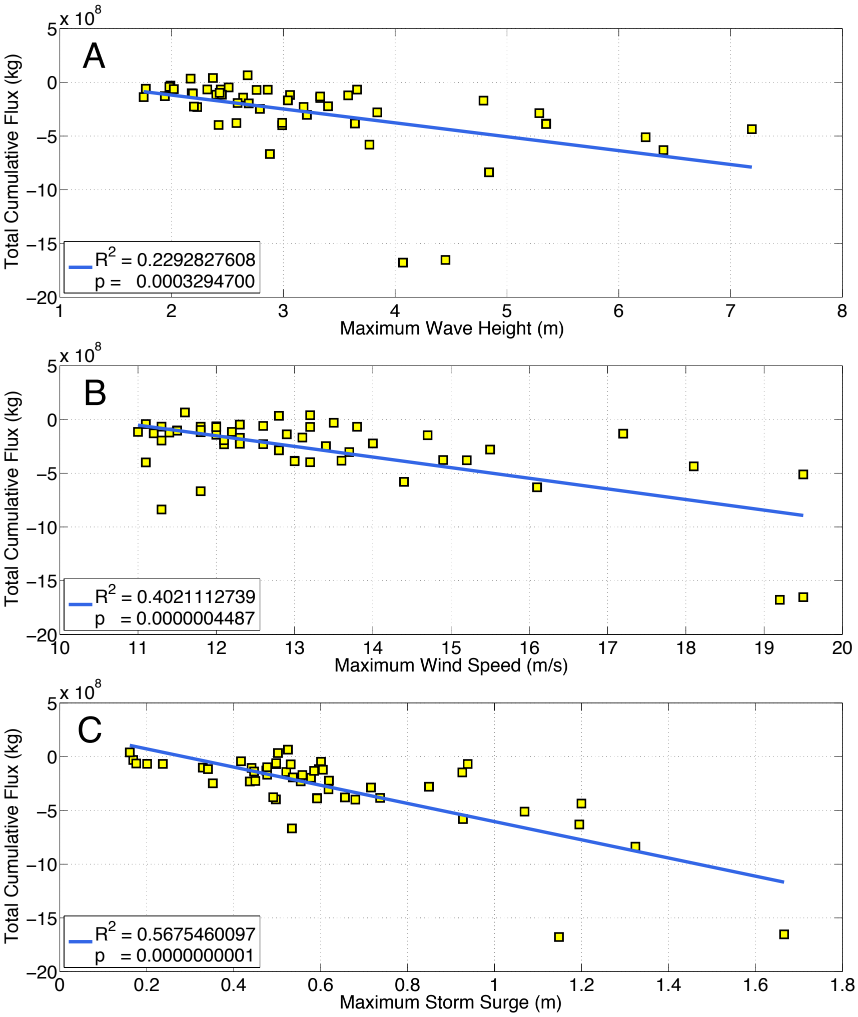

Figure 3.9: Relationship between total cumulative flux and A) maximum wave height, B) maximum wind speed and C) maximum storm surge. There is a negative total cumulative flux (net accumulation of sediment into the system) as all study parameters increase in intensity.

events and funneled into the bays. While the total cumulative flux indicates that more intense storms tend to result in net import of sediment to the study area, this result varies by type of sediment. For all three study parameters, very fine mud and mud (20μm and 63μm, respectively) display the same significant negative relationship with cumulative flux, where increased storm intensity results in increased import of sediment to the study area (Figure 3.12). There is a significant negative relationship between total cumulative flux and intensity of storm surge for very fine mud (20μm) and mud (63μm), indicating net accumulation. It must be observed that the intensity of sediment fluxes of mud 63μm is negligible in comparison with its values for mud 20μm. Sand (125μm), however, tends to be exported from the study area. Almost all storms (96%) exhibited net import of fine sand, regardless of intensity. Therefore, though there is a negative relationship between total cumulative flux and storm surge for sand (125μm), total cumulative flux is predominantly positive, indicating net erosion.

The spatial changes in bottom sediment composition provide insight into the sediment dynamics (Figure 3.13). Following an averaged event for all 52 study storms, very fine mud (20μm) from in front of the inlets is primarily deposited at the inlets, behind the inlets, and along the

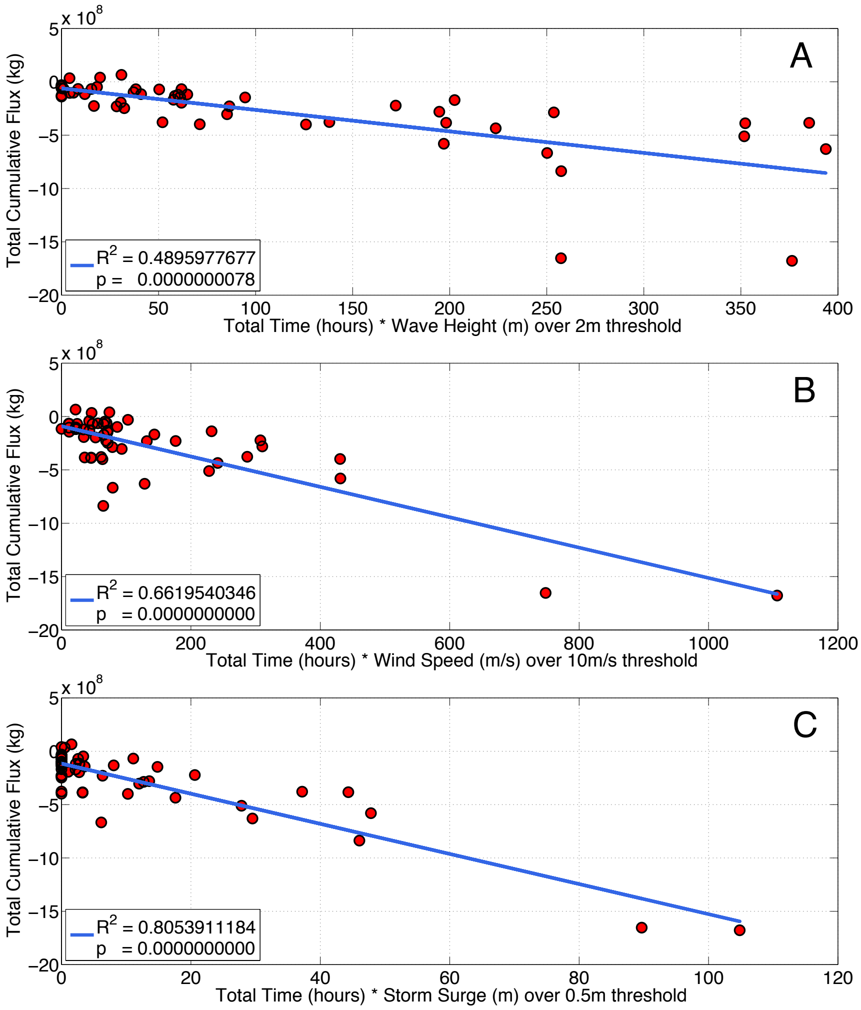

Figure 3.10: Relationship between total cumulative flux and the product between magnitude and duration of A) wave height above 2m B) wind speed above 10 m/s and C) storm surge above 0.5m. There is a negative total cumulative flux (net accumulation of sediment into the system) as all study parameters increase in magnitude and duration.

ocean side of the barrier islands. Mud (63μm) is primarily deposited offshore along the barrier islands. Sand (125μm) is eroded at and behind the inlets, as well as offshore along the barrier islands. Back-barrier marshes experience loss of very fine mud (20 μm) and deposition of mud and sand (63 and 125μm) along their edges.

Using the same duration thresholds as indicated previously, the fraction of sand (125μm) in the model domain consistently decreases its representation within the sediment bed across all study parameters and their respective products of duration and magnitude, whereas the fraction of very fine mud (20μm) in the model domain consistently increases its bed fraction. The sediment bottom composition of mud (63μm) is not correlated with storm surge or wave height duration and magnitude but is weakly positively correlated with wind speed duration and magnitude ($R^2 = 0.24$, $p < 0.001$). After a storm, bottom composition tends to lose sand from the barriers and gain mud from the mouths of the inlets.

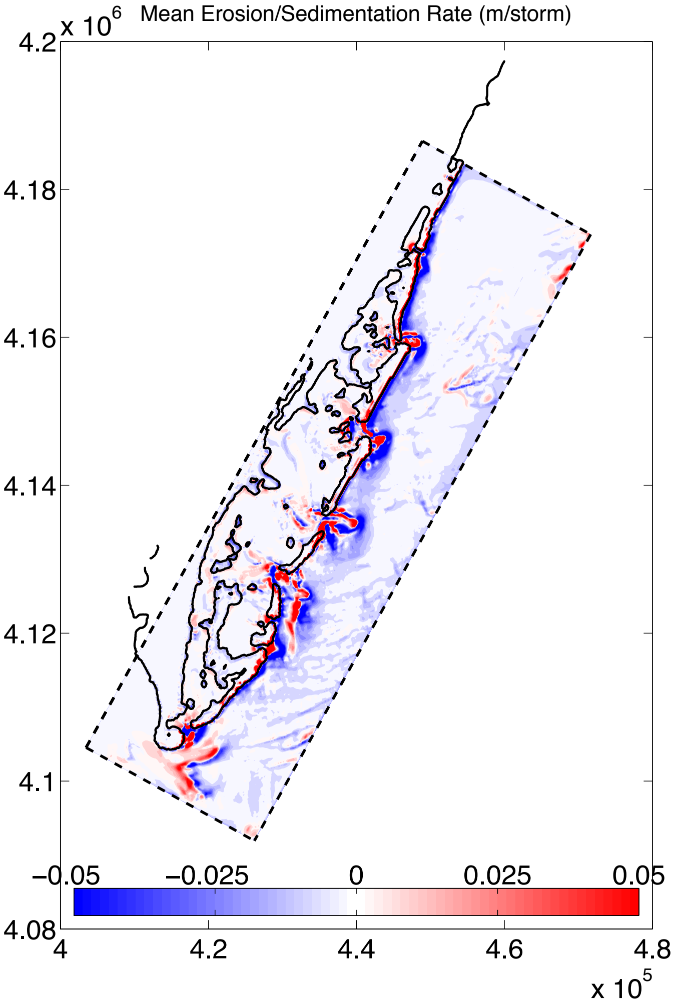

Figure 3.11: Mean cumulative elevation differences in the system for all 52 study storms. Red areas indicate accumulation. Blue areas indicate erosion. Black lines represent the water-land boundary.

3.3.3 Analysis of a specific storm event

A description of a particular storm event (storm number 38, see Table 3.1) is presented in Figure 3.14. It can be observed that the main sediment dynamic changes (Figures 3.14 (E), (F), and (G)) coincide with the most energetic time of this storm event, i.e., when wave height and storm surge reach a peak around 22-jan-2014 03:00 (Figures 3.14 (A) and (D) respectively). Although after this moment sand 125μm exits the VCR system, the total mud (mud 20μm and mud 63μm) is higher and thus, the total cumulative flux increases its intensity significantly and the system incorporates sediment (negative fluxes). We can state that after storm number 38, the VCR system increases its resilience. Firstly, it has consequences on the relation between deposition and erosion areas within the VCR system (Figure 3.6 (E)), i.e., area under accretion is higher than the area under erosion. A second consequence is the cell averaged percent changes on sediment composition. While sand 125μm decreases its mean proportion, bed composition of mud species increases.

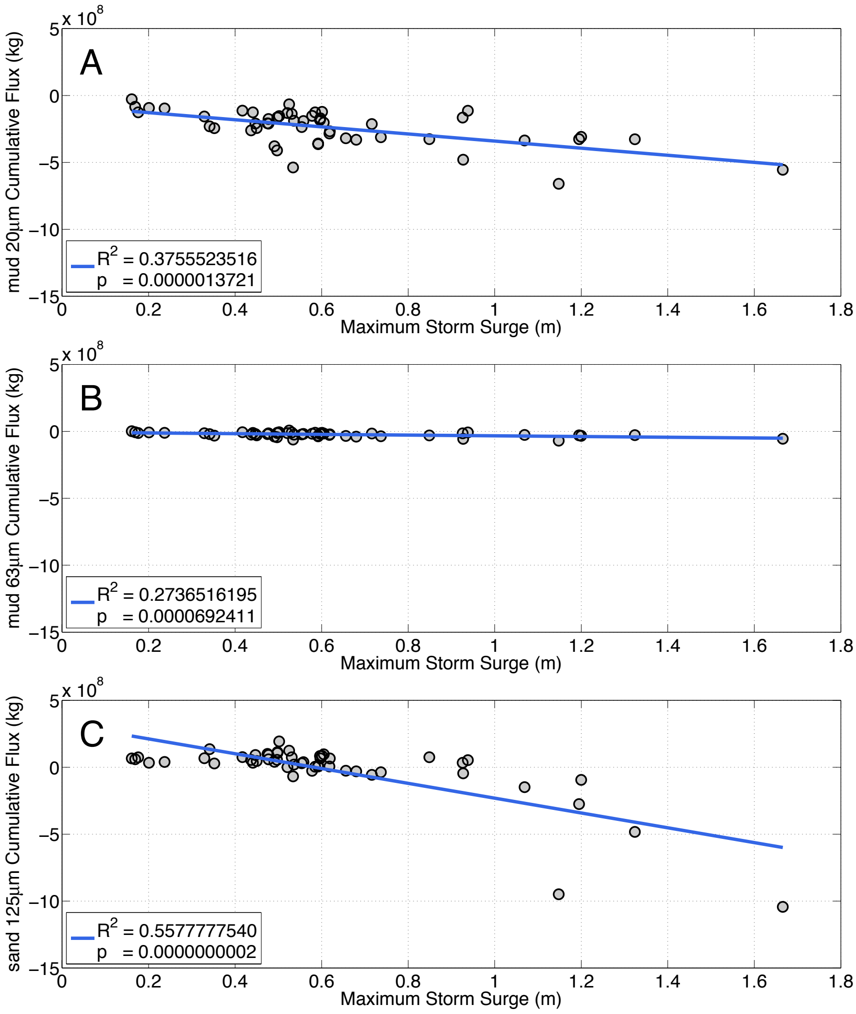

Figure 3.12: Relationship between maximum storm surge and total cumulative flux of A) 20μm very fine mud, B) 63μm mud, and C) 125μm sand. There is a significant negative relationship between total cumulative flux and intensity of storm surge for very fine mud (20μm) and mud (63μm), indicating net accumulation.

3.4 Discussion and conclusion

The duration and amount of storm surge has the most significant influence on the amount of sediment transported during a storm event. The wind and wave energy of a storm surge of sufficient size provides the shear stresses necessary for remobilization of sediment near the inlets and transport into the bay system. Storm surge has long been known to deposit sediment in marshes and bays following large storm events, on both historic and prehistoric timescales (Donnelly et al., 2001; Boldt et al., 2010; Tweel and Turner, 2012; Hodge and Williams, 2016). Here we show that these storms also funnel sediments through the inlets by depositing them in adjacent tidal flats. The system of tidal inlets in the VCR is imperative for the transport of this material, acting as a conduit for the sediment transport. Sediment transported through the inlets is thus available for further remobilization by waves and tides, feeding interior flats and salt marshes. Without a net input of sediment from the inlets, in the absence of riverine inputs, the system would soon deplete the material stored in the tidal flats and would thus be unable to counteract sea level rise in the long run. Our study suggests that a storm surge threshold of 0.5 m or greater is

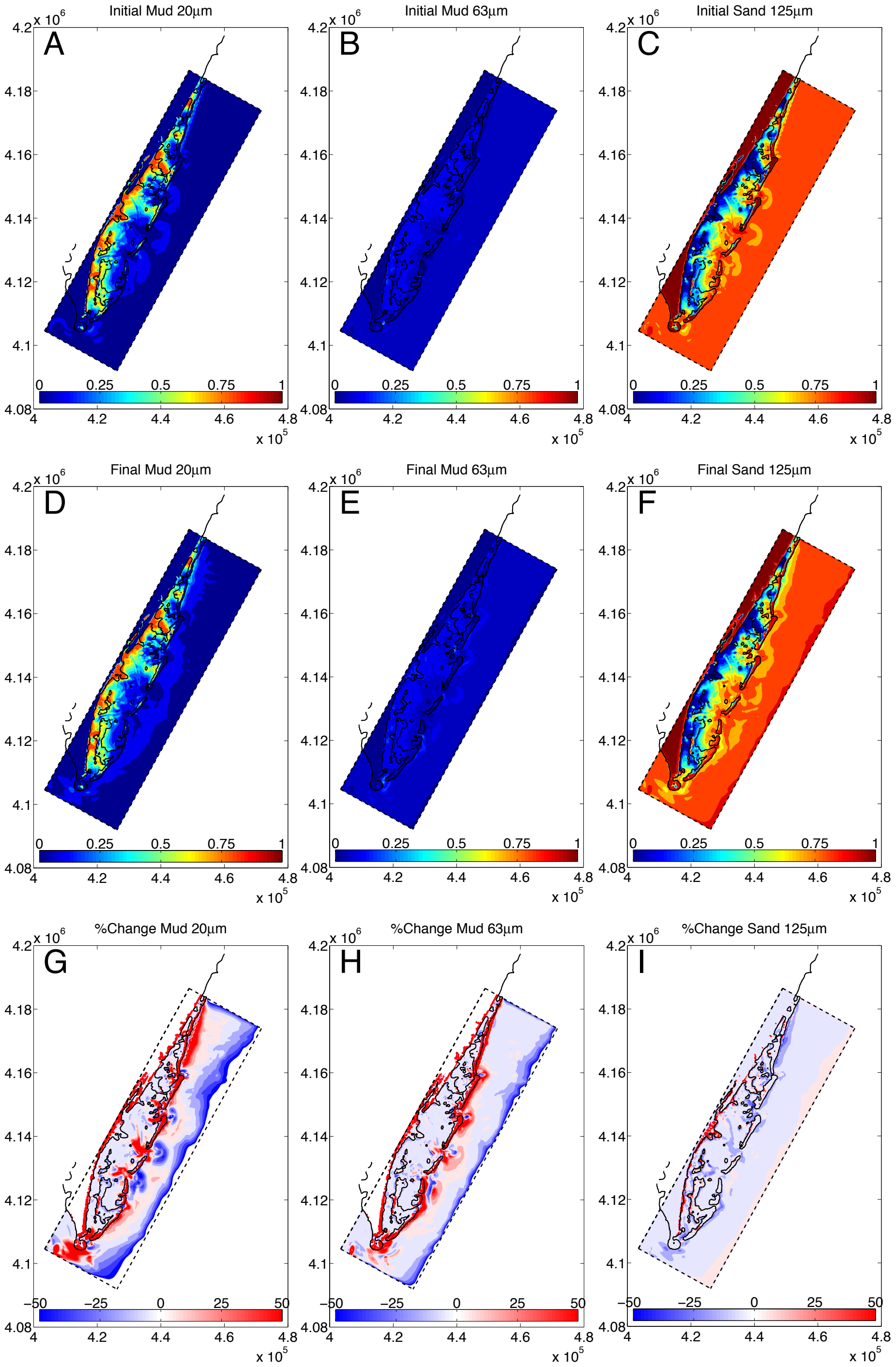
Initial Mud 20μm
A
Initial Mud 63μm
B
Initial Sand 125μm
C
Final Mud 20μm
D
Final Mud 63μm
E
Final Sand 125μm
F
%Change Mud 20μm
G
%Change Mud 63μm
H
%Change Sand 125μm
I
x 10^6
4.2
4.18
4.16
4.14
4.12
4.1
4.08
4
4.2
4.4
4.6
4.8
x 10^5
0
0.25
0.5
0.75
1
−50
−25
0
25
50

Figure 3.13: Initial spatial distribution of (A) very fine mud 20μm, (B) mud 63μm, and (C) sand 125μm, derived from Wiberg et al. (2015) and Fenster et al. (2016). Average final spatial distribution of (D) very fine mud 20μm, (E) mud 63μm, and (F) sand 125μm, for all 52 study storms. Scale is the proportion of the type of sediment. (G), (H), and (I) depict average change in bottom sediment composition for all 52 study storms, averaged for each kind of sediment, very fine mud 20μm, mud 63μm, and sand 125μm, respectively. Scale is percent change from initial to final bottom composition.

significant enough to cause a net import of mud to the system, regardless of the amount of time that the surge is above that threshold. With sea level rising approximately 4 mm per year (Wiberg

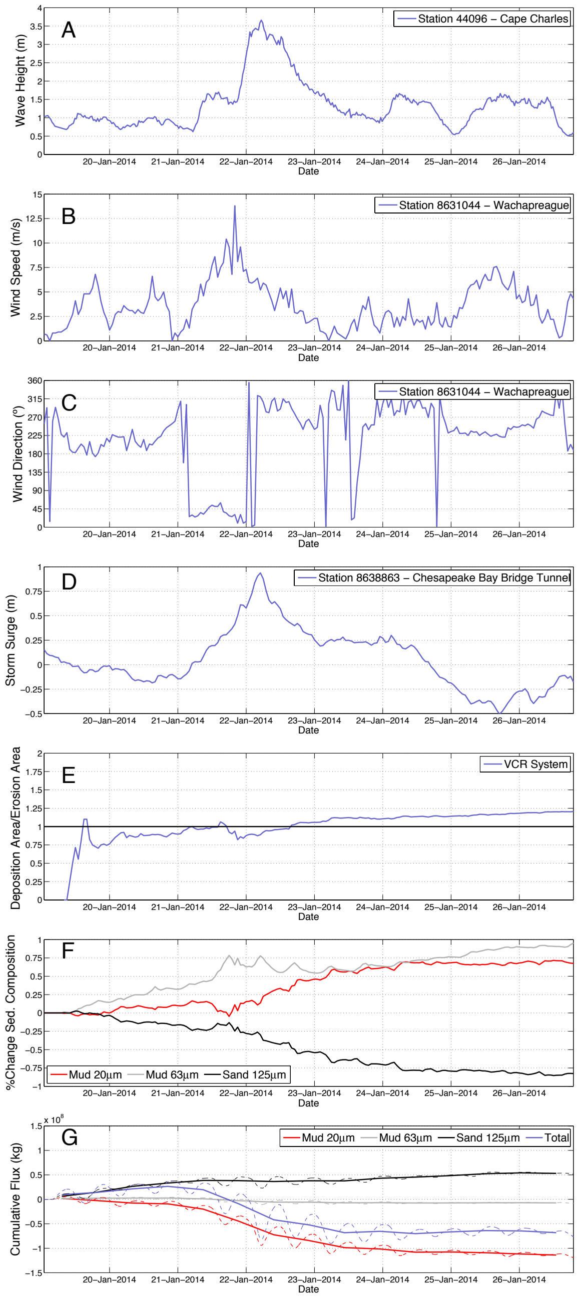

Figure 3.14: Storm number 38 (from 26-jan-2014 19:00 to 21-jan-2014 20:00) (A) wave height, (B) wind speed, (C) wind direction, (D) storm surge, (E) ratio of deposition area to erosion area within the VCR system, (F) percent change in bottom composition of each sediment specie within the VCR system, and (G) cumulative flux of each specie and total cumulative flux between the VCR system and the ocean (negative fluxes indicate sediment import).

et al., 2015) and annual sediment accumulation rates from our study storms ranging from 2.01 mm to 5.30 mm, accumulation of sediment from storms alone may be enough to largely offset the effects of sea-level rise in most years. Indeed, recent work has suggested that marshes in the VCR may be accreting quickly enough to avoid a serious threat from current rates of sea-level rise (Kirwan et al., 2016; Walters and Kirwan, 2016).

The sediment budget of a given system is often considered a metric of coastal stability. Ganju et al. (2013) suggested that marsh systems with net export of sediment may be more unstable, compared to marsh systems with net import of sediment. Though marsh stability can be influenced by a variety of factors, including net elevation change and suspended sediment source (Ganju et al., 2015), a marsh systems sediment budget has utility in predicting how the marsh will respond to rising sea levels over time, among other stressors. Our results suggest that larger storm events transport more sediment into lagoons, increasing their resilience in time.

Our results may also illuminate the geologic history of the VCR. Though the mainland of the system has many small watersheds, there are no major rivers flowing into the lagoons that contribute volumetrically important inputs of freshwater (Stanhope et al., 2009) or sediment (Morton and Donaldson, 1973) to the coastal bays. This, coupled with analysis revealing that much of the sediment in the VCR is marine-dominated with an offshore source (Robinson, 1994), suggests that the major driver of sediment for the system is likely storms. Since the presence of fine sediment is necessary for the development of salt marshes, the marshes in the VCR likely formed from storm-sourced sediment. This suggests that storm action was critical in the development of the system and continues to be critical in increasing the systems resilience today.

Many assessments agree that an increase in sea surface temperatures should result in an increase in the intensity of tropical cyclones (Holland and Webster, 2007; Emanuel, 2008; Sobel et al., 2016; Walsh et al., 2016), even with natural variability and confounding factors (Sobel et al., 2016). Our results suggest that increased storminess may continue to increase the resilience of coastal lagoons, providing the material necessary to counteract rising sea levels. This is particularly of interest for coastal protection schemes, since salt marshes and shallow tidal flats present a unique natural way to protect vulnerable communities from the effects of storm surge and flooding by dissipating energy, the effects of which will only increase as storminess increases.

Storm ID#	Beginning	End	Wind Peak Date	Wind Station	WL Station	Wave Station
1	26-feb-2009 12:00	05-mar-2009 12:00	02-mar-2009 05:00	WACH	WACH^{1} (CBBT)	44099
2	12-apr-2009 13:00	19-apr-2009 06:00	16-apr-2009 19:00	WACH	WACH^{1} (CBBT)	44099
3	27-apr-2009 12:00	02-may-2009 04:00	29-apr-2009 17:00	WACH	WACH^{1} (CBBT)	44099
4	12-sep-2009 15:00	21-sep-2009 00:00	17-sep-2009 13:00	WACH	WACH^{1}	44099
5	10-nov-2009 04:00	22-nov-2009 02:00	13-nov-2009 01:00	WACH	WACH^{1}	44099
6	30-nov-2009 21:00	13-dec-2009 08:00	03-dec-2009 07:00	WACH	WACH^{1}	44014
7	02-dec-2009 23:00	13-dec-2009 08:00	09-dec-2009 10:00	WACH	WACH^{1}	44014
8	13-dec-2009 08:00	24-dec-2009 04:00	19-dec-2009 14:00	WACH	WACH^{1}	44014
9	15-jan-2010 11:00	27-jan-2010 21:00	25-jan-2010 14:00	WACH	WACH^{1}	44099
10	01-feb-2010 00:00	10-feb-2010 21:00	06-feb-2010 08:00	WACH	WACH^{1}	44014
11	10-mar-2010 06:00	21-mar-2010 01:00	13-mar-2010 05:00	WACH	WACH^{1}	44099
12	15-may-2010 12:00	22-may-2010 18:00	18-may-2010 02:00	WACH	WACH^{1}	44099
13	28-sep-2010 13:00	08-oct-2010 10:00	30-sep-2010 17:00	WACH	WACH^{1}	44099
14	29-nov-2010 04:00	03-dec-2010 21:00	01-dec-2010 15:00	WACH	WACH^{1}	44099
15	24-jan-2011 02:00	30-jan-2011 21:00	26-jan-2011 16:00	WACH	WACH^{1}	44099
16	20-feb-2011 00:00	25-feb-2011 17:00	22-feb-2011 06:00	WACH	WACH^{1}	44099
17	06-apr-2011 12:00	12-apr-2011 17:00	09-apr-2011 05:00	WACH	WACH^{1}	44099
18	11-apr-2011 16:00	20-apr-2011 12:00	16-apr-2011 23:00	WACH	WACH^{1}	44099
19	11-jun-2011 06:00	23-jun-2011 04:00	20-jun-2011 16:00	WACH	WACH^{1}	44099
20	24-aug-2011 18:00	30-aug-2011 11:00	27-aug-2011 19:00	WACH	WACH^{1}	44014
21	27-oct-2011 10:00	31-oct-2011 13:00	29-oct-2011 11:00	WACH	WACH^{1}	44099
22	03-nov-2011 17:00	07-nov-2011 20:00	04-nov-2011 19:00	WACH	WACH^{1}	44014
23	17-feb-2012 07:00	23-feb-2012 12:00	20-feb-2012 00:00	WACH	WACH^{1}	44099
24	16-apr-2012 19:00	25-apr-2012 13:00	22-apr-2012 19:00	WACH	WACH^{1}	44099
25	15-may-2012 19:00	25-may-2012 01:00	18-may-2012 16:00	WACH	WACH^{1}	44099
26	16-sep-2012 10:00	21-sep-2012 02:00	18-sep-2012 16:00	WACH	WACH^{1}	44099
27	23-oct-2012 17:00	04-nov-2012 13:00	28-oct-2012 00:00	WACH	WACH^{1}	44099
28	12-nov-2012 21:00	26-nov-2012 22:00	18-nov-2012 17:00	WACH	WACH^{1}	44099
29	14-dec-2012 11:00	24-dec-2012 08:00	21-dec-2012 08:00	WACH	WACH^{1}	44099
30	23-dec-2012 20:00	01-jan-2013 13:00	26-dec-2012 18:00	WACH	WACH^{1}	44099
31	29-jan-2013 00:00	02-feb-2013 15:00	31-jan-2013 08:00	WACH	WACH^{1}	44099
32	05-feb-2013 19:00	13-feb-2013 1:00	08-feb-2013 12:00	WACH	WACH^{1}	44099
33	04-nov-2013 03:00	15-nov-2013 13:00	06-mar-2013 13:00	WACH	WACH^{1}	44099
34	20-apr-2013 06:00	26-apr-2013 23:00	22-apr-2013 21:00	WACH	WACH^{1}	44099
35	28-apr-2013 13:00	10-may-2013 23:00	03-may-2013 15:00	WACH	WACH^{1}	44099
36	06-oct-2013 00:00	19-oct-2013 00:00	13-oct-2013 21:00	WACH	WACH^{1}	44099
37	27-dec-2013 06:00	31-dec-2013 22:00	29-dec-2013 18:00	WACH	WACH^{1}	44099
38	19-jan-2014 01:00	26-jan-2014 19:00	21-jan-2014 20:00	WACH	WACH^{1}	44099
39	10-feb-2014 20:00	17-feb-2014 00:00	13-feb-2014 10:00	WACH	WACH^{1}	44099
40	28-feb-2014 22:00	11-mar-2014 07:00	07-mar-2014 15:00	WACH	WACH^{1}	44099
41	14-mar-2014 09:00	22-mar-2014 15:00	17-mar-2014 03:00	WACH	WACH^{1}	44099
42	23-mar-2014 03:00	28-mar-2014 21:00	25-mar-2014 21:00	WACH	WACH^{1}	44014
43	14-apr-2014 22:00	25-apr-2014 19:00	20-apr-2014 16:00	WACH	WACH^{1}	44099
44	24-apr-2014 19:00	03-may-2014 01:00	29-apr-2014 12:00	WACH	WACH^{1}	44099
45	26-may-2014 21:00	04-jun-2014 15:00	29-may-2014 01:00	WACH	WACH^{1}	44099
46	07-sep-2014 08:00	12-sep-2014 0:00	09-sep-2014 12:00	WACH	WACH^{1}	44099
47	22-sep-2014 09:00	29-sep-2014 13:00	25-sep-2014 00:00	WACH	WACH^{1}	44099
48	04-dec-2014 08:00	13-dec-2014 15:00	09-dec-2014 05:00	WACH	WACH^{1}	44099
49	28-apr-2015 19:00	05-may-2015 12:00	01-may-2015 13:00	WACH	WACH^{1}	44099
50	31-may-2015 09:00	08-jun-2015 15:00	03-jun-2015 14:00	WACH	WACH^{1}	44099
51	29-sep-2015 11:00	10-oct-2015 8:00	02-oct-2015 23:00	WACH	WACH^{1}	44099
52	26-dec-2015 11:00	03-jan-2016 18:00	28-dec-2015 15:00	WACH	WACH^{1}	44099

Table 3.1: Starting, ending and wind speed peak dates for the 52 storms simulated in this study. The stations in which wind, WL (water level) and wave data were acquired are also gathered (**WACH**: Wachapreague, VA-Station (ID: 8631044), **CBBT**: Chesapeake Bay Bridge Tunnel, VA - Station (ID: 8638863), **44099**: NOAA 44099 wave station, Cape Henry, VA, **44014**: NOAA 44014 wave buoy, 64 NM East of Virginia Beach, VA). The superscript ^{1} indicates that water level signal at Wachapreague Station was delayed and dampened as indicated in Section 3.2.3. In storms number 1,2 and 3 WACH^{1} (CBBT) means that, due to gaps in water level records at Wachapreague, an analog downscaling technique trained with data from the close Chesapeake Bay Bridge Tunnel, VA - Station (ID: 8638863) was applied to derive water levels at Wachapreague Station

Chapter 4

Effects of basin bottom slope on jet hydrodynamics and river mouth sedimentary patterns

River mouth bars are strategic morphological units primarily responsible for the development of entire deltaic systems. This Chapter addresses the role of receiving basin slope in the hydrodynamics of an exiting sediment-laden turbulent jet and in resulting mouth bar morphodynamics. We use Delft3D, a coupled hydrodynamic and morphodynamic numerical model, along with a theoretical formulation to reproduce the physics of the problem, characterized by a fluvially dominated inlet free of waves and tides. We propose an updated theoretical model with a slope-dependent entrainment coefficient, showing that the rate at which ambient fluid is incorporated into a jet increases with higher basin slopes. Transient results reveal that the magnitude of a basin slope can alter the stability of a jet, favoring the formation of an unstable meandering jet. While a stable jet give rise to “middle-ground" bars accompanied by diverging channels, a “lunate" mouth bar results from unstable jets. Additional morphodynamic simulations demonstrate that the time required for mouth bar stagnation in its final position increases linearly with the basin slope. In contrast, the distance at which the mouth bar eventually forms decreases until reaching an asymptotic value for slopes higher than 2%. Moreover, the basin slope highly influences sedimentary processes responsible for bar formation: for milder slopes, progradation processes prevail, while in steeper basins aggradation is more relevant. Finally, the minimum relative water depth over a bar crest that forces the flow to bifurcate around a fully developed bar decreases with the basin slope.

4.1 Introduction

Deltaic environments and river mouths host numerous biological and economical activities and, therefore, represent some of the most important ecosystems on earth (Syvitski and Saito, 2007; Syvitski et al., 2009; Díez-Minguito et al., 2012). From a management perspective, they are densely populated (Ericson et al., 2006), constitute strategic navigation channels (Lanzoni and Seminara, 2002; Winterwerp et al., 2013), accumulate important oil and gas deposits (Rainwater, 1975; Raghavendra Rao, 1991), comprise extensive industrial areas and agricultural lands (Syvitski and Saito, 2007), and shelter important fishing grounds (Pont et al., 2002). The exchange of sediments, nutrients and pollutants between rivers and oceans or lakes is thus crucial for the biogeochemical evolution of marine and lacustrine ecosystems (McKee et al., 2004; Bianchi and Allison, 2009; Yao et al., 2016). Hence, understanding the mechanisms that govern deltaic formation and evolution is fundamental for their optimum management.

When a river debouches into a receiving basin, it behaves as a bounded, sediment-laden, turbulent jet: the unconfined flow spreads laterally and decelerates seawards due to bottom friction and lateral diffusion in the ambient fluid (Joshi, 1982; Özsoy and Ünlüata, 1982; Wang, 1984; Ortega-Sánchez et al., 2008). A variety of depositional features arise as a consequence of sediment settling (Mikhailov, 1966; Coleman and Wright, 1975; Wright, 1977). One of these features are river mouth bars. Their formation is a key geomorphological process on delta evolution(Bates, 1953; Edmonds and Slingerland, 2007; Jerolmack and Swenson, 2007; Esposito et al., 2013). For a detailed review of the physics of these river mouth deposits, we refer the reader to Fagherazzi et al. (2015), who combine theoretical approaches, experimental data, field observations and numerical modeling to obtain novel process-based results.

Classical conceptual models for delta classification establish that long-term evolution of delta morphology is mainly dictated by the relative strengths of marine and riverine processes (Wright and Coleman, 1973; Galloway, 1975) along with sediment properties (Orton and Reading, 1993). Recently, advanced process-based numerical models have enabled more accurate examinations of the entire process of delta development at geological time scales under different forcing factors (Fagherazzi and Overeem, 2007; Storms et al., 2007; Edmonds and Slingerland, 2010; Geleynse et al., 2010; Caldwell and Edmonds, 2014). Concerning more specific delta units, such as river mouth bars, Wright (1977) summarized a conceptual model of mouth bar evolution according to the interactions between effluent forces and marine processes. More recently, the influences of purely fluvial systems (Edmonds and Slingerland, 2007) and mixed systems including waves (Nardin and Fagherazzi, 2012; Nardin et al., 2013) and tides (Leonardi et al., 2013, 2014) over river mouth bar formation have been analyzed using Delft3D numerical simulations.

These process-based, bar-modeling works are built on the basis of a stable jet, in agreement with the time-averaged solutions of the integral jet theory (Abramovich, 1963; Rajaratnam, 1976; Joshi, 1982; Özsoy and Ünlüata, 1982; Wang, 1984; Ortega-Sánchez et al., 2008). However, turbulence generated by shearing along the margins of the jet can destabilize it (Rowland et al., 2009). A characteristic feature of these unstable flows is the presence of large-scale coherent structures consisting of phase-correlated, 2D, counter-rotating vortical elements that appear across the width of the jet, giving it a meandering aspect (Hussain, 1983; Ho and Huerre, 1984). These structures play a significant role in mixing, entrainment and dispersal of sediment particles (Dracos et al., 1992; Jirka, 1994; Rowland et al., 2009). In this regard, Mariotti et al. (2013) and Canestrelli et al. (2014b) explore the implications that jet instabilities have on depositional patterns at river mouths.

Despite the current ability to simulate river mouth bar genesis, the geometric influence of the river mouth was not yet well established. The aforementioned works focusing on bar formation were conducted with outlet geometries characterized by horizontal or quasi-horizontal receiving basins. However, coastal inlets frequently exhibit high variability in their bathymetric profiles (Bárcenas et al., 2015). Although many authors have studied the dynamics of natural river-dominated deltas with gentle slopes (Özsoy, 1986; Edmonds and Slingerland, 2007; Leonardi et al., 2013; Caldwell and Edmonds, 2014), few have studied areas with steeper slopes. Steeply dipping foreset-dominated deltas, also known as Gilbert-type deltas (Gilbert, 1890), can be found in both marine and lacustrine environments characterized by low-energy basins where wave and tidal influences can be neglected (Postma, 1995; Viparelli et al., 2012; Bárcenas et al., 2015). These latter deltaic systems are usually fed by relatively small rivers with high seasonal variability and high slope due to the short distance between the mountain ranges and the coast. Besides, these rivers experience significant episodes of sediment discharge during seasonal flood events (Liquete et al., 2005; Urgeles et al., 2011). The evolution of these deltaic systems is distinct from areas with gently sloping basins (Storms et al., 2007). However, to our knowledge, no detailed studies have been performed to analyze how receiving basins with different slopes influence jet hydrodynamics and river mouth bar formation.

The purpose of this Chapter is to explore the effects of different bathymetries of the receiving basin on sediment-laden turbulent jet hydrodynamics and their connection with related deposition patterns. To this aim, we consider linearly varying flat bathymetries and employ a modified integral jet theory together with Delft3D numerical model to mimic a river debouching into a large body of quiescent water, in the absence of Coriolis effects, buoyancy forces, tides and wind waves.

4.2 Theoretical framework

Jet theory has been extensively used to describe processes experienced by rivers discharging into resting reservoirs of water (Wright et al., 1974; Özsoy, 1977; Ortega-Sánchez et al., 2008; Falcini and Jerolmack, 2010; Nardin et al., 2013; Leonardi et al., 2013). In river mouths characterized by width to depth ratios > 4, vertical motions of the water are much less significant than horizontal ones and the flow can be approximated with the shallow water equations (Leonardi et al., 2013). In these cases, the exiting flow behaves like a plane turbulent jet (Bates, 1953; Wright, 1977; Rowland et al., 2009; Falcini and Jerolmack, 2010; Leonardi et al., 2013; Nardin et al., 2013). Ideally, these flows can be divided into two different zones (Rajaratnam, 1976; Özsoy and Ünlüata, 1982): (1) a zone of flow establishment (ZOFE), located in the vicinity of the outlet and governed by a triangular inviscid core where centerline velocity can be assumed constant; and (2) a zone of established flow (ZOEF), where lateral shear turbulence reaches the jet axis and centerline velocity starts to decrease, leading to self-similarity conditions. Additionally, Ortega-Sánchez et al. (2008) included a transition region (ZOT) to match ZOFE and ZOEF.

Numerous studies have focused on the developmet of an integral jet theory. The earliest theoretical analysis were made for a plane jet assumed to be incompressible, stationary, frictionless, with constant depth, and constant momentum flux (Tollmien, 1926; Goertler, 1942; Albertson et al., 1950; Abramovich, 1963; Rajaratnam, 1976). Further analysis added the effects of bottom friction, bathymetric changes and cross-currents (Joshi, 1982; Özsoy and Ünlüata, 1982; Wang, 1984; Ortega-Sánchez et al., 2008). In this regard, Özsoy and Ünlüata (1982) performed a rigorous order-of-magnitude analysis of the shallow water equations that govern jet motion, obtaining:

$$\frac{\partial}{\partial x}(hu)+\frac{\partial}{\partial y}(hv)=0 \tag{4.1}$$

$$\frac{\partial}{\partial x}\left(hu^2\right)+\frac{\partial}{\partial x}(huv)=-\frac{g}{C_z^2}u^2+\frac{1}{\rho_w}\frac{\partial}{\partial y}\mathscr{F}_{xy} \tag{4.2}$$

where u and v are the depth-averaged velocities in the longitudinal (x) and transversal (y) directions, C_z is the Chezy's friction coefficient, h is the water depth, $\mathscr{F}_{xy}$ is the depth-integrated turbulent shear stress acting laterally on the jet, ρ_w is the fluid density, and g is the gravitational acceleration. The ratio v/u is assumed large enough to produce lateral entrainment of surrounding water but small enough to assume that bottom friction is only produced by the longitudinal velocity.

The mass conservation of sediment carried out in suspension by the river and the subsequent prediction of bed evolution can be estimated by adding a depth-averaged mass balance equation for suspended sediment. Özsoy (1986) proposed the simplified model:

$$\frac{\partial}{\partial x}(huc)+\frac{\partial}{\partial y}(hvc)=-S+\frac{\partial}{\partial y}\mathscr{C}_y \tag{4.3}$$

in which c represents depth-averaged suspended sediment concentration, S is an erosion or deposition term, and $\mathscr{C}_y$ is the $y-$directed turbulent flux of sediment concentration. The vertical flux of sediment between the bottom and the jet is quantified by the empirical expression (Nihoul and Adam, 1975):

$$S=-w_s c\left(1-\frac{|u|^2}{u_{cr,s}^2}\right) \tag{4.4}$$

where w_s represents the settling velocity of sediment particles, $|u|$ is the magnitude of local velocity, and $u_{cr,s}$ is the critical velocity for sediment entrainment into suspension.

The stationary, sediment-laden turbulent jet dynamics can be characterized by the velocity field $u(x,y)$, the jet half-width $b(x)$ and the suspended sediment concentration field $c(x,y)$. Experimental observations show that planar jets have a certain symmetry and can thus be considered self-similar (Abramovich, 1963). Indeed, solutions of jet theory operate on the assumption that the velocity and sediment concentration profiles are self-similar with respect to the normalized coordinate $\zeta = y/b(x)$. This assumption allows a simple parameterization of the dynamical variables in terms of scaling factors. For planar jets, the centerline velocity is generally used as the local velocity scale and the centerline sediment concentration is used as the characteristic scale for sediment concentration (Özsoy and Ünlüata, 1982; Özsoy, 1986). This reduces the number of independent variables in the problem and facilitates the integration of the equations of motion (equations (4.1) and (4.2)). Thus, the velocity and sediment concentration fields are parameterized as follows:

$$\frac{u(x,y)}{u_c(x)}=F(\zeta) \tag{4.5}$$

$$\frac{c(x,y)}{c_c(x)}=G(\zeta) \tag{4.6}$$

where subscript c refers to values attained by the variables along the jet centerline and $F(\zeta)$ and $G(\zeta)$ are similarity functions for velocity and sediment concentration profiles, respectively. These functions are related by a 1/2 power law since the eddy diffusivity of the scalar concentration doubles that of the momentum ($G(\zeta) = F(\zeta)^{1/2}$) (Abramovich, 1963; Stolzenbach and Harleman, 1971; Özsoy, 1986).

The following dimensionless variables are used hereafter: $\xi = x/b_0$, $H = h/h_0$, $U = u_c/u_0$, $B = b/b_0$, $C = c_c/c_0$, $f = gb_0/C_z^2 \cdot h_0$, $\gamma = w_s b_0/u_0 \cdot h_0$ and $\phi = u_0/u_{cr,s}$, where b_0 denotes the inlet half-width, h_0 is the inlet water depth, u_0 is the inflow velocity at the inlet, and c_0 is the concentration of suspended sediment at the inlet. I_1, I_2, I_3 and I_4 are numerical constants defined by:

$$I_n = \begin{cases} \int_0^1 F(\zeta)d\zeta & \text{for } n=1 \\ \\ \int_0^1 F(\zeta)^{n-2}G(\zeta)d\zeta & \text{for } n=2,3,4 \end{cases} \tag{4.7}$$

Integrating equations (4.1), (4.2) and (4.3) across the jet width and assuming that

$$v_e(x) = v(x,y)|_{y\to\infty} = \alpha u_c(x) \tag{4.8}$$

with α as an entrainment coefficient (Morton et al., 1956), we obtain:

$$\frac{d}{d\xi}(I_1 HUB) = \alpha HU \tag{4.9}$$

$$\frac{d}{d\xi}\left(HU^2B\right) = -fBU^2 \tag{4.10}$$

$$I_3\frac{d}{d\xi}(HBUC) = -\gamma BC\left(I_2 - \phi^2 U^2 I_4\right) \tag{4.11}$$

In previous works that investigated turbulent jet theory, this entrainment coefficient was generally assumed to be constant, regardless of the basin configuration (e.g., the bottom slope or the bottom friction) (Özsoy and Ünlüata, 1982; Wang, 1984; Nardin et al., 2013; Leonardi et al., 2013). In Section 4.4.1, we explore the influence of the basin bottom slope and friction on the entrainment coefficient by linking theoretical predictions and the numerical results obtained with Delft3D. Equations (4.9), (4.10) and (4.11) can be solved using a finite difference method for any arbitrary bathymetric profile $h(x)$. From equation (4.10), the following expression can be obtained:

$$J(\xi) = \exp\left(-\int_0^{\xi}\frac{f}{H}d\xi\right) = HBU^2 \tag{4.12}$$

with $J(0) = 1$ because $H(0) = B(0) = U(0) = 1$.

By reworking equation (4.9), a Bernoulli-type ordinary differential equation arises for the non-dimensional centerline velocity $U(\xi)$:

$$\frac{dU}{d\xi} - U\left(\frac{1}{J}\frac{dJ}{d\xi}\right) = -\frac{\alpha}{I_1}\frac{HU^3}{J} \tag{4.13}$$

Finally, equation (4.11) can be solved for the non-dimensional concentration $C(\xi)$, with the boundary condition $C(0) = 1$, by replacing the values previously obtained for the non-dimensional jet half-width $B(\xi)$ and centerline velocity $U(\xi)$ from equations (4.12) and (4.13) we obtain:

$$C(\xi) = \frac{\exp\left(-\frac{\gamma}{I_3}\int_0^{\xi}\frac{I_2-\phi^2U^2I_4}{UH}d\xi\right)}{HBU} \tag{4.14}$$

We will use $U(\xi)$, $B(\xi)$ and $C(\xi)$ (see Sections 4.4 and 4.5) to characterize the hydrodynamics and sediment deposition patterns in the proximity of river mouth. Note that all variables are computed for an entire ZOEF domain in which turbulence affects the jet axis as soon as the jet exits the channel. The suppression of the ZOFE agrees with the numerical results reported by Nardin et al. (2013), who showed that a jet begins decelerating once it exits the channel.

4.3 Numerical model

We conducted hydrodynamic and morphodynamic simulations using the high-resolution, fluid dynamics model Delft3D (Lesser et al., 2004; Deltares, 2013). This model can simulate non-steady flows, sediment transport phenomena and related bathymetric changes in a coupled modality. This model has been extensively used to investigate river mouth jet hydrodynamics and sediment depositional patterns (Edmonds and Slingerland, 2007; Nardin and Fagherazzi, 2012; Leonardi et al., 2013; Mariotti et al., 2013; Nardin et al., 2013; Canestrelli et al., 2014b; Leonardi et al., 2014). We assume a depth-averaged schematization of the problem based on previous theoretical, experimental and numerical works on planar jets (Joshi, 1982; Özsoy and Ünlüata, 1982; Rowland et al., 2010; Landel et al., 2012; Leonardi et al., 2013; Mariotti et al., 2013).

4.3.1 Hydrodynamic model

Delft3D solves the unsteady shallow water equations. The continuity and horizontal momentum equations are:

$$\frac{\partial \eta}{\partial t}+\frac{\partial hu}{\partial x}+\frac{\partial hv}{\partial y}=0 \tag{4.15}$$

$$\frac{\partial u}{\partial t}+u\frac{\partial u}{\partial x}+v\frac{\partial u}{\partial y}=-g\frac{\partial \eta}{\partial x}+g\frac{u\sqrt{u^2+v^2}}{C_z^2 h}+\epsilon_f\left(\frac{\partial^2 u}{\partial x^2}+\frac{\partial^2 u}{\partial y^2}\right) \tag{4.16}$$

$$\frac{\partial v}{\partial t}+u\frac{\partial v}{\partial x}+v\frac{\partial v}{\partial y}=-g\frac{\partial \eta}{\partial y}+g\frac{u\sqrt{u^2+v^2}}{C_z^2 h}+\epsilon_f\left(\frac{\partial^2 v}{\partial x^2}+\frac{\partial^2 v}{\partial y^2}\right) \tag{4.17}$$

where η represents water level with respect to datum, t is time, and ϵ_f is a horizontal eddy viscosity coefficient. The latter is computed via Horizontal Large Eddy Simulations (HLES) technique (Van Vossen, 2000; Uittenbogaard and Van Vossen, 2004). This closure model includes contributions from horizontal turbulent motions and forces that are not resolved on the original grid by adding a sub-grid scale (SGS) horizontal eddy-viscosity ($\epsilon_{f,SGS}$) to a constant or space-varying, user-defined background value ($\epsilon_{f,H}^{back}$):

$$\epsilon_f=\epsilon_{f,H}^{back}+\epsilon_{f,SGS} \tag{4.18}$$

4.3.2 Sediment transport

Sediment transport formulations employed by Delft3D allows one to compute bedload and suspended sediment transport for both non-cohesive ($> 64\ \mu m$) and cohesive sediments ($\leq 64\ \mu m$) and the subsequent sediment exchange between the water column and the bottom.

Bedload transport (S_b) for non-cohesive sediments is calculated using the empirical transport formula proposed by van Rijn (1984b):

$$S_b = \begin{cases} 0.053\sqrt{\Delta g D_{50}^3} D_*^{-0.3} T^{2.1} & \text{for } T < 3.0 \\ \\ 0.1\sqrt{\Delta g D_{50}^3} D_*^{-0.3} T^{1.5} & \text{for } T \geq 3.0 \end{cases} \tag{4.19}$$

where $\Delta = (\rho_s - \rho_w)/\rho_w$ is the submerged specific gravity of a sediment with density ρ_s, D_{50} is the median sediment diameter, and D_* is a non-dimensional particle diameter:

$$D_* = D_{50}\left(\frac{\Delta g}{\nu^2}\right)^{1/3} \tag{4.20}$$

where ν is the kinematic viscosity of water. T is a dimensionless bed shear parameter defined as:

$$T = \frac{\mu_c \tau_b - \tau_{b,cr}}{\tau_{b,cr}} \tag{4.21}$$

in which $\mu_c \tau_b$ is the effective shear stress associated with grain friction and $\tau_{b,cr}$ is the critical bed shear stress according to Shields curve. Moreover, Delft3D adjusts its formulae to account for bottom-slope effects on the direction and magnitude of the bedload vector in both the longitudinal (Bagnold, 1966) and transverse directions (Ikeda, 1982).

Suspended transport of both non-cohesive and cohesive sediments is computed by solving the depth-averaged simplified form of the general three-dimensional advection-diffusion equation:

$$\frac{\partial hc}{\partial t} + \frac{\partial huc}{\partial x} + \frac{\partial hvc}{\partial y} = h\left[\frac{\partial}{\partial x}\left(\epsilon_s \frac{\partial c}{\partial x}\right) + \frac{\partial}{\partial y}\left(\epsilon_s \frac{\partial c}{\partial y}\right)\right] + hS \tag{4.22}$$

where ϵ_s is the sediment eddy diffusivity and S is the source term modelling the net mass flux between the water column and the bed, which is computed separately for non-cohesive (S_{nc}) and cohesive (S_c) fractions. For the non-cohesive fraction, erosive and depositional fluxes are determined by

$$S_{nc} = \frac{c_{eq} - c}{T_s} \tag{4.23}$$

in which T_s is the adaptation time-scale, computed according to Galappatti and Vreugdenhil (1985), and c_{eq} is the depth-averaged equilibrium sediment concentration, derived from the suspended transport rate (S_s) and the magnitude of the local, depth-averaged velocity as follows:

$$c_{eq} = \frac{S_s}{h\sqrt{u^2 + v^2}} = f_{cs} c_a \tag{4.24}$$

where f_{cs} is a shape factor based on the Rouse formulation (van Rijn, 1984c), and c_a is the reference concentration at a roughness height ξ_c above the bed:

$$c_a = 0.015 \frac{D_{50}}{\xi_c} \frac{T^{1.5}}{D_*^{1.5}}. \tag{4.25}$$

For cohesive sediment fractions, sediment fluxes between the water phase and the bed are calculated using the well-known Partheniades-Krone formulations (Partheniades et al., 1965).

Spatial gradients in bedload transport and the source and sink terms associated with suspended sediments fluxes near the bottom ultimately determine the possible changes in bed bathymetry (Paola and Voller, 2005). To reduce differences between the time-scales at which morphological changes take place in relation to hydrodynamic changes, a morphological acceleration factor is used.

4.3.3 Model setup

Plane jet hydrodynamics and morphodynamics of river-mouth bar in fluvially-dominated deltas are computed with reference to a simplified, one-layered domain representing the shoreline and continental shelf receiving the river (Figure 4.1). The grid, made by rectangular cells aligned with the river axis, is smooth enough to minimize errors due to finite difference approximations and perfectly orthogonal, which saves some computationally expensive transformation terms. To meet stability and accuracy requirements of the numerical scheme, the time step has been varied to comply with the Courant-Friedrichs-Lewy condition.

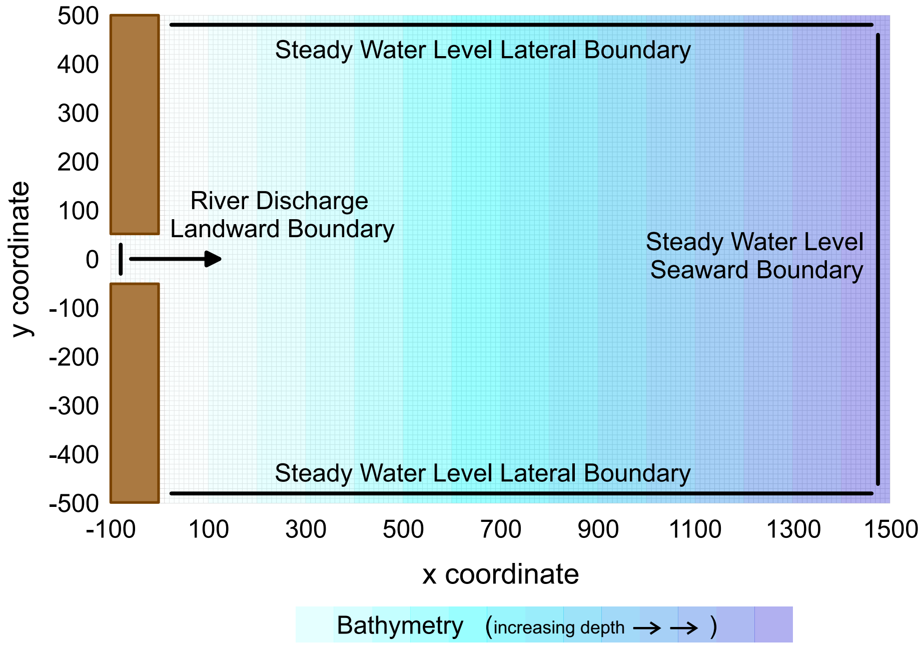
500
400
300
200
100
0
-100
-200
-300
-400
-500
y coordinate
-100
100
300
500
700
900
1100
1300
1500
x coordinate
Steady Water Level Lateral Boundary
River Discharge
Landward Boundary
Steady Water Level
Seaward Boundary
Steady Water Level Lateral Boundary
Bathymetry (increasing depth → →)

Figure 4.1: Computational domain and boundary conditions.

Every simulation begins with a receiving basin at rest, a uniform water level and a zero global sediment concentration. To simulate a river, a straight channel is carved into a 100 m wide coast. Previous tests have shown that channel length does not affect the numerical results (Nardin et al., 2013). We prescribe open boundaries of temporally and spatially constant water surface elevations at the seaward and lateral (perpendicular to coastline) boundaries, and specify a temporally constant river discharge flux that carries a mixture of cohesive and non-cohesive sediment at the channel on the landward boundary. Whereas the bedload exiting through the outlet is assume to perfectly adapt to the local flow conditions, condition usually employed when modeling alluvial estuaries connected to large water bodies, such as a bay, a sea, or an ocean (Lanzoni and Seminara, 2002; Bolla Pittaluga et al., 2015), the river discharge carries a user-defined discharge of cohesive suspended load and a non-cohesive suspended load at its equilibrium concentration profiles. This latter condition prevents accretion or erosion near the model boundaries (Deltares, 2013).

User-Defined Model Parameter	**Value**	**Units**
Basin length	1500	m
Basin width	1000	m
Cell size	10×10	m
Channel section (width×depth)	100×3	m
River discharge velocity	1.5	m/s
Bed roughness Chezy coefficient[a]	55	$m^{1/2}s^{-1}$
Background horizontal eddy viscosity	1	m^2s^{-1}
Horizontal eddy diffusivity	1	m^2s^{-1}
Reference density for hindered settling	1600	kg/m^3
Sediment specific density	2650	kg/m^3
Dry bed density	1600	kg/m^3
Suspended discharge for non-cohesive sediment[b]	Equilibrium[c]	kg/m^3
Suspended discharge for cohesive sediment	0.1	kg/m^3
Non-cohesive sediment dry bed density	1600	kg/m^3
Non-cohesive median diameter	200	μm
Cohesive sediment dry bed density	250	kg/m^3
Cohesive sediment settling velocity	0.0001	m/s
Cohesive sediment critical shear stress for erosion	0.5	N/m^2
Cohesive sediment critical shear stress for deposition	1000	N/m^2
Cohesive sediment erosion parameter	0.0001	$kg/m^2/s$
Morphological scale factor	20	—

Table 4.1: User-defined model parameters in Delft3D for numerical experiments in this work. The superscript ^{a} indicates that Chezy values equal to 40 and 70 $m^{1/2}s^{-1}$ were used in additional simulations. The superscript ^{b} indicates that incoming suspended sediment discharge for non-cohesive sediment equal to 0.2, 0.5, 0.8 and 1.1 kg/m^3 were used in additional simulations. The superscript ^{c} refers to an equilibrium sand concentration profile adapted to the local inflow conditions at the river mouth boundary. In our simulations, it corresponds to 0.56 kg/m^3.

The value of the horizontal eddy viscosity depends on the flow and grid sizes used, but generally, values between 1 and 10 m^2/s for grid sizes in the order of tens of metres will result in satisfactory results (Vlijm, 2011). In this work, the background horizontal eddy viscosity value was set to 1 m^2/s. Although it should be calibrated with measurements for nonidealized applications, this value was used in previous works focused on turbulent jets (Geleynse et al., 2011; Olabarrieta et al., 2014). Concerning the HLES technique, the default user-parameters of Kernkamp and Uittenbogaard (2001) were used.

The receiving sloping basin that mimics the continental shelf is composed of 5 m thick, erodible, non-cohesive sediment with characteristics similar to the sand-particles transported by the river. The topmost 2 m of the erodible bottom is divided into 10 stratigraphic layers to track the evolution of bed sediment composition. The model parameters are summarized in Table 4.1. With the exception of bottom slope, these values are similar to those employed in previous sediment-laden turbulent jet simulations (Edmonds and Slingerland, 2007; Geleynse et al., 2011; Leonardi et al., 2013; Caldwell and Edmonds, 2014; Canestrelli et al., 2014b; Olabarrieta et al., 2014). Different bottom slopes, ranging from a horizontal basin up to a 10% bottom slope, were used to produce 18 different numerical runs ($m = [0, 0.1, 0.25, 0.5, 0.75, 1, 1.25, 1.5, 1.75, 2, 3, 4, 5, 6, 7, 8, 9, 10]$ %). These slope values are consistent with river mouth geometries observed in the field (Bárcenas et al., 2015).

To achieve a fully developed hydrodynamic state, every numerical experiment is run for a spin-up "frozen bathymetry" interval of 24 hours before allowing any morphodynamic evolution of the bottom. These first 24 hours are used to study the influence of the receiving basin bottom slope on jet hydrodynamics, whereas the remaining movable bed simulation time allows investigation of how bottom slope influences depositional patterns at river mouths using an "active bathymetry". In Appendix A we perform a sensitivity analysis to show how model outcomes are sensitive to the imposed numerical parameters.

4.4 Influence of bottom slope on jet hydrodynamics

4.4.1 Time-mean hydrodynamics properties

The hydrodynamic results from Delft3D were time-averaged once the flow had become reasonably well established at the end of the spin-up interval. An equilibrium state, classified as meandering and therefore unstable, or time-invariant and stable, was visually confirmed during the frozen bathymetry period.

As previously observed, jet hydrodynamics are characterized by centerline velocity decay and lateral expansion. Experimentally, different length scales can be used to characterize the lateral expansion of a plane jet (Joshi, 1982; Agrawal and Prasad, 2003; Kernkamp and Uittenbogaard, 2001). In the present work we use a local velocity half-width, defined by the transverse location at which the time-averaged streamwise velocity is equal to half the centerline velocity (Giger et al., 1991).

To test whether jet hydrodynamics verifies self-similarity conditions under different receiving basin slopes, we compute a normalized streamwise velocity profile along a reference transverse transect located $\xi = 10$ from the river outlet. We select this section because it is the approximate distance at which river mouth bars completely form in our morphological tests. The time-averaged streamwise velocity component is normalized by the time-averaged jet center velocity, whereas the transverse distance y is scaled by local velocity half-width, yielding the similarity parameter ζ. Indeed, all longitudinal velocity distributions depicted in Figure 4.2 (a) collapse on one curve with a near-Gaussian shape, reflecting self-similarity conditions regardless of bottom slope. Therefore, these results show that the integral jet theory can be applied for any bottom slope within the analyzed range.

Different analytical closed-forms for the similarity profile have been proposed in different experimental studies of free-shear flows (Joshi, 1982; Özsoy and Ünlüata, 1982; Wang, 1984; Giger et al., 1991; Paillat and Kaminski, 2014). In the present work, each of these analytical functions was compared with the mean profile that arose from averaging the normalized longitudinal velocity profiles obtained with Delft3D for every bottom slope. After evaluating the determination coefficients computed for each similarity profile, the Gaussian function proposed by Giger et al.

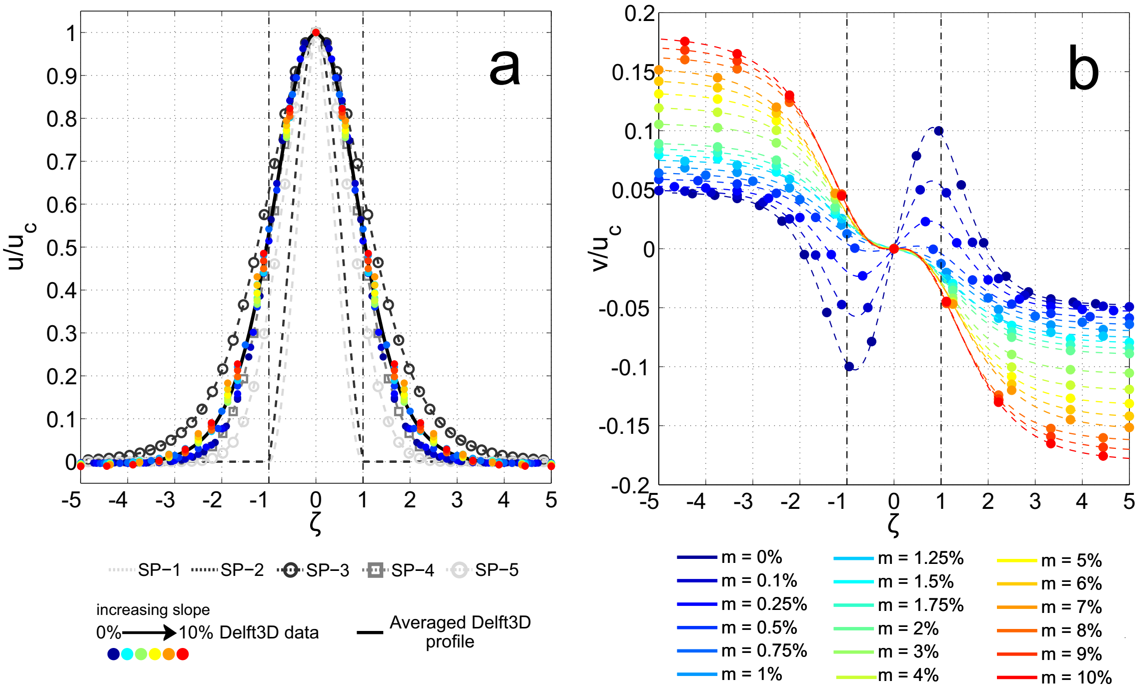

Figure 4.2: (a) Delft3D normalized distribution of the mean longitudinal velocity u and (b) Delft3D normalized distribution of transverse velocity v, both along a cross section located at $\xi = 10$ from the river outlet for different basin slopes, ranging from 0% to 10%. Blue colors represent a near horizontal bottom, whereas the red colors represent higher bottom slopes. Vertical dashed lines mark the width of the jet. The thick black line in (a) represents the slope-mean profile from the Delft3D data, and the dashed curves represent the similarity profiles proposed by several authors (SP-1 : Özsoy and Ünlüata (1982), SP-2: Wang (1984), SP-3: Joshi (1982), SP-4: Giger et al. (1991), and SP-5: Paillat and Kaminski (2014)).

(1991) had the best fit ($R^2 = 0.9922$) (Figure 4.2 (a)). Therefore, we chose this distribution for our theoretical computations.

Figure 4.2 (b) shows the normalized velocity distributions along the transect located at $\xi = 10$. The asymptotic values ($\zeta \gg 1$) of the different curves are strickly linked with the entrainment of ambient non-turbulent fluid into the jet at different bottom slopes (equation 4.8), i.e., the entrainment coefficient in the numerical simulations α_{NS} (red dots in Figure 4.3). The differences in these asymptotic values reveal that the entrainment coefficient cannot be kept constant regardless of the bottom slope, as assumed by the planar jet theory.

Hence, in this work we propose a slope-dependent entrainment coefficient for the jet theory. To this aim, we calibrate the entrainment coefficient of the turbulent jet theory α_{JT} (blue dots in Figure 4.3) to optimize the fit of theoretically and numerically computed with Delft3D centerline velocities. The trend of α_{JT} is similar to the trend followed by α_{NS}, demonstrating that the ability of a jet to capture ambient fluid increases for higher bottom slopes. Nevertheless, there is an approximately constant difference between the α_{JT} and α_{NS} curves. This is due to the considerable simplifications used to derive the turbulent jet equations in the integral jet theory, which reduces the highly nonlinear behavior of the system resolved by Delft3D. Indeed, Delft3D account for the entrainment and incorporation of ambient non-turbulent fluid into the jet by large turbulent eddies, a process that is not resolved in the theoretical model.

To further explore the influence of basin configuration on the entrainment coefficient, we also analyzed the effects of bottom friction. Additional hydrodynamic simulations were carried

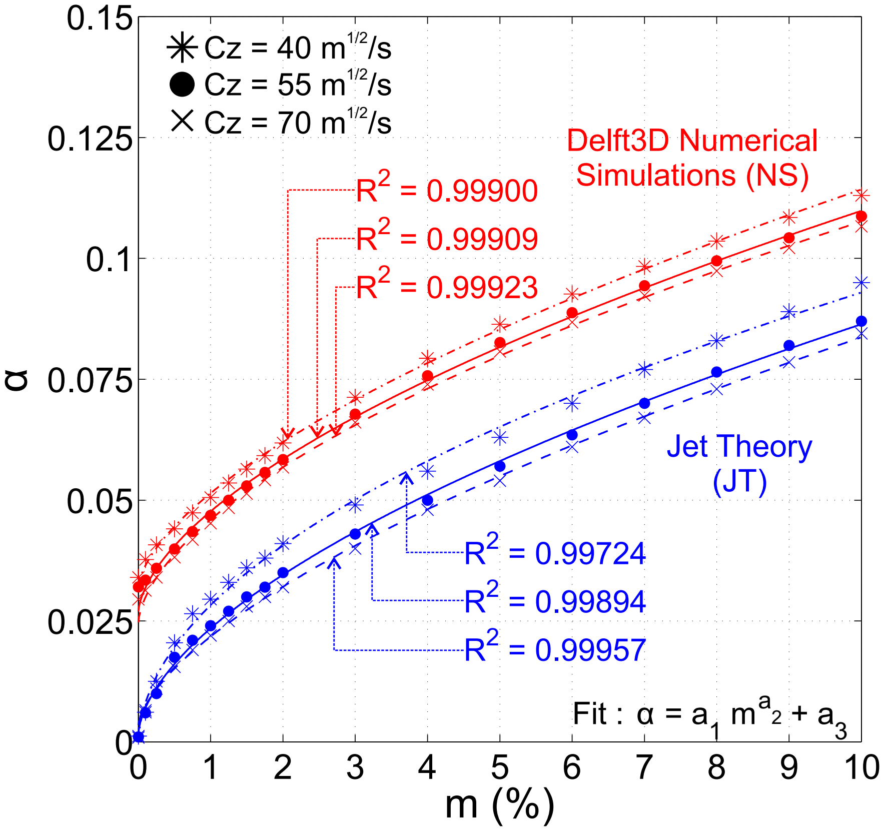

Figure 4.3: Values of the entrainment coefficient against the receiving basin bottom slope for three different bottom friction values (C_z = 40 m$^{1/2}$/s, C_z = 55 m$^{1/2}$/s and C_z = 70 m$^{1/2}$/s) in planar turbulent jets calculated from both numerical simulations in Delft3D (red elements) and by adjusting analytical solutions to the numerical simulations (blue elements). Dots represent the computed values, and lines show a power law fit of the dots. For α_{JT} adjustments $a_1 = [0.024, 0.022, 0.019]$, $a_2 = [0.504, 0.583, 0.637]$ and $a_2 = [0.002, 0.002, 0.002]$, respectively for $C_z = [40, 55, 70]$ m$^{1/2}$/s. Fittings are significant with 95 % confidence.

out in Delft3D using a “frozen bathymetry” configuration. We increased and reduced the friction with Chezy coefficients of 40 m$^{1/2}$/s and 70 m$^{1/2}$/s, respectively (see Table 4.1). Figure 4.3 shows that greater bottom friction (a smaller Chezy coefficient) leads to a higher lateral entrainment of ambient water into the jet. In addition, although the entrainment of water also varies with bottom friction, the basin bottom slope has a greater influence.

Hence, for a given bottom friction value, we recommend a new relation for the entrainment coefficient of the turbulent jet theory, that depends on bottom slope as follows:

$$\alpha_{JT} = a_1 m^{a_2} + a_3, \tag{4.26}$$

where m is the bottom slope expressed as a percentage, while the coefficients a_1, a_2 and a_3 are obtained from the power law fitting of the theoretical entrainment coefficients (see caption of Figure 4.3).

The along-jet normalized centerline velocity (Figure 4.4 (a) and (b)) and jet half-width (Figure 4.4 (c) and (d)) profiles for different bottom slopes can be readily computed using both the classic theoretical model presented in Section 4.2 along with the new slope-dependent entrainment coefficient (equation (4.26)) and the Delft3D numerical model. We observe that jet hydrodynamics is dictated by different quantities depending on bottom slope. Thus, for milder slopes ($m \leq 1\%$), the shallow water depth allows the bottom-friction to increase the spreading and deceleration of the jet. Conversely, for higher slopes ($m > 1\%$), the influence of bottom friction is sufficiently reduced due to the higher depth, and the high entrainment capacity of the jet dictates its dynamic behaviour. As such, the jet widens and decelerates as a consequence of the incorporation of still surrounding water. In these cases, an initial contraction of the jet width close to the river mouth is observed both in the numerical and theoretical results. This is related to the inward (axis-directed) cross-stream velocity distribution at the edge of the jet ($\zeta = 1$) (Figure 4.2 (b)).

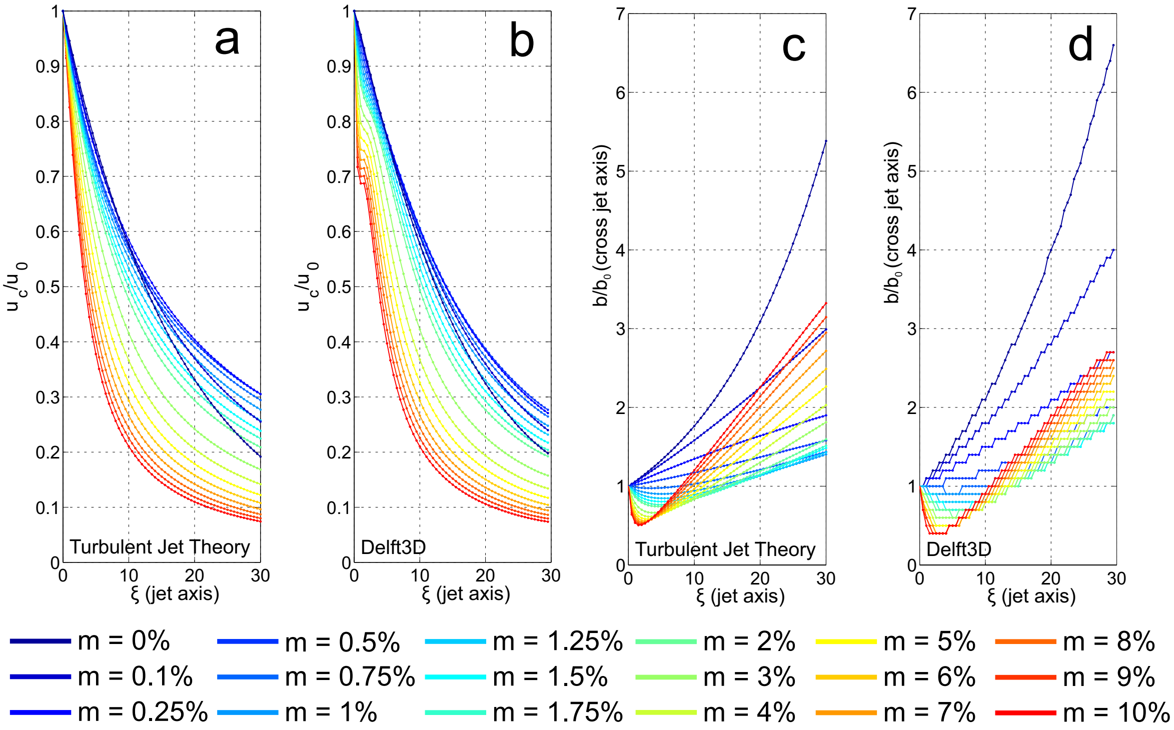

Figure 4.4: Normalized centerline velocity computed with (a) turbulent jet theory and (b) Delft3D, and normalized velocity half-width computed with (c) turbulent jet theory and (d) Delft3D, for different basin slopes ranging from 0% to 10%.

Finally, for all simulated cases, the centerline velocity starts to decay as soon as the jet leaves the channel. This agrees with the results reported by Nardin et al. (2013) and reinforces our hypothesis that ZOFE can be neglected in the theoretical framework.

4.4.2 Effects of bottom slope on jet stability

Rowland et al. (2009) found that the large-scale meandering structures that appear under unstable conditions are not always achieved in river discharges such as those simulated in this work. For plane jets, horizontal eddy viscosity and bed-friction can damp perturbations and stabilize the flow. Canestrelli et al. (2014b) embedded these stabilizing mechanisms in a local river-mouth Reynolds number and stability parameter, respectively. According to these parameters, our simulations lay on the same point of the transition zone in the stability diagram defined by Canestrelli et al. (2014b), since all of them have identical river mouth conditions. However, a visual inspection of our simulations provides new insight into these instability processes: whereas the jet remains unaltered for quasi-horizontal slopes (Figure 4.5 (a) and (b)), for higher slopes the jet becomes unstable, leading to the appearance of a meandering configuration characterized by

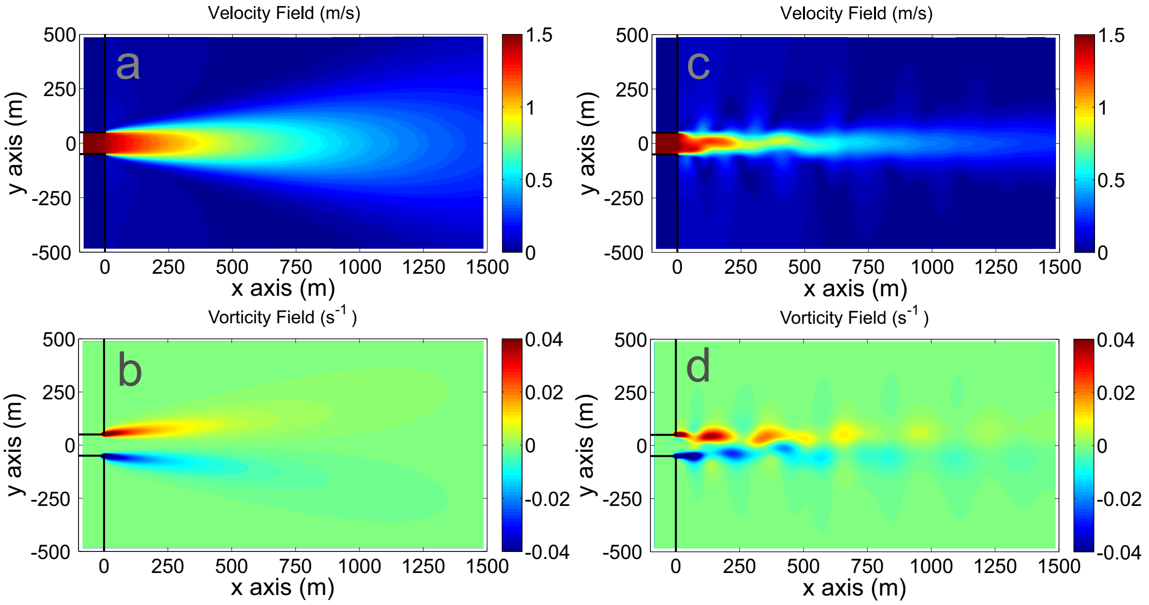

Figure 4.5: Effects of bottom slope on jet stability. Given river discharge conditions ($u_0 = 1.5$ m/s, $b_0 = 50$ m, $h_0 = 3$ m, and $C_z = 55\ \mathrm{m}^{1/2}\mathrm{s}^{-1}$), a sufficient bed slope makes flow unstable. (a) and (c) are snapshots of depth-averaged velocity fields for a horizontal bottom (m = 0%) and a sloping bottom (m = 4%), respectively. (b) and (d) are the vorticity fields corresponding to the velocity fields in (a) and (c), respectively. In (d) the presence of two asymmetric rows of aligned vortices with opposite directions of rotation can be observed.

the passage of 2D vortical structures (Figure 4.5 (c) and (d)). This fact reveals that the local stability parameters analyzed by Canestrelli et al. (2014b) remain insufficient to characterize plane jet stability under the effect of bottom slope. A section-by-section variable Reynolds number (Re_ξ) and stability parameter (S_ξ) that account for variations in the bathymetric profile provide more appropriate results:

$$Re_\xi(\xi) = \frac{2b(\xi)u_c(\xi)}{\nu} \tag{4.27}$$

$$S_\xi(\xi) = \frac{gb(\xi)}{C_z^2 h(\xi)}. \tag{4.28}$$

We plotted these parameters at different locations along the jet axis for different bottom slopes on the stability diagram defined by Canestrelli et al. (2014b) (Figure 4.6). The results show that despite different simulations possessing similar stability conditions at the river mouth (black star in Figure 4.6), the bottom slope affects stability. While gentler slopes move the stability points of the downstream sections towards the stable region or at least maintain them in the transition zone of the diagram, higher slopes (m > 1%) move them to the unstable region.

The visual prominence of these 2D vortical structures in unstable jets should display a distinct spectral signature in frequency versus power space plots (Jirka, 1994; Rowland et al., 2009). We analyzed the one-dimensional energy spectra for different bottom slopes corresponding to the signal of cross-stream velocity turbulent fluctuations (v') (Figure 4.6 (inset)). In the stable case, the energy spectrum shows a negligible turbulence structure. Conversely, the energy spectrum for unstable cases depict a similar shape to those reported by Dracos et al. (1992), Jirka (1994), Rowland et al. (2009), and Cohen (2012) in bounded-jet laboratory experiments.

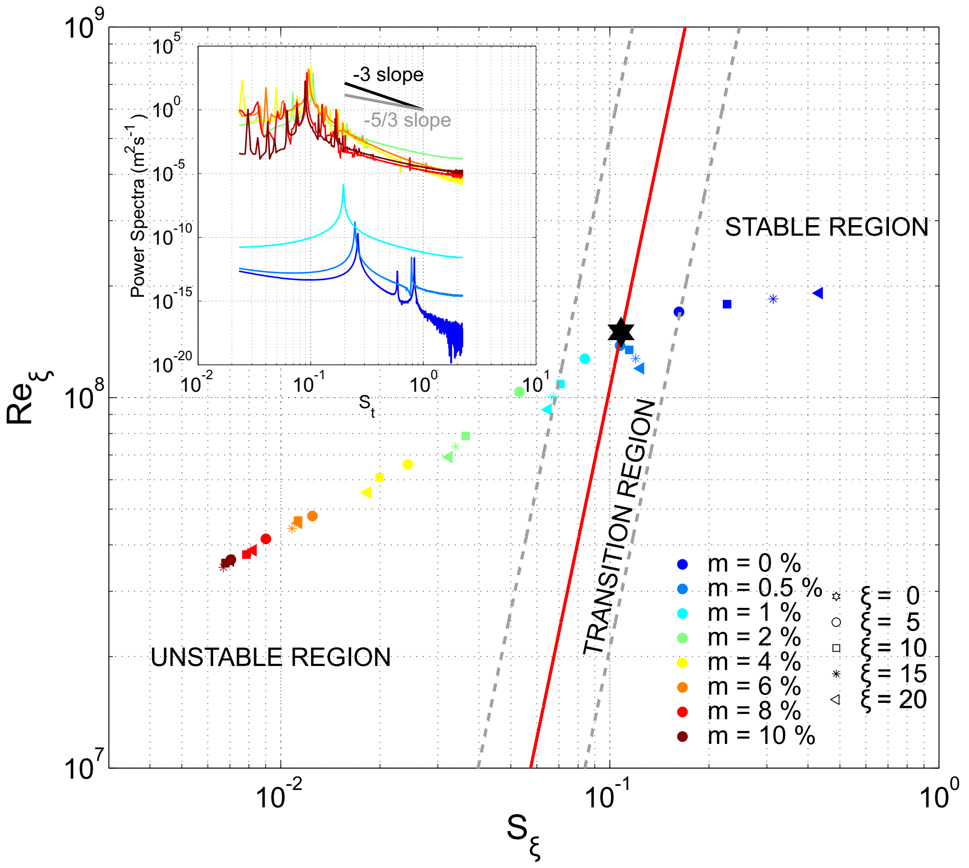

Figure 4.6: Jet stability diagram from Canestrelli et al. (2014b). The continuous red line (Eq. (10) from Canestrelli et al. (2014b)) divides the plot space into a stable and unstable jet region. The dotted grey lines delimit a transition zone where both stable and unstable jets can be present. Different sections ($\xi = 0$ (river mouth), 5, 10, 15 and 20) along the jet axis for different bottom slopes (m = 0%, 0.5%, 1%, 2%, 4%, 6%, 8%, and 10%) were characterized. The increase in bottom slope tends to diminish the stability of the flow downstream. The black star depicts the river mouth bar conditions in the different cases. Inset: Corresponding one-dimensional energy spectra of turbulent fluctuations of the cross-stream velocity v' at a point on the x-axis. The data were collected at $\xi = 10$. The black and grey dotted lines follow -3 and $-5/3$ power laws respectively, and are depicted to highlight changes in spectral decay from the peak for unstable cases.

The normalized frequency abscissa represents a Strouhal number ($S_t = f b_0 / u_0$). A distinct energy peak found around $S_t \simeq 0.1$ (Figure 4.6 (inset)) agrees with those measured in laboratory experiments (Dracos et al., 1992; Jirka, 1994; Cohen, 2012). This peak corresponds to the passage frequency of the vortical structures in our Deflt3d simulations. From this peak, a characteristic -3 power law consistent with a quasi two-dimensional turbulence structure arises in the frequency subrange dominated by 2D lateral shear instability. This stretch is followed by a -5/3 power law typical of three-dimensional, bed-driven turbulence at high frequencies (Jirka, 1994; Rowland et al., 2009). Thus, the usage of Delft3D in combination with HLES technique represents a suitable method for capturing the unsteady structure of a plane jet similarly to experimental studies (Jirka, 2001). Finally, Rowland et al. (2009) found that the presence of these 2D vortical structures has little influence on the mean structure of a jet, but dominates the jet turbulence.

4.5 Morphological results: river mouth bar

4.5.1 River mouth bar formation

Edmonds and Slingerland (2007) developed a seminal conceptual framework for the evolution of river-mouth bars on river-dominated deltas. According to this approach, bar formation at river mouth results from sediment settling on the receiving basin bottom due to a sharp reduction in centerline velocity and jet spreading once the flow exits the channel. The river mouth bar is subject to a process of vertical aggradation and seaward progradation until its height rises to approximately 60% of the water depth. At this time, the upstream pressure is high enough to force the flow to bifurcate around the mouth bar in the runaway aggradation phase, and eventually the bar stagnates, triggering channel bifurcation. Several recent studies seeking to explain river mouth bar formation used this criterion to define fully developed mouth bars (Nardin and Fagherazzi, 2012; Nardin et al., 2013; Leonardi et al., 2013; Mariotti et al., 2013; Canestrelli et al., 2014b). Nonetheless, these studies assume horizontal or quasi-horizontal receiving basins. Esposito et al. (2013) extended this conceptual model to assess bed layering records of sand and mud fractions throughout the bar evolution, establishing that during the ending runaway stage only mud can be deposited over a bar since the ability to transport sand becomes insufficient. We use both models to examine river mouth bar formation under the influence of the bottom slope.

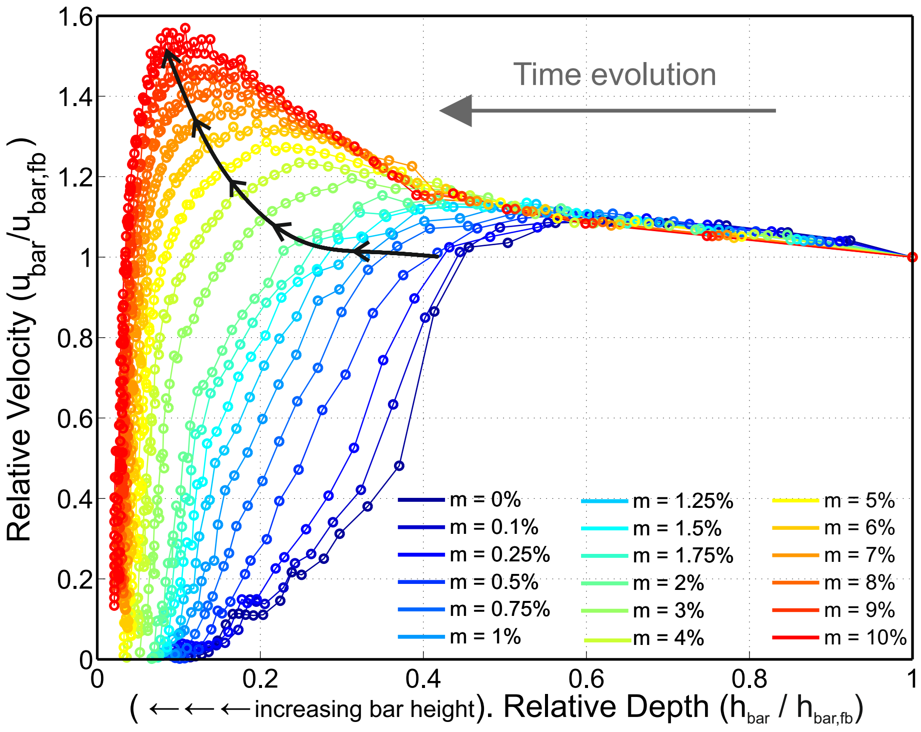

Figure 4.7: Centerline relative velocity over the crest of the river mouth bar as a function of the relative depth over the crest of the bar for different basin slopes, ranging from 0% to 10%. The black line shows the decreasing relative water depth necessary to cause bar stagnation with higher slopes.

We suggest that the contribution of Edmonds and Slingerland (2007) should be extended to account for distinct bottom slopes. Calculating the centerline velocity over the crest of the river mouth bar (u_{bar}) as a function of water depth (h_{bar}) during river mouth evolution provides insight into the bar height that is required to stop progradation. Both variables were normalized by their values in the "frozen bathymetry" scenario ($u_{bar,fb}$ and $h_{bar,fb}$, respectively) (Figure 4.7). For quasi-horizontal cases, there is a sudden drop in the jet velocity over the bar crest as the river mouth bar reaches a height equal to 60% of the initial water depth. This rapid decrease in velocity is due to the high-pressure level over the bar, which forces the flow to bifurcate rather than to flow over the bar and therefore determines bar stagnation (Edmonds and Slingerland, 2007). Thus, our results are concordant with those reported by Edmonds and Slingerland (2007) for quasi-horizontal basin cases. However, this criterion seems to fail for higher bottom slope values: as bottom slope increases, the relative water depth over the bar crest necessary for generating the pressure gradient that is capable of forcing fluid bifurcate around the bar becomes smaller (black line in Figure 4.7).

A qualitative analysis of sediment stratigraphy along the "active bathymetry" simulations shows that the topmost sediment layer, prescribed in our runs as initially uniform and non-cohesive, starts to store over the mouth bar the cohesive volume fraction delivered by the river once the stagnation point is reached (Figure 4.8 (a)). Because the cohesive fraction was initially transferred further seawards, this stratigraphic redistribution of sediment fractions leads to runaway aggradation and bar stagnation. This observation is consistent with the stratigraphic sequences model of Esposito et al. (2013) in river mouth bar evolution under a stationary fluvial regime and with the numerical results from lithologic cross sections of delta deposits of Storms et al. (2007).

We also tested four different suspended sediment loads (0.2+0.1, 0.5+0.1, 0.8+0.1 and 1.1+0.1 kg/m^3 for non-cohesive and cohesive fractions) to calculate the mouth bar formation time (T_{rmbf}) and mouth bar stagnation distance (L_{rmbf}) as a function of the bottom slope. Both variables were normalized by the time and distance computed for the horizontal case in the equilibrium non-cohesive suspended discharge case (Figure 4.9 (a) and (b)). Closely tied to filling in the accommodation space, the modeled dimensionless formation time increased linearly with increasing bottom slope. Moreover, the smaller the solid discharge, the higher the increase in the rate of bar formation time (Figure 4.9 (a)). For milder slopes, the distance to the final river mouth bar location decreases when the basin slope increases; however, we found that for steeper slopes, the distance from the river mouth to the bar crest is independent of the basin slope, displaying asymptotic behavior, for $m > 2\%$. Finally, higher solid discharges caused river mouth bars to form closer to the river mouth (Figure 4.9 (b)).

4.5.2 River mouth bar geometry

River mouth bar results from the constant combination of aggradation and progradation sediment processes. The evolution experienced by the sea bottom for different river mouth slopes (Figure 4.10) can be characterized considering the movement of the bar profile centroid (Figure 4.8 (b) and (c)). The longitudinal and vertical coordinates of the centroid can be computed as:

$$x_c(t) = \frac{\int_0^{\xi_{rmb}} \xi [H(t)+1] d\xi}{A_p(t)}, \quad z_c(t) = \frac{1}{2} \frac{\int_0^{\xi_{rmb}} [H(t)+1]^2 d\xi}{A_p(t)} \tag{4.29}$$

where $A_p(t) = \int_0^{\xi_{rmb}} [H(t)+1] d\xi$ is the area of every longitudinal bar profile, ξ_{rmb} is the dimensionless seawards distance of bar crest, and H is the relative water depth over the bar.

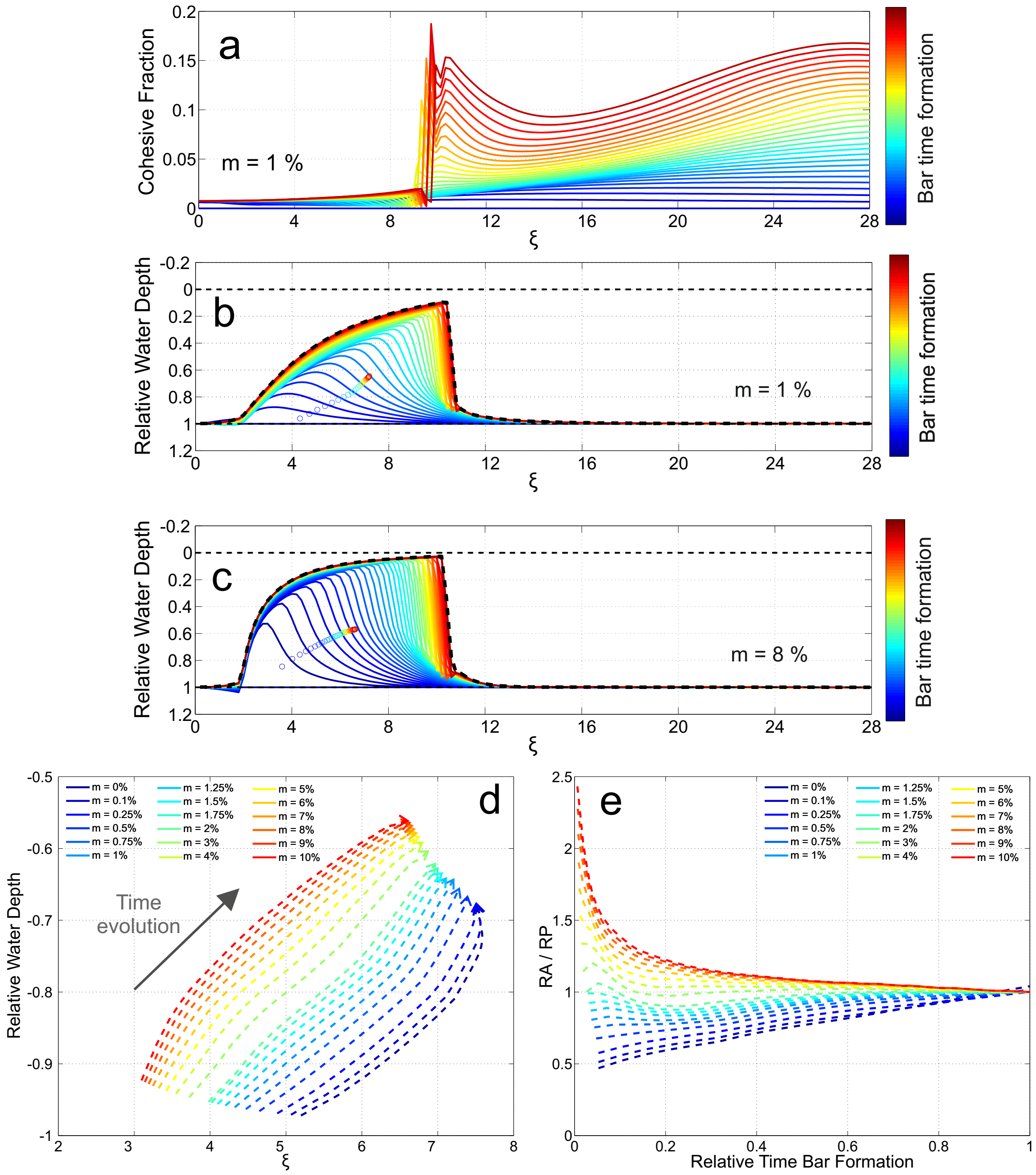

Figure 4.8: (a) Stratigraphic record of the cohesive to non-cohesive sediment ratio in the topmost 20 cm of the bottom over the time of bar formation (shown by the colorbar) along the jet axis for a case with an initial bottom slope of m = 1%. Temporal evolution of a river mouth bar for a bottom slope of (b) $m = 1\%$ and (c) $m = 8\%$. Colored dots depict the location of the centroid of every bar profile at every temporal stage (shown by the colorbar). Black dashed lines define the final bar configuration. (d) Temporal evolution of the centroid location of the river mouth bar for different initial bottom slopes. (e) Temporal evolution of the relative aggradation to progradation rate of the river mouth bar for different initial bottom slopes.

Figure 4.8 (d) depicts the temporal record of the centroid positions for all of the considered slopes. We observe that an increase in the longitudinal coordinate of the centroid leads to bar progradation, whereas an increase in its vertical coordinate implies bar aggradation. To clarify

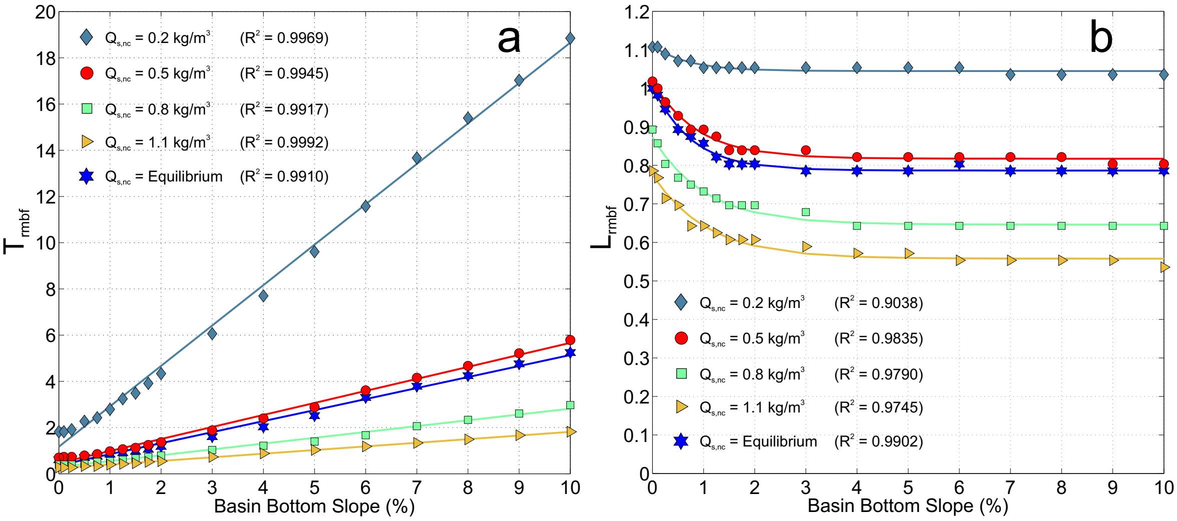

Figure 4.9: (a) Relative time of river mouth bar formation (T_{rmbf}) as a function of basin bottom slope for different suspended load values for non-cohesive sediment. Solid lines represent the best linear regression fit. (b) Relative distance of river mouth bar formation (L_{rmbf}) as a function of the basin bottom slope for different suspended load values for non-cohesive sediment. Solid lines represent the best negative exponential regression fit. All values were normalized using the value of the horizontal bottom and equilibrium non-cohesive suspended discharge case.

which process is more important during bar formation, for every bottom slope, the $x-z$ centroid coordinates were normalized with respect to their total horizontal and vertical displacement over the bar formation period, giving rise to the dimensionless variables RP and RA, respectively. Their temporal evolution provides valuable information about the sedimentological processes that prevail during bar building (Figure 4.8 (e)). Aggradation prevails during the river bar formation period for higher slopes. This is clearly connected with the increased space for sediment infilling due to higher water depth for the steepest profiles. Conversely, for gentler slopes, progradation processes are more relevant, and a larger fraction of sediment will be used to push the bar seawards. Regardless of the initial bathymetric configuration, as the river mouth bar evolves, the relative importance of aggradation and progradation tends to balance when the bar reaches its final configuration.

To characterize the plan view of sediment deposition at the river mouth, we use the first x-axis moment of the normalized bar height distribution defined as (Nardin et al., 2013):

$$I_{x,rmb} = \frac{\int_{\Omega}[1-H]y}{\int_{\Omega}[1-H]} \tag{4.30}$$

where Ω is the half-bar surface. These results are normalized with respect to the equivalent values for the horizontal case, indicated by the subscript “0”. Figure 4.11 (a) shows that the inertia of the bar with respect to the x-axis decreases at higher basin slopes: gentler initial bottom slopes produce high lateral spreading of sediment, while higher slopes reduce lateral sediment delivery. A marked change in the trend of $I_{x,rmb}/I_{x,rmb,0}$ is found for $m = 1\%$, which reveals a direct relationship between sediment delivery and jet stability (Mariotti et al., 2013; Canestrelli et al., 2014b). This can be visually addressed by directly comparing deposition patterns in a horizontal basin (Figure 4.11 (b)) and in a sloping basin (Figure 4.11 (c)). An initial bottom slope of m = 10% leads to an unstable jet (Figure 4.6) that delivers sediments to a vast area across the jet width and not only to the jet edges, giving rise to a compact bar around the x-axis that is similar

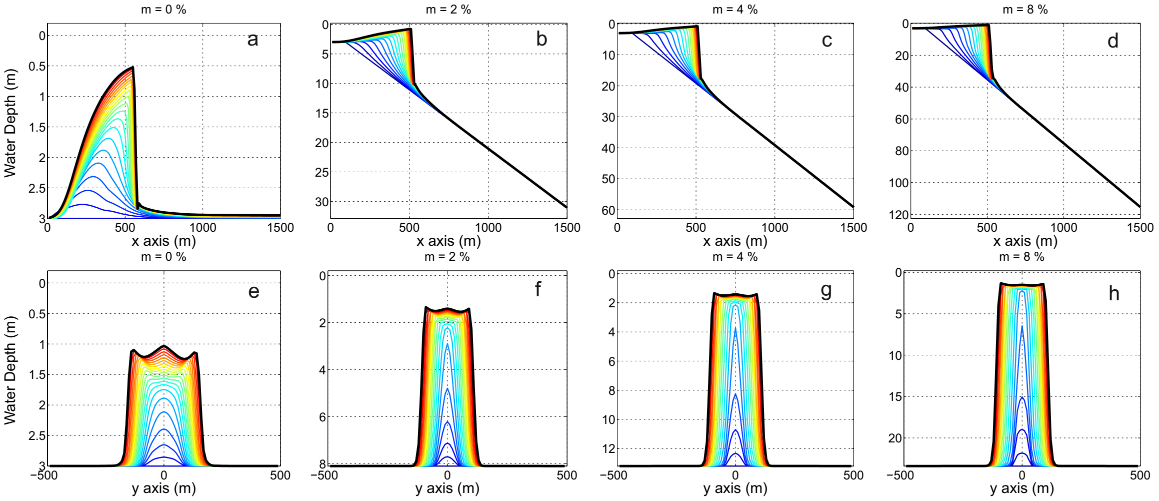

Figure 4.10: Longitudinal (a, b, c, d) and transversal (e, f, g, h) bathymetric profiles of the absolute bar height variation over time (indicated with the color evolution) for different bottom slopes. The transversal section is located 400 m from the river mouth. Black lines indicate the final bar configuration.

to the “lunate" bar described by Wright (1977). Otherwise, in the case of a horizontal bottom, a stable jet tends to concentrate sediment deposition near each side of the jet, where the velocity is lower, forming short and divergent lateral levees. In the seaward direction, the jet centerline is unable to push the material farther, and a “middle-ground" bar, similar to the one defined by Wright (1977), forms.

4.5.3 Theoretical model for bar formation

The theoretical model proposed in Section 4.2 and calibrated for different bottom slopes, using the entrainment coefficient described in Section 4.4.1, can be used to easily predict the deposition and erosion patterns near to the inlet mouth. However, because jet theory cannot account for the feedback influence between the bottom evolution and jet hydrodynamics, it should only be used to predict bed changes when computing the initial rates of erosion and deposition during which the jet remains unaltered. In addition, deposition and erosion processes alter the bathymetry in both the longitudinal and transverse directions, which prevents the use of the similarity hypothesis.

Given the solutions for velocity and concentration along the jet centerline, the amount of material deposited or eroded, per unit area of the bed and unit time, can be obtained by considering the source and sink function (equation (4.4)). A normalized form of this function allows us to compute the rate of changes in bottom depth as:

$$K(\xi,\zeta) = \frac{\partial \sigma}{\partial t}\frac{b_0}{c_0 h_0 u_0} = \frac{\gamma C(\xi) G(\xi)}{1-p}\left[1-\phi^2 F^2(\xi) U^2(\xi)\right] \tag{4.31}$$

where σ is the amount of material per unit area of the bottom (kg/m^2), p is the porosity of the bottom, and K is a dimensionless deposition and erosion rate. The threshold value of the flow velocity for sediment entrainment into suspension ($u_{cr,s}$) has been computed using the empirical criteria reported by Niño et al. (2003) for a bed covered with particles at the same size as those in suspension. We computed the fall velocity of sand particles in the marine environment (w_s) using the expression proposed by Soulsby (1997).

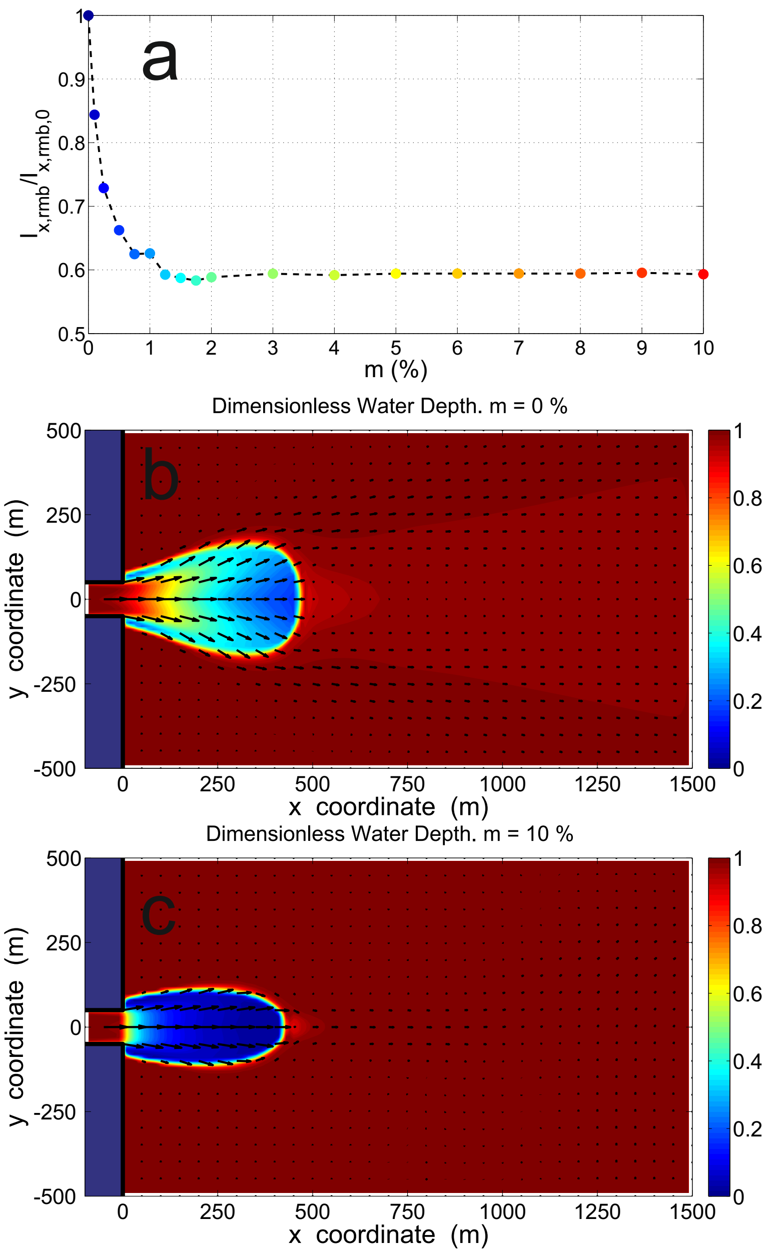

Figure 4.11: (a) Spreading bar factor normalized with respect to the spreading bar factor for the horizontal case as a function of initial bottom slope. Dimensionless water depth map of a river mouth bar forcing the flow to bifurcate around it for cases with initial bottom slope of (b) 0% (stable jet) and (c) 10% (unstable jet). The depth-averaged velocity vectors are superimposed.

Here, we adopt the same conditions simulated with Delft3D, however without taking into account the cohesive fraction for simplicity. Despite the theoretical model does not resolve the fully formed river mouth bar, the initial trend in erosion/deposition consequent to a riverine discharge shows a high dependence on bottom slope (Figure 4.12). An initial erosive region next to the river mouth always appears. The extension of this region varies in accordance with changes in jet velocity, as described in Section 4.4.1. The initial sharp drop in the axial jet velocity for the steepest slopes gives rise to shorter erosive zones due to the reduced ability of the flow to entrain sediment into suspension. On the contrary, for the milder slopes, the larger quantity of eroded material close to the outlet is responsible for higher deposition rates downstream. For all cases, maximum deposition occurs along the two sides of the jet centerline, where elongated lateral shoals arise. These shoals eventually merge into a central bar at a distance that decreases with increasing bottom slope (black dots in Figure 4.12). Moreover, the deposition rate in this central bar increases with increasing bottom slope. Finally, because jet spreading increases as bottom slope decreases, the lateral diffusion of sediments is enhanced, and a wider depositional pattern arises for milder slopes.

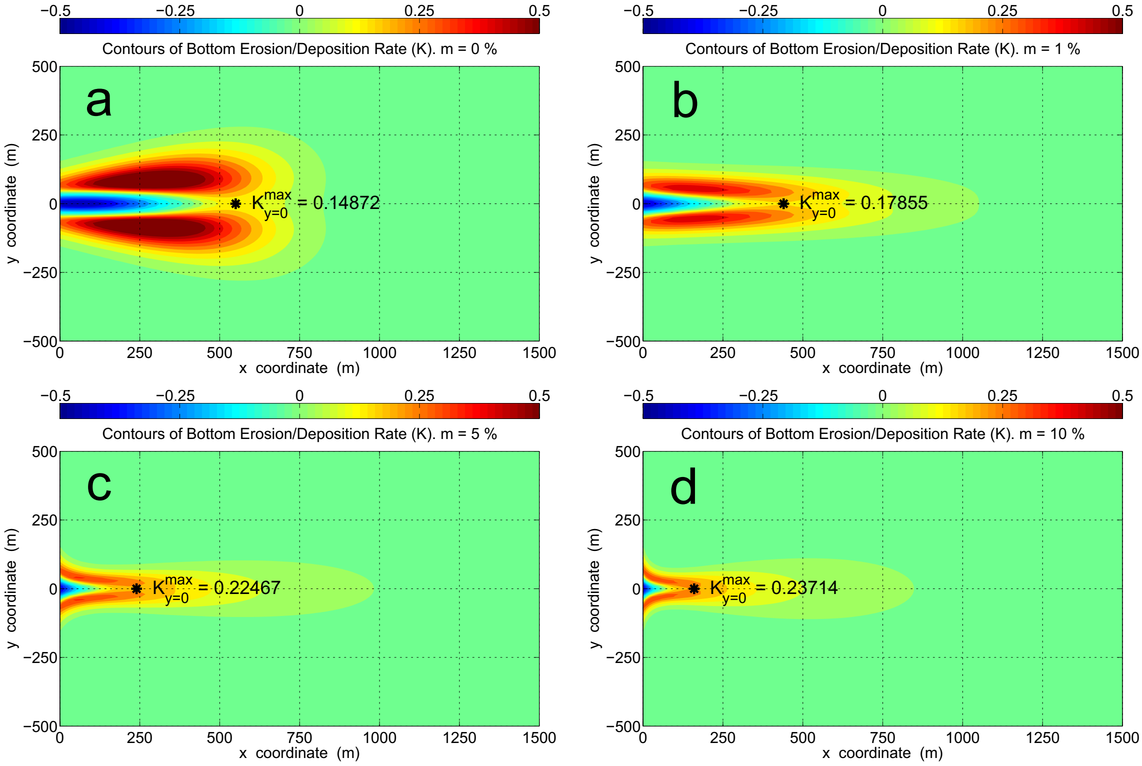

Figure 4.12: Theoretical solutions for normalized fields of bottom deposition and erosion thickness rates (K) for different basin bottom slopes: (a) $m = 0\%$, (b) $m = 1\%$, (c) $m = 5\%$, and (d) $m = 10\%$. The river discharge properties are $c_0 = 0.5$ kg/m^3, $b_0 = 50$ m, $h_0 = 3$ m and $u_0 = 1.5$ m/s. The black dots depict the location of the maximum deposition rate along the centerline.

These theoretical results are in good qualitative agreement with those obtained using Delft3D for mild slope cases. Both morphological models predict a wide depositional pattern characterized by the formation of prominent lateral shoals that merge in a central bar seaward. Conversely, for steeper slopes, the theoretical model is unable to capture jet instabilities and the resulting morphologies related to this meandering dynamic. However, despite this fact, both models show a more elongated and concentrated form along the jet axis in the steepest cases.

4.6 Discussion

4.6.1 Application to natural river mouths and deltas

Due to the simplified forcings and idealized geometrical configuration adopted in our simulations to exclude site-specific conditions, the above results are not expected to reproduce the conditions of a real location. Alternatively, this work is intended to provide a theoretical framework for river mouth bar formation, under different receiving basin slopes, that is potentially applicable to fluvially dominated mouths, which are typical of rivers entering enclosed bays, microtidal lakes, lagoons or reservoirs. Some representative natural, gently sloping, river-dominated deltas around the world (with slopes less than 0.01%) are presented by Edmonds and Slingerland (2007) and Caldwell and Edmonds (2014); these include, among others, the Atchafalaya Delta, Apalachicola Delta, Mossy Delta, Wax Lake and Laitaure Delta. In contrast, steeper slopes are generally typical of Gilbert deltas. These deltas generally occur in inefficient sediment dispersal systems with low tide and wave energy, where sands and gravels are deposited a short distance from the effluent outlet because of the sudden decrease in velocity (and bed shear stress) caused by a sudden increase in water depth (Orton and Reading, 1993). Most of the Mediterranean drainage network is made of rivers that, during their seasonal flood events, share a large degree of similarity and comply with the simulated conditions in the steeper cases of this work (Urgeles et al., 2011). Their water discharges are low on a mean annual basis, but they exhibit a marked seasonal variability and the drainage basins have undergone numerous catastrophic floods in response to torrential rains (Brázdil et al., 1999). Examples of such deltas fed by torrential rivers were reported by Bárcenas et al. (2015) along the coast of the Alboran Sea (western Mediterranean Basin), characterized by low wave energy and microtidal conditions (Ortega-Sánchez et al., 2014; Lobo et al., 2014). A total of twelve deltaic systems were identified related to the following rivers: Güi, Torrox, Chillar, Jate, Seco, Verde, Guadalfeo, Gualchos, Haza de Trigo, Albuñol, Huarea and the Adra river. A broad range of bathymetric profiles exists in these systems, with slopes ranging from 3.5% (Güi River) and 11.4% (Huarea river), though most are below 8%. Sediment discharge during specific flood events in these Andalusian river systems flowing into the Alboran Sea can be volumetrically more important than total sediment discharge during the rest of the year. These floods events, frequently considered as catastrophic with maximum river discharges exceeding 1000 m^3/s (Poesen and Hooke, 1997), are repetitive and consequently play a major role in the development of deltaic bodies (Liquete et al., 2005). In addition, the river basins are located in the hottest, driest and less vegetated regions of the Iberian Peninsula, providing greater sediment availability. These factors lead to significant episodes of sediment discharge, with values of sediment flux up to 630 kg/s (Lobo et al., 2014). In these cases, the formation of central river mouth bars is expected after flood events as the ones simulated in this work. Meanwhile, during dry periods the oceanographic regime (even a low energy one, as in the Alboran Sea) plays a major role in re-shaping these sedimentary deposits. Thus, the distinctive geometric patterns of these deltaic systems, linked to short, mountainous streams with strong seasonal behavior, are related to central bar deposits during flood events combined with sediment redistribution during dry periods.

The theoretical solutions for jet dynamics provided in Section 4.2 have been updated to include the hydrodynamic implications of bottom slope on jet dynamics. To the best of our knowledge, published experimental works related to jet hydrodynamics are mainly limited to horizontal receiving basins (Giger et al., 1991; Dracos et al., 1992; Rowland et al., 2009, 2010; Landel et al., 2012). We used numerical experiments with Delft3D as a feasible method of revealing the direct relationship between bottom slope and the ability of a jet to capture surrounding ambient water. This allowed us to calibrate the entrainment coefficient for different basin slopes with different friction coefficients. The value obtained in our numerical simulations for the horizontal case takes the values 0.031, 0.028 and 0.026 for C_z = 40, 55 and 70 $m^{1/2}s^{-1}$, respectively (red lines in Figure 4.3), agree with those observed experimentally by Kotsovinos (1975) ($\alpha = 0.033$), Fischer (1979) ($\alpha = 0.035$), Ramaprian and Chandrasekhara (1985) ($\alpha = 0.034$), Andreopoulos et al. (1986) ($\alpha = 0.036$) and Agrawal and Prasad (2003) ($\alpha = 0.041$). Regarding our theoretical results, the entrainment coefficient in the horizontal case was found to be $\alpha_{JT,0} = 0.002$ regardless of the bottom friction (blue lines in Figure 4.3), which is much smaller than those proposed by Özsoy and Ünlüata (1982) ($\alpha = 0.05$) and Wang (1984) ($\alpha = 0.075$). However, our value agrees with the order of magnitude recommended by Nardin et al. (2013) ($\alpha = 0.005$), who also compared Delft3D and theoretical results for a turbulent jet.

Despite not predicting the unsteady jet features, the revised theoretical model proposed in this work can be used to easily determine mean quantities of a river discharging in basins with arbitrary slope, such as diffusion of conservative pollutants and the initial deposition stages of suspended sediments influenced by gravitational settling (Özsoy, 1986). This is possible since the meandering structure of an unstable jet has little influence on its mean structure (Rowland et al., 2009). Due to the limitations of this theoretical tool, it should be used with care when applied to practical purposes. Nevertheless, because of its simplicity and computational efficiency, it is useful as a first-level modeling tool to provide qualitative information in pre-designing of river projects.

Additionally, this work has implications for coastal systems restoration projects. Currently, numerous deltas are experiencing land loss due to anthropogenic and natural forcings, mainly due to dam constructions, land subsidence and sea-level rise (Bianchi and Allison, 2009; Edmonds, 2012). The main idea of many natural restoration projects on adjacent coastlines consists of delta-building through sediment diversions from a main channel into basins subject to erosion or subsidence (Paola et al., 2011). As shown by our morphological results, basin slope is a key parameter for delta restoration because it determines the spatial distribution of the diverted sediment. Whereas stable jets favor the formation of short and divergent channels around a central bar that laterally deliver material and hence optimize coast nourishment, unstable jets tend to channelize the flow seawards by suppressing these bifurcations. Since basin slope is initially a fixed parameter, when it leads to jet instability, the optimal solution from a land-building perspective would be to maximize S_ξ and minimize Re_ξ. This can be achieved by reducing the discharge velocity or increasing the grain size of the delivered sediment to obtain higher friction effects over the discharge.

Looking forward, the evolution of an entire delta is dictated by the initial morphology of the mouth bar (Edmonds and Slingerland, 2007). Different deltaic systems will be produced when upscaling our morphological results under different basin slopes. Related to our research topic, Storms et al. (2007) modeled the formation of entire deltas in fluvially dominated systems with shallow or deep receiving basins. In the former case, corresponding to our gentle slope simulations, they found a pattern of bifurcated channels and shoals that accreted both seaward and crosswise. In steeper basins, the reduced capacity to produce jet bifurcations would give rise to the classic birdfoot delta morphology that progrades rapidly in the seaward direction through channel margins breaching.

4.6.2 Comparison with previous works on bar formation

Based on the results of our simulations, the following two well-stablished theories regarding sediment-laden turbulent jets in horizontal basins were addressed, highlighting the influence of a sloping bed.

1. The stability criterion for turbulent jets proposed by Canestrelli et al. (2014b) was analyzed. They evaluated the importance of the friction over the jet dynamics based on stability and Reynolds numbers at the river mouth. They found that high bottom friction leads to jet

stability, whereas low bottom friction leads to low stability numbers and meandering jets. However, for a non-horizontal basin, we observed that jet stability classification by means of local parameters remains insufficient. It was proven that two effluents with identical mouth conditions may exhibit completely different jet dynamics in open waters, depending on the bed slope of the receiving basin: either a stable or unstable jet can develop. We suggest that the main reason for this alteration in jet stability is the reduction in the bottom friction term as the water depth increases in the momentum conservation equations (4.16) and (4.17). Because this term is inversely proportional to the total water depth, sloping bed basins will alter the friction experienced by a jet along its axis. Thus, in cases where the effluent jet discharges into a sloping basin, stability analysis should be performed section-by-section downstream.

According to the decisive role of friction in jet dynamics, we can establish an analogy between the stability character of a jet and the dynamic classification of homopycnal effluents proposed by Wright (1977). A stable jet can be associated with friction-dominated effluents, whereas an unstable jet can be associated with inertia-dominated effluents. Additionally, the morphological units resulting from our numerical simulations display a high degree of similarity with Wright's conceptual depositional patterns. Stable jets produce a triangular "middle-ground" accompanied by short and divergent subaqueous levees (Figure 4.11 (b)). On the contrary, a slender "lunate" mouth bar results from unstable jets (Figure 4.11 (c)). We also note that our morphological results for unstable jets differ from those reported by Canestrelli et al. (2014b), who suggested that jet instability increases the tendency for sediment transfer at the margins of the jet. This tendency would create elongated channels that are confined by lateral levees instead of central deposits that are concentrated along the x-axis. This discrepancy can be explained using the conceptual model for sediment eddy diffusivity proposed by Mariotti et al. (2013) with Delft3D. This conceptual model establishes that the ability of a jet to spread sediment particles laterally and thus promote levee formation is dependent on the relationship between a sediment settling timescale ($T_D = h/(2w_s)$), i.e., the time needed for the sediment to reach the bed, and a meandering timescale (T_E), i.e., the time needed for a meander to complete a half revolution. Whereas values of $T_D/T_E \sim 1$ maximize the capacity of the jet to spread sediment laterally and thus form lateral levees, values of $T_D/T_E \ll 1$ or $T_D/T_E \gg 1$ favor central deposits. Based on the similar energy spectra of turbulent lateral fluctuations for various bottom slopes (Figure 4.6 (inset)), we assume that the bottom slope does not significantly influence T_E. However, because T_D is directly proportional to the total water depth, it increases as the bottom slope increases. In this case, sediments move back and forth within an eddy, resulting in a smaller eddy diffusivity and creating a central deposit.

2. The relative mouth bar height necessary to stop its progradation, estimated around 60% for quasi horizontal basins by Edmonds and Slingerland (2007), was addressed. The relative height that the mouth bar has to reach to force the flow to bifurcate around it, hence stopping progradation, exceeds 60% for high bottom slopes. For instance, at the highest bottom slope considered in the present work (10%), the bar would not completely form until the water depth over it is $\leq$ 10% of the original depth, as opposed to the 40% required for the horizontal case. Additionally, this higher relative mouth bar height is accompanied by an increase (up to 1.5-fold for the higher bottom slope) in jet velocity. This explains why the lower initial velocities found on discharges into steeper basins produce mouth bars at the same distance as those created by higher initial jet velocities in horizontal basins (Figure 4.4 (b)). This flow acceleration is shown in Figure 4.7, where the peak of $u_{bar}/u_{bar,fb}$

increases with increasing bottom slope. The higher accelerations present in basins with steeper bathymetry counterbalance the effects of low initial velocity. An increase in bottom shear stress increases sediment transport and, ultimately, leads to bar formation farther from the location than would initially be expected.

In summary, although we have considered a limited spectrum of river discharge conditions and sediment properties, the results of the present work (1) corroborate the theories of Edmonds and Slingerland (2007) and Canestrelli et al. (2014b) regarding bar stagnation point and jet stability in horizontal and quasi-horizontal basins and (2) reveal the need to update these criteria to account for the influence of basin slopes on jet dynamics.

4.7 Conclusions

In this work, we explored how receiving basins with different slopes affect the hydrodynamic structure of an entering turbulent jet and its consequences on river mouth bar formation. Both a theoretical model and the hydro-morphodynamic software Delft3D were employed to simulate a river-dominated system devoid of tides and waves.

We show that the entrainment coefficient displays a power law increase as the slope of the receiving basin increases. Regarding the mean properties that characterize a turbulent jet, we found high non-linearity with respect to bottom slope. A marked change in the jet trend was found around a basin slope of $m = 1\%$. As a general rule, while velocity increases and jet width decreases up to a basin slope of $m = 1\%$, beyond this value velocity decreases and the jet widens. Since the theoretical model can only capture the mean properties of a jet, advanced analyses were carried out with the aid of Delft3D. Accordingly, we observed that jet stability can be altered depending on the slope of the basin where the river debouches. We suggest that the local stability analysis proposed by Canestrelli et al. (2014b) must be extended along the jet axis by determining section-by-section a Reynolds number (Re_ξ) and a stability parameter (S_ξ) that take into account variations in bathymetric profile. Analyses of the turbulent structure of unstable jets showed a distinct energy peak around $S_t \simeq 0.1$ that corresponds to the passage frequency of 2D vortical structures.

Regarding our morphological results, we observed that shear-induced lateral instability dominates sediment delivery and the resulting deposition patterns. While stable jets give rise to “middle-ground" bars accompanied by bifurcating channels, a “lunate" mouth bar results from unstable jets. Moreover, the relative importance of the sedimentary processes responsible for mouth bar formation changes with the bottom slope: in basins with milder slopes progradation processes predominate, whereas aggradation processes prevail in steeper basins. Mouth bars require more time to form in steeper basins due to the higher accommodation space of the receiving basin. In general, the time needed for bar formation normalized by that obtained for a horizontal basin increases linearly at a higher rate for higher entering sediment discharges. The distance at which bars form, which is higher for lower entering sediment loads, decreases as the basin slope increases up to a slope of 2%. Beyond this slope, the bar distance is independent of basin slope, despite the lower velocities of jets in steeper basins. This is due to the progressive increase in jet velocity that occurs during bar formation. This acceleration is higher for higher slopes, which allows the bar to be pushed further. Related to this mechanism of bar formation, we found that the necessary relative bar height that forces the flow to bifurcate around it and makes the bar stagnate increases with higher bottom slope. Hence, whereas Edmonds and

Slingerland (2007) established that this depth should be $\leq 40\%$ for quasi-horizontal cases, in the present work this value dropped to 10% for the highest slope ($m = 10\%$).

Chapter 5

Influence of river mouth geometry on mouth bar morphology and discharge hydrodynamics

River mouth bars are strategic morphological units primarily responsible for the development of entire deltaic systems and coastline configuration. Although many works during last decades analyzed the effects of factors such as tides, wind waves or sediment properties, the control that the geometrical configuration of the river mouth exerts on the sedimentary processes remains unclear. This Chapter addresses the role of the receiving basin slope and the river discharge angle in the hydrodynamics of an exiting sediment-laden turbulent jet and in the resulting mouth bar morphodynamics using Delft3D. Keeping all other factors constant, we find that varying the discharge angle and the receiving basin bottom slope the turbulent jet changes its direction and spreading rate. We also establish a theoretical framework for the specific morphology of the mouth bar as a function of the river mouth geometry, highlighting its importance for properly designing managing strategies. Finally, predicted mouth bar morphologies are compared with good agreement to river mouths in real locations.

5.1 Introduction

Deltaic environments and river mouths host numerous biological and economical activities and, therefore, represent some of the most populated ecosystems on Earth (Bianchi and Allison, 2009; Syvitski et al., 2009). Their social implications led to an increasing study of delta formation and evolution in recent years (Edmonds and Slingerland, 2007; Fagherazzi and Overeem, 2007; Geleynse et al., 2011; Fagherazzi et al., 2015). Particularly, river mouths play a critical role for these ecosystems since they constitute the dynamic dispersal exit of the sediment-laden turbulent jet that results in depositional river mouth bars (Bates, 1953; Coleman, 1976; Wright, 1977). These river mouth bars are a key geomorphological process on delta evolution(Edmonds and Slingerland, 2007). For a detailed review of the physics of these river mouth deposits, we refer the reader to Fagherazzi et al. (2015), who combine theoretical approaches, experimental data, field observations, and numerical modeling to obtain novel process-based results.

Despite the current ability to simulate river mouth bar genesis, the geometric influence of the river mouth remains unclear. Previous works focused on river mouth bars dynamics are limited to river discharging orthogonally to the coastline and with gently sloping basins (Edmonds and Slingerland, 2007; Nardin and Fagherazzi, 2012; Leonardi et al., 2013). However, steeply dipping forest-dominated deltas can be found in both marine and lacustrine environments characterized by low-energy basins where wave and tidal influences can be neglected (Postma, 1995; Viparelli et al., 2012; Bárcenas et al., 2015). The evolution of these deltaic systems is distinct from areas with gently sloping basins (Storms et al., 2007). Besides, satellite image of fluvial systems reveals that the river discharge angle can be significantly lower than 90° with respect to the shoreline.

To address these gaps, here we extend the work by Jiménez-Robles et al. (2016), where the effects of the receiving basin slope on sediment-laden turbulent jet hydrodynamics and their connection with related deposition patterns were tackled. Now, we investigate how different geometrical configurations of the river mouth alters the jet hydrodynamics and river mouth bars evolution using Delft3D to mimic a river debouching into a large body of quiescent water in the absence of Coriolis effects, buoyancy forces, tides, and wind waves. The river mouth geometry will be characterized by i) the river discharge angle (α) and ii) the receiving basin bottom slope (m) (Figure 5.1).

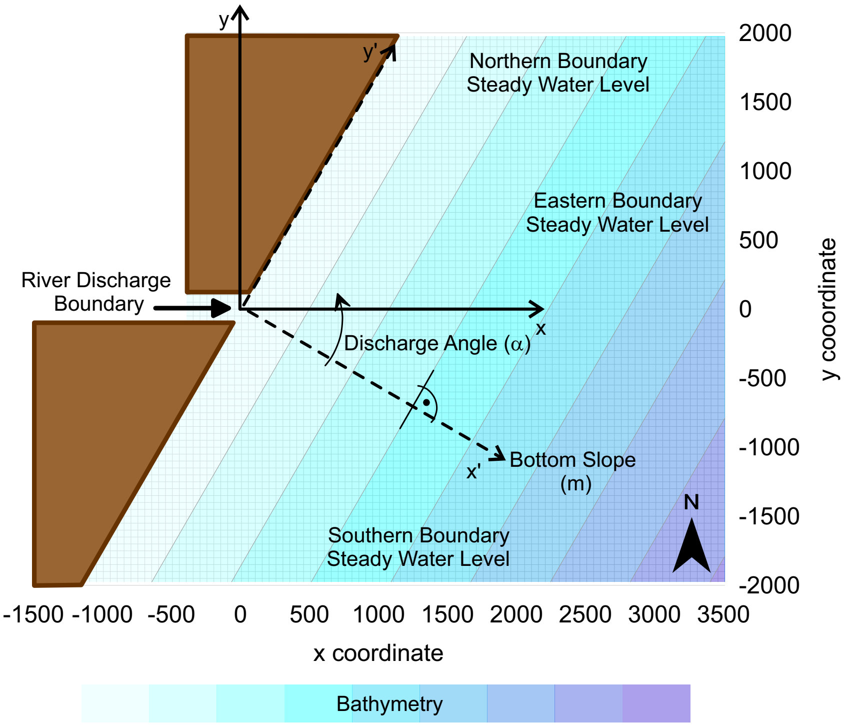
y
y'
Northern Boundary
Steady Water Level
Eastern Boundary
Steady Water Level
River Discharge
Boundary
x
Discharge Angle (α)
x'
Bottom Slope
(m)
N
Southern Boundary
Steady Water Level
2000
1500
1000
500
0
-500
-1000
-1500
-2000
y cooordinate
-1500 -1000 -500 0 500 1000 1500 2000 2500 3000 3500
x coordinate
Bathymetry

Figure 5.1: Sketch of the computational domain and boundary conditions.

5.2 Methods

We conducted hydrodynamic and morphodynamic simulations using the high-resolution, fluid dynamics model Delft3D (Lesser et al., 2004) that simulate nonsteady flows, sediment transport phenomena, and related bathymetric changes in a coupled modality. This model has been recently used to investigate river mouth jet hydrodynamics and sediment depositional patterns (Edmonds and Slingerland, 2007; Nardin and Fagherazzi, 2012; Leonardi et al., 2013; Nardin et al., 2013; Canestrelli et al., 2014b; Jiménez-Robles et al., 2016). We assume a depth-averaged schematization of the problem based on previous theoretical, experimental, and numerical works on planar jets (Abramovich, 1963; Özsoy and Ünlüata, 1982; Ortega-Sánchez et al., 2008; Rowland et al., 2010). For a detailed discussion on the methods of Delft3D-FLOW see Deltares (2013).

5.2.1 Hydrodynamic model

Delft3D solves the unsteady shallow water equations. The continuity and horizontal momentum equations read as:

$$\frac{\partial \eta}{\partial t}+\frac{\partial hu}{\partial x}+\frac{\partial hv}{\partial y}=0 \tag{5.1}$$

$$\frac{\partial u}{\partial t}+u\frac{\partial u}{\partial x}+v\frac{\partial u}{\partial y}=-g\frac{\partial \eta}{\partial x}+g\frac{u\sqrt{u^2+v^2}}{C_z^2 h}+\epsilon_f\left(\frac{\partial^2 u}{\partial x^2}+\frac{\partial^2 u}{\partial y^2}\right) \tag{5.2}$$

$$\frac{\partial v}{\partial t}+u\frac{\partial v}{\partial x}+v\frac{\partial v}{\partial y}=-g\frac{\partial \eta}{\partial y}+g\frac{u\sqrt{u^2+v^2}}{C_z^2 h}+\epsilon_f\left(\frac{\partial^2 v}{\partial x^2}+\frac{\partial^2 v}{\partial y^2}\right) \tag{5.3}$$

where η is water level with respect to datum, h is the water depth , u an v are the depth-averaged velocities in x and y directions respectively, t is time, g is the gravitational acceleration, C_z is the Chézy friction coefficient and ϵ_f is the horizontal turbulent eddy viscosity coefficient. The latter is computed through the Horizontal Large Eddy Simulation (HLES) technique (Uittenbogaard and Van Vossen, 2004). This closure model includes contributions from horizontal turbulent motions and forces that are not resolved on the original grid by adding a subgrid scale horizontal eddy-viscosity to a constant or space-varying, user-defined background value.

5.2.2 Morphological model

The sediment transport relations of non-cohesive sediment in situations without waves for bed load (van Rijn, 1984b) and suspended load (van Rijn, 1984c) are added directly into the hydrodynamic solver.

The bed load transport rate (S_b) is given by:

$$S_b=\begin{cases}0.053\sqrt{\Delta g D_{50}^3}D_*^{-0.3}T^{2.1} & \text{for } T<3.0\\ 0.1\sqrt{\Delta g D_{50}^3}D_*^{-0.3}T^{1.5} & \text{for } T\geq 3.0\end{cases} \tag{5.4}$$

where $\Delta=(\rho_s-\rho_w)/\rho_w$ is the submerged specific gravity of a sediment with density ρ_s, ρ_w is water density, D_{50} is the median sediment diameter, D_* is a non-dimensional particle diameter, and T is the transport stage parameter according to Shields curve.

Suspended load transport is computed by solving the depth-averaged simplified form of the general three-dimensional advection-diffusion equation:

$$\frac{\partial hc}{\partial t}+\frac{\partial huc}{\partial x}+\frac{\partial hvc}{\partial y}=h\left[\frac{\partial}{\partial x}\left(\epsilon_s\frac{\partial c}{\partial x}\right)+\frac{\partial}{\partial y}\left(\epsilon_s\frac{\partial c}{\partial y}\right)\right]+hS \tag{5.5}$$

where c represents depth-averaged suspended sediment concentration, ϵ_s is the sediment eddy diffusivity and S is the source term modeling the net mass flux between the water column and the bed.

Spatial gradients in bed load transport and the source and sink terms associated with suspended sediment fluxes ultimately determine the possible changes in bed bathymetry. The Exner equation (Paola and Voller, 2005) is employed to quantify them:

$$(1-\epsilon_b)\frac{\partial z_b}{\partial t} = -\frac{\partial S_{b,x}}{\partial x} - \frac{\partial S_{b,y}}{\partial y} + S \tag{5.6}$$

where ϵ_b is the bed porosity, z_b is the bed level, and $S_{b,x}$ and $S_{b,y}$ are the total sediment bed transport per unit width in the x and y directions respectively.

5.2.3 Experimental setup

Plane jet hydrodynamics and river mouth bar morphodynamics in fluvially dominated deltas are computed in a schematized one-layer rectangular computational domain (Figure 5.1). The grid cells are aligned with the river axis, giving rise to a perfectly orthogonal mesh grid. To simulate the river, a rectangular 200 m wide and 3 m depth channel (h_0) is carved at the western boundary into a sandy coast. We prescribe open boundaries of temporally and spatially constant water surface elevations at the seaward, northern and southern boundaries, whereas at the channel boundary we specify a temporally constant river discharge flux ($u_0 = 1\ m/s$) that carries a noncohesive sediment load of a single characteristics ($D_{50} = 125\ \mu m$ and ρ_s=2650 kg/m^3). Whereas the bedload exiting through the outlet is assumed to perfectly adapt to the local flow conditions, the river discharge carries a user-defined discharge noncohesive suspended load at its equilibrium concentration profile. This latter condition prevents accretion or erosion near the model boundaries. The receiving basin that mimics the continental shelf is composed of 5 m thick, erodible, noncohesive sediment with characteristics similar to the sand particles carried by the river. Bed roughness is set to be spatially and temporally constant with a Chezy value of 30 $m^{1/2}s^{-1}$ and the background horizontal eddy viscosity and diffusivity values are set equal to 1 m^2s^{-1}. To reduce differences between the timescales at which morphological changes take place in relation to hydrodynamic changes, a morphological acceleration factor of 20 is used.

Two reference systems are used in our calculations (Figure 5.1): i) $x-y$, the grid fixed reference system and ii) $x'-y'$, the discharge angle turned reference system, in which x' is directed along the basin maximum slope and y' is located above the shoreline. The discharge angle α is geometrically defined as the counter rotation formed by x axis respect to x' axis, i.e., the complementary angle between river axis and the main coastal alignment. Different combinations of basin bottom slope m = [0, 0.5, 1, 2, 3, 4, 5]% and discharge angles α = [0, 10, 15, 20, 30, 40, 45, 50, 60]° produced 63 different model runs. These simulations were carried out on the basis of the work of Jiménez-Robles et al. (2016), who performed sensitivity analysis to ensure that the general trend followed by the hydrodynamic and morphodynamic results do not show any deviation from a qualitative point of view for different values of the numerical parameters. Finally, to meet stability and accuracy requirements of the numerical scheme, the time step was varied to comply with the Courant-Friedrichs-Lewy condition.

5.3 Jet hydrodynamic

The physics of the problem suggests that, for a given river discharge, changes in expanding turbulent jets should be a function of the basin geometry. By varying the discharge angle and the basin slope significant changes over the jet dynamics appear: the jet direction and the planform shape are highly altered (Figure 5.2). We analyze the hydrodynamic results after 24h of simulation when the model is at steady state.

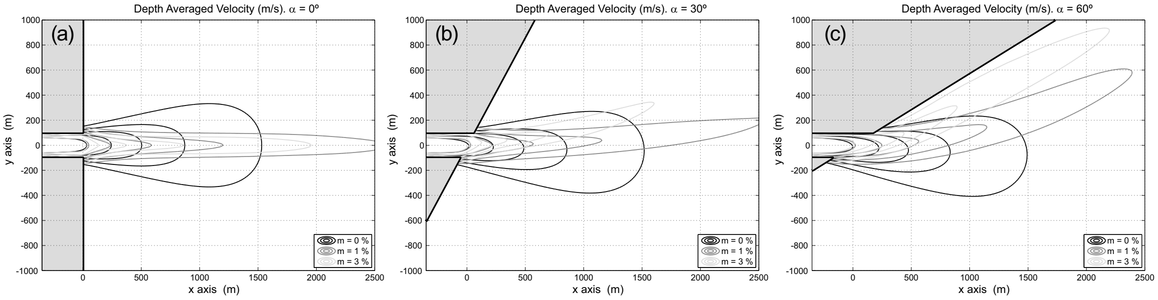

Figure 5.2: Depth-averaged velocity contours lines for different discharge angles ((a) $\alpha = 0^{\circ}$, (b) $\alpha = 30^{\circ}$ and (c) $\alpha = 60^{\circ}$) and basin slopes (m =0, 1 and 3%). In every jet, the velocity contours refer to 1, 0.8, 0.6, 0.4 and 0.2 m/s, being the $0.2m/s$ contour the external one.

Figure 5.3(a) shows the path followed by the jet axis once it debouches into the receiving basin. The interplay between basin slope and discharge angle leads to a deflection of the river jet towards lower depths. The deflection increases for high discharge angles and high basin slope combinations. On the contrary, low discharge angles prevent jet deflection independently of the basin bottom slope (Figure 5.2(a) and Figure 5.3(a) solid black lines). The deflection experienced by the jet is computed as the angle between the x axis and the line that connects the reference system origin and the point of the the jet axis with a velocity equal to 20% the outlet velocity ($u_{jet,20}$):

$$D_R = \arctan\left(\frac{y_{u_{jet,20}}}{x_{u_{jet,20}}}\right), \tag{5.7}$$

where (D_R) is the deflection rate, and $x_{u_{20}}$ and $y_{u_{20}}$ are the coordinates of the $u_{jet,20}$ point. Results from Figure 5.3(b) reveal that the discharge angle is triggering factor for jet deflection, whereas once the discharge angle favors the jet deflection, the basin slope acts as an amplifying factor. However, this increasing jet deflection trend is asymptotic due to the presence of the coastline, which avoid an indefinitely increasing deflection rate and the jet remains laterally confined (see Figure 5.3(b) dotted black line).

River mouth geometry also have a second effect on the river jet. The increase in basin bottom slope results in a lower lateral spreading of the jet (Figure 5.3(c)) due to the decreasing influence of bottom friction over the jet structure in higher water depths (Leonardi et al., 2013; Jiménez-Robles et al., 2016). To compute jet spreading factor (S_R) we adopt the relative distance of the distance measured along the jet axis where the jet velocity equals 20% of the outlet velocity ($d_{u_{jet,20}}$) affected by the the relative water depth at this point ($h_{u_{jet,20}}$). We include the water depth to take into account the influence of the bathymetric changes and the vertical expansion of the jet. Both variables are normalized with respect to the values in the basis case in which $\alpha = 0^{\circ}$ and $m = 0\%$ (denoted by the subscript 0). It reads as:

$$S_R = \frac{d_{u_{jet,20_0}}}{d_{u_{jet,20}}}\frac{h_0}{h_{u_{jet,20}}}. \tag{5.8}$$

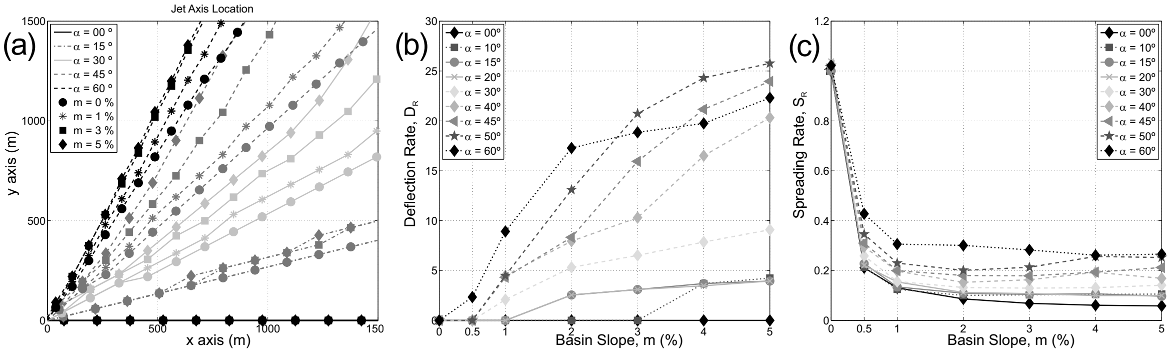

Figure 5.3: (a) Jet axis path in the receiving basin with respect to the fixed reference system (x-y) for different discharge angles and basin bottom slopes. (b) Deflection Rate for different discharge angles and basin bottom slopes. (c) Spreading Rate for different discharge angles and basin bottom slopes.

With this definition of the S_R, for the case of two jets with similar plan shapes and different basin slopes, a lower spreading (elongated jet) is experienced for the jet in the higher bottom slope case (its spreading would be much higher if the bottom slope reduces and a rounded jet arises). Furthermore, Figure 5.3(c) shows that for a given value of α, jet spreading highly decreases for increasing slopes up to 1%. Beyond this value S_R remains approximately constant due to the deflection experiences by the jet towards lower water depths.

5.4 River mouth bar morphology

Numerical simulations of bar formation under the influence of river mouth geometry result in five possible river mouth morphologies: central river mouth bar with or without lateral levees, side bar with or without lateral levees, and sand-spits (Figure 5.4).

In analogy with Edmonds and Slingerland (2007) we consider the bar to be fully developed when it forces the flow to change its initial direction. Whereas the central and sided bars make the flow bifurcate around them, the sand spit produces a complete deviation of the jet towards the direction perpendicular to the coastline. Similarly to Nardin and Fagherazzi (2012), the projection along the x' axis of the top part of the bar with respect to the river mouth determines if the final morphology is a central or sided bar. We define a central bar when its projection is located inside the river mouth, and sided bar when it falls outside.

The influence of the basin geometry on jet hydrodynamics marks the morphological evolution of a mouth bar. For low discharge angles the jet does not experience deflection and a central river mouth bar emerges. In this case, a higher bottom slope promotes jet narrowing, favoring the lateral deposition of sediment close to the jet margins. It allows a configuration in which elongated levees emerge first channelizing the jet and a lengthened mouth bar eventually emerges to trigger flow bifurcation. The same occurs when the discharge angle is not perpendicular to the coastline. In this case the higher discharge angle and the consequent jet deflection trigger a transition from central to sided bar. As in the central river mouth, the formation of lateral levees depends on the slope of the shelf basin slope. Higher slopes favors the formation of these lateral levees.

For the highest discharge angles along with sloping basins ($\alpha > 30^{\circ}$ and $m > 0\%$) cases, the increasing deflection rate with increasing slopes causes a transition from a sided bar with lateral

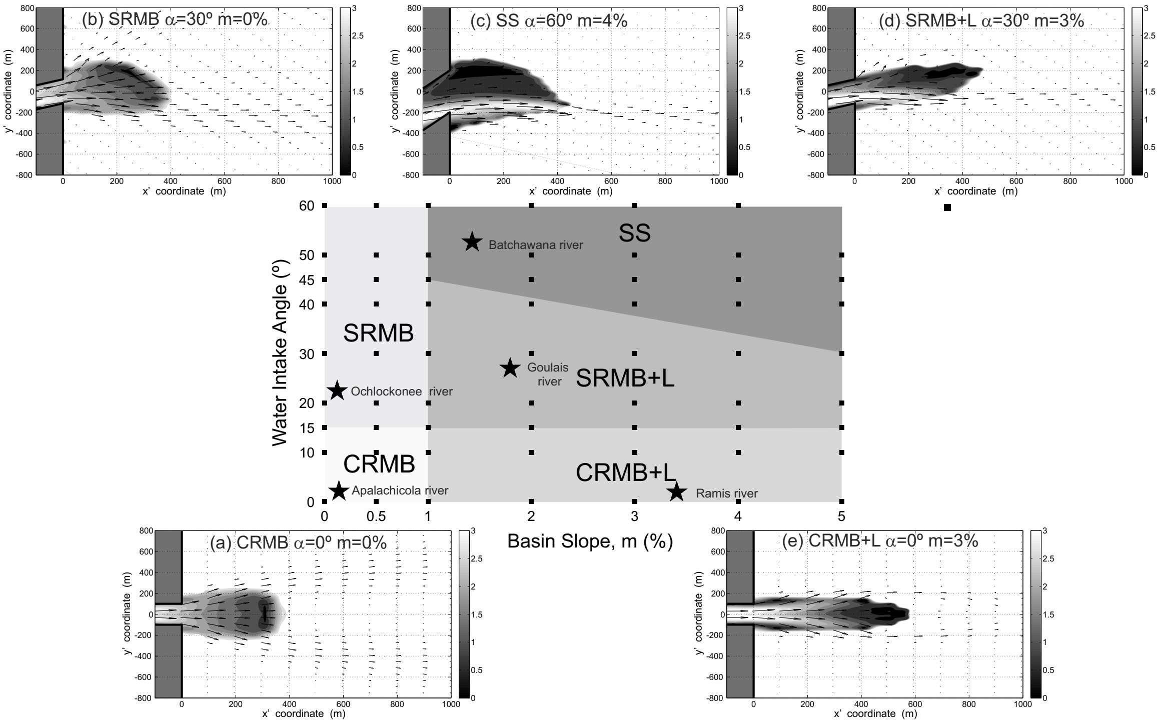

Figure 5.4: Phase space plot of river mouth bar morphology as a function of discharge angle (α) and basin slope (m). Each area identifies a specific morphology of deposited sediments with an example snapshot depicting the bottom depth contour map with superimposed velocity vectors: (a) CRMB: central river mouth bar, (b) SRMB: sided river mouth bar, (c) SS: sand-spit, (d) SRMB+L: sided river mouth bar with lateral levees, and (e) CRMB+L: central river mouth bar with lateral levees. Stars represent the river mouth bar geometry of different natural systems reported in Section 5.5.

levees to an updrift sand-spit. In these case the jet is deviated towards a direction almost parallel to the coast, leading to a ridge of sand connected with the shoreline that completely diverts the jet.

5.5 Discussion and concluding remarks

This Chapter follows recent efforts on improving the mathematical modeling of physical processes governing the morphodynamics of river mouth and deltas (Edmonds and Slingerland, 2007, 2010; Falcini and Jerolmack, 2010; Nardin and Fagherazzi, 2012; Leonardi et al., 2013; Mariotti et al., 2013; Nardin et al., 2013; Caldwell and Edmonds, 2014; Canestrelli et al., 2014b; Leonardi et al., 2014; Fagherazzi et al., 2015; Jiménez-Robles et al., 2016). These processes include the effect of waves, tides, vegetation, sediment characteristics, sediment eddy diffusivity, potential vorticity on sediment redistribution, tidal bedding, and mouth geometry. They account for the inherent complexity of the coastal environment where these landforms are commonly used to build new land or restore deltaic shorelines threatened by erosion (Paola and Voller, 2005).

In this work we address the influence of the river mouth geometry on a sediment-laden discharge. In particular, we focus on the role of the receiving basin slope and the river discharge angle. Two main consequences arise. Firstly, the change experienced in the plan view of the jet was reported by Özsoy and Ünlüata (1982) and Jiménez-Robles et al. (2016). The cause for this jet narrowing with increasing basin slope is related to mass continuity and the vertical expansion experienced by the jet. The second one is related to the deviation of the jet due to the combined effect of the bottom topography and convective terms. Previous works on coastal flows found that the path of a jet may be deviated from its straight direction near a boundary and tends to adhere to this boundary by a phenomenon known as the Coanda effect (Khanin, 1978; Lalli et al., 2010; Miozzi et al., 2010). Through this boundary layer attachment, the lateral entrainment of the fluid on the side of the jet closer to the boundary effects a pressure gradient which accelerates the jet toward the boundary (Hamblin and Carmack, 1978). In our case, the role of the boundary is played by the updrift coastline. Furthermore, the non-deviation of the jet in our horizontal cases can be explained by the results of Wind and Vreugdenhil (1986). They investigated the interaction of rip currents and coastal structures and found that the streamlines of the rip current remains straight and unaltered for an horizontal bottom.

Our morphological simulations suggest that these hydrodynamics implications over a jet play an important role in the diffusion of conservative pollutants and the initial deposition stages of suspended sediments influenced by gravitational settling (Özsoy, 1986). From a sedimentary perspective, five different morphologies arise by modifying the discharge angle and the basin slope: central or sided river mouth bar, with or without levees, and sand-spits.

The main motivation of this work is to investigate the effect of basin geometry on jet hydrodynamics. However, where along the worlds coastline would one find the geometry described here? One of the main concern of the authors is about the fact that many river-deltas and mouth bar locations characterized by an oblique mouth present such obliquity due to the presence of waves (Nardin and Fagherazzi, 2012; Nienhuis et al., 2015). Indeed, there are classifications where the wave dominance is identified trough the inclination of the mouth (Ashton and Giosan, 2011; Anthony, 2015). Besides, relatively steep offshore slopes are formed most often because of ocean waves (Nava-Sanchez et al., 1999; Buonaiuto and Kraus, 2003). On the contrary, on active deltaic coasts not affected by waves (e.g. Wax Lake Delta, LA, USA), the geometry of river mouths is more often characterized by the jet eroding into river mouth deposits and therefore negative slopes arise (Lane, 1957). However, the topic of the present work is of interest for a better understanding of fluvial mouths, located in microtidal shallow seas and coastal lagoons, but also in lakes and reservoirs.

In this sense, the final river mouth bar configurations obtained in our simulations display similarities to natural systems in which our imposed conditions are present. Figure 5.5 shows the mouth morphology of five systems whose main mouth geometrical characteristics were reported in Figure 5.4: Apalachicola river mouth deposits (CRMB, Figure 5.4 (a)), Ochlockonee river mouth deposits (SRMB, Figure 5.4 (b)), Batchawana river mouth deposits (SS, Figure 5.4 (c)), Goulais river mouth deposits (SRMB+L, Figure 5.4 (d)), and Ramis river mouth deposits (CRMB+L, Figure 5.4 (e)).

These systems are all fluvially-dominated. Firstly, rivers debouches into lakes (Batchawana and Goulais rivers in Lake Superior, and Ramis river in Lake Titicaca) or shelter bays (Apalachicola and Ochlockonee rivers in the bays of the same name) in which the effect of waves can be reasonably neglected. On the other hand, the analysis of the free available data of river discharges data from USGS station 02359170 (Apalachicola river), USGS station 02330000 (Ochlockonee river), Government of Canada station 02BF001 (Batchawana river), Government of Canada station 02BF014 (Goulais river), and discharge data of the river Ramis from Dejoux (2012) confirm the fluvial dominated character of these systems against the tidal influence. The information of USGS and Government of Canada stations is freely available in their respective webpages.

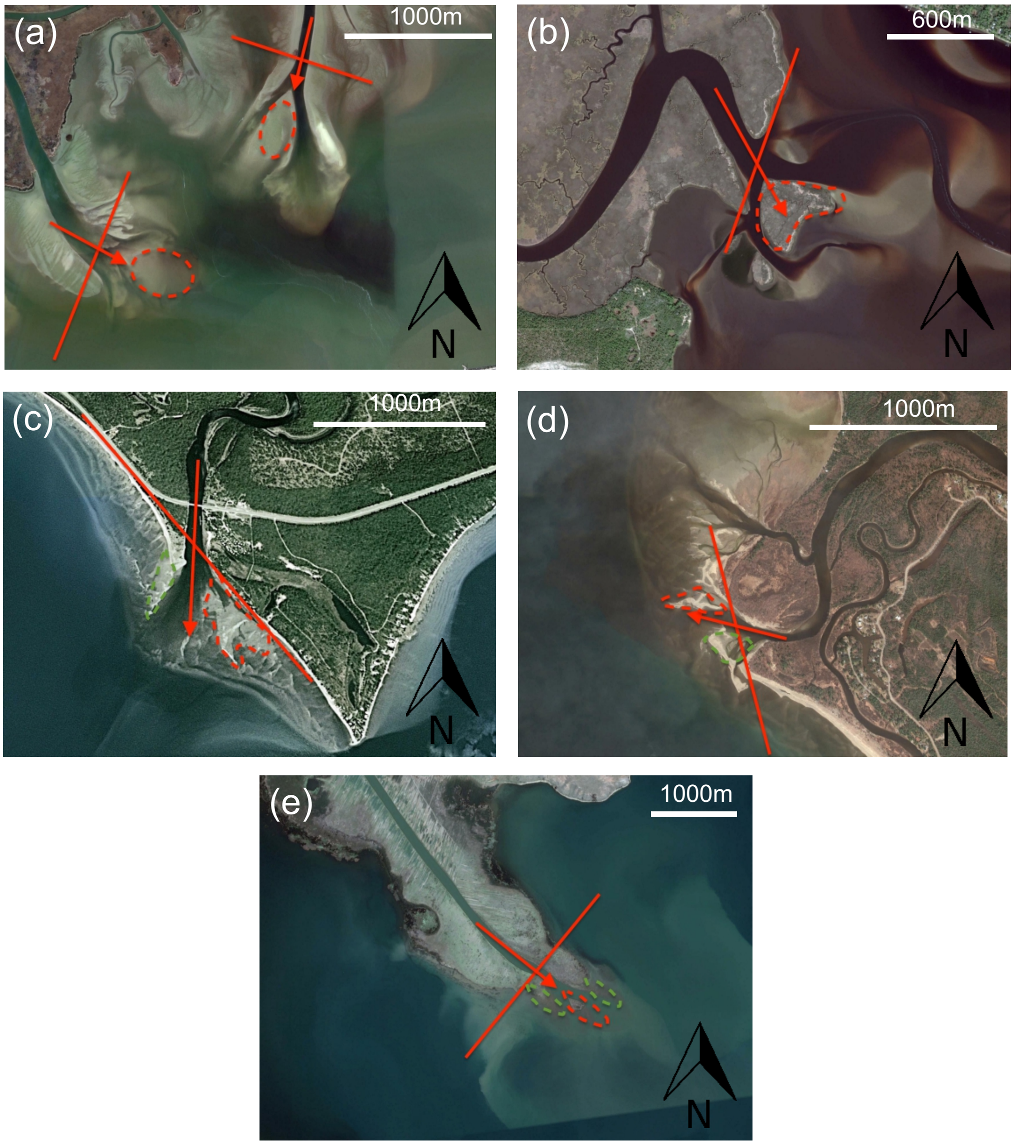

Figure 5.5: Satellite images of (a) Apalachicola river mouth deposits (CRMB) [Apalachicola Bay, USA, 29°44'N, 84°56'W, Image Landsat/Copernicus], (b) Ochlockonee river mouth deposits (SRMB) [Ochlockonee Bay, USA, 29°58'N, 84°26'W, ImageI'2016 DigitalGloble], (c) Batchawana river mouth deposits (SS) [Batchawana Bay, Lake Superior, Canada, 46°55'N, 84°31'W, I'2016 Cnes/Spot Image], (d) Goulais river mouth deposits (SRMB+L) [Goulais Bay, Lake Superior, Canada, 46°43'N, 84°27'W, ImageI'2016 DigitalGloble], and (e) Ramis river mouth deposits (CRMB+L) [Lake Titicaca, Peru, 15°19'S, 69°45'W, ImageI'2016 CNES/Astrium]. Red arrows indicate discharge directions, red lines indicate shoreline alignment, red dashed lines indicate bar deposits and green dashed lines indicate lateral levees. [Images courtesy of Google Earth].

While the discharge angle was inferred from satellite images courtesy of Google Earth, the value of the mean continental shelf slope was extracted from different sources: NOAA Nautical Chart 11404 (Apalachicola river), NOAA Nautical Chart 11405 (Ochlockonee river), NOAA Nautical Chart 14962 (Batchawana and Goulais rivers), and bathymetric data from D'Agostino et al. (2002) (Ramis river) (see star markers in Figure 5.4).

Finally, despite the basin slope was found to be a triggering factor for jet instability (Jiménez-

Robles et al., 2016), the simulations of the present work where constructed on the basis of a stable jet. Therefore, the classical coherent structures consisting of phase-correlated, 2-D, counterrotating vortical elements that appear across the width of the jet giving it a meandering aspect were suppressed (Rowland et al., 2009) due to the relatively high bottom friction and low river velocities imposed on the model set up.

Chapter 6

Influence of the inner shelf characteristics on turbidity current deposits

This Chapter addresses the role of the slope and friction of the inner shelf on the formation of sedimentary wedges and seafloor undulations over the latter by turbidity currents usually linked to short, mountainous, and seasonal fluvial systems. A numerical model of hyperpycnal plumes is used. Results suggest that the receiving basin slope highly dominates the formation and subsequent development of deltaic wedges, whereas the bottom friction dictates the evolution of their wavy structure.

6.1 Introduction

Coastal deltas are accumulations of allochthonous sediment deposited where rivers enter into the sea, giving rise to the most important depositional facies around the world (Bates, 1953; Coleman and Wright, 1975; Wright et al., 1974; Orton and Reading, 1993; Masselink et al., 2003). There is a huge volumen of literature on deltaic environments classification based on qualitative approaches (Galloway, 1975; Postma, 1990; Boggs, 1995; Reading and Collinson, 1996). There are several major controlling factors that can be used to formulate a classification of deltas, all of which can vary between wide limits, producing markedly different resulting deltas and making the possible combinations between them to be endless.

For the purposes of this current study, classification schemes that focus on the delta-front regime as well as feeder/basin characteristics are preferred because of the insight they can give on delta formation processes. We will use the classification scheme proposed by Galloway (1975) because it has been extensively used, it is simple and has an effective nature, and it offers a suitable context for focussing on the scope of the present chapter. The ternary classification system of Galloway (1975) is based on the relative magnitude of fluvial flow, wave energy and tidal currents. The interaction and relative strengths of fluvial and marine processes are capable of producing a variety of characteristic morphologies and accompanying sedimentary stratigraphies (Figure 6.2). This is a tripartite classification with three end-members, i.e., fluvial-dominated, wave-dominated, and tide-dominated, that exemplify the effects of each process when it is the most relevant controlling factor. Obviously, a wide range of intermediate systems exists between the three end-member types that mix delta front reworking processes characteristics to varying degrees of relative magnitude of river, wave and tide power.

This chapter focuses on fluvial-dominated deltas characterized by high-energy events river discharge, such as storms, into protected seas with minimal nearshore wave energy and a small tidal prism. These are situations where sediments are delivered by the river faster than they are

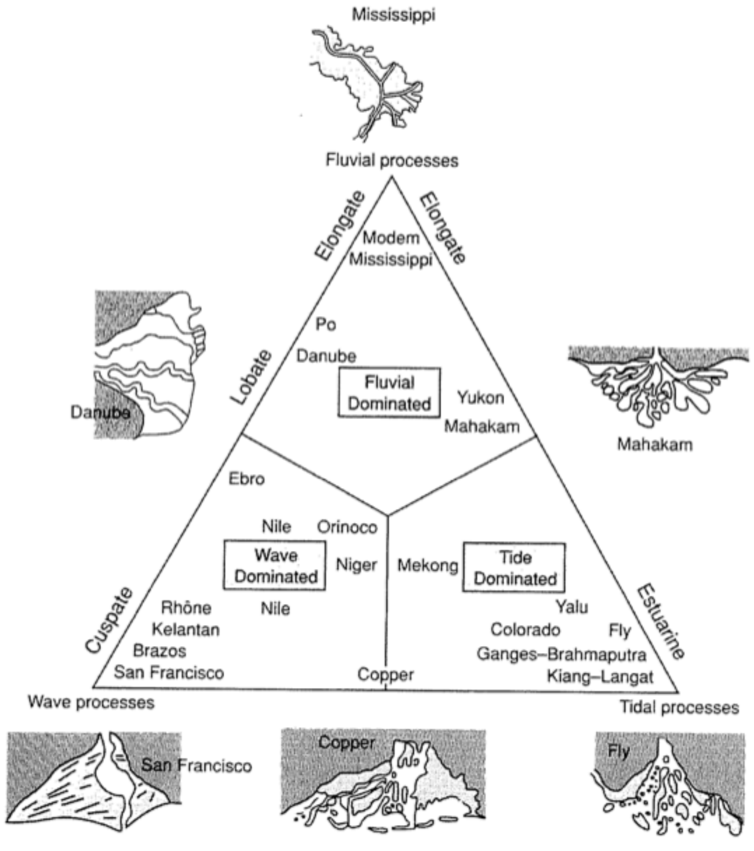
Mississippi
Fluvial processes
Elongate
Elongate
Modern Mississippi
Po
Danube
Lobate
Fluvial Dominated
Yukon
Mahakam
Danube
Mahakam
Ebro
Nile
Orinoco
Wave Dominated
Niger
Mekong
Tide Dominated
Cuspate
Rhône
Kelantan
Brazos
San Francisco
Nile
Yalu
Colorado
Fly
Ganges–Brahmaputra
Kiang–Langat
Estuarine
Copper
Wave processes
Tidal processes
San Francisco
Copper
Fly

Figure 6.1: Triangular classification of deltaic depositional systems of Galloway (1975). [From Masselink et al. (2003)].

dispersed by waves, tides or ocean currents, causing the adjacent coastline to prograde. The sedimentary record of these cases may include the occurrence of sandy deltaic bodies that occur off these rivers (Fernández-Salas et al., 2015). These are the main morphological feature in which this work is focused on. They are characterized by a well-defined sigmoidal wedge-shaped clinoform that experiences a transition from convex to concave as the water depth increases (Salas et al., 2008; Ortega-Sánchez et al., 2014; Bárcenas, 2013). Although detailed morphology of deltas varies from one example to the next, there are a tripartite cross-sectional subdivision of deltaic clinoforms common to almost all of them (Masselink et al., 2003):

- Delta plain or *topset*: it is the most active part of the delta and it is where the most of the sediment delivered from the distributary mouth is deposited, favoring its aggradation. The topset lies in a quasi horizontal layer over the sediments of past delta fronts.
- Delta front or *foreset*: it is the steepest part of the delta and marks the location of the delta during its progradation. It can be seen as a situation in which the distributary delivers sediment to the open sea and causes the delta front to prograde seaward through deposition of the relatively coarse sediments closest to the coast and the finer sediments further seaward. A distinctive feature of the deltaic profile is the *offlap break*, i.e., the morphological boundary between topsets and foresets characterized by a well-defined break in the slope of the deltaic profile (Adams and Schlager, 2000).

- Prodelta or *bottomset*: it is the most seaward region of the deltaic system where only the finest sediments are able to deposit. The lack of bedload transport, due to the negligible effect of both waves and tides, and a generally horizontal bed means that the prodelta aggrades vertically to produce relatively flat-lying bottomset bed.

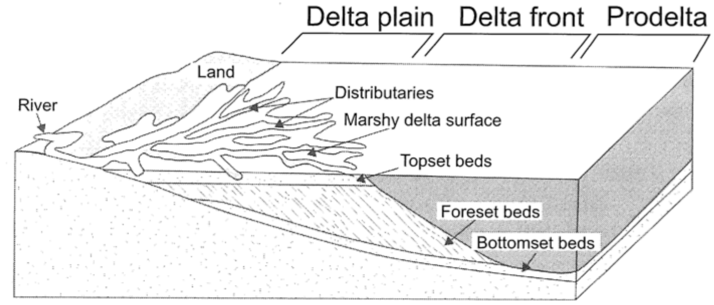

Figure 6.2: The three generic morpho-stratigraphic units found in a typical deltaic system: delta plain or *topset*, delta front or *foreset*, and prodelta or *bottomset*. [From Masselink et al. (2003)].

These deltaic systems are densely populated and they are among the most productive environments on earth (Syvitski and Saito, 2007). However, anthropogenic and natural changes, such as river regulation and related variations in sediment supply, changes in land-use practices, sea-level rise, increase in storm frequency, and land subsidence, threaten these valuable environments (Ericson et al., 2006; Paola et al., 2011; Syvitski et al., 2009; Bianchi and Allison, 2009). Therefore, is thus crucial for their proper management and restoration new efforts to unravel the basic mechanisms responsible for formation and evolution of the entire deltaic system (Fagherazzi and Overeem, 2007). In this sense, numerical models constitute a significant tool that allows the prediction of delta evolution in situations in which it is hard to fully substantiate it with field observations due to the large spatial and temporal scales that characterize delta evolution (Geleynse et al., 2011; Caldwell and Edmonds, 2014).

There are a variety of distinct agents that take place in these environments and whose interactions could make complex the comprehension of the processes involved: wind waves, tides, buoyancy, sediment properties, river mouth geometry, frictional effects. That is why in the recent years there have been a flurry of research activities focused on the isolated influence of one of these factors when on the entire system evolution. (Wright, 1977; Storms et al., 2007; Edmonds and Slingerland, 2010; Geleynse et al., 2010; Nardin and Fagherazzi, 2012; Leonardi et al., 2013; Nardin et al., 2013; Caldwell and Edmonds, 2014; Canestrelli et al., 2014b; Jiménez-Robles et al., 2016).

In this regard, in the present chapter we address the impact of turbidity currents over the morphology of the continental shelves and ocean basins. When a river contains an elevated concentration of suspended sediment, to the extent that the river density is greater than that of the receiving water body, the river can plunge and create a turbidity current. Turbidity currents, also known as hyperpycnal flows, are negatively buoyant, highly-concentrated, near-bed suspensions that flow downslope under their own weight (Masselink et al., 2003). These turbidity currents are a major process of sediment transport and erosion in coastal and lacustrine environments and have been revealed as a major mechanism for delta formation and evolution (Parker et al., 1986; Gerber et al., 2008). Their occurrence is typical of short, mountainous fluvial systems and creeks characterized by seasonal and torrential behavior, as rivers found along the coast of the Alboran Sea (western Mediterranean basin, Spain) (Bárcenas et al., 2015). Sedimentary morphologies associated with this type of hyperpycnal flows have been studies in small and steep deltas such as Fujikawa fan delta (Japan) (Soh et al., 1995), El Coyote fan delta in the Gulf of California (Mexico) (Nava-Sanchez et al., 1999), Eratini River in the NW Gulf of Corinth (Greece) (Hasiotis et al., 2006), bedforms produced by the Kuroshio Current passing over the northern Izu Ridge (Japan) (Kubo, 2004), and the small deltaic environments linked to the previously mentioned rivers in the northern shelf of the Alboran Sea (Bárcenas et al., 2015).

The difficulty in monitoring turbidity currents in the natural environment because of the unpredictable nature of these events make that most o our knowledge about these flows is derived from small scale laboratory experiments (Middleton, 1967; Garcia and Parker, 1993; Alexander and Morris, 1994; Kubo and Nakajima, 2002; Kubo, 2004). Based on laboratory experiments of turbidity currents, Chu et al. (1979); Bradford and Katopodes (1999); Kubo and Nakajima (2002) and Khan et al. (2005) developed turbidity currents numerical model. However, these classical layer-averaged model present some drawbacks, namely, (i) they do not preserve freshwater mass, (ii) their equations do not include a pressure term, (iii) the do not considerer effects of deposition and erosion and (iv) the ambient water entrainment are neglected in their momentum equations. In the extended model of Morales et al. (2009) a new turbidity current model was proposed trying to overcome all these drawbacks by taking into account all these missing terms and transport of particles at the bottom. However, the numerical results obtained by this model when applied to real river systems were not satisfactory. Finally, more sophisticated models as the ones developed by Mulder and Syvitski (1995) and Macías et al. (2016) have been used to simulate sediment transport by turbidity currents, with particular application to hyperpycnal plumes, finding favorably results when comparing marine deposits to model simulations.

The main goal of the present work is to determine the influence of both the receiving basin slope and the bottom friction coefficient on the formation of the classical submarine deltaic wedges and on the development of the sea-floor undulations fields located in these deltaic wedges as a consequence of a highly-concentrated river discharge. Sea-floor undulations are small-scale morphological features with dimensions ranging between several meters to hundreds of meters in length and between centimeters to several meters in height. Such sea-floor undulations have been widely reported from a variety of deep-water deltaic environments (Fernández-Salas et al., 2007, 2015).

Our investigation is limited to a simple geometry and a hyperpycnal effluent in which wind waves, tides, and Coriolis forces are neglected. To this end, we make use of the turbidity current model proposed by Macías et al. (2016). This model, which extends and faces the weak points of the one of Morales et al. (2009), is part of a wider project whose final goal is the development of realistic two-dimensional turbidity current models to simulate hyperpycnal river flows entering the sea and spreading over the sea bed producing complex patterns of undulations and bottom morphology. It was developed by the EDANYA (*Ecuaciones Diferenciales, Análisis Numérico y Apliaciones*) group of the Málaga University in the framework of MOSAICO project. The numerical simulations were carried out through the HySEA numerical computing platform managed by the EDANYA group.

6.2 Numerical model description

The numerical model proposed by Macías et al. (2016) and used in this chapter for simulating hyperpycnal flows is a one-dimensional layer-averaged model. This finite volume model solves in a coupled way the depth-averaged equation of (i) continuity, (ii) momentum, (iii) sediment conservation in the turbidity flow, (iv) sediment conservation in the erodible bottom of a density driven flow along with (v) the Exner Equation of bed sediment continuity. This type of model has been widely used in the simulation of turbidity currents (Bradford and Katopodes, 1999; Kubo and Nakajima, 2002; Khan et al., 2005; Morales et al., 2009) and has the advantage of being less expensive computationally than a fully two-dimensional model. The equations that form the basis of this shallow water model, considering n_s species of sediment transported by the river, read:

$$\left\{\begin{array}{l} \dfrac{\partial h}{\partial t}+\dfrac{\partial}{\partial x}(hu)=\phi_\eta+\phi_b, \\ \dfrac{\partial}{\partial t}(hu)+\dfrac{\partial}{\partial x}\left(hu^2+g(R_0+R_c)\dfrac{h^2}{2}\right)= \\ \quad =g(R_0+R_c)h\dfrac{\partial}{\partial x}(H-z_b)+u\phi_\eta+\dfrac{u}{2}\phi_b+\tau, \\ \dfrac{\partial}{\partial t}\left(hc_j\right)+\dfrac{\partial}{\partial x}\left(huc_j\right)=\phi_b^j, \text{ with } j=1,\dots,n_s, \\ \dfrac{\partial}{\partial t}\left(z_b p_j\right)=-\phi_b^j, \text{ with } j=1,\dots,n_s, \\ \dfrac{\partial z_b}{\partial t}+\xi\dfrac{\partial q_b}{\partial x}=-\xi\phi_b, \end{array}\right. \tag{6.1}$$

where u is the depth-average velocity of the turbidity current, h is the turbidity flow thickness, x is the longitudinal coordinate of the system, t is time, ϕ_η represents the ambient water of the receiving basin that is entrained in the turbidity flow by turbulence, ϕ_b represent the net flux of sediment deposition and erosion of all the species ($\phi_b=\sum_{j=1}^{n_s}\phi_b^j$) which models the transference of sediments between the turbidity current and the seabed, g is acceleration due to gravity, R_0 is the submerged specific gravity of the turbidity flow defined as:

$$R_0=\frac{\rho_0-\rho_w}{\rho_0}, \tag{6.2}$$

in which ρ_0 and ρ_w are the density of the freshwater transported by the river and the density of the ambient fluid (in general de sea) respectively, R_c is the averaged submerged specific gravity of the sediments defined as:

$$R_c=\sum_{j=1}^{n_s}R_j c_j, \tag{6.3}$$

where R_j is the averaged submerged specific gravity of each of the n_s species of sediment:

$$R_j=\frac{\rho_j-\rho_0}{\rho_0}, \tag{6.4}$$

in which ρ_j is the density of each sediment specie, H is the nonerodible bottom depth measured from a given fixed level (mean sea level or free surface of water), z_b is the erodible sediment layer thickness, τ is the friction term, c_j is the vertically averaged volume concentration of the

j^{th} specie of sediment in the turbidity plume, ξ is a porosity term ($\xi = 1/(1-\gamma)$), γ is the porosity of the erodible layer, p_j is the volume fraction of the j^{th} specie of sediment in the erodible layer, and q_b is the sediment bedload flux per unit width in the x direction. A sketch of a turbidity current along with the variables described above is presented in Figure 6.3.

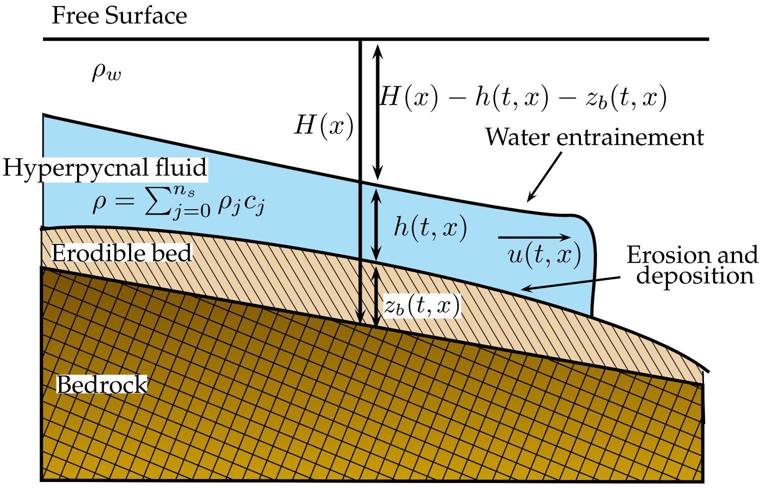

Figure 6.3: Sketch of a turbidity current and basic notation.

Variables to be determined by the model are the hyperpycnal plume thickness h, the depth-average velocity of the turbidity current u, the n_s sediment volumetric concentrations c_j, and the erodible bottom layer thickness z_b. The rest of the terms must be parametrized as functions of these unknowns and other known variables in order to close the model conveniently.

The parametrization used for describing the physics of the water entrainment mechanism (ϕ_η) is the one employed by Kubo and Nakajima (2002):

$$\phi_\eta = E_w u, \tag{6.5}$$

in which E_w is a water entrainment coefficient given by the empirical relationship:

$$E_w = \frac{0.00153}{0.0204 + \Re i}, \tag{6.6}$$

where the Richardson number, $\Re i$, is defined as:

$$\Re i = \frac{R_c g h}{u^2}. \tag{6.7}$$

With respect to the parametrization of the exchange of the j^{th} specie of sediment between the erodible bed and the hyperpycnal plume, ϕ_b^j, the addition of two different sediment fluxes, one for erosion, F_e^j, and another one for deposition, F_d^j, are employed. The total sediment transfer between the bottom and the plume, ϕ_b, is described as the sum of all the sediment fluxes for the n_s species:

$$\phi_b = \sum_{j=1}^{n_s} \phi_b^j = \sum_{j=1}^{n_s} \left(F_e^j - F_d^j \right). \tag{6.8}$$

The rate of deposition, F_d^j, is described as the product of the settling velocity of the sediment specie j^{th}, w_s^j, and its fractional concentration of suspension at the bed, c_b^j:

$$F_d^j = w_s^j c_b^j. \tag{6.9}$$

A number of relations for terminal fall velocity for the case of nonspherical (natural) particles can be found in the literature. Dietrich (1982) analyzed fall velocity data for natural particles and used dimensional analysis to obtain the useful fit:

$$w_s^j = \sqrt{g R_j d_s^j} \left\{ \exp\left[-b_1 + b_2 \ln(\Re_p^j) - b_3 [\ln(\Re_p^j)]^2 - b_4 [\ln(\Re_p^j)]^3 + b_5 [\ln(\Re_p^j)]^4 \right] \right\} \tag{6.10}$$

where $b_1 = 2.891394$, $b_2 = 0.95296$, $b_3 = 0.056835$, $b_4 = 0.002892$, $b_5 = 0.000245$, $\Re_p^j$ is the Reynolds particle number of the j^{th} specie:

$$\Re_p^j = \frac{\sqrt{R_j g d_s^j}\, d_s^j}{\nu}, \tag{6.11}$$

d_s^j is the mean diameter size of the j^{th} specie of sediment, and ν is the kinematic viscosity of the plume water. The sediment concentration at the bed, c_b^j, can be related to the layer-averaged concentration by a factor of 2 (García, 1993; Altinaker et al., 1996). However, the expression employed by Bradford and Katopodes (1999) for poorly sorted sediments is used for its estimation. This expression is:

$$\frac{c_b^j}{c_j} = 0.4 \left(\frac{d_s^j}{d_{sg}} \right)^{1.64} + 1.64, \tag{6.12}$$

in which d_{sg} denotes the geometric mean size of the suspended sediment mixture.

In order to describe the rates of erosion flux from the bed to the turbidity current of the j^{th} specie of sediment a sediment entrainment coefficient, E_s^j, is used:

$$F_e^j = w_s^j p_j E_s^j. \tag{6.13}$$

The expression proposed by Garcia and Parker (1993) is used to determine the j^{th} sediment entrainment coefficient:

$$E_s^j = \frac{1.3 \cdot 10^{-7} Z_j^5}{1 + 4.3 \cdot 10^{-7} Z_j^5}, \tag{6.14}$$

in which

$$Z_j = \alpha_1 \frac{\sqrt{c_D}|u|}{w_s^j} \Re_p^{j^{\alpha_2}}, \tag{6.15}$$

where

$$(\alpha_1, \alpha_2) = \begin{cases} (1.000, 0.600) & \text{for } \Re_p^j > 2.36, \\ (0.586, 1.230) & \text{for } \Re_p^j \leq 2.36, \end{cases} \tag{6.16}$$

and c_D is a bed drag coefficient which in the present model of Macías et al. (2016) is parametrized as a function of the turbidity plume thickness and the Manning's roughness coefficient (M):

$$c_D = g \frac{M^2}{h^{1/3}}. \tag{6.17}$$

On the other, in this work the influence of the bedload fluxes of sediment are neglected and only the effects due to vertical fluxes of sediment exchange between erodible bed and turbidity plume (erosion/deposition) are considered.

With respect to the friction term τ, experimental tests suggested that the main drawbacks of the original model of Morales et al. (2009) resulted from the simple parameterization of this term, by which:

$$\tau = \tau_b + \tau_i = -c_D|u|u - \alpha c_D|u|u = -(1+\alpha)c_D|u|u, \tag{6.18}$$

where the term τ_b parametrizes the friction between the hyperpycnal plume and the sea bottom, the term τ_i represents the friction between fluids (hyperpycnal plume and ambient fluid), and α is the ratio between these two friction terms ($\alpha = \tau_i/\tau_b$). In order to improve results from Morales et al. (2009), Macías et al. (2016) proposed a separately parameterization of this term.

A Manning-type parameterization is imposed for the friction in the erodible bottom-hyperpycnal flow interface:

$$\tau_b = -gh \frac{M^2}{h^{4/3}}|u|u. \tag{6.19}$$

With respect to parameterization of the friction term in the plume-ambient water interface, a law that considers both the turbidity current and fresh ambient water layers thickness is considered:

$$\tau_i = -\frac{\alpha(h_1)h}{rh_1 + h}|u|u, \tag{6.20}$$

where $h_1 = \max\{H - (z_b + h), 0\}$ represents the ambient fluid layer thickness, and $r = \rho_w/\rho_t$ is the ratio between the density of the ambient fluid, ρ_w, and the density of the turbidity flow, ρ_t, which is defined as:

$$\rho_t = \rho_0 \left(1 - \sum_{j=1}^{n_s} c_j\right) + \sum_{j=1}^{n_s} c_j \rho_j. \tag{6.21}$$

The function $\alpha(h_1)$ models the intensity of the friction term as a function of the ambitent fluid layer thickness, which ranges between a user-defined minimal value of α_{max} and a user-defined maximum value of α_{min} through the following expression:

$$\alpha(h_1) = (\alpha_{min}(1-\mathscr{F}(\chi)) + \alpha_{max}\mathscr{F}(\chi))h_1, \tag{6.22}$$

where

$$\mathscr{F}(\chi) = \left(\frac{\chi(1+\chi)}{1+\chi^2}\right)^2, \tag{6.23}$$

$$\chi = \begin{cases} \dfrac{h_1}{H_R} & \text{if } h_1 \leq H_R \\ 1 & \text{if } h_1 > H_R, \end{cases} \tag{6.24}$$

and H_R is a reference depth. For a detailed description of the numerical scheme followed in the resolution of the problem, the reader is referred to Macías et al. (2013).

6.3 Numerical experiments

The simulations presented herein are designed to reproduce the sedimentological conditions of a river debouching into a sheltered bay devoid of tides and waves, but with the presence of buoyancy forces due to the high concentration of sediment carried by the river. Two main factors are going to be varied in order to assess how do they influence the formation of deltaic wedges and seafloor undulations: initial slope of the receiving continental shelf and its bottom friction factor.

Seven different bathymetric profiles are considered. All of them have a piecewise linear profile composed by two regions of different slope. A first one close the coast of 2000 m length with varying slope between simulations of values 0.3°, 0.5°, 1.0°, 1.25°, 1.5°, 1.75°, and 2°; and a second one (offshore profile) of 1000 m length with constant slope between simulations of 0.3°(Figure 6.4).

On the other hand, seven different Manning coefficients have been used between simulations. The imposed values were 0.0075, 0.01, 0.015, 0.0175, 0.0225, 0.03 and 0.045. The combination of these values with the different initial bathymetric profiles gave rise to a total of 49 simulations, all of them along a period of 5 days.

Boundary conditions: A river discharge is assumed to be constant and equal to 1 m^2/s throughout the simulations in the river mouth boundary (x = 0 m) of the model. Recall that m^2/s are flow units since model is 1D. This value must be multiplied by river mouth width to obtain usual S.I. units for flow, i.e., m^3/s. According to Mulder and Syvitski (1995), an imposed sediment volumetric concentration equal to 20 % in the river discharge will produce a hyperpycnal plumes. This mixture of sediment is composed by the same proportion of three different species of sediment. The properties of each one of these species is gathered in Table 6.1. On the other hand, the seaward boundary (x = 3000 m) of the system is assumed to be an open boundary through which the sediment leaves the computational domain.

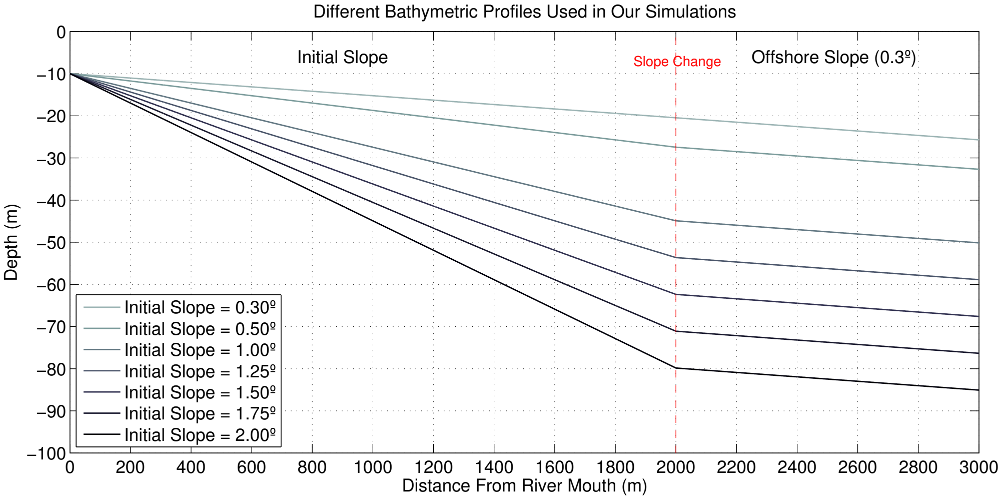

Figure 6.4: Piecewise linear bathymetric profiles used for the numerical simulations.

Initial conditions: All simulations starts from the simplifying condition of a sediment-laden flow entering a standing body of water devoid of marine processes such as waves and tides. The erodible bed layer is initialized with an initial thickness of 25 m. This layer thickness guarantees the positivity of the volumetric concentration of sediments in the erodible sediment layer during the simulation. In addition, it is composed by the same proportion of the three species of sediment presented in Table 6.1.

Sediment Properties			
	Specie 1	*Specie 2*	*Specie 3*
Mean diameter d_s (μm)	400	350	300
Sediment Density ρ_s (kg/m^3)	1930	1922	1900
Settling Velocity w_s (m/s)	0.0295	0.0243	0.0191

Table 6.1: Sediments properties of the three species composing the granular material of the simulations.

The rest of the parameters that remain unchanged in all the numerical simulations are collected in Table 6.2.

6.4 Results

In this Section we present the results of the set of 49 numerical experiments of 5 days duration in which we have simulated the influence that a turbidity plume of constant flow has on the evolution of the continental shelf. We address the influence that the receiving basin slope and receiving basin floor friction have on the formation and evolution of a deltaic wedge (morphological units of large scale) and on the genesis of seafloor undulations (morphological unit of small scale) over the foreset of the deltaic wedge. Computed seafloor bathymetric data obtained from the HySEA numerical computing platform and using the numerical model of turbidity currents simulation of Macías et al. (2016) provide complete information of the sedimentological processes that are intended to study.

Simulation Paramenters	
Sediment species	3
Ocean density ρ_w (kg/m^3)	1020
Water plume density ρ_0 (kg/m^3)	1028
kinematic viscosity of water (m^2/s)	$1.36 \cdot 10^{-6}$
Reference depth H_R (m)	30.0
Time step (s)	1.0
Number of computational elements	3001
Entrainment coefficient E_w	0.001
Erodible bed porosity γ	10%
α_{min}	0.001
α_{max}	0.015

Table 6.2: Parameters used in the numerical experiments.

In this regard, Figure 6.5 depicts the temporal evolution of the deltaic wedge and seafloor undulations in some case in which the initial bathymetric profile of the receiving basin slope is fixed and the bottom friction is varied between simulations, whereas in Figure 6.6 result of simulations in which we set the bottom friction and the initial slope of the bathymetric profile changes between simulations are shown. The results obtained are described below, focusing our attention both in the large scale morphological units (deltaic wedges, Section 6.4.1) and in the small clase morphological units (seafloor undulations, Section 6.4.2).

6.4.1 Characterization of large scale morphological units: deltaic wedges

In the present contribution we consider that a deltaic wedge is formed and can be considered as completely developed once a topset with a total length higher than a threshold value of 100 m emerges from the coastline up to the offlap-break position. For its part, the position of the offlap-break will be defined by the location at which the mean alignment of the first 100 m of the topset is away from the computed seafloor bathymetry more than 0.25 m. The most seaward part of the deltaic wedge or is here named distal limit. This distal limit will be defined as the position at which the sedimentological deposit of the deltaic wedge at the end of the simulation is lower than a threshold value of 0.25 m.

The morphological parameters that define a deltaic wedge and that have computed from the simulated bathymetric profile after 5 days of simulation are in order to characterize these large scale morphological units are: (i) deltaic wedge length (x_{LD}), measured as horizontal distance between the coast and the distal limit of the deltaic wedge, (ii) distal limit depth (y_{LD}), (iii) topset length or distance of the offlap-break from the coastline (x_{OB}), (iv) offlap-break elevation (y_{OB}), (v) foreset slope (S_f), and (vi) formation or not formation of a distal deposit (D_d) where the initial bathymetry changes its slope. The results obtained for these variables are shown graphically in Figure 6.7 and are numerically gathered in Table 6.3.

In order to compute the foreset slope, a curve fitting of the morphology of submarine deltaic profiles seawards from the offlap-break and up to the distal limit, i.e., the foreset part of a typical clinoform, has been performed following the methodology introduced by Adams and Schlager (2000). They assume that most of the profiles submarine slope profiles can be quantified using three simple mathematical equations: a linear equation, a negative exponential, and a Gaussian

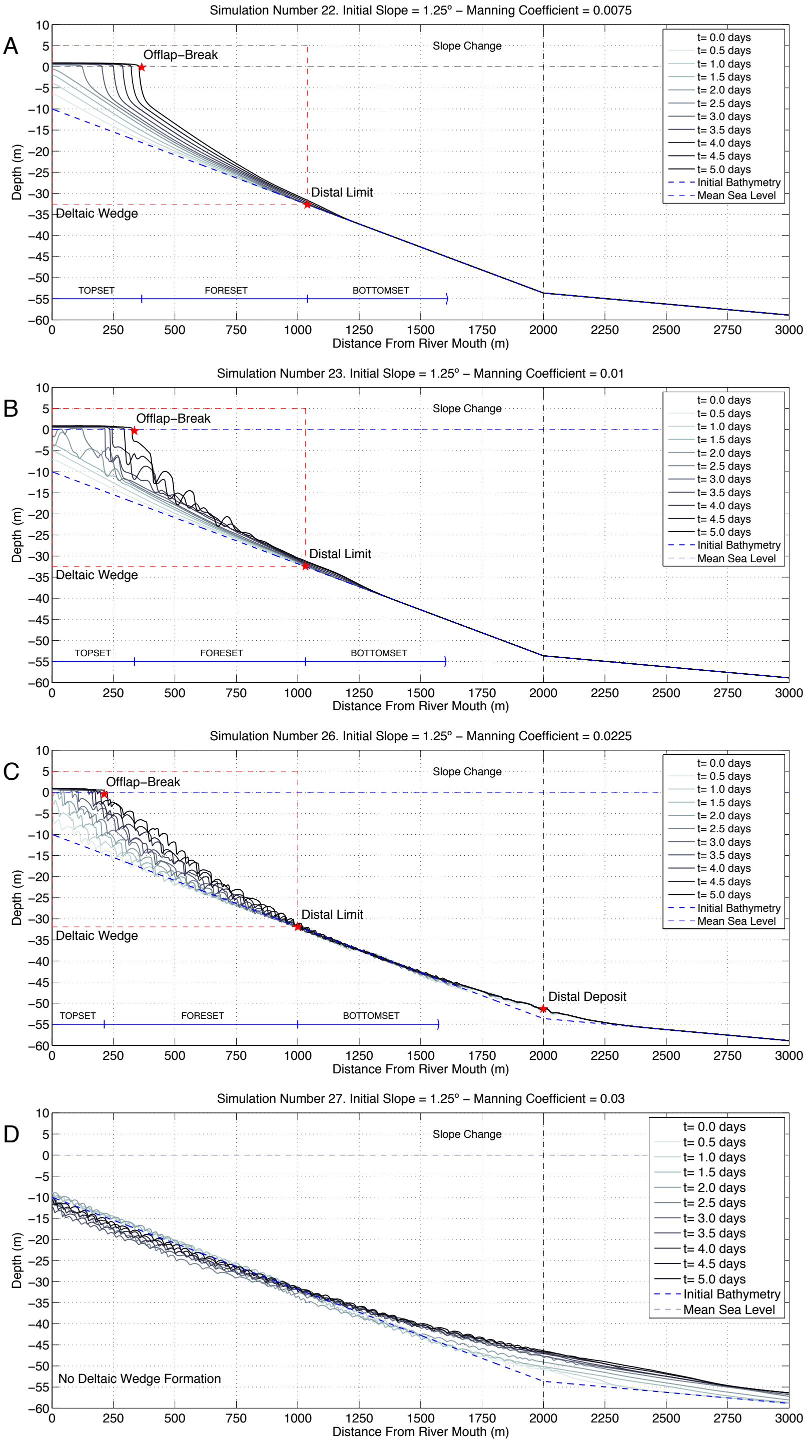

Figure 6.5: Deltaic wedge and seafloor undulations formation and evolution at different stages (every 12 hours) of the numerical simulations during a total period of 5 days. All simulations are carried out over a fixed initial piecewise linear bathymetric profile (initial slope = 1.25°, offshore slope = 0.3°) and different Manning coefficients between simulations: 0.0075 (A), 0.01 (B), 0.0225 (C), and 0.03 (D). Flow inputs, sediment properties and the remaining numerical parameters are given in Section 6.3.

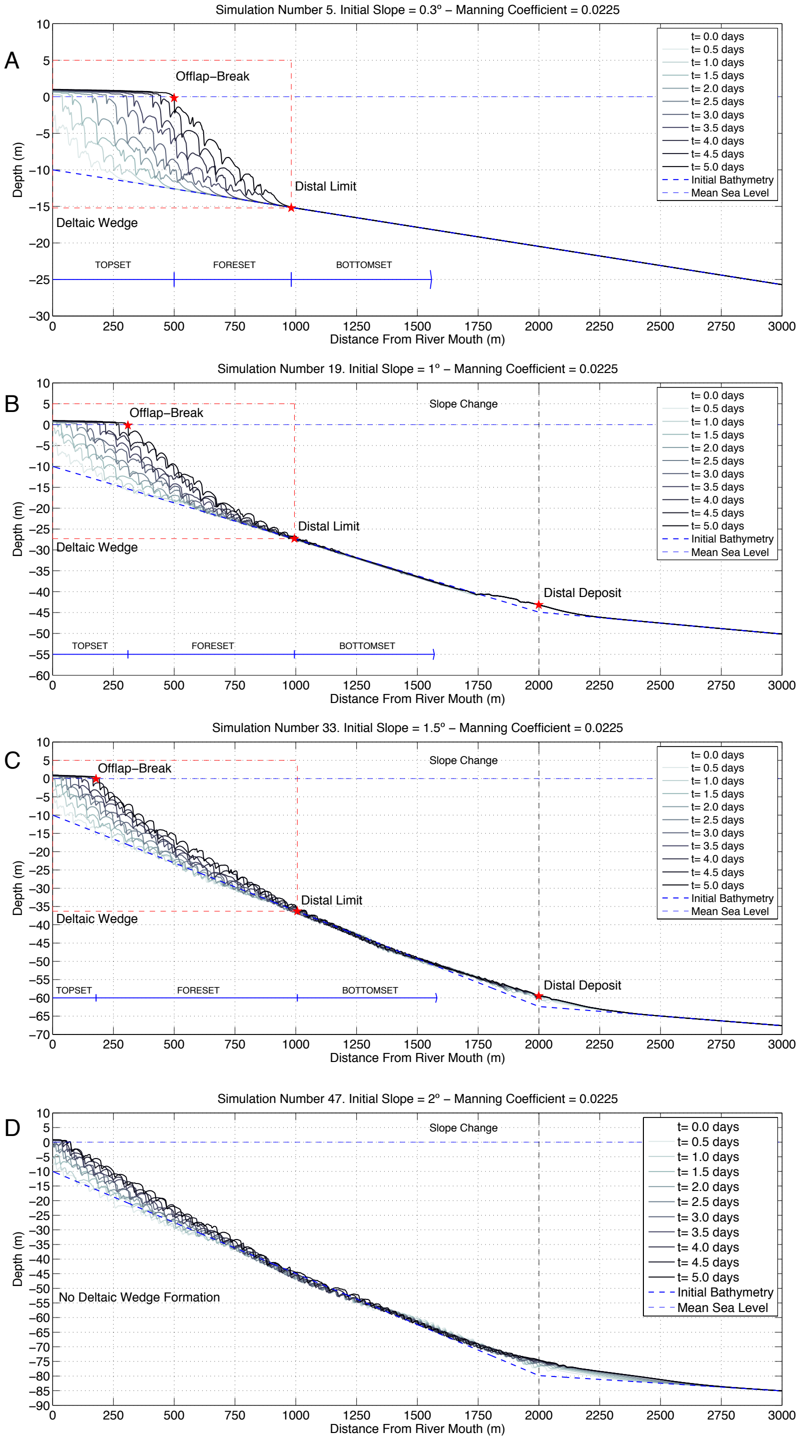

Figure 6.6: Deltaic wedge and seafloor undulations formation and evolution at different stages (every 12 hours) of the numerical simulations during a total period of 5 days. All simulations are carried out with a fixed Manning coefficient of 0.0225 and over a different initial piecewise linear bathymetric profile with initial slope: 0.3°(A), 1°(B), 1.5°(C), and 2°(d), and offshore slope = 0.3°). Flow inputs, sediment properties and the remaining numerical parameters are given in Section 6.3.

function. In this work we have fitted the foreset to a linear profile due its simplicity and simple implementation. Thus, the foreset slope is defined as:

$$S_f = \mathrm{atan}\left(\frac{\mathrm{x_{LD}} - \mathrm{x_{OB}}}{|\mathrm{y_{OB}} - \mathrm{y_{LD}}|}\right). \tag{6.25}$$

From Figure 6.7 we can state that the morphometric parameters of the deltaic wedge, with the exception of the offlap-break elevation, follow a more or less important relationship of proportionality with the initial slope of the bathymetric profile. It can be inferred from the existence of vertical contours in the different subplots in Figure 6.7. In what concerns the interplay between the slope of the initial bathymetric profile and the bottom friction coefficient for the deltaic wedge to form, it is observed that the system is unable to develop a deltaic wedge for high Manning coefficient values in the simulation time that we have imposed. This limit value of friction for the formation of deltaic wedge increases with smaller values of the bathymetric slope of the continental shelf. The cases in which no deltaic wedges arise are plotted with white colors in Figure 6.7. These cases are characterized by laminar deposits, i.e., not wedge-shaped (Figure 6.5 (F) and Figure 6.6 (D)).

The deltaic wedge length (Figure 6.7 (A)) and the topset length (Figure 6.7 (B)) depict a similar behaviour with respect to the seafloor bottom friction. These morphological parameters decrease when the Manning coefficient increases. However, these parameters follow an inverse trend with respect to the receiving basin slope. While the deltaic wedge length increases under higher values of the receiving basin slope, the topset length decreases. It has a direct consequence on the average foreset slope (Figure 6.7 (C)). Computed values of this slope using equation 6.25 show that the resulting foreset slope increase with higher values of the initial receiving basin slope, which makes the offlap-break sharper. On the other hand, its trend as a function of the Manning friction coefficient is not as direct as in the case of the bottom slope. Nevertheless, we can state that the foreset slope decreases with higher values of Manning friction coefficient. As expected, distal limit depth shows a clear linear trend to increase when the initial slope increase (Figure 6.7 (D)). However, it does not seem to be a clear connection between distal limit and bottom friction since contour lines in Figure 6.7 (D) are vertical. As previously mentioned, offlap-break elevation do not follow an evident trend as a function of both the receiving basin slope and friction (Figure 6.7 (E)). Obtained values, which ranges between 0 and 0.5 meters, show a high variability regardless initial conditions imposed to the model. We argue this can be due to this low ranges of variability and the high degree of sedimentary activity of these systems, in which the existence or not of a undulation crest in the offlap-break position can significantly alter its elevation with respect to the mean sea level (Figures 6.5 and 6.6). Finally, the existence of distal deposits arises in simultions characterized by high values of basin slope (Figure 6.7 (F)). In these cases, the higher is this slope, the higher is the ability of the system to form these distal deposits with lower values of bottom friction.

Finally, with respect to the internal structure of the deltaic wedge with time, it is observed that the separation between two consecutive bathymetric profiles is smaller for higher friction values and higher for steeper slopes of the receiving basin (Figures 6.5 and 6.6 respectively). Regarding the erosive power of the simulated turbidity flow, for higher values and higher initial slopes of the bottom friction erosive effects on the initial seafloor are observed. This eroded areas, which takes place mainly in the middle portion of the profile, are determined by the regions in which the computed bathymetric profiles lie below the initial bathymetry. Besides, these areas subjected to erosive processes are located further seaward when both the the friction and the slope of the initial seafloor are high (Figures 6.5 and 6.6)

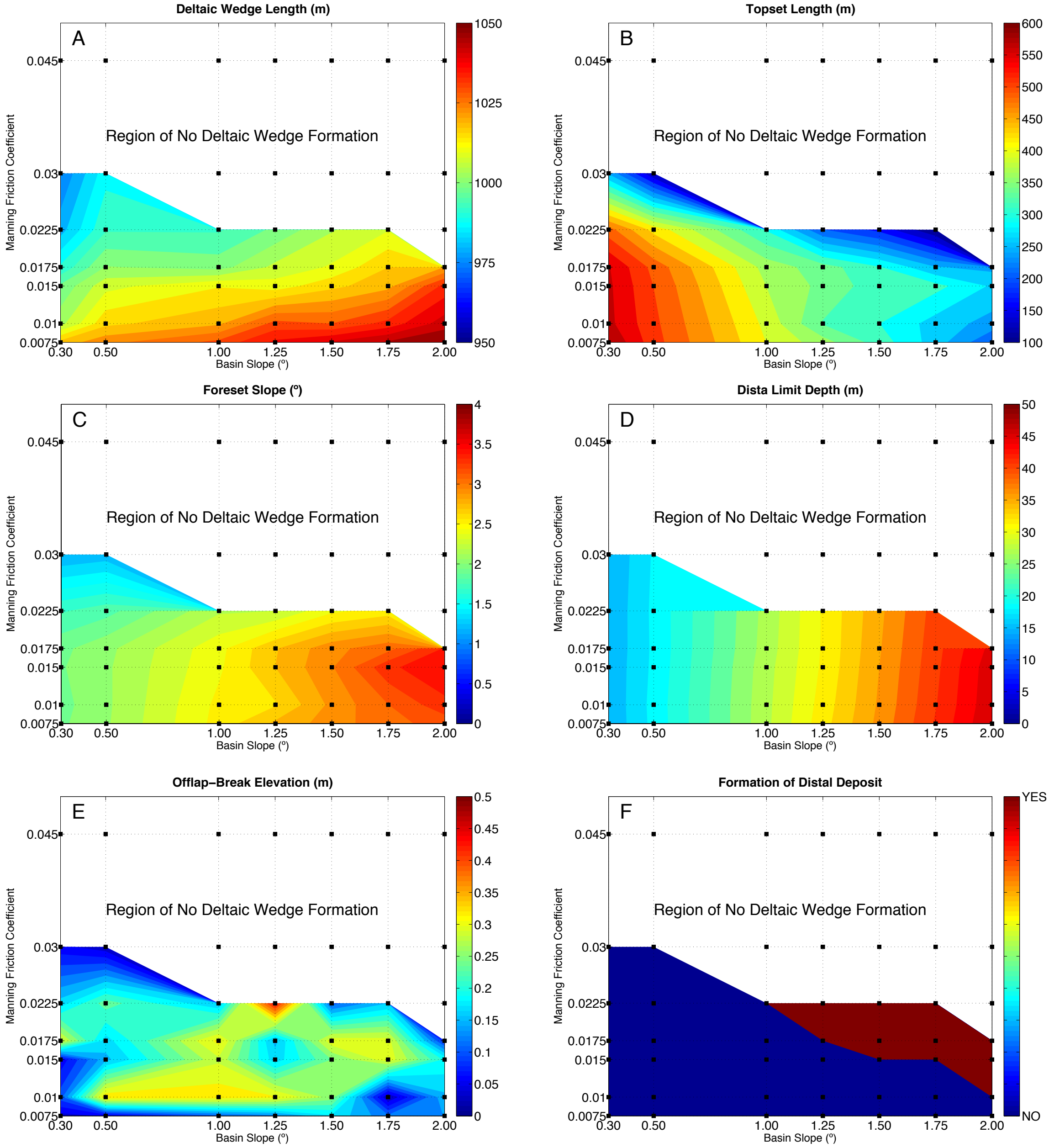

Figure 6.7: Contour plots of the main morphological parameters that characterize the deltaic wedges as a function of the slope of the receiving basin and the Manning friction coefficient of the seafloor: Deltaic wedge length (A), topset length (B), foreset slope (C), distal limit depth (D), offlap-break elevation (E), and formation of a distal deposit (F). Black markers represents the simulated values of each morphological parameters obtained with our numerical simulations. Flow inputs, sediment properties and the remaining numerical parameters are given in Section 6.3.

6.4.2 Characterization of small scale morphological units: seafloor undulations

Seafloor undulations are sediment waves over the foreset of the deltaic wedge formed by the action of the turbidity current flowing across the seabed. These morphological units of small scale have been identified over some deltaic foresets around the Alboran Sea (Fernández-Salas et al., 2007; Lobo et al., 2015).

A simple algorithm has been implemented to determine the seafloor undulations properties for a given deltaic bathymetric profile. A Butterworth low pass filter has been applied to the topset profile at the end of each simulation in which a deltaic wedge was formed in order to remove the profile oscillations in bathymetric data while keeping the global trend of the profile (Figure 6.8). Then, the filtered foreset (red broken line) was subtracted from the foreset obtained with the numerical model (black line), giving rise to the isolated seafloor undulations profile depicted in Figure 6.9. Over this profile we have determined the basis of each undulations (blue circles in Figure 6.9) and the crest of the undulations (red asterisks in Figure 6.9). In the cases in which several crests were detected over a single undulations, the one with the highest elevation was chosen as the undulation crest. Using these singular points, different morphometric characteristics of the seafloor undulations can be used to describe the shape of seafloor undulations. These morphometric characteristics are: (i) number of seafloor undulations (N_u, number of undulation crests over a given foreset), (ii) mean seafloor undulations length that quantifies the dominant visual scale in the flow direction (L_u, average distance between two consecutive undulation basis point of the entire foreset), (iii) mean seafloor undulations height (H_u, average crest elevation of the entire foreset), (iv) mean seafloor undulation form index ($I_f = L_u/H_u$), and (v) the mean seafloor undulation asymmetry index ($I_s = L_s/L_l$, where L_s and L_l are the average length of the wave seaward and landward respectively, i.e., the average distance between the undulation crest and the closest seaward and landward undulation basis of the entire foreset). The results obtained for these variables are shown graphically in Figure 6.10 and are numerically gathered in Table 6.3.

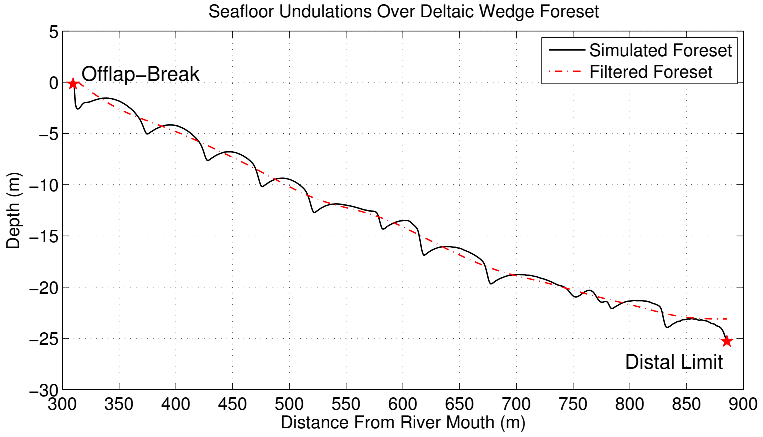

Figure 6.8: Seafloor undulations over the foreset of the deltaic wedge and filtered foreset at the end of the simulation (5 days). This simulation corresponds to the numerical experiments with an initial piecewise linear bathymetric profile with initial slope of 1 and a Manning coefficient of 0.0225. Flow inputs, sediment properties and the remaining numerical parameters are given in Section 6.3.

From Figure 6.10 it is shown that friction is the main factor controlling the formation os these seafloor undulations and that the basin slope plays a negligible role in their genesis. It can be observed from the horizontal contours in Figures 6.10 (A), (B), and (C). In this sense, the number of seafloor undulations over the foreset increases with higher Manning friction coefficient of the bed. Indeed, in the simulations in which the Manning coefficient was set smaller than 0.01 no seafloor undulations where developed and a flat foreset arose (see for example Figure 6.6 (A)). Both the mean seafloor undulation length (Figure 6.10 (B)) and the mean seafloor undulation height (Figure 6.10 (C)) tend to decrease with higher values of Manning friction coefficient.

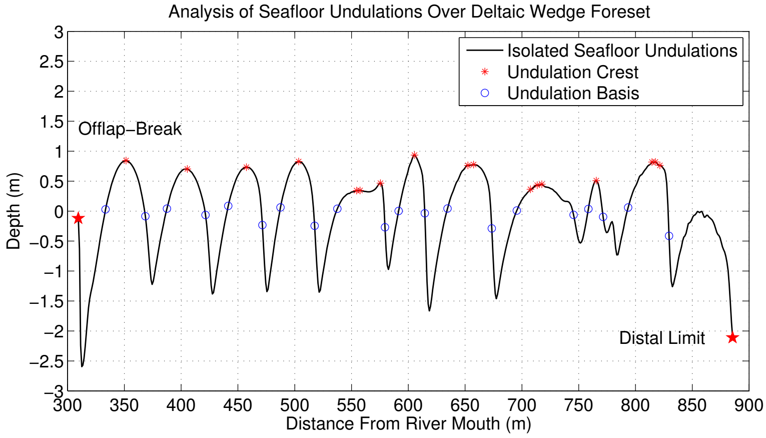

Figure 6.9: Seafloor undulations elevations over the foreset of the deltaic wedge at the end of the simulation (5 days). Red stars and blue circles depict the undulation crests and the basis of the undulation respectively. This simulation corresponds to the numerical experiments with an initial piecewise linear bathymetric profile with initial slope of 1 and a Manning coefficient of 0.0225. Flow inputs, sediment properties and the remaining numerical parameters are given in Section 6.3.

Thus, higher Manning friction coefficient give rise to shorter and flatter undulations. Besides, the previous three variables remain approximately constant regardless the initial receiving basin slope. On the other hand, the mean seafloor undulations form index, which provides a measure of the steepness of the undulations, shows a clear basin slope dependence, while its value seems to be independent of its friction. Steeper basins generate steeper undulation ($I_f \longrightarrow 0$). Finally, the asymmetry index, which defines the plan-view aspect ratio of the undulations field, does not depict a clear dependence of the basin slope and Manning friction coefficient.

Regarding the time required for the system to develop a seafloor undulations field, we observe that the smaller is the friction coefficient, the higher is this time (see panels (A), (B), and (C) in Figure 6.5).

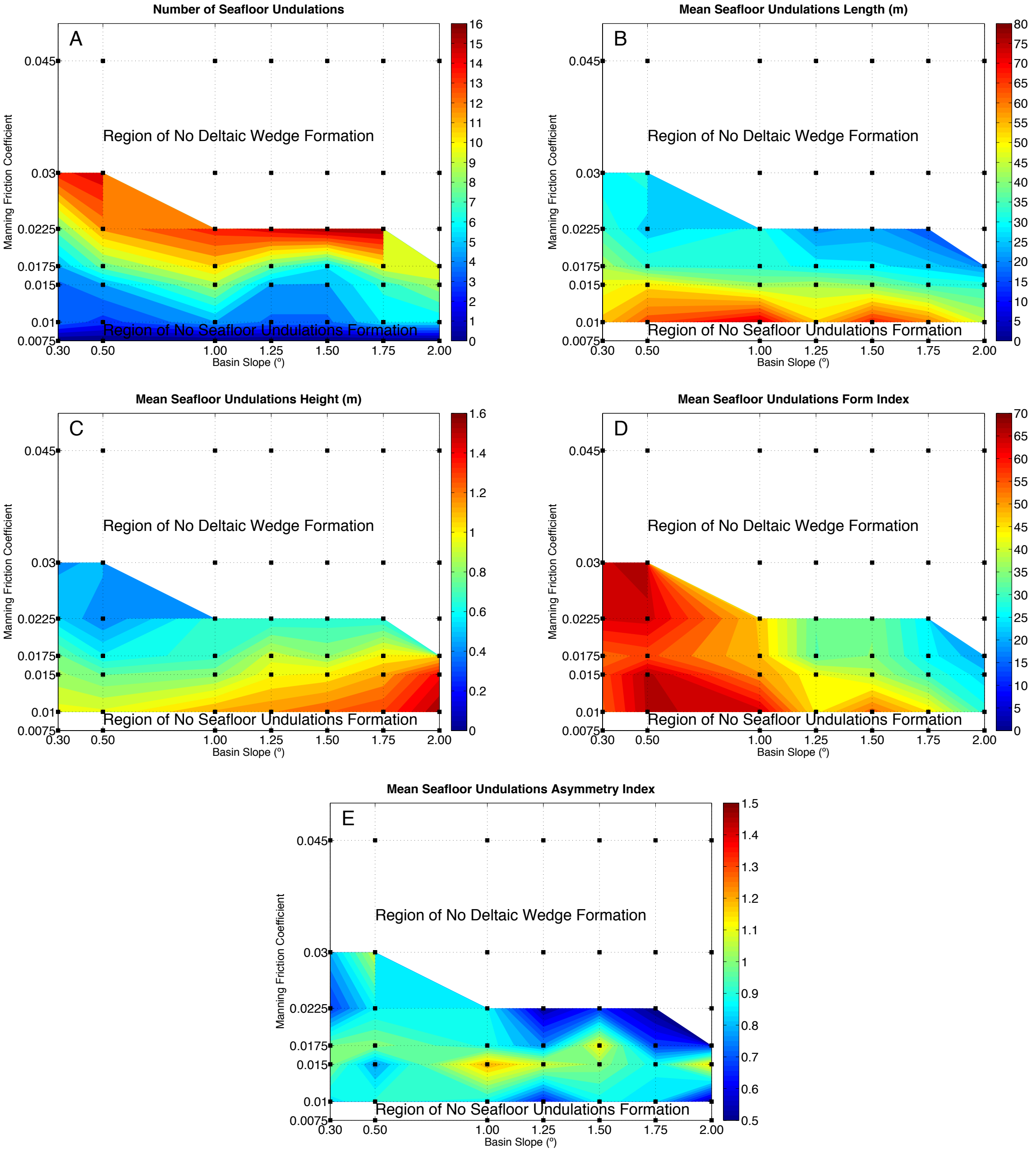

Figure 6.10: Contour plots of the main morphological parameters that characterize the seafloor undulations over a deltaic wedge as a function of the slope of the receiving basin and the Manning friction coefficient of the seafloor: number of seafloor undulations (A), mean seafloor undulations length (B), mean seafloor undulations height (C), mean seafloor undulation form index (D), and mean seafloor undulation asymmetry index (E). Black markers represents the simulated values of each morphological parameters obtained with our numerical simulations. Flow inputs, sediment properties and the remaining numerical parameters are given in Section 6.3.

Sim#	Slope (°)	Manning Coeff.	x_{LD} (m)	y_{LD} (m)	x_{OB} (m)	y_{OB} (m)	S_f (°)	D_d	N_u	L_u (m)	H_u (m)	I_f	I_s
1	0.30	0.01	1020.10	15.28	589.50	0.05	2.03	No	No Seafloor Undulations Formation				
2	0.30	0.01	1005.40	15.35	571.50	0.11	2.01	No	4.00	55.00	0.99	55.56	0.86
3	0.30	0.01	999.70	15.27	569.50	0.06	2.02	No	4.00	49.00	0.86	57.04	1.01
4	0.30	0.02	991.80	15.11	566.50	0.30	1.99	No	5.00	44.00	0.80	55.00	1.00
5	0.30	0.02	981.50	15.22	499.50	0.17	1.79	No	8.00	35.38	0.55	64.32	0.68
6	0.30	0.03	975.40	15.09	258.50	0.06	1.20	No	14.00	30.24	0.46	65.73	0.81
7	0.30	0.04	No Deltaic Wedge Formation										
8	0.50	0.01	1025.30	18.90	524.50	0.06	2.15	No	No Seafloor Undulations Formation				
9	0.50	0.01	1017.50	18.84	520.50	0.34	2.13	No	3.00	65.40	0.98	66.99	0.93
10	0.50	0.01	1009.40	18.75	513.50	0.16	2.15	No	5.00	52.40	0.78	67.36	0.78
11	0.50	0.02	1003.10	18.72	505.50	0.18	2.13	No	8.00	34.75	0.61	57.01	1.01
12	0.50	0.02	994.50	18.74	429.50	0.24	1.88	No	12.00	27.33	0.42	65.08	0.88
13	0.50	0.03	989.60	18.61	135.50	0.04	1.25	No	15.00	34.52	0.50	69.03	1.08
14	0.50	0.04	No Deltaic Wedge Formation										
15	1.00	0.01	1031.50	28.03	412.50	0.11	2.58	No	No Seafloor Undulations Formation				
16	1.00	0.01	1021.70	27.92	405.50	0.33	2.56	No	5.00	75.33	1.16	65.13	0.89
17	1.00	0.01	1014.30	27.61	387.50	0.29	2.50	No	9.00	42.33	0.82	51.44	1.22
18	1.00	0.02	1001.20	27.42	377.50	0.32	2.49	No	11.00	34.00	0.70	48.57	0.91
19	1.00	0.02	994.50	27.43	309.50	0.16	2.28	Yes	14.00	33.20	0.69	47.98	0.88
20	1.00	0.03	No Deltaic Wedge Formation										
21	1.00	0.04	No Deltaic Wedge Formation										
22	1.25	0.01	1039.10	32.77	373.50	0.13	2.81	No	No Seafloor Undulations Formation				
23	1.25	0.01	1031.70	32.55	335.50	0.32	2.65	No	4.00	54.29	1.20	45.29	0.63
24	1.25	0.01	1012.50	32.05	355.50	0.17	2.78	No	5.00	44.00	1.01	43.56	1.09
25	1.25	0.02	1007.80	32.04	349.50	0.16	2.77	Yes	8.00	31.00	0.94	33.05	0.78
26	1.25	0.02	999.80	31.77	212.50	0.45	2.28	Yes	15.00	22.00	0.66	33.34	0.54
27	1.25	0.03	No Deltaic Wedge Formation										
28	1.25	0.04	No Deltaic Wedge Formation										
29	1.50	0.01	1042.70	37.24	325.50	0.18	2.96	No	No Seafloor Undulations Formation				
30	1.50	0.01	1030.30	37.05	312.50	0.26	2.93	No	4.00	69.67	1.26	55.27	0.90
31	1.50	0.01	1017.40	36.64	322.50	0.25	3.00	Yes	5.00	41.00	1.04	39.44	1.02
32	1.50	0.02	1011.20	36.41	314.50	0.31	2.97	Yes	6.00	30.00	0.83	36.04	1.15
33	1.50	0.02	1006.40	36.27	178.50	0.11	2.50	Yes	16.00	24.24	0.68	35.44	0.67
34	1.50	0.03	No Deltaic Wedge Formation										
35	1.50	0.04	No Deltaic Wedge Formation										
36	1.75	0.01	1046.60	41.91	274.50	0.13	3.10	No	No Seafloor Undulations Formation				
37	1.75	0.01	1035.70	41.63	276.50	0.03	3.14	No	6.00	61.33	1.33	46.23	0.85
38	1.75	0.01	1021.10	41.14	320.50	0.31	3.34	Yes	7.00	35.00	1.15	30.50	0.90
39	1.75	0.02	1018.50	41.07	263.50	0.31	3.09	Yes	10.00	27.70	1.04	26.70	0.69
40	1.75	0.02	1010.40	40.80	110.50	0.16	2.59	Yes	16.00	17.00	0.66	25.81	0.51
41	1.75	0.03	No Deltaic Wedge Formation										
42	1.75	0.04	No Deltaic Wedge Formation										
43	2.00	0.01	1049.90	46.70	212.50	0.14	3.18	No	No Seafloor Undulations Formation				
44	2.00	0.01	1044.10	46.44	251.50	0.16	3.34	Yes	6.00	46.00	1.56	29.40	0.53
45	2.00	0.01	1035.50	46.24	283.50	0.20	3.50	Yes	9.00	34.00	1.43	23.85	1.17
46	2.00	0.02	1022.50	45.74	254.50	0.09	3.40	Yes	10.00	22.00	1.07	20.47	0.66
47	2.00	0.02	No Deltaic Wedge Formation										
48	2.00	0.03	No Deltaic Wedge Formation										
49	2.00	0.04	No Deltaic Wedge Formation										

Table 6.3: Main geomorphic characteristics of both the deltaic wedge and seafloor undulations obtained as a function of the receiving basin slope and Manning friction coefficient. Flow inputs, sediment properties and the remaining numerical parameters are given in Section 6.3.

6.5 Discussion and concluding remarks

A total of 49 numerical experiments have been carried out using the one dimensional model proposed by Macías et al. (2016) based on the depth-averaged equation of mass, momentum and sediment conservation of turbidity currents along with the Exner Equation of bed sediment continuity. This model has the capability to simulate the the evolution of an erodible bed due to sediment entrainment and deposition effects related to a turbidity current. This study has presented new insights into the formation of deltaic wedges and sediment waves (seafloor undulations over the deltaic wedge) by turbidity currents as a function of the slope of the receiving basin (continental shelf) and of the Manning friction coefficient of the seabed. The results obtained from the numerical experiments focus on the geomorphic characterization of both large scale morphological units (typical deltaic wedges with a tripartite cross-sectional subdivision topset, foreset, and bottomset) and small scale morphological units (seafloor undulations developed over the foreset).

Simulations suggest that the receiving basin slope and the bottom friction has a strong influence on the development of these morphological units. While the receiving basin slope highly dominates the formation and subsequent development of deltaic wedges, the bottom friction dictates the evolution of seafloor undulations. As a general rule, higher slopes give rise to larger deltaic wedges, shorter topsets, and steeper foresets. On the other hand, rougher beds (higher Manning friction coefficients) favor the formation of a greater number of seafloor undulations, but reduces both the length and the height of the undulation. Finally, higher values of the Manning coefficient produce shorter deltaic wedges. It is due to the reduction of the ability of the river flow to carry sediment further seaward as a consequence of the higher deceleration that it experiences.

Many work still remains to be done on this research line of turbidity currents. The one-dimensional model employed here is a simplified representation of the flow and sedimentary processes which occur in subaqueous turbidity currents. The model represents an initial effort to quantify the effects of basin slope and bottom friction on the mechanics of turbidity currents and of the characteristics of the resulting deposits from a theoretical point of view. Besides, it includes some arbitrary assumptions and parameterizations due to lack of thorough understanding of turbidity current dynamics that can put results under judgment. In this sense, the verification of model results through field observations is a key task that must be done in order to validate the model performance. Despite not having imposed boundary or initial conditions of real situations observed in the nature, results from the model agree with field observations reported by Fernández-Salas et al. (2007). In this work, seafloor undulations lengths and heights measured in the Alboran Sea undulations (Guadalfeo and Verde river deltas) have the same order of magnitude as the ones computed with the model, with values of undulations length ranging from 50 to 100 m, and values of undulations height ranging from 0.5 to 1 m. Thus, the wavy structures reproduced in the model predictions are likely natural. This agreement encourages us in the task of addressing which are the most suitable parametrizations of the different processes involved in turbidity current simulations based on real bathymetric profiles and river discharge conditions that feed the model. Finally, natural sea bed undulations are the result of many events of turbidity currents over long periods of time (Khan et al., 2005). However, we have considered only one event in each simulation. Simulation of numerous turbidity events (and not only an unique event, as in our simulations) may lead to a better understanding of the seabed structure of the continental shelf.

Chapter 7

Conclusions and future research

7.1 Main conclusions

Coastal environments are crucial systems from ecological and socio-economic perspectives. They are subjected to a variety of static and dynamic factors that drive and control them. Besides, coastal environments encompass a large variety of coastal units which response to particular environmental conditions is aimed to be understood. The global assessment of how the coastal environment dynamically evolves is a challenge that can only be addressed if a systematic analysis of its behavior under specific conditions is accomplished. In this connection it is useful to deal with the complexity of specific units of the coastal environment subjected to particular environmental conditions following a zoning criterion. This Thesis is then based on a sequential methodology organized around the spatial zonation of different coastal units, namely, tidal channels, systems of shallow coastal bays, river mouth, and inner shelf. To gain insight into some questions that still remain unclear with regard to the hydrodynamic and morphodynamic processes that govern their evolution, a series of numerical models have been developed/employed.

The main objective of this Thesis was then "*to numerically explore and understand the quantitative testing of specific and unclear hydro-morphodynamic processes that take place at different spatial- and temporal-scales on fluvial/tide-dominated coastal environments, encompassing different coastal units: tidal channel, a shallow coastal bays, river mouth bar, and inner shelf*". Important questions concerning the fate of these different coastal units were raised in Chapter 1. We can now provide answers to these questions as an attempt to gather the most significant conclusions and results associated with this work. The response to these questions, in turn, constitutes the accomplishment of the objectives contemplated in Section 1.2:

- *To develop a coupled onshore and offshore numerical model in order to analyze the hydro-morphodynamics feedbacks between tidal channels and related discharge plumes in semienclosed tidal embayments.*

  The numerical model of Lanzoni and Seminara (2002) concerning hydro-morphodynamic evolution of funnel-shaped tidal channels was used and extended with the aim of including the influence of the offshore discharge plumes. Thus, in the offshore flow motion two well-differentiated phases with a particular flow treatment, based on a numerical/analytical 2D model, were considered: the ebb and flood offshore flow field. For the ebb-phase, jet theory has been extensively used to describe processes experienced by water discharges into resting reservoirs of water. Regarding the flood-phase, potential flow theory allows for an analytic determination of the flow characteristics. Flood field was then modeled as a plane, irrotational and inviscid sink flow, and a Scharwz-Christoffel conformal transformation was finally used to map the flow field near the inlet region. Besides, the sediment flux analysis is not restricted to classical algebraic sediment transport equations that adapt the sediment load instantaneously to local flow conditions. This assumption is particularly severe close to the slack water periods when equilibrium between erosion and deposition cannot occur, as sediments simply settle in a quasi-quiescent water body. Thus, onshore and offshore regions are morphodynamically coupled through an advection-difussion equation of the suspended material. This formulation allows for a consideration of scour and settling lag effects, which in turn may contribute appreciably to the residual flux in tidal channels. Model results are in good agreement with the bathymetric profile of the Punta Umbría ría, a tidal channel in Southwestern Spain.

Our numerical experiments show that the tidal channel bed evolves asymptotically leading to a progressive decrease of the tidal distortion and therefore of the net sediment flux everywhere up to reach an equilibrium state characterized by a concave upwards profile and by a well-defined depth at the inlet section. Besides, the presence of the offshore plume makes the seaward concavity of the profile reduce and consequently smaller inlet depths arise. This condition can be also attained for tidal channels as their convergence length decreases. The feedback between channel and plume also makes the plume reduce its velocity, width and sediment concentration over time, which in turn reduces the net erosion/deposition of material in the continental shelf and the consequent ability for tidal channel to generate mouth bars.

- *To evaluate how intense storm events affect the resilience of a coastal bays system.*

  Recent geological evidence suggests that some extreme storm events may cause significant marsh erosion in shallow coastal bays systems. This has major implications for coastal inundation risk to lives and property, as well as the resilience of these coastal wetlands to a changing climate. We studied the relationship between storm intensity and net sediment fluxes in the Virginia Coast Reserve (VCR), a system of salt marshes and coastal bays along the Atlantic side of the Delmarva Peninsula, USA. To investigate the processes that determine sediment fluxes between the VCR and open sea, we used the fully coupled coastal hydrodynamic, sediment transport and wave model Delft3D-SWAN. This work builds on high-resolution bottom sediment distributions in the Virginia Coast Reserve (VCR), bathymetric and climate data which allowed for the model calibration and validation. A sediment budget was developed for these coastal bays is imperative to understanding how the sediment fluxes exchanges and how storm events affect the resilience of the system. We found that the duration and amount of storm surge have the most significant influence on the amount of sediment imported during a storm event. Thus, results suggest that increased storminess may continue to increase the resilience of coastal bays, providing the material necessary to counteract rising sea levels and increasing the systems resilience. Indeed, yearly mean accumulation of sediment within the domain from the modeled storms during the 5 years of simulations ranged from 2.01 mm to 5.30 mm.

- *To analyze the effects of basin bottom slope at the river mouth on the discharge dynamics and on the related sedimentary processes.*

  A theoretical model of jet-theory and the high-resolution hydro-morphodynamic model Delft3D were employed to explore how the receiving basins slope alter the hydrodynamic structure of an entering sediment-laden turbulent jet and its consequences on related sedimentary patterns. An updated turbulent jet theory is proposed with a slope-dependent entrainment coefficient. Numerical results suggested that the entrainment coefficient displays a power law increase as the slope of the receiving basin increases. Besides, the basin slope alters jet dynamics and favors the formation of an unstable meandering jet, i.e., stability analysis must considerer variations in the bathymetric profile. On the other hand, jet instability dominates sediment delivery and the resulting deposition patterns. While stable jets give rise to "middle-ground" bars accompanied by bifurcating channels, a "lunate" mouth bar results from unstable jets. Moreover, river mouth bar time formation and sedimentary processes are governed by basin slope: mouth bars require more time to form in steeper basins, and the ratio of progradation to aggradation sedimentary processes decreases with higher basin slopes. Their formation is a key geomorphological crucial to delta progradation. Delta networks are formed predominantly by bifurcation around fossilized location of mouth bars. In this sense, we found that the minimum relative water depth over a bar crest that forces the flow to bifurcate around a fully developed bar decreases with the basin slope.

- *To establish a framework of mouth bar morphologies as a function of the basin slope and the river discharge angle.*

  We addressed the role of the receiving basin slope and the river discharge angle in the hydrodynamics of an exiting sediment-laden turbulent jet and in the resulting mouth bar morphologies using the high-resolution hydro-morphodynamic model Delft3D. Changes in the discharge angle and the basin slope of the river mouth alter the jet direction and its planform shape. The jet deviation increases for high discharge angles and high basin slope combinations. The discharge angle is triggering factor for jet deflection, whereas the basin slope acts as an amplifying factor of the jet deviation. On the other hand, the increase in basin bottom slope results in a lower lateral spreading of the jet. Besides, for a given discharge angle, higher slopes give rise to wider jets due to their deviation towards shallower waters due to mass continuity and the lower vertical expansion experienced by the jet.

  The influence of the basin geometry on jet hydrodynamics marks the sedimentary processes at the river mouth, resulting in five possible morphologies: central river mouth bar with or without lateral levees, side bar with or without lateral levees, and sand-spits. A phase space plot of mouth bar morphology as a function of the receiving basin slope and the river discharge angle is then defined. The final bar configurations display similarities to natural systems whose river mouth geometries are mimicked by the geometries set in our simulations.

- *To determine the role of the inner shelf characteristics on the sedimentary processes of turbidity currents.*

  The role of the slope and friction of the inner shelf on the formation of sedimentary wedges and seafloor undulations over the latter by turbidity currents usually linked to short, mountainous, and seasonal fluvial systems is addressed using a numerical model developed by the EDANYA group of the Málaga University. Results suggest that the receiving basin slope dominates the formation and subsequent development of deltaic wedges (higher slopes give rise to larger deltaic wedges, shorter topsets, and steeper foresets), whereas the bottom friction dictates the evolution of seafloor undulations (rougher beds favor the formation of a greater number of seafloor undulations, and reduces both the length and the height of the undulation).

7.2 Future research

After the analysis of the results, many questions remain concerning the evolution of these coastal units subjected to different environmental conditions. Between these environmental factors, the wide variety of different sources of coastal energy, mainly terrestrial (river outflow) and marine (waves and tides), will undoubtedly alter the fate of these systems. However, our studies focused on tidal channels (Chapter 2) and river mouths (Chapters 4 and 5) have been carried out by isolating the effects of tidal currents and river outflows respectively. Because these external forcings drive and control coastal systems, the combination of all of them and variations in their relative intensity are responsible for the morphological diversity in the coastal geomorphology. These external forcings comprise real boundary conditions which relative influence must be addressed in order to go further in the analysis of hydro-morphodynamic processes in coastal environments. For these reasons, the following lines for future research arise:

- Although tidal currents play a dominant role in controlling hydro-morphodynamics of tidal channels, wave activity and the possible influence of river discharge may become progressively important in the outer and inner portions of an estuary linked to its offshore plume. Previous attempts to evaluate the effects of opposing waves on discharge plumes were done by Ismail and Wiegel (1983), Bolla Pittaluga et al. (2015) investigated the morphodynamic equilibrium of tidally dominated alluvial estuaries concerning combined tidal-fluvial cases, and Tambroni and Seminara (2006) included a littoral current in the modeling of the flood field in the near inlet region which can be used to simulate the stokes drift velocity related to the wave motion. For more realistic simulations, the integration of these physical processes into our tidal channel-plume model, whose validity is strictly restricted to estuaries where the tide is the dominant forcing mechanism, becomes an essential task. The presence of intertidal areas flanking the main channel (tidal flats and salt marshes) must be also considered in future works.
- To include the effects of tides and waves in the definition of a conceptual framework of river mouth bar morphology as a function of the river mouth geometry with the aim of covering a wider spectrum of river mouth conditions. Leonardi et al. (2013) and Nardin et al. (2013) isolated the effects of tides and waves, respectively, on a sediment-laden discharge and related river mouth bar formation. The inclusions of these forcings on our simulations will also require attention in the future.

Appendix A

Sensitive analysis

In this appendix of Chapter 4, we perform a sensitivity analysis to test the influence of several numerical parameters on the computed hydrodynamic and morphological outcomes of Delft3D (Table A.1). A total of 44 additional simulations were carried out. We tested the following numerical parameters: grid size (GS), horizontal eddy diffusivity (ϵ_s), morphological scale factor (MSF) and spin-up interval before morphological changes (SU). For all simulations, the geometrical configuration of the study area and boundary conditions are kept constant. In order to quantify the accuracy of the obtained results, the relative errors of the tested values (TV) with respect to the reference value (RV) obtained with the parameters listed in Table 4.1 of centerline velocity (u_c/u_0) and lateral expansion of the jet (b/b_0) at $\xi = 10$, entrainment coefficient (α_{NS}), and relative time (T_{rmbf}) and relative distance (L_{rmbf}) of river mouth bar formation are computed. We also visually classified the resulting jets as stable (S) or unstable (U).

Although logical differences in the detail of Delft3D outcomes can be detected by varying the numerical parameters, the general trend followed by the hydrodynamic and morphodynamic results do not show any deviation from a qualitative point of view for different model parameter settings. Furthermore, all results provided in this work have been normalized, which allows a general comprehension of the behavior of the modeled processes not focussed on absolute results. Finally, the imposed grid size, morphological scale factor and spin-up interval allow a good equilibrium between computational efficiency and results accuracy.

				Relative errors (%) = $\lvert 100\times(\text{TV-RV})/\text{RV}\rvert$					**Stability**	
	RV	**TV**	**m** (%)	$\mathbf{u_c/u_0}$	$\mathbf{b/b_0}$	α_{NS}	$\mathbf{T_{rmbf}}$	$\mathbf{L_{rmbf}}$	**RV**	**TV**
GS (m)	10×10	[5×5,20×20]	0	[1.38,1.12]	[2.38,4.76]	[2.00,1.93]	[0.00,0.00]	[0.00,0.00]	[S]	[S,S]
			1	[0.22,1.18]	[5.56,11.11]	[0.16,0.88]	[0.00,1.50]	[1.92,3.85]	[S]	[S,S]
			4	[2.12,7.98]	[0.00,12.50]	[3.81,5.09]	[1.49,2.12]	[0.98,1.96]	[U]	[U,U]
			8	[3.66,13.51]	[0.00,11.11]	[6.88,11.21]	[1.43,3.01]	[0.98,1.96]	[U]	[U,U]
ϵ_s ($\mathbf{m^2s^{-1}}$)	1	[0.5,5,10]	0	[0.00,0.00,0.00]	[0.00,0.00,0.00]	[0.00,0.00,0.00]	[0.00,0.00,0.00]	[0.00,0.00,0.00]	[S]	[S,S,S]
			1	[0.00,0.00,0.00]	[0.00,0.00,0.00]	[0.00,0.00,0.00]	[7.14,7.14,8.22]	[0.00,2.21,0.86]	[S]	[S,S,S]
			4	[0.00,0.00,0.00]	[0.00,0.00,0.00]	[0.00,0.00,0.00]	[5.97,6.77,8.55]	[3.92,2.36,2.83]	[U]	[U,U,U]
			8	[0.00,0.00,0.00]	[0.00,0.00,0.00]	[0.00,0.00,0.00]	[15.00,1.10,2.83]	[3.92,2.36,1.09]	[U]	[U,U,U]
MSF (-)	20	[10,35,50]	0	[0.00,0.00,0.00]	[0.00,0.00,0.00]	[0.00,0.00,0.00]	[0.00,0.00,0.00]	[0.00,0.00,0.00]	[S]	[S,S,S]
			1	[0.00,0.00,0.00]	[0.00,0.00,0.00]	[0.00,0.00,0.00]	[4.76,1.19,4,76]	[0.00,1.92,0.14]	[S]	[S,S,S]
			4	[0.00,0.00,0.00]	[0.00,0.00,0.00]	[0.00,0.00,0.00]	[6.18,2.99,7.13]	[1.96,0.00,0.17]	[U]	[U,U,U]
			8	[0.00,0.00,0.00]	[0.00,0.00,0.00]	[0.00,0.00,0.00]	[14.63,14.29,9.52]	[1.96,0.00,0.17]	[U]	[U,U,U]
SU (hr)	24	[6,12,36]	0	[0.26,0.00,0.00]	[0.00,0.00,0.00]	[1.02,0.00,0.00]	[0.00,0.00,0.00]	[0.00,0.00,0.00]	[S]	[S,S,S]
			1	[0.46,0.00,0.00]	[0.00,0.00,0.00]	[2.17,0.00,0.00]	[0.00,0.00,0.00]	[0.00,0.00,0.00]	[S]	[S,S,S]
			4	[3.45,1.11,0.23]	[2.38,0.00,0.00]	[4.81,1.21,0.99]	[0.00,0.00,0.00]	[0.00,0.00,0.00]	[U]	[U,U,U]
			8	[2.29,1.77,0.66]	[5.56,4.76,0.00]	[3.22,2.88,0.14]	[0.00,0.00,0.00]	[0.00,0.00,0.00]	[U]	[U,U,U]

Table A.1: Parameters sensitivity analysis.

Bibliography

Abramovich, G. N. (1963). The theory of turbulent jets. *The Massachussets Institute of Technology Press, Cambridge.*

Adams, E. W. and Schlager, W. (2000). Basic types of submarine slope curvature. *Journal of Sedimentary Research*, 70(4):814–828.

Agrawal, A. and Prasad, A. K. (2003). Integral solution for the mean flow profiles of turbulent jets, plumes, and wakes. *Journal of fluids engineering*, 125(5):813–822.

Akiyama, J. and Fukushima, Y. (1985). Entrainment of noncohesive bed sediment into suspension, external memorandom no. 195, st. *Anthony Falls Hydraulic Laboratory, U. of Minnessota.*

Albertson, M. L., Dai, Y., Jensen, R., and Rouse, H. (1950). Diffusion of submerged jets. *Transactions of the American Society of Civil Engineers*, 115(1):639–664.

Alexander, J. and Morris, S. (1994). Observations on experimental, nonchannelized, high-concentration turbidity currents and variations in deposits around obstacles. *Journal of Sedimentary Research*, 64(4).

Altinaker, M., Graf, W., and Hopfinger, E. (1996). Flow structure in turbidity currents. *Journal of Hydraulic Research*, 34(5):713–718.

Andreopoulos, J., Praturi, A., and Rodi, W. (1986). Experiments on vertical plane buoyant jets in shallow water. *Journal of Fluid Mechanics*, 168:305–336.

Anthony, E. J. (2015). Wave influence in the construction, shaping and destruction of river deltas: A review. *Marine Geology*, 361:53–78.

Ashton, A. D. and Giosan, L. (2011). Wave-angle control of delta evolution. *Geophysical Research Letters*, 38(13).

Bagnold, R. (1966). An approach to the sediment transport problem from general physics. *US Geol. Surv. Prof. Paper*, 422:231–291.

Barbier, E. B., Hacker, S. D., Kennedy, C., Koch, E. W., Stier, A. C., and Silliman, B. R. (2011). The value of estuarine and coastal ecosystem services. *Ecological monographs*, 81(2):169–193.

Bárcenas, P. (2013). *Procesos Morfogenéticos y Evolución Reciente de los Depósitos Prodeltaicos del Sureste de la Península Ibérica: Aplicaciones de Modelos Matemáticos.* PhD thesis, Universidad de Málaga.

Bárcenas, P., Lobo, F., Macías, J., Fernández-Salas, L., López-González, N., and del Río, V. D. (2015). Submarine deltaic geometries linked to steep, mountainous drainage basins in the northern shelf of the Alboran Sea: Filling the gaps in the spectrum of deltaic deposition. *Geomorphology*, 232:125–144.

Bates, C. C. (1953). Rational theory of delta formation. *American Association of Petroleum Geologists Bulletin*, 37(9):2119–2162.

Bhallamudi, S. M. and Chaudhry, M. H. (1991). Numerical modeling of aggradation and degradation in alluvial channels. *Journal of Hydraulic Engineering*, 117(9):1145–1164.

Bianchi, T. S. and Allison, M. A. (2009). Large-river delta-front estuaries as natural recorders of global environmental change. *Proceedings of the National Academy of Sciences*, 106(20):8085–8092.

Blondeaux, P., De Bernardinis, B., and Seminara, G. (1982). Correnti di marea in prossimità di imboccature e loro-influenza sul ricambio lagunare. *Atti del XVIII convegno di idraulica e costruzioni idrauliche, Bologna*, pages 21–23.

Boggs, S. (1995). *Principles of sedimentology and stratigraphy*, volume 23117923. Prentice Hall New Jersey.

Boldt, K. V., Lane, P., Woodruff, J. D., and Donnelly, J. P. (2010). Calibrating a sedimentary record of overwash from Southeastern New England using modeled historic hurricane surges. *Marine Geology*, 275(1):127–139.

Bolla Pittaluga, M., Tambroni, N., Canestrelli, A., Slingerland, R., Lanzoni, S., and Seminara, G. (2015). Where river and tide meet: The morphodynamic equilibrium of alluvial estuaries. *Journal of Geophysical Research: Earth Surface*, 120(1):75–94.

Booij, N., Ris, R., and Holthuijsen, L. H. (1999). A third-generation wave model for coastal regions: 1. Model description and validation. *Journal of geophysical research: Oceans*, 104(C4):7649–7666.

Borrego, J. (1992). *Sedimentología del estuario del río Odiel (Huelva, SO España)*. PhD thesis, Universidad de Sevilla, Spain.

Bradford, S. F. and Katopodes, N. D. (1999). Hydrodynamics of turbid underflows. i: Formulation and numerical analysis. *Journal of hydraulic engineering*, 125(10):1006–1015.

Brázdil, R., Glaser, R., Pfister, C., Dobrovolnỳ, P., Antoine, J.-M., Barriendos, M., Camuffo, D., Deutsch, M., Enzi, S., Guidoboni, E., et al. (1999). Flood events of selected European rivers in the sixteenth century. *Climatic change*, 43(1):239–285.

Buonaiuto, F. S. and Kraus, N. C. (2003). Limiting slopes and depths at ebb-tidal shoals. *Coastal Engineering*, 48(1):51–65.

Caldwell, R. L. and Edmonds, D. A. (2014). The effects of sediment properties on deltaic processes and morphologies: A numerical modeling study. *Journal of Geophysical Research: Earth Surface*, 119(5):961–982.

Canestrelli, A., Lanzoni, S., and Fagherazzi, S. (2014a). One-dimensional numerical modeling of the long-term morphodynamic evolution of a tidally-dominated estuary: The lower fly river (papua new guinea). *Sedimentary Geology*, 301:107–119.

Canestrelli, A., Nardin, W., Edmonds, D., Fagherazzi, S., and Slingerland, R. (2014b). Importance of frictional effects and jet instability on the morphodynamics of river mouth bars and levees. *Journal of Geophysical Research: Oceans*, 119(1):509–522.

Chadwick, D. B. and Largier, J. L. (1999). Tidal exchange at the bay-ocean boundary. *Journal of Geophysical Research: Oceans*, 104(C12):29901–29924.

Chanson, H. (2009). *Applied hydrodynamics: an introduction to ideal and real fluid flows*. CRC Press.

Chatanantavet, P. and Lamb, M. P. (2014). Sediment transport and topographic evolution of a coupled river and river plume system: An experimental and numerical study. *Journal of Geophysical Research: Earth Surface*, 119(6):1263–1282.

Chatanantavet, P., Lamb, M. P., and Nittrouer, J. A. (2012). Backwater controls of avulsion location on deltas. *Geophysical Research Letters*, 39(1).

Chaudhry, M. H. (2007). *Open-channel flow*. Springer Science & Business Media.

Chen, S.-N., Geyer, W. R., Ralston, D. K., and Lerczak, J. A. (2012). Estuarine exchange flow quantified with isohaline coordinates: Contrasting long and short estuaries. *Journal of Physical Oceanography*, 42(5):748–763.

Chu, F., Pilkey, W., and Pilkey, O. (1979). An analytical study of turbidity current steady flow. *Marine Geology*, 33(3):205–220.

Cohen, C. (2012). *Shallow-Water Plane and Tidal Jets*. PhD thesis, University of Otago.

Coleman, J. M. (1976). *Deltas: Processes of deposition & models for exploration*. Continuing Education Publication Company.

Coleman, J. M. and Wright, L. (1975). *Deltas: Models for Exploration*, chapter Modern river deltas: variability of processes and sand bodies, pages 99–149. Houston Geological Society.

D'Agostino, K., Seltzer, G., Baker, P., Fritz, S., and Dunbar, R. (2002). Late-Quaternary lowstands of Lake Titicaca: evidence from high-resolution seismic data. *Palaeogeography, Palaeoclimatology, Palaeoecology*, 179(1):97–111.

D'Alpaos, A., Lanzoni, S., Marani, M., and Rinaldo, A. (2007). Landscape evolution in tidal embayments: modeling the interplay of erosion, sedimentation, and vegetation dynamics. *Journal of Geophysical Research: Earth Surface*, 112(F1).

D'Alpaos, A., Lanzoni, S., Marani, M., and Rinaldo, A. (2010). On the tidal prism–channel area relations. *Journal of Geophysical Research: Earth Surface*, 115(F1).

Dalrymple, R. W., Mackay, D. A., Ichaso, A. A., and Choi, K. S. (2012). Processes, morphodynamics, and facies of tide-dominated estuaries. In *Principles of tidal sedimentology*, pages 79–107. Springer.

Dalrymple, R. W., Zaitlin, B. A., and Boyd, R. (1992). Estuarine facies models: conceptual basis and stratigraphic implications: perspective. *Journal of Sedimentary Research*, 62(6).

Davies, G. and Woodroffe, C. D. (2010). Tidal estuary width convergence: Theory and form in north australian estuaries. *Earth Surface Processes and Landforms*, 35(7):737–749.

De Swart, H. and Zimmerman, J. (2009). Morphodynamics of tidal inlet systems. *Annual review of fluid mechanics*, 41:203–229.

Deaton, C. D., Hein, C. J., and Kirwan, M. L. (2017). Barrier island migration dominates ecogeomorphic feedbacks and drives salt marsh loss along the Virginia Atlantic Coast, USA. *Geology*, 45(2):123–126.

Defina, A. (2000). Two-dimensional shallow flow equations for partially dry areas. *Water Resources Research*, 36(11):3251–3264.

Dejoux, C. (2012). *Lake Titicaca: a synthesis of limnological knowledge*, volume 68. Springer Science & Business Media.

DelCharco, M. J. (1992). *Tidal flood water withdrawal, with special reference to Jupiter Inlet, Florida.* PhD thesis.

Deltares (2013). Delft3d-flow, simulation of multi-dimensional hydrodynamic flows and transport phenomena, including sediments. *User Manual. Deltares, Delft, Netherlands.*

Dias, F., Elcrat, A. R., and Trefethen, L. N. (1987). Ideal jet flow in two dimensions. *Journal of Fluid Mechanics*, 185:275–288.

Dietrich, W. E. (1982). Settling velocity of natural particles. *Water resources research*, 18(6):1615–1626.

Díez-Minguito, M., Baquerizo, A., Ortega-Sánchez, M., Navarro, G., and Losada, M. (2012). Tide transformation in the Guadalquivir estuary (SW Spain) and process-based zonation. *Journal of Geophysical Research: Oceans*, 117(C3):2156–2202.

Donnelly, J. P., Bryant, S. S., Butler, J., Dowling, J., Fan, L., Hausmann, N., Newby, P., Shuman, B., Stern, J., Westover, K., et al. (2001). 700 yr sedimentary record of intense hurricane landfalls in southern New England. *Geological Society of America Bulletin*, 113(6):714–727.

Dracos, T., Giger, M., and Jirka, G. (1992). Plane turbulent jets in a bounded fluid layer. *Journal of Fluid Mechanics*, 241:587–614.

Drew, D. A. (1983). Mathematical modeling of two-phase flow. *Annual review of fluid mechanics*, 15(1):261–291.

Dronkers, J. (1986). Tidal asymmetry and estuarine morphology. *Netherlands Journal of Sea Research*, 20(2-3):117–131.

Dyer, K. R. (1973). *Estuaries: a physical introduction.* Wiley, New York.

Dyer, K. R. (1995). Sediment transport processes in estuaries. *Developments in Sedimentology*, 53:423–449.

Edmonds, D. A. (2012). Restoration sedimentology. *Nature Geoscience*, 5:758–759.

Edmonds, D. A. and Slingerland, R. L. (2007). Mechanics of river mouth bar formation: Implications for the morphodynamics of delta distributary networks. *Journal of Geophysical Research: Earth Surface*, 112(F2).

Edmonds, D. A. and Slingerland, R. L. (2010). Significant effect of sediment cohesion on delta morphology. *Nature Geoscience*, 3(2):105–109.

Einstein, H. A. (1950). *The bed-load function for sediment transportation in open channel flows*, volume 1026. U.S. Department of Agriculture, Soil Conservation Service, Washington, D.C.

Emanuel, K. (2008). The hurricaneâĂŤclimate connection. *Bulletin of the American Meteorological Society*, 89(5):ES10–ES20.

Engelund, F. and Fredsøe, J. (1976). A sediment transport model for straight alluvial channels. *Hydrology Research*, 7(5):293–306.

Ericson, J. P., Vörösmarty, C. J., Dingman, S. L., Ward, L. G., and Meybeck, M. (2006). Effective sea-level rise and deltas: causes of change and human dimension implications. *Global and Planetary Change*, 50(1):63–82.

Esposito, C. R., Georgiou, I. Y., and Kolker, A. S. (2013). Hydrodynamic and geomorphic controls on mouth bar evolution. *Geophysical Research Letters*, 40(8):1540–1545.

Fagherazzi, S., Edmonds, D. A., Nardin, W., Leonardi, N., Canestrelli, A., Falcini, F., Jerolmack, D., Mariotti, G., Rowland, J. C., and Slingerland, R. L. (2015). Dynamics of river mouth deposits. *Reviews of Geophysics*, 53(3):642–672.

Fagherazzi, S., Kirwan, M. L., Mudd, S. M., Guntenspergen, G. R., Temmerman, S., D'Alpaos, A., Koppel, J., Rybczyk, J. M., Reyes, E., Craft, C., et al. (2012). Numerical models of salt marsh evolution: Ecological, geomorphic, and climatic factors. *Reviews of Geophysics*, 50(1).

Fagherazzi, S., Mariotti, G., Wiberg, P., and McGlathery, K. (2013). Marsh collapse does not require sea level rise. *Oceanography*, 26(3):70–77.

Fagherazzi, S. and Overeem, I. (2007). Models of deltaic and inner continental shelf landform evolution. *Annu. Rev. Earth Planet. Sci.*, 35:685–715.

Fagherazzi, S. and Wiberg, P. (2009). Importance of wind conditions, fetch, and water levels on wave-generated shear stresses in shallow intertidal basins. *Journal of Geophysical Research: Earth Surface*, 114(F3).

Falcini, F. and Jerolmack, D. J. (2010). A potential vorticity theory for the formation of elongate channels in river deltas and lakes. *Journal of Geophysical Research: Earth Surface*, 115(F4).

Fenster, M. S., Dolan, R., and Smith, J. J. (2016). Grain-size distributions and coastal morphodynamics along the southern maryland and virginia barrier islands. *Sedimentology*, pages 809–823.

Fernandez-Luque, R. and Van Beek, R. (1976). Erosion and transport of bed-load sediment. *Journal of Hydraulic Research*, 14(2):127–144.

Fernández-Salas, L., Lobo, F., Sanz, J., Díaz-del Río, V., García, M., and Moreno, I. (2007). Morphometric analysis and genetic implications of pro-deltaic sea-floor undulations in the northern alboran sea margin, western mediterranean basin. *Marine Geology*, 243(1):31–56.

Fernández-Salas, L. M., Durán, R., Mendes, I., Galparsoro, I., Lobo, F., Bárcenas, P., Rosa, F., Ribó, M., García-Gil, S., Ferrín, A., et al. (2015). Shelves of the iberian peninsula and the balearic islands (i): Morphology and sediment types. *Boletín Geológico y Minero*, 126(2-3):327–376.

Fischer, H. B. (1979). *Mixing in Inland and Coastal Waters*. Academic Press.

Friedrichs, C., Armbrust, B., and De Swart, H. (1998). Hydrodynamics and equilibrium sediment dynamics of shallow, funnel-shaped tidal estuaries. *Physics of estuaries and coastal seas*, pages 315–327.

Friedrichs, C. T. (1995). Stability shear stress and equilibrium cross-sectional geometry of sheltered tidal channels. *Journal of Coastal Research*, pages 1062–1074.

Friedrichs, C. T. and Aubrey, D. G. (1988). Non-linear tidal distortion in shallow well-mixed estuaries: a synthesis. *Estuarine, Coastal and Shelf Science*, 27(5):521–545.

Galappatti, G. and Vreugdenhil, C. (1985). A depth-integrated model for suspended sediment transport. *Journal of Hydraulic Research*, 23(4):359–377.

Galloway, W. E. (1975). Process framework for describing the morphologic and stratigraphic evolution of deltaic depositional systems.

Ganju, N. K., Defne, Z., Kirwan, M. L., Fagherazzi, S., D'alpaos, A., and Carniello, L. (2017). Spatially integrative metrics reveal hidden vulnerability of microtidal salt marshes. *Nature communications*, 8.

Ganju, N. K., Kirwan, M. L., Dickhudt, P. J., Guntenspergen, G. R., Cahoon, D. R., and Kroeger, K. D. (2015). Sediment transport-based metrics of wetland stability. *Geophysical Research Letters*, 42(19):7992–8000.

Ganju, N. K., Nidzieko, N. J., and Kirwan, M. L. (2013). Inferring tidal wetland stability from channel sediment fluxes: Observations and a conceptual model. *Journal of Geophysical Research: Earth Surface*, 118(4):2045–2058.

Garcia, M. and Parker, G. (1991). Entrainment of bed sediment into suspension. *Journal of Hydraulic Engineering*, 117(4):414–435.

Garcia, M. and Parker, G. (1993). Experiments on the entrainment of sediment into suspension by a dense bottom current. *Journal of Geophysical Research: Oceans (1978–2012)*, 98(C3):4793–4807.

García, M. H. (1993). Hydraulic jumps in sediment-driven bottom currents. *Journal of Hydraulic Engineering*, 119(10):1094–1117.

Garcia, M. H. (2008). Sediment transport and morphodynamics. *Sedimentation engineering: Processes, measurements, modeling, and practice*, (110):21–163.

Geleynse, N., Storms, J., Stive, M., Jagers, H., and Walstra, D. (2010). Modeling of a mixed-load fluvio-deltaic system. *Geophysical Research Letters*, 37(5).

Geleynse, N., Storms, J. E., Walstra, D.-J. R., Jagers, H. A., Wang, Z. B., and Stive, M. J. (2011). Controls on river delta formation; insights from numerical modelling. *Earth and Planetary Science Letters*, 302(1):217–226.

Gerber, T. P., Pratson, L. F., Wolinsky, M. A., Steel, R., Mohr, J., Swenson, J. B., and Paola, C. (2008). Clinoform progradation by turbidity currents: modeling and experiments. *Journal of Sedimentary Research*, 78(3):220–238.

Giger, M., Dracos, T., and Jirka, G. (1991). Entrainment and mixing in plane turbulent jets in shallow water. *Journal of hydraulic research*, 29(5):615–642.

Gilbert, G. K. (1890). *Lake Bonneville*, volume 1. US Government Printing Office.

Goertler, H. (1942). Berechnung von aufgaben der freien turbulenz auf grund eines neuen näherungsansatzes. *ZAMM-Journal of Applied Mathematics and Mechanics/Zeitschrift für Angewandte Mathematik und Mechanik*, 22(5):244–254.

Hamblin, P. and Carmack, E. (1978). River-induced currents in a fjord lake. *Journal of Geophysical Research: Oceans*, 83(C2):885–899.

Hasiotis, T., Charalampakis, M., Stefatos, A., Papatheodorou, G., and Ferentinos, G. (2006). Fan delta development and processes offshore a seasonal river in a seismically active region, nw gulf of corinth. *Geo-Marine Letters*, 26(4):199–211.

Hibma, A., Schuttelaars, H. M., and Wang, Z. B. (2003). Comparison of longitudinal equilibrium profiles of estuaries in idealized and process-based models. *Ocean Dynamics*, 53(3):252–269.

Hirsch, C. (2007). *Numerical computation of internal and external flows: The fundamentals of computational fluid dynamics.* Butterworth-Heinemann.

Ho, C.-M. and Huerre, P. (1984). Perturbed free shear layers. *Annual Review of Fluid Mechanics*, 16(1):365–422.

Hodge, J. and Williams, H. (2016). Deriving spatial and temporal patterns of coastal marsh aggradation from hurricane storm surge marker beds. *Geomorphology*, 274:50–63.

Holland, G. J. and Webster, P. J. (2007). Heightened tropical cyclone activity in the North Atlantic: natural variability or climate trend? *Philosophical Transactions of the Royal Society of London A: Mathematical, Physical and Engineering Sciences*, 365(1860):2695–2716.

Hussain, A. F. (1983). Coherent structures–reality and myth. *Physics of Fluids*, 26(10):2816–2850.

Ikeda, S. (1982). Incipient motion of sand particles on side slopes. *Journal of the Hydraulics Division*, 108(1):95–114.

Inman, D. L. and Brush, B. M. (1973). The coastal challenge. *Science*, 181:20–32.

Ismail, N. M. and Wiegel, R. L. (1983). Opposing wave effect on momentum jets spreading rate. *Journal of waterway, port, coastal, and ocean engineering*, 109(4):465–483.

Jarrett, J. T. (1976). Tidal prism - inlet area relationships. *General Investigation of Tidal Inlets, Report 3*.

Jerolmack, D. J. and Swenson, J. B. (2007). Scaling relationships and evolution of distributary networks on wave-influenced deltas. *Geophysical Research Letters*, 34(23).

Jiménez-Robles, A. M., Ortega-Sánchez, M., and Losada, M. (2016). Effects of basin bottom slope on jet hydrodynamics and river mouth bar formation. *Journal of Geophysical Research: Earth Surface*, 121:1110–1133.

Jirka, G. (1994). Shallow jets. In *Recent Research Advances in the Fluid Mechanics of Turbulent Jets and Plumes*, volume 255, pages 155–175. Springer Netherlands.

Jirka, G. H. (2001). Large scale flow structures and mixing processes in shallow flows. *Journal of hydraulic research*, 39(6):567–573.

Joshi, P. B. (1982). Hydromechanics of tidal jets. *Journal of the Waterway Port Coastal and Ocean Division*, 108(3):239–253.

Kabiri-Samani, A., Amirabdollahian, M., and Farshi, F. (2012). Analytical solution for the free over-fall weir flow using conformal mapping and potential flow theory. *International Journal of Hydraulic Engineering*, 1(6):75–82.

Kernkamp, H. and Uittenbogaard, R. (2001). 2d-les of a free-surface mixing layer. In *Direct and Large-Eddy Simulation IV*, pages 409–418. Springer.

Keulegan, G. H. (1938). Laws of turbulent flow in open channels. *Journal of Research of the National Bureau of Standards*, 21(6):707–841.

Khan, S. M., Imran, J., Bradford, S., and Syvitski, J. (2005). Numerical modeling of hyperpycnal plume. *Marine Geology*, 222:193–211.

Khanin, V. (1978). Potential model of the coanda effect. *Fluid Dynamics*, 13(4):492–503.

Kirwan, M. L. and Murray, A. B. (2007). A coupled geomorphic and ecological model of tidal marsh evolution. *Proceedings of the National Academy of Sciences*, 104(15):6118–6122.

Kirwan, M. L., Temmerman, S., Skeehan, E. E., Guntenspergen, G. R., and Fagherazzi, S. (2016). Overestimation of marsh vulnerability to sea level rise. *Nature Climate Change*, 6(3):253–260.

Kotsovinos, N. E. (1975). *A study of the entrainment and turbulence in a plane bouyant jet.* PhD thesis, California Institute of Technology.

Kubo, Y. (2004). Experimental and numerical study of topographic effects on deposition from two-dimensional, particle-driven density currents. *Sedimentary Geology*, 164(3):311–326.

Kubo, Y. and Nakajima, T. (2002). Laboratory experiments and numerical simulation of sediment-wave formation by turbidity currents. *Marine Geology*, 192(1):105–121.

Lalli, F., Bruschi, A., Lama, R., Liberti, L., Mandrone, S., and Pesarino, V. (2010). Coanda effect in coastal flows. *Coastal Engineering*, 57(3):278–289.

Lamb, M. P., Nittrouer, J. A., Mohrig, D., and Shaw, J. (2012). Backwater and river plume controls on scour upstream of river mouths: Implications for fluvio-deltaic morphodynamics. *Journal of Geophysical Research: Earth Surface (2003–2012)*, 117(F1).

Landel, J. R., Caulfield, C., and Woods, A. W. (2012). Meandering due to large eddies and the statistically self-similar dynamics of quasi-two-dimensional jets. *Journal of Fluid Mechanics*, 692:347–368.

Lane, E. W. (1957). *A study of the shape of channels formed by natural streams flowing in erodible material.* US Army Engineer Division, Missouri River.

Lanzoni, S. and Seminara, G. (1998). On tide propagation in convergent estuaries. *Journal of Geophysical Research*, 103:30–793.

Lanzoni, S. and Seminara, G. (2002). Long-term evolution and morphodynamic equilibrium of tidal channels. *Journal of Geophysical Research: Oceans*, 107(C13001).

Leonardi, N., Canestrelli, A., Sun, T., and Fagherazzi, S. (2013). Effect of tides on mouth bar morphology and hydrodynamics. *Journal of Geophysical Research: Oceans*, 118(9):4169–4183.

Leonardi, N. and Fagherazzi, S. (2014). How waves shape salt marshes. *Geology*, 42(10):887–890.

Leonardi, N. and Fagherazzi, S. (2015). Effect of local variability in erosional resistance on large-scale morphodynamic response of salt marshes to wind waves and extreme events. *Geophysical Research Letters*, 42(14):5872–5879.

Leonardi, N., Sun, T., and Fagherazzi, S. (2014). Modeling tidal bedding in distributary-mouth bars. *Journal of Sedimentary Research*, 84(6):499–512.

Lesser, G. R., Roelvink, J. A., van Kester, J. A. T. M., and Stelling, G. S. (2004). Development and validation of a three-dimensional morphological model. *Coastal Engineering*, 51(8-9):883–915.

Liquete, C., Arnau, P., Canals, M., and Colas, S. (2005). Mediterranean river systems of Andalusia, southern Spain, and associated deltas: a source to sink approach. *Marine Geology*, 222:471–495.

Lobo, F., Goff, J., Mendes, I., Bárcenas, P., Fernández-Salas, L., Martín-Rosales, W., Macías, J., and del Río, V. D. (2014). Spatial variability of prodeltaic undulations on the Guadalfeo River prodelta: support to the genetic interpretation as hyperpycnal flow deposits. *Marine Geophysical Research*, 36(4):309–333.

Lobo, F., Goff, J., Mendes, I., Bárcenas, P., Fernández-Salas, L., Martín-Rosales, W., Macías, J., and del Río, V. D. (2015). Spatial variability of prodeltaic undulations on the guadalfeo river prodelta: support to the genetic interpretation as hyperpycnal flow deposits. *Marine Geophysical Research*, 36(4):309–333.

MacCormack, R. (2003). The effect of viscosity in hypervelocity impact cratering. *Journal of spacecraft and rockets*, 40(5):757–763.

Macías, J., Bárcenas, P., MJ, C., Fernández-Salas, L., and Morales, T. (2013). Improvements on turbidity currents models for application to real cases.

Macías, J., Castro, M. J., and Morales, T. (2016). A turbidity current model for real world applications. In *EGU General Assembly Conference Abstracts*, volume 18, page 4025.

Marani, M., D'Alpaos, A., Lanzoni, S., Carniello, L., and Rinaldo, A. (2007). Biologically-controlled multiple equilibria of tidal landforms and the fate of the venice lagoon. *Geophysical Research Letters*, 34(11).

Mariotti, G. and Fagherazzi, S. (2010). A numerical model for the coupled long-term evolution of salt marshes and tidal flats. *Journal of Geophysical Research: Earth Surface*, 115(F1).

Mariotti, G., Fagherazzi, S., Wiberg, P., McGlathery, K., Carniello, L., and Defina, A. (2010). Influence of storm surges and sea level on shallow tidal basin erosive processes. *Journal of Geophysical Research: Oceans*, 115(C11).

Mariotti, G., Falcini, F., Geleynse, N., Guala, M., Sun, T., and Fagherazzi, S. (2013). Sediment eddy diffusivity in meandering turbulent jets: Implications for levee formation at river mouths. *Journal of Geophysical Research: Earth Surface*, 118(3):1908–1920.

Masselink, G., Hughes, M., et al. (2003). *Introduction to coastal processes and geomorphology.* Arnold, Hodder Headline Group.

Mathews, J. H. and Howell, R. W. (2012). *Complex analysis for mathematics and engineering.* Jones & Bartlett Publishers.

McKee, B., Aller, R., Allison, M., Bianchi, T., and Kineke, G. (2004). Transport and transformation of dissolved and particulate materials on continental margins influenced by major rivers: benthic boundary layer and seabed processes. *Continental Shelf Research*, 24(7):899–926.

McLoughlin, S. M., Wiberg, P. L., Safak, I., and McGlathery, K. J. (2015). Rates and forcing of marsh edge erosion in a shallow coastal bay. *Estuaries and coasts*, 38(2):620–638.

Meyer-Peter, E. and Müller, R. (1948). Formulas for bed-load transport. In *Proceedings of the 2nd Meeting of the International Association for Hydraulic Structures Research*, pages 39–64. International Association of Hydraulic Research Delft.

Middleton, G. V. (1967). Experiments on density and turbidity currents: Iii. deposition of sediment. *Canadian Journal of Earth Sciences*, 4(3):475–505.

Mikhailov, V. (1966). Hydrology and formation of river mouth bars. *Problems of the Humid Tropical Zone Deltas*, 1:59–64.

Miozzi, M., Lalli, F., and Romano, G. P. (2010). Experimental investigation of a free-surface turbulent jet with coanda effect. *Experiments in Fluids*, 49(1):341–353.

Morales, J. A., Borrego, J., and Davis, R. A. (2014). A new mechanism for chenier development and a facies model of the Saltés Island chenier plain (SW Spain). *Geomorphology*, 204:265–276.

Morales, T., Díaz, M. C., Madronal, C. P., and Fernandez Nieto, E. (2009). On a shallow water model for the simulation of turbidity currents. *Communications in Computational Physics*, 6(4):848.

Morton, B., Taylor, G., and Turner, J. (1956). Turbulent gravitational convection from maintained and instantaneous sources. *Proceedings of the Royal Society of London. Series A. Mathematical and Physical Sciences*, 234(1196):1–23.

Morton, R. A. and Donaldson, A. C. (1973). Sediment distribution and evolution of tidal deltas along a tide-dominated shoreline, Wachapreague, Virginia. *Sedimentary Geology*, 10(4):285–299.

Mulder, T. and Syvitski, J. P. (1995). Turbidity currents generated at river mouths during exceptional discharges to the world oceans. *The Journal of Geology*, pages 285–299.

Nakagawa, H. and Tsujimoto, T. (1980). Sand bed instability due to bed load motion. *Journal of the Hydraulics Division*, 106(12):2029–2051.

Nardin, W. and Fagherazzi, S. (2012). The effect of wind waves on the development of river mouth bars. *Geophysical Research Letters*, 39(12).

Nardin, W., Mariotti, G., Edmonds, D., Guercio, R., and Fagherazzi, S. (2013). Growth of river mouth bars in sheltered bays in the presence of frontal waves. *Journal of Geophysical Research: Earth Surface*, 118(2):872–886.

Nava-Sanchez, E. H., Gorsline, D. S., Cruz-Orozco, R., and Godinez-Orta, L. (1999). The El Coyote fan delta: a wave-dominated example from the Gulf of California, Mexico. *Quaternary International*, 56(1):129–140.

Nielsen, P. (1992). Coastal bottom boudary layers and sediment transport.

Nienhuis, J. H., Ashton, A. D., and Giosan, L. (2015). What makes a delta wave-dominated? *Geology*, 43(6):511–514.

Nihoul, J. and Adam, Y. (1975). Dispersion and settling around a waste disposal point in a shallow sea. *Journal of Hydraulic Research*, 13(2):171–186.

Niño, Y., Lopez, F., and Garcia, M. (2003). Threshold for particle entrainment into suspension. *Sedimentology*, 50(2):247–263.

O'Brien, M. P. (1969). Equilibrium flow areas of inlets on sandy coasts. *Journal of the Waterways and Harbors Division*, 95(1):43–52.

Olabarrieta, M., Geyer, W. R., and Kumar, N. (2014). The role of morphology and wave-current interaction at tidal inlets: An idealized modeling analysis. *Journal of Geophysical Research: Oceans*, 119(12):8818–8837.

Olabarrieta, M., Warner, J. C., and Kumar, N. (2011). Wave-current interaction in Willapa Bay. *Journal of Geophysical Research: Oceans*, 116(C12).

Ortega-Sánchez, M., Lobo, F., López-Ruiz, A., Losada, M., and Fernández-Salas, L. (2014). The influence of shelf-indenting canyons and infralittoral prograding wedges on coastal morphology: The Carchuna system in Southern Spain. *Marine Geology*, 347:107–122.

Ortega-Sánchez, M., Losada, M., and Baquerizo, A. (2003). On the development of large-scale cuspate features on a semi-reflective beach: Carchuna beach, Southern Spain. *Marine Geology*, 198(3):209–223.

Ortega-Sánchez, M., Losada, M. A., and Baquerizo, A. (2008). A global model of a tidal jet including the effects of friction and bottom slope. *Journal of Hydraulic Research*, 46(1):80–86.

Orton, G. and Reading, H. (1993). Variability of deltaic processes in terms of sediment supply, with particular emphasis on grain size. *Sedimentology*, 40(3):475–512.

Özsoy, E. (1977). *Flow separation and related phenomena at tidal inlets.* PhD thesis, University of Florida.

Özsoy, E. (1986). Ebb-tidal jets: a model of suspended sediment and mass transport at tidal inlets. *Estuarine, Coastal and Shelf Science*, 22(1):45–62.

Özsoy, E. and Ünlüata, Ü. (1982). Ebb-tidal flow characteristics near inlets. *Estuarine, Coastal and Shelf Science*, 14:251–263.

Paillat, S. and Kaminski, E. (2014). Second-order model of entrainment in planar turbulent jets at low reynolds number. *Physics of Fluids*, 26(045110).

Paola, C., Twilley, R. R., Edmonds, D. A., Kim, W., Mohrig, D., Parker, G., Viparelli, E., and Voller, V. R. (2011). Natural processes in delta restoration: Application to the Mississippi Delta. *Annual review of marine science*, 3:67–91.

Paola, C. and Voller, V. (2005). A generalized exner equation for sediment mass balance. *Journal of Geophysical Research: Earth Surface*, 110(F04014).

Parker, G., Fukushima, Y., and Pantin, H. M. (1986). Self-accelerating turbidity currents. *Journal of Fluid Mechanics*, 171:145–181.

Partheniades, E. et al. (1965). Erosion and deposition of cohesive soils. *Journal of the Hydraulics Division, ASCE*, 91(1):105–139.

Poesen, J. and Hooke, J. (1997). Erosion, flooding and channel management in Mediterranean environments of southern Europe. *Progress in Physical Geography*, 21(2):157–199.

Pont, D., Day, J. W., Hensel, P., Franquet, E., Torre, F., Rioual, P., Ibànez, C., and Coulet, E. (2002). Response scenarios for the deltaic plain of the rhone in the face of an acceleration in the rate of sea-level rise with special attention tosalicornia-type environments. *Estuaries*, 25(3):337–358.

Postma, G. (1990). Depositional architecture and facies of river and fan deltas: a synthesis. *Coarse-grained deltas*, 10:13–28.

Postma, G. (1995). Sea-level-related architectural trends in coarse-grained delta complexes. *Sedimentary Geology*, 98(1):3–12.

Postma, H. (1967). Sediment transport and sedimentation in the estuarine environment. *Estuaries. AAAS*, 83:158–179.

Prandle, D. (1991). Tides in estuaries and embayments. *Tidal hydrodynamics*, pages 125–152.

Prandle, D. (2003). Relationships between tidal dynamics and bathymetry in strongly convergent estuaries. *Journal of Physical Oceanography*, 33(12):2738–2750.

Raghavendra Rao, V. (1991). Giant petroleum accumulations in delta environments. *MemoirsÃćÂĂŤGeological Society of India*, 20:95–108.

Rainwater, E. (1975). Petroleum in deltaic sediments. *Deltas: Models for Exploration*, pages 3–11.

Rajaratnam, N. (1976). *Turbulent jets*. Elsevier.

Ramaprian, B. and Chandrasekhara, M. (1985). LDA measurements in plane turbulent jets. *Journal of Fluids Engineering*, 107(2):264–271.

Reading, H. and Collinson, J. (1996). Clastic coasts. *Sedimentary environments: processes, facies and stratigraphy*, pages 154–231.

Reyes-Merlo, M. Á. (2016). *Multiscale analysis of morphodynamic processes in estuaries and their integration into dredging projects*. PhD thesis, University of Granada.

Reyes-Merlo, M. Á., Tintoré-Parra, Á., Díez-Minguito, M., Ortega-Sánchez, M., and Losada, M. A. (2015). Morphodynamic evolution and influence of dredging activities in small-scale mesotidal estuaries: the case of Punta Umbría (Southwestern Spain). In *Proceedings of the 36th IAHR-International Association for Hydro-Environment Engineering and Research World Congress*.

Robinson, S. E. (1994). *Clay mineralogy and sediment texture of environments in a barrier island-lagoon system*. PhD thesis, University of Virginia.

Roelvink, J. (2006). Coastal morphodynamic evolution techniques. *Coastal Engineering*, 53(2):277–287.

Rowland, J. C., Dietrich, W. E., and Stacey, M. T. (2010). Morphodynamics of subaqueous levee formation: Insights into river mouth morphologies arising from experiments. *Journal of Geophysical Research: Earth Surface*, 115(F04007).

Rowland, J. C., Stacey, M. T., and Dietrich, W. E. (2009). Turbulent characteristics of a shallow wall-bounded plane jet: experimental implications for river mouth hydrodynamics. *Journal of Fluid Mechanics*, 627:423–449.

Salas, L. F., Sánchez, F. J. L., Molina, F. J. H., del Río, V. D., and Losada, L. S. (2008). Modelo estratigráfico secuencial de muy alta resolución de los depósitos del alto nivel del mar del holoceno superior en el sur de la península ibérica. *Geotemas (Madrid)*, (10):523–525.

Sanford, L. P. and Halka, J. P. (1993). Assessing the paradigm of mutually exclusive erosion and deposition of mud, with examples from upper chesapeake bay. *Marine Geology*, 114(1):37–57.

Savenije, H. H. (2006). *Salinity and tides in alluvial estuaries*. Elsevier.

Savenije, H. H. and Veling, E. J. (2005). Relation between tidal damping and wave celerity in estuaries. *Journal of Geophysical Research: Oceans*, 110(C4).

Schuttelaars, H. and Swart, H. d. (1996). An idealized long-term morphodynamic model of a tidal embayment. *European Journal of Mechanics - B/Fluids*, 15:55–80.

Schuttelaars, H. and Swart, H. d. (2000). Multiple morphodynamic equilibria in tidal embayments. *Journal of Geophysical Research: Oceans*, 105(C10):24105–24118.

Seminara, G., Lanzoni, S., Tambroni, N., and Toffolon, M. (2010). How long are tidal channels? *Journal of Fluid Mechanics*, 643:479–494.

Small, C. and Nicholls, R. J. (2003). A global analysis of human settlement in coastal zones. *Journal of Coastal Research*, 19(3):584–599.

Smith, J. D. and McLean, S. (1977). Spatially averaged flow over a wavy surface. *Journal of Geophysical research*, 82(12):1735–1746.

Sobel, A. H., Camargo, S. J., Hall, T. M., Lee, C.-Y., Tippett, M. K., and Wing, A. A. (2016). Human influence on tropical cyclone intensity. *Science*, 353(6296):242–246.

Soh, W., Tanaka, T., and Taira, A. (1995). Geomorphology and sedimentary processes of a modern slope-type fan delta (Fujikawa fan delta), Suruga Trough, Japan. *Sedimentary Geology*, 98(1-4):79–95.

Solari, S., Egüen, M., Polo, M. J., and Losada, M. A. (2017). Peaks Over Threshold (POT): A methodology for automatic threshold estimation using goodness of fit p-value. *Water Resources Research*, 53.

Soulsby, R. (1997). *Dynamics of marine sands: a manual for practical applications*. Thomas Telford.

Speer, P. E., Aubrey, D. G., and Friedrichs, C. T. (1991). Nonlinear hydrodynamics of shallow tidal inlet/bay systems. *Tidal hydrodynamics*, pages 321–339.

Stanhope, J. W., Anderson, I. C., and Reay, W. G. (2009). Base flow nutrient discharges from lower Delmarva Peninsula watersheds of Virginia, USA. *Journal of Environmental Quality*, 38(5):2070–2083.

Stolzenbach, K. D. and Harleman, D. R. (1971). Analytical and experimental investigation of surface discharges of heated water.

Stommel, H. M. and Former, H. G. (1952). On the nature of estuarine circulation: part I (chapters 3 and 4). Technical report, Woods Hole Oceanographic Institution.

Storms, J. E., Stive, M. J., Roelvink, D., Walstra, D. J., et al. (2007). Initial morphologic and stratigraphic delta evolution related to buoyant river plumes. In *Coastal Sediments 07*, pages 736–748. ASCE.

Syvitski, J. P., Kettner, A. J., Overeem, I., Hutton, E. W., Hannon, M. T., Brakenridge, G. R., Day, J., Vörösmarty, C., Saito, Y., Giosan, L., et al. (2009). Sinking deltas due to human activities. *Nature Geoscience*, 2(10):681–686.

Syvitski, J. P. and Saito, Y. (2007). Morphodynamics of deltas under the influence of humans. *Global and Planetary Change*, 57(3):261–282.

Tambroni, N., Bolla Pittaluga, M., and Seminara, G. (2005). Laboratory observations of the morphodynamic evolution of tidal channels and tidal inlets. *Journal of Geophysical Research: Earth Surface*, 110(F4).

Tambroni, N. and Seminara, G. (2006). Are inlets responsible for the morphological degradation of venice lagoon? *Journal of Geophysical Research: Earth Surface*, 111(F3).

Thomas, C. R. and Blum, L. K. (2010). Importance of the fiddler crab Uca pugnax to salt marsh soil organic matter accumulation. *Marine Ecology Progress Series*, 414:167–177.

Todeschini, I., Toffolon, M., and Tubino, M. (2008). Long-term morphological evolution of funnel-shape tide-dominated estuaries. *Journal of Geophysical Research: Oceans*, 113(C5).

Toffolon, M. and Lanzoni, S. (2010). Morphological equilibrium of short channels dissecting the tidal flats of coastal lagoons. *Journal of Geophysical Research: Earth Surface*, 115(F4).

Toffolon, M., Vignoli, G., and Tubino, M. (2006). Relevant parameters and finite amplitude effects in estuarine hydrodynamics. *Journal of Geophysical Research: Oceans*, 111(C10).

Tollmien, W. (1926). Berechnung turbulenter ausbreitungsvorgänge. *ZAMM-Journal of Applied Mathematics and Mechanics/Zeitschrift für Angewandte Mathematik und Mechanik*, 6(6):468–478.

Tweel, A. W. and Turner, R. E. (2012). Landscape-scale analysis of wetland sediment deposition from four tropical cyclone events. *PloS one*, 7(11):e50528.

Uittenbogaard, R. and Van Vossen, B. (2004). Subgrid-scale model for quasi-2d turbulence in shallow water. *Jirka and Uijttewaal (Eds) Shallow Flows, Taylor and Francis.*

Urgeles, R., Cattaneo, A., Puig, P., Liquete, C., De Mol, B., Amblàs, D., Sultan, N., and Trincardi, F. (2011). A review of undulated sediment features on Mediterranean prodeltas: distinguishing sediment transport structures from sediment deformation. *Marine Geophysical Research*, 32(1-2):49–69.

Vallentine, H. R. (2013). *Applied hydrodynamics.* Springer.

Van der Wegen, M. and Roelvink, J. (2008). Long-term morphodynamic evolution of a tidal embayment using a two-dimensional, process-based model. *Journal of Geophysical Research: Oceans*, 113(C3).

Van Maanen, B., Coco, G., and Bryan, K. R. (2011). A numerical model to simulate the formation and subsequent evolution of tidal channel networks. *Australian Journal of Civil Engineering*, 9(1):61–72.

van Rijn, L. (2013). Simple general formulae for sand transport in rivers, estuaries and coastal waters. *Retrieved fro m www.leovanrijn-sediment.com*.

Van Rijn, L., Roelvink, J., and Horst, W. t. (2001). Approximation formulae for sand transport by currents and waves and implementation in DELFT-MOR. Technical report, Deltares (WL).

van Rijn, L. C. (1984a). Sediment pick-up functions. *Journal of Hydraulic Engineering*, 110(10):1494–1502.

van Rijn, L. C. (1984b). Sediment transport, part I: Bed load transport. *Journal of hydraulic engineering*, 110(10):1431–1456.

van Rijn, L. C. (1984c). Sediment transport, part II: Suspended load transport. *Journal of Hydraulic Engineering*, 110(11):1613–1641.

van Rijn, L. C. (1984d). Sediment transport, part III: Bed forms and alluvial roughness. *Journal of hydraulic engineering*, 110(12):1733–1754.

Van Vossen, B. (2000). Horizontal large eddy simulations; evaluation of computations with delft3d-flow. report meah-197. *Delft University of Technology*.

Vanvyve, E., Delle Monache, L., Monaghan, A. J., and Pinto, J. O. (2015). Wind resource estimates with an analog ensemble approach. *Renewable Energy*, 74:761–773.

Viparelli, E., Blom, A., and Parker, G. (2012). Modeling stratigraphy formed by prograding Gilbert-type deltas. In *River Flow 2012: Proceedings of the International Conference on Fluvial Hydraulics*, volume 365, pages 5–7.

Vlijm, R. (2011). *Process-based modelling of morphological response to submerged breakwaters*. PhD thesis, TU Delft, Delft University of Technology.

Walsh, K. J., McBride, J. L., Klotzbach, P. J., Balachandran, S., Camargo, S. J., Holland, G., Knutson, T. R., Kossin, J. P., Lee, T.-c., Sobel, A., et al. (2016). Tropical cyclones and climate change. *Wiley Interdisciplinary Reviews: Climate Change*, 7(1):65–89.

Walters, D., Moore, L. J., Duran Vinent, O., Fagherazzi, S., and Mariotti, G. (2014). Interactions between barrier islands and backbarrier marshes affect island system response to sea level rise: Insights from a coupled model. *Journal of Geophysical Research: Earth Surface*, 119(9):2013–2031.

Walters, D. C. and Kirwan, M. L. (2016). Optimal hurricane overwash thickness for maximizing marsh resilience to sea level rise. *Ecology and evolution*, 6(9):2948–2956.

Wang, F. C. (1984). The dynamics of a river-bay-delta system. *Journal of Geophysical Research: Oceans*, 89(C5):8054–8060.

Wells, J. T. (1995). Tide-dominated estuaries and tidal rivers. *Developments in Sedimentology*, 53:179–205.

Wiberg, P. L., Carr, J. A., Safak, I., and Anutaliya, A. (2015). Quantifying the distribution and influence of non-uniform bed properties in shallow coastal bays. *Limnology and Oceanography: Methods*, 13(12):746–762.

Wind, H. and Vreugdenhil, C. (1986). Rip-current generation near structures. *Journal of fluid mechanics*, 171:459–476.

Winterwerp, J. (2007). On the sedimentation rate of cohesive sediment. *Proceedings in Marine Science*, 8:209–226.

Winterwerp, J. C., Wang, Z. B., van Braeckel, A., van Holland, G., and Kösters, F. (2013). Man-induced regime shifts in small estuaries–II: a comparison of rivers. *Ocean Dynamics*, 63(11-12):1293–1306.

Wolanski, E. and Imberger, J. (1987). Friction-controlled selective withdrawal near inlets. *Estuarine, Coastal and Shelf Science*, 24(3):327–333.

Woodruff, J. D., Irish, J. L., and Camargo, S. J. (2013). Coastal flooding by tropical cyclones and sea-level rise. *Nature*, 504(7478):44–52.

Wright, L. (1977). Sediment transport and deposition at river mouths: a synthesis. *Geological Society of America Bulletin*, 88(6):857–868.

Wright, L. and Coleman, J. M. (1973). Variations in morphology of major river deltas as functions of ocean wave and river discharge regimes. *AAPG Bulletin*, 57(2):370–398.

Wright, L. and Coleman, J. M. (1974). Mississippi river mouth processes: effluent dynamics and morphologic development. *The Journal of Geology*, pages 751–778.

Wright, L. D., Coleman, J. M., and Erickson, M. W. (1974). Analysis of major river systems and their deltas: Morphologic and process comparisons. Technical report, DTIC Document.

Yao, H., Leonardi, N., Li, J., and Fagherazzi, S. (2016). Sediment transport in a surface-advected estuarine plume. *Continental Shelf Research*, 116:122–135.

Yu, Q., Wang, Y., Gao, S., and Flemming, B. (2012). Modeling the formation of a sand bar within a large funnel-shaped, tide-dominated estuary: Qiantangjiang Estuary, China. *Marine Geology*, 299:63–76.

Zhou, Z., Coco, G., Townend, I., Olabarrieta, M., van der Wegen, M., Gong, Z., D'Alpaos, A., Gao, S., Jaffe, B. E., Gelfenbaum, G., et al. (2017). Is "Morphodynamic Equilibrium" an oxymoron? *Earth-Science Reviews*, 165:257–267.